



HAL
open science

Experimental investigation of corner stall in a linear compressor cascade

Wei Ma

► **To cite this version:**

Wei Ma. Experimental investigation of corner stall in a linear compressor cascade. Other. Ecole Centrale de Lyon, 2012. English. NNT : 2012ECDL0002 . tel-00728374

HAL Id: tel-00728374

<https://theses.hal.science/tel-00728374>

Submitted on 5 Sep 2012

HAL is a multi-disciplinary open access archive for the deposit and dissemination of scientific research documents, whether they are published or not. The documents may come from teaching and research institutions in France or abroad, or from public or private research centers.

L'archive ouverte pluridisciplinaire **HAL**, est destinée au dépôt et à la diffusion de documents scientifiques de niveau recherche, publiés ou non, émanant des établissements d'enseignement et de recherche français ou étrangers, des laboratoires publics ou privés.

ÉCOLE CENTRALE DE LYON

École Doctorale Mécanique, Energétique, Génie Civil et Acoustique

THÈSE

Experimental Investigation of Corner Stall in a Linear Compressor Cascade

Soutenue le 15 Février 2012

par

MA Wei (马威)

en vue d'obtenir le titre de

DOCTEUR DE L'ÉCOLE CENTRALE DE LYON

spécialité

MÉCANIQUE

Devant le jury composé de :

Julian SCOTT	Professeur, École Centrale de Lyon, France	<i>Président</i>
Michel STANISLAS	Professeur, École Centrale de Lille, France	<i>Rapporteur</i>
SUN Xiaofeng	Professeur, Beihang University, Chine	<i>Rapporteur</i>
Jean-François BROUCKAERT	Professeur, Von Karman Institute, Belgique	<i>Examineur</i>
Francis LEBOEUF	Professeur, École Centrale de Lyon, France	<i>Directeur</i>
LU Lipeng	Professeur, Beihang University, Chine	<i>Directeur</i>
Xavier OTTAVY	Chargé de Recherche au CNRS, France	<i>Co-directeur</i>

Acknowledgements

The research described in this thesis was carried out at Laboratoire de Mécanique des Fluides et d'Acoustique (LMFA), Ecole Centrale Lyon in France between September 2008 and February 2012, under the collaboration with Beihang University in China, and supported by China Scholarship Council (CSC). This support is gratefully acknowledged. Without the support and encouragement of many people, I would not have arrived at this position and stage of my life.

First of all, I would like to express my sincere gratitude to my supervisors Prof. Francis LEBOEUF and Prof. LU Lipeng for giving me the opportunity to research in France. They are my invaluable inspiring mentors and always challenged me to think further.

I owe a debt of gratitude to my co-supervisor Dr. Xavier OTTAVY for the continuous guidance, tremendous supports and great encouragement. Besides in research, I also appreciate your help during my incessant pursuit of better understanding French culture and refining my French. I thank you as a supervisor but even more as a friend.

I want to thank the two referees of my manuscript, Prof. Michel STANISLAS and Prof. SUN Xiaofeng for the time and energy they have put in reading my manuscript and their valuable comments on my work. I am also grateful to Prof. Julian SCOTT and Prof. Jean-François BROUCKAERT for accepting to be members of the jury.

This work would not have been the same without the help of colleagues in LMFA. I wish to thank Sébastien GOGUEY, Pierre LAUCHER, Benoît PAOLETTI, Gilbert HALTER, for their fine work in the experimental set-up. I would like to thank Emmanuel JONDEAU for his help in hot-wire anemometry and Nathalie GROSJEAN for her help in PIV. I especially want to thank Dr. Faouzi LAADHARI for useful discussions on turbulent boundary layer. I thank Dr. FANG Le for the many inspiring discussions and for the answers for my uncountable number of questions. The numerical work was with the help of GAO Feng, thanks very much. Thanks also to Dr. Antoine GODARD and Dr. Véronique PENIN for their help and interesting discussions. I thank Philippe Eyraud for his help in finding many references in the library. I thank the colleagues, Andrea AMICARELLI, Cyril MAUGER and Guillaume DESPRES for the nice international atmosphere in our office.

Finally I am most grateful to my parents and my elder sister for their love and for always encouraging me to go my own ways. All my love goes to my girl friend YU Fang with whom I share my entire heart and soul.

Abstract

In applied research, a lack of understanding of corner stall, i.e. the three-dimensional (3D) separation in the juncture of the endwall and blade corner region, which has limited the efficiency and the stability of compressors. Both Reynolds-averaged Navier-Stokes (RANS) and large eddy simulation (LES) still need to be calibrated for turbomachinery applications. In the fundamental research of the turbulent boundary layer (TBL), there are a lot of findings of the effects of curvature and pressure gradients, which also play an important role in physics of corner stall. The purpose of this thesis is (i) to carry out an experiment in a cascade, (ii) to gain a database that could be used to calibrate both RANS and LES, and (iii) to give some basic explanations of corner stall through investigating the TBL on the suction side at the mid-span which is more complex than those in the basic investigations but simpler than those in a real engine.

A detailed and accurate experiment of 3D flow field through a linear compressor cascade has been set up. Experimental data were acquired for a Reynolds number of 3.82×10^5 based on blade chord and inlet flow conditions. Measurements have been achieved by hot-wire anemometry, pressure taps on blade and endwall, five-hole pressure probe, oil visualization, 2D particle image velocimetry (PIV), and two-component laser Doppler anemometry (LDA). An original and complete database was thus obtained.

The TBL on the suction side at mid-span was investigated. The wall-normal negative pressure gradient restrains the separation, on the contrary to its influence in the corner stall. The streamwise adverse pressure gradient can be responsible for the development of Reynolds stresses. The remarkable phenomenon at measurement stations near the trailing edge of blade is that an inflection point occurs in each profile of the mean streamwise velocity. At this inflection point, the magnitudes of the Reynolds stresses reach their maximum values, and the direction of energy diffusion also changes.

The velocity field in the corner stall was presented. Bimodal histograms of velocity exist in the experiment. The bimodal points mainly appear in the region around the mean interface of separated flow and non-separated flow. At a bimodal point the local two velocity components are non-independent from each other, due to the aperiodic interplay of two basic modes in the flow field. Two modes were proposed to interpret the physics of bimodal behaviour.

Keywords: compressor cascade, corner stall, corner separation, experimental data, turbulent boundary layer, bimodal histograms.

Résumé

Dans le domaine de la recherche appliquée, les turbomachinistes sont confrontés à un manque de compréhension de la physique du décollement de coin. Ce décollement tridimensionnel (3D) à la jonction de l'extrados des aubages et du moyeu limite l'efficacité et la stabilité des compresseurs. Les simulations numériques utilisant les deux types de modélisations, «Reynolds Averaged Navier-Stokes» (RANS) et «Large Eddy Simulation» (LES), doivent encore être étalonnées pour des applications turbomachines. Dans la recherche fondamentale concernant la couche limite turbulente (TBL), il existe beaucoup d'études sur les effets de courbure et de gradients de pression qui jouent également un rôle important dans la physique du décollement de coin. Le but de cette thèse est de réaliser une expérience dans une grille d'aubes de compresseur pour acquérir une base de données qui pourrait être utilisée non seulement pour calibrer à la fois les approches RANS et LES, mais aussi pour donner quelques explications fondamentales sur le décollement de coin. Cette expérience permet aussi une étude de la TBL se développant sur l'extrados à mi-envergure des aubages, qui est plus complexe que les TBL rencontrées dans des configurations plus fondamentales, mais plus simples que celles existant d'un turboréacteur.

Une expérience précise et détaillée de l'écoulement 3D au passage d'une grille d'aubes de compresseur a été mis en place. Les mesures ont été réalisées pour un nombre de Reynolds basé sur les conditions d'entrée et la corde de l'aubage de $3,82 \times 10^5$. Des mesures ont été réalisées par anémométrie à fil chaud, par des prises de pression sur la paroi latérale et sur l'aubage, par une sonde de pression à cinq trous, par la visualisation d'huile, par la Vélocimétrie par Images de Particules (PIV) 2D, ainsi que par Anémométrie Laser Doppler (LDA) à deux composants. Une base de données originale et complète a ainsi été obtenue.

Concernant l'étude de la TBL sur l'extrados à mi-envergure, le gradient négatif de pression normal à la paroi retarde le décollement, ce qui est paradoxal avec son influence sur le décollement de coin tel que présentée dans la littérature. Le gradient de pression adverse dans la direction de l'écoulement est responsable de l'accroissement des tensions de Reynolds. Un phénomène remarquable proche du bord de fuite de l'aubage est qu'il existe un point d'inflexion dans le profil de la vitesse moyenne de l'écoulement. A ce point d'inflexion, les grandeurs des tensions de Reynolds atteignent leurs valeurs maximales et la direction de diffusion de l'énergie est inversée.

Le champ de vitesse dans le décollement de coin a été présenté. L'expérience met en évidence l'existence d'histogrammes bimodaux de vitesse. Les points de mesures faisant apparaître ce caractère bimodal sont essentiellement localisés dans la région de l'interface du décollement de l'écoulement moyenné en temps. Deux modes ont été proposés pour interpréter la physique du comportement bimodal. Pour un point bimodal, les deux composantes de vitesse sont localement non-indépendantes, en raison de l'interaction aperiodique de ces deux modes.

Mots Clés: grille d'aubes de compresseur, décollement de coin, base de données expérimental, couche limite turbulente, histogrammes bimodaux.

Contents

Acknowledgements	i
Abstract	ii
Résumé	iii
Nomenclatures	vii
1 Introduction	1
1.1 Background and motivation	1
1.2 Research objectives	3
1.3 Thesis outline	4
2 Literature survey	5
2.1 Introduction	6
2.2 Linear cascade	6
2.3 Turbulent boundary layer	8
2.4 Corner stall	17
2.5 Conclusions	26
3 Experimental and numerical methods	27
3.1 Geometry of cascade	28
3.2 Experimental methods	34
3.3 Inlet reference parameters	73
3.4 Test procedure	74
3.5 Numerical method	76

4	Cascade performance	81
4.1	Introduction	82
4.2	Inlet flow conditions	84
4.3	Effects of incidence	89
4.4	Development of outlet flow	98
4.5	Conclusions	105
5	Turbulent boundary layer at mid-span	106
5.1	Introduction	107
5.2	Influences of three factors in traditional TBL studies	108
5.3	Magnitudes of three factors in our case	109
5.4	Mean velocity profiles	114
5.5	Backflow coefficient and histogram of velocity	119
5.6	Boundary layer thicknesses and shape factors	121
5.7	Determinations of skin friction and friction velocity	128
5.8	Mean velocity profiles in inner coordinate and velocity defect profiles	130
5.9	Pressure gradient parameters	131
5.10	Reynolds stresses	132
5.11	Second-order turbulent correlation coefficients	143
5.12	Triple correlations	147
5.13	Skewness and flatness	148
5.14	Examining scalings	150
5.15	Conclusions	152
6	Velocity flow field in corner stall	155
6.1	Introduction	156
6.2	Choice of incidence	156
6.3	Choice of experimental layout	158
6.4	Mean velocity	159
6.5	Comparisons of PIV and LDA	166
6.6	Backflow coefficients	169

6.7	Bimodal histograms of velocity	170
6.8	Conclusions	187
7	Conclusions and Prospects	188
7.1	Conclusions	188
7.2	Prospects	191
A	Uncertainty analysis	192
A.1	Total measurement error	192
A.2	Infinite number of samples	193
A.3	Finite number of samples	194
A.4	Uncertainty in the results derived from these primary measurements	195
B	Correction of five-hole pressure probe according to total pressure gradient	197
C	Influences of trips	199
C.1	Transition and extent of corner stall	200
C.2	Pressure distribution on the blade	200
C.3	Nearby flow field	201
C.4	Conclusions	202
D	Numerical simulation	203
D.1	Turbulence models and boundary conditions	204
D.2	Effects of incidence	205
D.3	Development of outlet flow	209
D.4	Outlet angles	210
D.5	Velocity field	211
E	Code for decomposition of PDF	214
	References	215
	List of Figures	223
	List of Tables	227

Nomenclatures

Roman letters

a_1	[-]	ratio of Reynolds normal stresses, $a_1 = -\overline{u'v'}/2k$
AR	[-]	aspect ratio of the blade, $AR = h/c$
B	[-]	additive constant in the law of the wall
c	[m]	chord
c_a	[m]	axial chord
C_p	[-]	coefficient of static pressure, $C_p = (P_s - P_{s\infty})/(P_{t\infty} - P_{s\infty})$
C_f	[-]	skin friction coefficient, $C_f = \tau_w/(0.5\rho U_e^2)$
d	[m]	diameter of hot-wire probe
D	[-]	Lei's diffusion parameter
DF	[-]	Lieblein diffusion factor
F_x, F_y	[-]	pressure force on blade along spanwise in x direction and y direction
F_x^*, F_y^*	[-]	pressure force on blade in x direction and y direction
h	[m]	blade span
H_{12}	[-]	shape factor, $H_{12} = \delta^*/\theta$
H_{23}	[-]	shape factor, $H_{23} = \theta/\delta_3$
H_{32}	[-]	shape factor, $H_{32} = 1/H_{23}$
H	[-]	shape factor, $H = 0.5442H_{23}[H_{23}/(H_{23} - 0.5049)]^{0.5}$
i	[°]	incidence angle
i^*	[°]	optimum incidence
\vec{i}, \vec{j}	[-]	unit normal vector of x axis and y axis
k	[m ² /s ²]	turbulent kinetic energy, $k = \frac{1}{2}(\overline{u'^2} + \overline{v'^2} + \overline{w'^2})$
	[-]	air specific heat ratio, $k=1.4$
K	[m ⁻¹]	curvature of blade suction side, $ K =1/R$; convex, $K<0$; concave, $K>0$
	[m ⁻¹]	wave number
l	[m]	active length of hot-wire probe
l^+	[-]	dimensionless characteristic of hot-wire length scale, $l^+ = lu_\tau/\nu$
L	[m]	length of arc from leading edge to trailing edge
	[m]	energy containing scale, $L = k^{3/2}/\epsilon$
Ma	[-]	Mach number
n	[m]	distance to the blade surface in the normal direction to the surface
P, P_s	[Pa]	mean static pressure
P_t	[Pa]	mean total pressure
$P_{s\infty}$	[Pa]	reference mean static pressure
$P_{t\infty}$	[Pa]	reference mean total pressure
P^+	[-]	pressure gradient parameter, $P^+ = \frac{1}{\rho} \frac{\nu}{u_\tau^2} \frac{dP}{ds}$

R	[m]	radius of curvature, $R = 1/K$
	[J/(kg·K)]	ideal gas constant, $R=287.06$ J/(kg·K)
$R_{u'_i u'_n}$	[-]	correlation coefficient
Re_c	[-]	Reynolds number based on blade chord
Re_θ	[-]	Reynolds number based on momentum thickness
s, n, z	[m]	curvilinear coordinates of cascade
s	[m]	pitch of cascade
	[m]	length of arc from leading edge to other point on the blade surface
S	[-]	Lei's stall indicator
s^*	[-]	position of LDA measurement station, $s^* = s/L$
T_s	[K]	static temperature
T_t	[K]	total temperature
Tu	[-]	turbulence intensity, $Tu = \sqrt{u'^2}/U_\infty$
Tu_{local}	[-]	local turbulence intensity, $Tu_{local} = \sqrt{u'^2}/U_{local}$
u_x, u_y, u_z	[m/s]	instantaneous velocity components in x, y, z directions, respectively
u'_x, u'_y, u'_z	[m/s]	fluctuation velocity components in x, y, z directions, respectively
U_x, U_y, U_z	[m/s]	time mean velocity components in x, y, z directions, respectively
u_τ	[m/s]	friction velocity, $u_\tau = \sqrt{\tau_w/\rho}$
U_∞	[m/s]	reference velocity
U_e	[m/s]	mean velocity at the limit of the boundary layer
U_{pw}	[m/s]	potential flow velocity at the wall
x, y, z	[m]	Cartesian coordinates of cascade

Greek letters

α	[-]	relative position of the two Gaussian distributions at a bimodal point
β	[-]	Clauser pressure gradient parameter, $\beta = \frac{\delta^*}{\tau_w} \frac{dp}{ds}$
β_1	[°]	actual upstream flow angle
β'_1	[°]	design upstream flow angle
β_2	[°]	actual downstream flow angle
β'_2	[°]	design downstream flow angle
γ	[°]	stagger angle of the cascade
δ, δ_{99}	[m]	thickness of boundary layer
δ^0	[°]	flow deviation angle
δ^*	[m]	displacement thickness of boundary layer
δ_3	[m]	energy thickness of boundary layer
ϵ	[m ² /s ³]	turbulent dissipation rate
η	[m]	Kolmogorov micro scale, $\eta = (v^3/\epsilon)^{1/4}$
η_1	[-]	first backflow percent coefficient
η_2	[-]	second backflow percent coefficient
κ	[-]	Von Karman constant
Λ	[-]	Castillo & George pressure parameter, $\Lambda = \frac{\delta}{\rho U_\infty^2} \frac{dp}{(d\delta/ds) ds}$
μ	[kg/(m·s)]	dynamic molecular viscosity
μ_t	[kg/(m·s)]	dynamic eddy viscosity

ν	[m ² /s]	kinematic turbulence viscosity
θ	[m]	momentum thickness of boundary layer
	[°]	flow turning angle
	[°]	angle of the mean vector of a mode at a bimodal point
ρ	[kg/m ³]	density
σ		standard deviation
τ_w	[kg/(m·s ²)]	wall shear stress
φ	[°]	camber angle of the blade
ω	[-]	coefficient of total pressure loss, $\omega = (P_{t\infty} - P_t)/(P_{t\infty} - P_{s\infty})$
	[s ⁻¹]	specific turbulent dissipation rate, $\omega = \epsilon/k$
ω^*	[-]	pitchwise-mass-averaged total pressure loss coefficient
ω'	[-]	mass-averaged total pressure loss coefficient

Superscripts

'	fluctuation quantity	+	inner quantity	-	time averaged quantity
~	averaged by Favre decomposition	→	vector quantity		

Subscripts

∞	reference quantity	<i>max</i>	maximum value	<i>min</i>	minimum value
<i>rms</i>	root-mean-square	<i>s</i>	secondary flow quantity		

Symbols

<> time averaged quantity

Acronyms

1/2/3C	one-/two-/three-component	1/2/3D	one-/two-/three-dimensional
APG	adverse pressure gradient	CFD	computational fluid dynamics
DES	detached eddy simulation	DNS	direct numerical simulation
FFT	fast Fourier transform	FPG	favourable pressure gradient
HWA	hot-wire anemometry	LDA	laser Doppler anemometry
LES	large eddy simulation	NPG	negative pressure gradient
PDF	probability density function	PPG	positive pressure gradient
RANS	Reynolds-averaged Navier-Stokes	PIV	particle image velocimetry
RMS	root-mean-square	S-A	Spalart-Allmaras
TBL	turbulent boundary layer	ZPG	zero pressure gradient

Chapter 1

Introduction

Contents

1.1 Background and motivation	1
1.2 Research objectives	3
1.3 Thesis outline	4

1.1 Background and motivation

Compressor is one of the vital parts of an axial gas engine. Today the length of compressor is about 50-60% of the total length of an axial gas engine; the mass of compressor is almost 35-40% of the total mass of an axial gas engine; and the compressor pressure ratio is already as high as 30-40. With the gradual increase in aircraft performance, an increase in the engine thrust-weight ratio is still required. To increase this trust-weight ratio of the gas turbine, it is necessary to achieve the target of compressor pressure ratio using minimum mass of the compressor. Increasing the blade loading is one way to achieve this arduous task, because it can increase the stage pressure ratio and eventually reduce the number of compressor stages.

However the blade loading is strongly limited by the three-dimensional (3D) flow separations in the compressor passage, as shown in Fig. 1.1. Corner separation is one of these kinds of separations (Wisler, 1985). In the extremely complicated flow field in an axial flow compressor (as shown in Fig. 1.2), corner separations are 3D flow separation in the hub region, which involve flow separation on both the endwall and the blade suction surface. They are commonly referred to as corner stall or wall stall. These separated flows cause blockage in the passage and reattach and mix with the mainstream in the hub region downstream. The blockage is usually

large enough to affect the performance of compressors and the endwall and corner regions are responsible for most of the loss generation. There have been a lot of studies that discussed the importance and the physics of 3D flows in axial compressors. Among these are [Dong *et al.* \(1987\)](#), [Schulz *et al.* \(1990a\)](#), [Barankiewicz & Hathaway \(1998\)](#), [Hah & Loellbach \(1999\)](#) and [Gbadebo \(2003\)](#). About the mechanism, corner stall is caused mainly by the strong streamwise pressure gradient, the presence of secondary flows, merging of the wall and blade boundary layers, and the presence of horseshoe vortices in the case of a thick leading edge (the effect of horseshoe vortices is more severe in a turbine than in a compressor). However, an effective control of these effects has been very difficult to achieve, although there has been substantial progress in understanding the physics of corner stall over the years. This is mainly due to the fact that the nature and characteristics of corner stall are still not clearly understood, and the mechanisms and factors that influence their growth and size are not well quantified.

Today computational fluid dynamics (CFD) has been a more and more powerful tool to understand the physics of the flow field in the compressor and to shorten the design cycle, with a gradual increase in computing power. However, the current 3D computations of Reynolds-averaged Navier-Stokes (RANS) equations can only capture the overall pattern of corner separation, but not the flow details such as the separation points and extent of separations. Recently large eddy simulation (LES) is one of the more promising models of numerical simulation of turbulence, but it still needs to be calibrated for turbomachinery applications.

The curvature and the pressure gradients play an important role in physics of corner stall, through their effects on the turbulent boundary layers (TBLs) on the blade and the endwall. In the literature, a lot of basic investigations on the TBL have been dedicated to investigate the individual effects of the streamwise pressure gradient and of the curvature, as well as their combined effects. Considerable research findings have been obtained through these basic investigations. However most of these basic investigations are restricted to relatively simple geometries. Therefore it is necessary to apply these basic findings to a TBL, which suffers a more complex influence than those in the basic investigations but simpler than those in a real engine. This investigation could give some explanations of the characteristic of more complex TBLs such as that in the region of the corner stall.

The present work is therefore intended to carry out a careful experiment of the corner stall in a linear cascade, which is a simplified model for compressor. The TBL at mid-span of the cascade suffers a more complex influence than those in the basic investigations but simpler than those in a real engine.

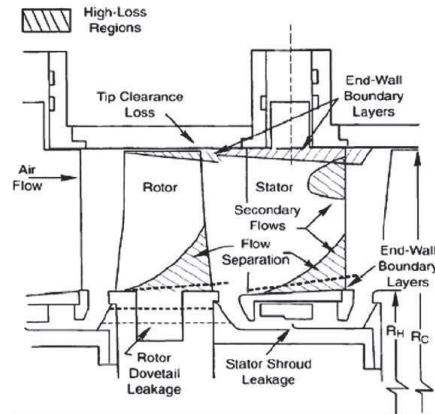


Figure 1.1: High-loss regions in compressors (Wisler, 1985).

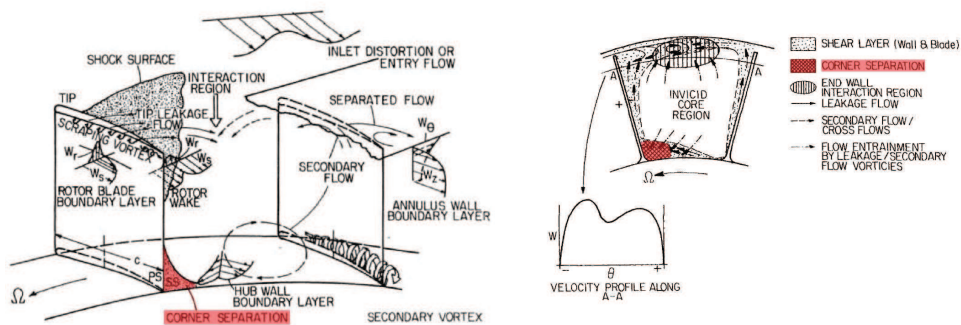


Figure 1.2: Schematic representation of the flow field in an axial flow compressor rotor passage (Lakshminarayana, 1996, left figure, pp.17; right figure, pp.508)

1.2 Research objectives

This thesis started in September 2008 and was under the collaboration of Ecole Centrale de Lyon in France and Beihang University in China. The objectives of this research are:

1. Carrying out an experiment of the 3D flow field through a linear compressor cascade. These data should be usable to evaluate and improve the capability of both RANS and LES.
2. Investigating the TBL at mid-span using the research findings in fundamental researches.
3. Gaining a better knowledge of the mechanisms of the 3D corner stall.

1.3 Thesis outline

In this chapter, the background and the research objectives were introduced.

The first part of Chapter 2 gives a review of the basic features of a linear cascade. This is followed by a review of the related aspects of TBL and corner stall.

Chapter 3 is devoted to the experimental and numerical methods used in this study. This includes the geometry of cascade, the description and the uncertainties of the measurements, and the presentation of the numerical simulations that have been carried out for the test configuration.

In Chapter 4, inlet flow conditions are presented first of all. Then, to assess the effects of the incidence on the flow behavior and the overall performance of the cascade, measurements have been carried out in a range of incidences from -2° to 6° . The measurements include the static pressure on the blade and the endwall measured by pressure taps and outlet flow variables measured by a five-hole pressure probe. Finally, the development of outlet flow is presented.

In Chapter 5, the research findings in the fundamental researches on TBLs are used to understand the TBL at mid-span, which is not separated but suffers the combined effects of curvature and adverse pressure gradients.

In Chapter 6, the velocity field in the corner region is presented. Bimodal histograms of velocity, which has two peaks, are found in our experiment. Then the properties of velocity histograms are presented. Finally, an interpretation of the physics of bimodal behaviour is proposed.

The conclusions and prospects will be laid out in Chapter 7.

Chapter 2

Literature survey

Contents

2.1	Introduction	6
2.2	Linear cascade	6
2.2.1	Features of linear cascades	6
2.2.2	Presence of trips	7
2.3	Turbulent boundary layer	8
2.3.1	Turbulent boundary layer with zero-pressure-gradient	8
2.3.1.1	Mean velocity	8
2.3.1.2	Reynolds stresses	12
2.3.2	Influence of curvature	13
2.3.3	Influence of streamwise pressure gradient	16
2.4	Corner stall	17
2.4.1	Impacts	17
2.4.2	Topologies	19
2.4.3	Influencing factors	21
2.4.4	Criteria	23
2.4.4.1	Diffusion factor	23
2.4.4.2	Lei's criterion	23
2.5	Conclusions	26

2.1 Introduction

In the thesis, the experiments are performed in a linear compressor cascade. In this chapter, we firstly review some issues of the cascade. Then the findings in the basic investigations of TBL will be reviewed. At last, the impacts, topologies and the influencing factors of corner stall are reviewed.

2.2 Linear cascade

In this section, the features of linear cascades are reviewed. Because the transition is induced ahead near the leading edge by trips, the reasons of using trips are then discussed.

2.2.1 Features of linear cascades

In general, the stage of tests to understand turbomachinery flows are:

- linear cascade;
- annular cascade;
- low speed large scale rigs;
- high speed rigs;
- real engine.

From linear cascade to real engine, the information that can be obtained increases. However at the same time the complexity and the difficulty of the measurements become a severe problem, and thus it is more and more difficult to obtain accurate descriptions.

A linear cascade model is an array of airfoils stacked at uniform pitch and stagger angle representing a section of a turbomachinery blade row. Linear cascade testing is a simplified experimental method for evaluating aerodynamics performance of compressor. [Swamy & Kumaran \(2009\)](#) summarized the significance and limitations of the cascade.

The significance of the cascade tests includes:

- Flow parameters such as inlet flow angle, true relative Mach number, true Reynolds number etc., can be relatively easily simulated;
- A cascade test can provide aerodynamic performance data like blade loading/lift coefficient, profile loss/drag coefficient;
- It is easy to measure pressure and velocity distribution on the blade and in the passage;

- Detailed studies on laminar, transition and turbulent boundary layers over blade can be carried out;
- Separation and vortex formation can be studied;
- Local boundary layer profile and shear stress measurements over the blades can also be achieved;
- It is simple to generate data at off design conditions;
- It provides ideal method for comparison of different blade shapes at the same design condition;
- It can provide data for the validation of CFD codes.

The limitations of cascade tests include:

- Coriolis effects and the curvature of the endwall are ignored;
- It is without radial pressure gradients that are found in real engine;
- Turbulence intensity (generally speaking, less than 1%) without inlet flow treatment is much less than that in real engine (about 5%);
- The periodicity of the cascade is difficult to achieved because of the influence of cascade skewness.

2.2.2 Presence of trips

Usually in the cascade experiments, the transition occurs on both the suction and the pressure sides with a laminar separated bubble. If the transition has a significant size, it can lead to a change in the pressure gradient, and thus plays an important role in the corner stall process. A lot of research have studied this phenomenon, for example [Halstead *et al.* \(1997\)](#) and [Schreiber *et al.* \(2002\)](#). The transition can be induced ahead near the leading edge by a trip (e.g. sandpaper). This treatment can be found in a lot of fundamental researches (e.g. [Baskaran *et al.*, 1987, 1991](#); [Skåre & Krogstad, 1994](#); [Spalart & Watmuff, 1993](#)). However in the experiment of cascade, the trip not only induces the transition but also causes some additional effects. These additional effects include the change of the geometry of the blade and the increase in the thickness of the inlet boundary layer. Therefore whether the trip is used or not in the experiment of cascade has always been a controversial topic.

The trip was used in a lot of experiments of cascade (e.g. [Muthanna & Devenport, 2004](#); [Wang & Devenport, 2004](#); [Wenger *et al.*, 2004](#)). [Evans \(1971\)](#) proposed a reason why the trip is used. He claimed that the TBL on the blade with trip would better represent the high turbulence and unsteadiness levels usually encountered in a turbomachine.

2.3 Turbulent boundary layer

The findings in the basic investigations of TBL will be used to investigate the TBL at mid-span. Therefore the basic issues of the TBL are reviewed here.

The main parameters in TBLs are mean velocity and Reynolds stresses. Firstly, these two main parameters in TBLs with zero-pressure-gradient (ZPG) are reviewed.

The main influencing factors of the TBL that will be investigated are the curvature and the pressure gradients. A lot of basic investigations on the TBL have been dedicated to investigate the individual effects of the streamwise pressure gradient and of the curvature, as well as their combined effects. Then these influences of the curvature and the streamwise pressure gradients will be reviewed.

2.3.1 Turbulent boundary layer with zero-pressure-gradient

2.3.1.1 Mean velocity

The classical approach to the scaling of the TBL considers an inner region and an outer region.

In the inner region, the viscosity plays a major role, and the mean velocity can be expressed as

$$U^+ = g(y^+) \quad (2.1)$$

where $U^+ = U/u_\tau$, $y^+ = yu_\tau/\nu$ and g denotes a function. In inner region, the length and velocity scales are ν/u_τ and u_τ , respectively.

In the outer region, the viscosity can be neglected and the velocity defect can be expressed as

$$\frac{U_e - U}{u_\tau} = f\left(\frac{y}{\delta}\right) \quad (2.2)$$

where f denotes a function. This relation is also called ‘‘defect law’’. In this outer region, the length and velocity scales are δ and u_τ , respectively.

In the inner region very close to the wall, the total shear stress is all viscous stress, and then

$$U^+ = y^+ \quad (2.3)$$

This region is also called linear sublayer. In the inner region and outer the linear sublayer, a region exists where the viscous stress are of the same order as the Reynolds shear stresses, and

$$U^+ = \frac{1}{\kappa} \ln(y^+) + B \quad (2.4)$$

where κ is the Von Karman constant, and B is the additive constant. In the classical view, κ is regarded as universal, and B depends on the geometry (e.g. pipe, channel, or boundary layer) and the wall conditions (e.g. surface roughness). This region is also called logarithmic layer. Eq. 2.4 is called log-law. The region between linear sublayer and logarithmic layer is called buffer layer.

The velocity profile outside the viscous-dominated near-wall region can also be expressed by the law of the wake of [Coles \(1956\)](#). It is the sum of a logarithmic part and a wake component, such as

$$U^+ = \frac{1}{\kappa} \ln(y^+) + B + \frac{2\Pi}{\kappa} W\left(\frac{y}{\delta}\right) \quad (2.5)$$

where Π is the wake parameter, W is the wake function. In addition, a lot of formulas can express the region from the linear sublayer to the logarithmic layer, such as

(I) van Driest formula ([van Driest, 1956](#)),

$$U^+ = \int_0^{y^+} \frac{2}{1 + \sqrt{1 + 4a(y^+)}} dy^+ \quad (2.6)$$

where $a(y^+) = (\kappa y^+)^2 [1 - \exp(-y^+/A^+)]^2$, $A^+ = 26$.

(II) Spalding formula ([Spalding, 1961](#)),

$$y^+ = U^+ - e^{-\kappa B} \left[e^{\kappa U^+} - 1 - \kappa U^+ - \frac{(\kappa U^+)^2}{2} - \frac{(\kappa U^+)^3}{6} \right] \quad (2.7)$$

(III) Bailly & Comte-Bellot formula ([Bailly & Comte-Bellot, 2003, p.74](#)),

$$U^+ = \frac{1}{\kappa} \frac{1 - \sqrt{1 + 4(\kappa x^+)^2}}{2\kappa x^+} + \frac{1}{\kappa} \ln[2\kappa x^+ + \sqrt{1 + 4(\kappa x^+)^2}] \quad (2.8)$$

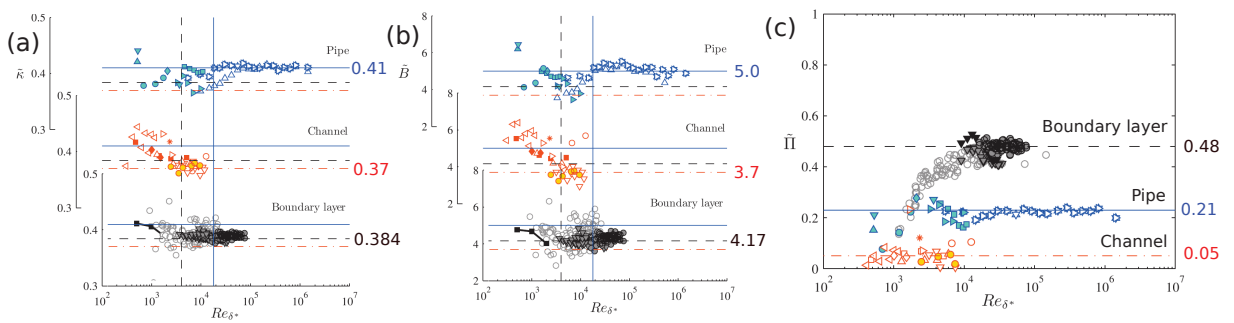


Figure 2.1: The variation of the constants in the law of the wall (κ , B and Π) with Reynolds number, from [Nagib & Chauhan \(2008\)](#). For the symbols, consult the original paper.

The value of κ is very important in turbulence models used in the turbomachinery industry, because the turbulence models often depend on the assumption that the flow very close to the wall surface can be described by the logarithmic profile. As mentioned by [Spalart \(2006\)](#), a decrease in κ can lead to a decrease in skin friction coefficient, and thus induces a decrease in the estimated overall drag. In the classical view, κ was regarded as universal, and the accepted

values were from 0.40 to 0.41. This argument has been brought into question, since there is considerable evidence that κ depends on the flow (Smits *et al.*, 2011).

Nagib & Chauhan (2008) investigated the variation of the constants (κ , B and Π) in the law of the wake (Eq. 2.5) with the Reynolds number in boundary layer, pipe and channel flows, as shown in Fig. 2.1. All of these three constants (κ , B and Π) vary with not only the type of the flow but also the Reynolds number. Since in this thesis we only focus on the boundary layer flows, only the results of the TBLs (TBLs with ZPG more precisely) will be reviewed here.

For κ in the TBLs with ZPG (Fig. 2.1a), DNS data exhibit the decreasing trend at low Reynolds numbers, and the experimental results demonstrate a constant behaviour near a value of 0.384. By excluding the scatter at low Reynolds numbers it is concluded that κ for the TBLs with ZPG remains constant for $Re_{\delta^*} > 4000$.

For B in the TBLs with ZPG (Fig. 2.1b), the relative trend is the same as that of κ discussed above. B remains the constant value of 4.17 for $Re_{\delta^*} > 4000$.

For the local wake parameter Π in the TBLs with ZPG (Fig. 2.1c), it increases at low Reynolds numbers. This indicates that the outer part is still growing and the flow is not fully developed. Π asymptotes to a constant of 0.48 at high Reynolds numbers as the boundary layer develops.

Besides the log-law (Eq. 2.4), the power-law is a main alternative formulation for the mean velocity profile in the TBLs with ZPG. George W. K. is one of the most contributors for the power-law. He and his co-authors have been devoting to power-law (e.g. George, 2006, 2007; George & Castillo, 1997). Indeed until now there is no justification for using the friction velocity as the velocity scale for both the inner and outer regions. The basic disagreement is the appropriate velocity scale for the outer region of the turbulent boundary layers. Based on the fact that scaling with the free stream velocity (U_∞) leads to a mathematically valid similarity solution of the momentum equation for the outer region in the asymptotic limit of infinite Reynolds number, George (2007) suggested that U_∞ is the only theoretically acceptable velocity scale for the outer region of the turbulent boundary layers. Of course, the power-law has been challenging by a lot of researches that believe the classical log-law. One of the recent heated debates is Jones *et al.* (2008). Jones *et al.* showed that the classical velocity scale u_τ is equally acceptable in the asymptotic limit, and thus challenged the argument of George (2007) that U_∞ is the only theoretically acceptable velocity scale for the outer region. Although the debate over power-law versus log-law already has a long history (about 20 years), Marusic *et al.* (2010) considered that this debate may continue until very clear differences can be shown in high-fidelity experimental data at high Reynolds numbers.

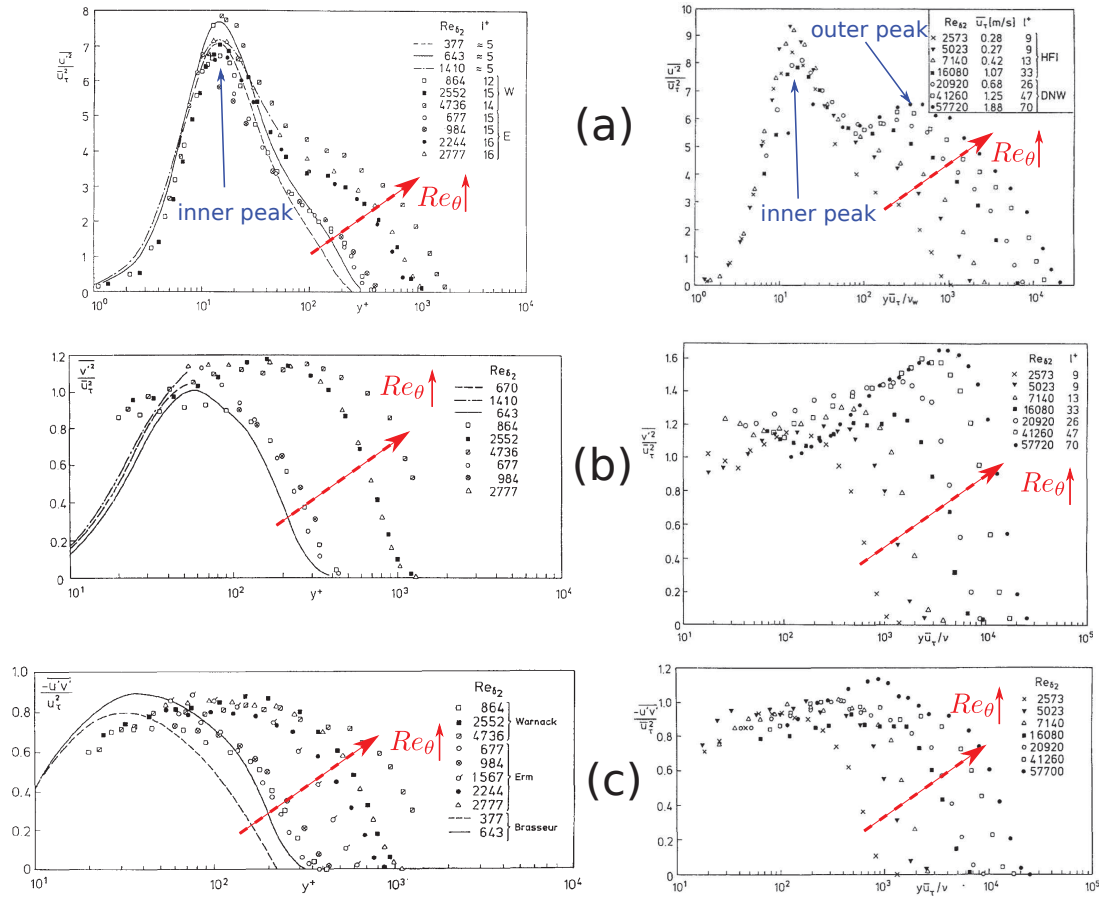


Figure 2.2: Developments of Reynolds stresses in a TBL with ZPG, summarized by **Fernholz & Finley (1996)**. (a) $\overline{u'^2}/u_\tau^2$, (b) $\overline{v'^2}/u_\tau^2$, (c) $-\overline{u'v'}/u_\tau^2$, in which the left part figures the lower range of Reynolds number, the right part figures the higher range of Reynolds number.

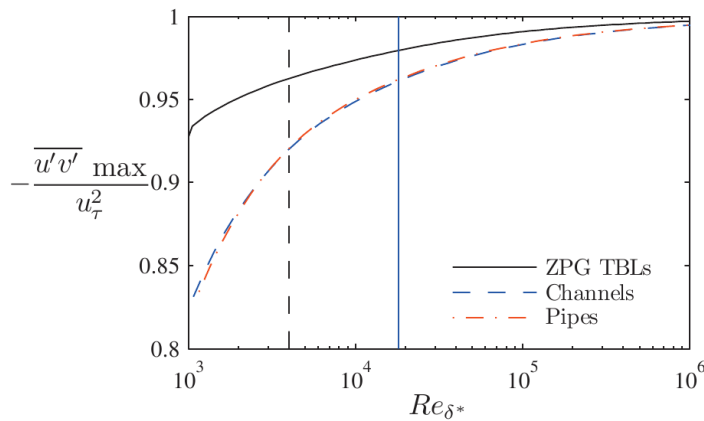


Figure 2.3: Variation of maximum of Reynolds shear stress ($-\overline{u'v'}$) with the Reynolds number, from **Nagib & Chauhan (2008)**.

2.3.1.2 Reynolds stresses

Profiles of $\overline{u'^2}/u_\tau^2$ display similarity only in the viscous sub-layer and buffer layer in inner scaling. One of the most obvious phenomenon is that the profiles of $\overline{u'^2}/u_\tau^2$ show a peak very near the wall, and a second peak occurs with increasing Reynolds number (see Fig. 2.2a). The peak very near the wall is usually called inner peak; and the second peak is usually called outer peak. For the inner peak, there are a lot of investigations in the literature about its location and value. However for the outer peak, the knowledge only stays in the level that it occurs with increasing Reynolds number. Here the issues about the inner peak are reviewed.

The location of the inner peak of $\overline{u'^2}/u_\tau^2$ as a function of the Reynolds number is still in doubt. [Sreenivasan \(1989\)](#) investigated ten experiments over a wide range of Reynolds number, and concludes that the location of the inner peak of $\overline{u'^2}/u_\tau^2$ is sensibly independent of the Reynolds number and locates at $y^+ \sim 14$. [Fernholz & Finley \(1996\)](#) summarized more data including experimental and numerical results, and claimed that the location of the inner peak of $\overline{u'^2}/u_\tau^2$ varies from $y^+ = 12$ to $y^+ = 16$ with increasing Reynolds number (see Fig. 2.2a). Anyway, it is widely accepted recently that the inner peak locates at $y^+ = 15 \pm 1$ with the emergence of more and more data.

The magnitude of the inner peak of $\overline{u'^2}/u_\tau^2$ has been found to increase with Reynolds number. However a uniform expression has not been found in the literature. [Metzger et al. \(2001\)](#) studied the effects of a wide range of Reynolds number ($Re_\theta = 2 \times 10^3 \sim 5 \times 10^3$) and proposed an empirical relation

$$\frac{\overline{u'^2}_{max}}{u_\tau^2} = 1.86 + 0.28 \log(Re_\theta) \quad (2.9)$$

In practices if hot-wire anemometry is used in the experiments, the maximum value of $\sqrt{\overline{u'^2}}/u_\tau$ is influenced by the dimensionless characteristic of the hot-wire length scale $l^+ = lu_\tau/\nu$. Since a hot wire measures the average heat transfer rate over its length, it will weaken the measured velocity fluctuation if that fluctuation occurs over a length-scale smaller than the length of the hot wire. As a result, the peak of $\sqrt{\overline{u'^2}}/u_\tau$ has a slightly rising trend with falling l^+ . Besides l^+ , this inner peak is also influenced by the Reynolds number. The inner peak slightly increases with rising Re_θ . Considered simultaneously the effects of l^+ and the Reynolds number, [Hutchins et al. \(2009\)](#) proposed an empirical formula to calculate the magnitude of the inner peak in streamwise intensity,

$$\frac{\overline{u'^2}_{max}}{u_\tau^2} = A \log Re_\tau - Bl^+ - C \left(\frac{l^+}{Re_\tau} \right) + D \quad (2.10)$$

where $A=1.0747$, $B=0.0352$, $C=23.0833$, $D=4.8371$.

The fluctuation component v' , which is normal to the wall, provides the turbulence transport, and thus makes turbulent boundary layers so different from laminar layers. The profiles

of $\overline{v'^2}/u_\tau^2$ initially rise until their maximum values and then decrease slowly (see Fig. 2.2b for example). The maximum value of $\overline{v'^2}/u_\tau^2$ generally increases with increasing Reynolds number. The location of the maximum value also increases with increasing Reynolds number. In the literature, the relations between the location of the maximum value and the Reynolds number usually are empirical expressions, which are obtained by fitting to experimental data. [Sreenivasan \(1989\)](#) summarized 12 experimental data and recommend an empirical relation

$$y^+ \left(\frac{\overline{v'^2}_{max}}{u_\tau^2} \right) = \left(\text{Re}_\delta \sqrt{\frac{C_f}{2}} \right)^{0.75} \quad (2.11)$$

[Fernholz & Finley \(1996\)](#) summarized a large number of experimental data, and also provides another empirical equation

$$y^+ \left(\frac{\overline{v'^2}_{max}}{u_\tau^2} \right) = 0.071 \text{Re}_\theta \quad (2.12)$$

for $\text{Re}_\theta=400\sim 60\,000$.

The profiles of $-\overline{u'v'}/u_\tau^2$ initially rise until their maximum values and then decrease slowly (see Fig. 2.2c for example). [Sreenivasan \(1989\)](#) plotted the y^+ location of the peak in $-\overline{u'v'}/u_\tau^2$, and fitted the correlation

$$y^+ \left(\frac{-\overline{u'v'}_{max}}{u_\tau^2} \right) = 2 \left(\text{Re}_\delta \sqrt{\frac{C_f}{2}} \right)^{0.5} \quad (2.13)$$

[Fernholz & Finley \(1996\)](#) summarized a large number of experimental data, and also provided another empirical equation for the location of the peak of $-\overline{u'v'}/u_\tau^2$

$$y^+ \left(\frac{-\overline{u'v'}_{max}}{u_\tau^2} \right) = \text{Re}_\theta^{0.61} \quad (2.14)$$

for $\text{Re}_\theta=400\sim 60\,000$. From the comparison between Eq. 2.13 with Eq. 2.11, the location of the peak of $-\overline{u'v'}/u_\tau^2$ is a weaker function of Re_θ than that of $\overline{v'^2}/u_\tau^2$. The same conclusion can come from the comparison between Eq. 2.14 with Eq. 2.12. [Fernholz & Finley](#) also claimed that the maximum value of Reynolds shear stress does not depend on Reynolds number. However [Nagib & Chauhan \(2008\)](#) reviewed more recent experimental results of TBLs with ZPG and claimed that the maximum value of $-\overline{u'v'}/u_\tau^2$ increases with increasing Reynolds number, as shown in Fig. 2.3.

2.3.2 Influence of curvature

In order to investigate the influence of curvature, a long time ago [Bradshaw \(1973\)](#) derived the mean momentum equations in a 2D (s, n) system, where s is along the surface and n is the

normal distance.

★ The s -component mean momentum equation:

$$\begin{aligned} & \frac{\partial U_s^2}{\partial s} + \left(1 + \frac{n}{R}\right) \frac{\partial U_s U_n}{\partial n} + \frac{2U_s U_n}{R} \\ &= -\frac{1}{\rho} \frac{\partial P}{\partial s} - \frac{\partial \overline{u_s'^2}}{\partial s} - \left(1 + \frac{n}{R}\right) \frac{\partial \overline{u_s' u_n'}}{\partial n} - \frac{2\overline{u_s' u_n'}}{R} + \nu h \frac{\partial}{\partial n} \left(\frac{\frac{\partial}{\partial n}(hU_s) - \frac{\partial U_n}{\partial s}}{h} \right) \end{aligned} \quad (2.15)$$

★ The n -component mean momentum equation:

$$\begin{aligned} & \frac{\partial U_s U_n}{\partial s} + \left(1 + \frac{n}{R}\right) \frac{\partial U_n^2}{\partial n} + \frac{U_n^2 - U_s^2}{R} \\ &= -\left(1 + \frac{n}{R}\right) \frac{1}{\rho} \frac{\partial P}{\partial n} - \frac{\partial \overline{u_s' u_n'}}{\partial s} - \left(1 + \frac{n}{R}\right) \frac{\partial \overline{u_n'^2}}{\partial n} - \frac{\overline{u_n'^2} - \overline{u_s'^2}}{R} + \nu h \frac{\partial}{\partial s} \left(\frac{\frac{\partial}{\partial n}(hU_s) - \frac{\partial U_n}{\partial s}}{h} \right) \end{aligned} \quad (2.16)$$

where U_s , U_n and P are mean variables, u_s' and u_n' are fluctuations, ν is the molecular viscosity, ρ is the density, R is the curvature radius and $h=1+n/R$.

From Eqs. 2.15 and 2.16, [Castro & Bradshaw \(1976\)](#) derived the transport equation for turbulent kinetic energy and shear stresses, in which the viscous diffusion term and the complete viscous terms are omitted because of the high Reynolds number.

★ The transport equation for turbulent kinetic energy

$$\begin{aligned} & \underbrace{\left[U_s \frac{\partial}{\partial s} + \left(1 + \frac{n}{R}\right) U_n \frac{\partial}{\partial n} \right]}_{\text{A1:advection}} (k) = \underbrace{-\overline{u_s' u_n'} \left(1 + \frac{n}{R}\right) \frac{\partial U_s}{\partial n}}_{\text{A2:shear production}} - \underbrace{(\overline{u_s'^2} - \overline{u_n'^2}) \left[\frac{\partial U_s}{\partial s} + \frac{U_n}{R} \right]}_{\text{A3:normal stress production}} - \underbrace{\overline{u_s' u_n'} \left[\frac{\partial U_n}{\partial s} - \frac{U_s}{R} \right]}_{\text{A4:curvature production}} \\ & \underbrace{-\frac{\partial}{\partial s} \left(\frac{\overline{p' u_s'}}{\rho} + \frac{1}{2} \overline{q^2 u_s'} \right) - \frac{\partial}{\partial n} \left[\left(1 + \frac{n}{R}\right) \left(\frac{\overline{p' u_n'}}{\rho} + \frac{1}{2} \overline{q^2 u_n'} \right) \right]}_{\text{A5:pressure cum turbulent diffusion}} \underbrace{-\epsilon}_{\text{A6:dissipation}} \end{aligned} \quad (2.17)$$

where $k = \frac{1}{2}(\overline{u_s'^2} + \overline{u_n'^2} + \overline{u_z'^2})$.

★ The transport equation for shear stresses

$$\begin{aligned} & \underbrace{\left[U_s \frac{\partial}{\partial s} + \left(1 + \frac{n}{R}\right) U_n \frac{\partial}{\partial n} \right]}_{\text{B1:advection}} (-\overline{u_s' u_n'}) = \underbrace{\overline{u_n'^2} \left(1 + \frac{n}{R}\right) \frac{\partial U_s}{\partial n}}_{\text{B2:shear generation}} + \underbrace{\overline{u_s'^2} \left(\frac{\partial U_n}{\partial s} - \frac{U_s}{R} \right)}_{\text{B3:curvature generation}} - \underbrace{(\overline{u_s'^2} - \overline{u_n'^2}) \frac{U_s}{R}}_{\text{B4:coordinate rotation}} \\ & \underbrace{\frac{\partial}{\partial s} \left(\frac{\overline{p' u_n'}}{\rho} + \overline{u_s'^2 u_n'} \right) + \frac{\partial}{\partial n} \left[\left(1 + \frac{n}{R}\right) \left(\frac{\overline{p' u_s'}}{\rho} + \overline{u_s' u_n'^2} \right) \right]}_{\text{B5:pressure cum turbulent transport}} + \underbrace{\left(\frac{\overline{u_s' u_s'^2} - \overline{u_s'^3}}{R} \right)}_{\text{B6:pressure-stain redistribution}} \\ & \underbrace{-\frac{p'}{\rho} \left[\frac{\partial u_n'}{\partial s} + \left(1 + \frac{n}{R}\right) \frac{\partial u_s'}{\partial n} \right]}_{\text{B6:pressure-stain redistribution}} \end{aligned} \quad (2.18)$$

The terms in both equations have been given their usual names, except that the production and generation terms have been split into three separate parts to help identify their origin.

Castro & Bradshaw (1976) considered that the curvature decreases k and $-\overline{u'_s u'_n}$, because R in Eqs. 2.17 and 2.18 reduces the magnitude of the total term. Unfortunately, they also pointed out that the effects of curvature cannot only be based on the explicit curvature terms in Eqs. 2.17 and 2.18 (A4 and B3). This is due to the fact that R exists in all the terms in Eqs. 2.17 and 2.18. The effects of curvature is often an order of magnitude higher than the effects generated by the term A4 in Eq. 2.17 and the term B3 in Eq. 2.18 (Bradshaw, 1973).

Besides Bradshaw (1973) and Castro & Bradshaw (1976), Patel & Sotiropoulos (1997) also reviewed the effects of curvature on turbulent boundary layers. The equations so-called second-order boundary layer equations for curved surfaces have been derived, in order to indicate the order of the effects of surface curvature. These equations contain explicit term of surface curvature. Solutions of these equations for a laminar boundary layer indicate that the effects of curvature on the boundary layer properties would have the order of the magnitude of $|K\delta|$, with δ the boundary layer thickness and K the curvature. This is also true in turbulent flow. The behaviour of the turbulent boundary layer is very sensitive to streamline curvature. The magnitude of $|K\delta|$ of order 0.01 are generally regarded as *weak* curvatures, of order 0.1 are regarded as *moderate* curvatures, and of order 1.0 are regarded as *strong* curvatures. The effects of concave curvature are found to be opposite to those of convex curvature. Moreover, the effects of concave curvature on the behaviour of the turbulent boundary layer are weaker than that of convex curvature at the same value of $|K\delta|$.

Patel & Sotiropoulos (1997) reviewed experiments and theoretical analyses in which curvature affects the law of the wall. For example, one of the theoretical analyses is ¹

$$U^+ = U_0 + \alpha K^+ y^+ \left(U_0^+ - \frac{1}{\kappa} \right) \quad (2.19)$$

where $U_0 = 1/\kappa \ln y^+ + B$ is the law of the wall without curvature with classical constants ($\kappa=0.41$), $K^+ = K\nu/u_\tau$, α is a constant, $\alpha > 0$ for convex curvature, and $\alpha < 0$ for concave curvature. From this equation, on a convex wall ($\alpha > 0$), the velocity at a given y^+ will be larger than that on a flat wall, and the effect of concave curvature ($\alpha < 0$) is the opposite. This is consistent with the experiments they reviewed. Patel & Sotiropoulos eventually concluded that the status of the law of the wall with the effects of the curvature or the pressure gradient remains unclear.

About the log-law, there is a new agreement that the constants in the log-law (κ and B) are not universal constants, and depend on the boundary conditions (Smits *et al.*, 2011). From this new argument, curvature influences κ and B , but the law of the wall holds. The quantitative influence of curvature on κ and B still needs to be investigated.

¹Eq. 16 in Patel & Sotiropoulos (1997), neglected the third term on the right-hand side which is small quantity.

Fig. 2.4 shows the influence of curvature on three representative turbulent quantities reviewed by Patel & Sotiropoulos (1997). With increasing curvature, the shear stress (see Fig. 2.4a) reduces rapidly throughout the boundary layer, practically $y/\delta > 0.6$; and the turbulent kinetic energy (see Fig. 2.4b) only decreases gradually in the inner boundary layer ($y/\delta < 0.7$). From Figs. 2.4a-b, the structure parameter $a_1 = -\overline{u'v'}/2k$ decreases from the nearly constant value of about 0.15 in standard 2D flows, specially in $0.7 < y/\delta < 1.0$. The ratio of the two normal stresses $\overline{v'^2}/\overline{u'^2}$ (see Fig. 2.4c) increases in the inner region with the influence of curvature.

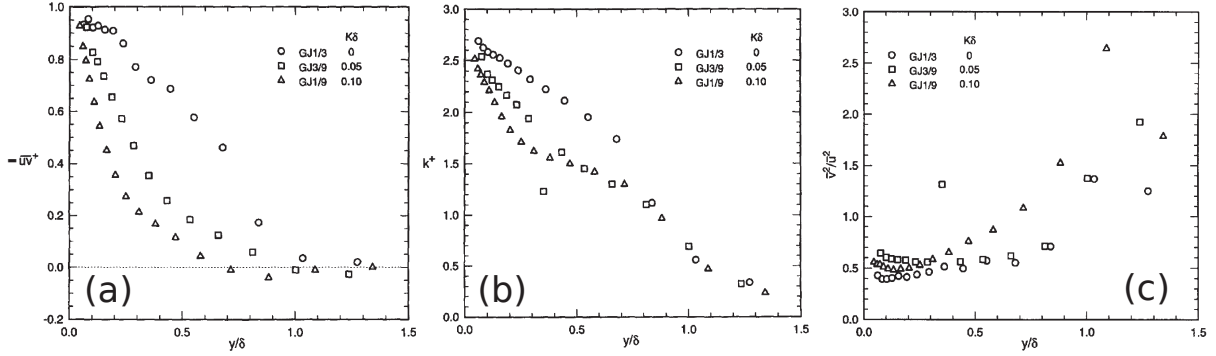


Figure 2.4: Influences of curvature on (a) Reynolds shear stress, (b) turbulent kinetic energy, (c) ratio of Reynolds normal stresses, reviewed by Patel & Sotiropoulos (1997).

2.3.3 Influence of streamwise pressure gradient

To investigate the effects of the streamwise pressure gradient, Eqs. 2.17 and 2.18 were also used by Baskaran *et al.* (1991). By using the continuity equation, the normal stress production in Eq. 2.17 can be written as $(u_s'^2 - u_n'^2)(1 + n/R)\partial U_n/\partial n$, and the effect of the streamwise pressure gradient can also be interpreted in terms of $\partial U_n/\partial n$, therefore the effect of the streamwise pressure gradient can be interpreted in terms of normal stress production. There is no contribution to the shear stress generation from the extra strain rate due to pressure gradient in the transport equation of shear stress (Eq. 2.18). This implies that the shear stress is not affected directly by the pressure directly.

Patel & Sotiropoulos (1997) reviewed the theoretical analysis to quantify the effects of pressure gradient on the law of the wall, and mentioned that ¹

$$U^+ = U_0^+ + \frac{1}{2\kappa} P_x^+ y^+ + \frac{1}{4\kappa^3} T_x^+ (\ln y^+)^2 y^+ \quad (2.20)$$

where

$$P_x^+ = \frac{\nu}{\rho u_\tau^3} \frac{dp}{dx}; T_x^+ = \frac{\nu}{\rho u_\tau^3} \frac{d\tau_w}{dx} \quad (2.21)$$

¹Eq. 25 in Patel & Sotiropoulos (1997).

They claimed that the wall shear stress gradient parameter T_x^+ generally depends on the pressure gradient history of the boundary layer, and is not known a priori. In addition, in a TBL with APG, $P_x^+ > 0$ and $T_x^+ < 0$, the net effect is to increase U^+ over the value obtained in a TBL with ZPG. On the contrary, U^+ lies below the logarithmic law in a TBL with FPG.

As for the conclusions on the effects of the curvature, the constants (κ and B) are not universal constants, and quantitative influence of the streamwise pressure gradient on κ and B still needs to be investigated.

2.4 Corner stall

In the literature, some of the deleterious consequences of corner stall have been identified. However an effective control of these effects has been very difficult to achieve. This is due to the fact that the nature and characteristics of these separations are still not clearly understood, and factors that influence their growth and size are not well quantified. Therefore firstly the impacts of corner stall are reviewed in this section. Secondly the topology, one of most important features of corner stall, is reviewed. Thirdly the influencing factors of corner stall are reviewed. The criteria of corner stall, which predict whether the corner stall occurs, are very useful in design. Finally, some criteria are reviewed.

2.4.1 Impacts

Dring et al. (1982, 1983) investigated the flow in an isolated rotor with high aerodynamic loading and low aspect ratio. Large areas of separated flow on the surfaces near the hub of the isolated rotor were identified through flow visualization. The observed regions of high loss were near the end walls both at the hub and at the tip. At the hub, the high loss was associated with the flow separation of the blade and endwall surface boundary layers near the trailing edge of the suction surface. At the tip, the high loss region was thought to be due to the rotor tip leakage flow. When the flow coefficient was reduced, the high loss region near the hub extended radially over the entire span.

Joslyn & Dring (1985) assessed the impact of hub corner separation on the performance of a two-stage research compressor. Their measurements showed that the growth of 3D flow separation, from the design condition to the near stall condition, increased the loss coefficient near the endwall (from 0% to 5% span) by a factor of two. The blockage associated with the separation reduced the circumferentially averaged axial velocity by 20% over the lower 25%

span. They suggested that the increased loss downstream of the rotor trailing edge generates a significant decrease of the axial velocity component thereby producing also an increase of the incidence in the downstream stator, promoting hub corner separation in the stator.

Dong et al. (1987) investigated flow and loss mechanisms in a single-stage low-speed axial flow compressor. They showed a clear hub separation on the stator. The separation was revealed using oil flow visualization and the region extended almost to the mid-span of the blade suction surface at the trailing edge. However, by introducing a clearance (of the order of 1% of chord) between the blade and the stationary hub, the separated region was considerably reduced and this resulted in an improved efficiency. The removal of separation was attributed to leakage flow energizing the low-momentum fluid in the suction surface endwall corner. While it is possible that the leakage flow spills over to the suction surface and energizes the separated region, it may also be viewed as opposing the secondary flow, thus preventing the low momentum boundary fluid from migrating to the suction surface.

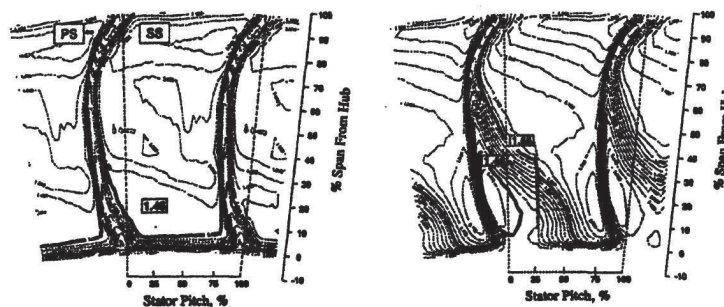


Figure 2.5: Impact of corner separation (*Barankiewicz & Hathaway, 1998*).

Barankiewicz & Hathaway (1998) confirmed that hub corner separation does exist in a well designed and highly efficient compressor. This compressor is a low-speed four-stage model of the General Electric Energy Efficient Engine compressor rear stages. Despite design features such as end bend and dihedral to reduce loss in the endwall regions, corner separation appeared when loading increased beyond the design level. The contours of stagnation pressure coefficient at stator exit are shown in Fig. 2.5. With loading increasing from design (left) to near stall (right), the development of corner separation increases the size of the high loss region.

From time-accurate unsteady simulation, *Choi et al. (2008)* suspected that corner stall might be a trigger for the rotating stall. After an asymmetric disturbance is initiated at hub-corner-separation, this disturbance is transferred to the tip leakage flows and grows to become an attached stall cell, which adheres to the blade passage and rotates at the same speed as the rotor. When the attached stall cell reaches a critical size, it moves along the blade row and becomes the rotating stall. The rotating speed of the stall cell decreases to 79% of the rotor so the stall cell rotates in the opposite direction to the rotor in the rotating frame.

2.4.2 Topologies

Until now there is not a unique topology of corner stall that is widely accepted. Here two of the most famous topologies of corner stall are reviewed. Generally the critical point theory, as well as the topological rules on critical points, needs to be used in understanding the topology of corner stall, which has been reviewed in the thesis of [Sachdeva \(2009\)](#).

The first topology is proposed by Schulz et al. ([1988](#); [1990a](#); [1990b](#)) (see Fig. 2.6). They performed detailed flow measurements in an isolated subsonic compressor stator at various blade loadings. Their extensive measurements included blade and endwall flow visualization, steady and unsteady static pressure measurements, blade boundary layer investigations with hot wires and hot films, and five-hole probe measurements at the stator exit. In their study, hub corner stall was observed at all blade loadings. The hub corner stall and the related secondary flows were responsible for the high loss region observed at the stator exit. Based on extensive experimental results, they formulated a composite model for structure of this corner flow in the absence of an upstream rotor. The streamlines on the surfaces show the presence of a vortex on the hub (marked *a*). In the core of these vortices the flow is transported out normal to the surface; points *a* and *b* seem to represent the saddle points. At the leading edge of the separated region, vortex *c* is formed by the main flow when a sudden obstruction due to flow separation is encountered. The back flow inside the separated region moves upstream and coils up into another vortex marked *d*. The separated region is closed off from the main flow by limiting streamlines (the angle of limiting streamline as the wall is approached) at the hub and on the suction side. The vortex axis is normal to the hub on the hub wall and normal to the blade on the blade surface. Hence, it is anticipated that a ring vortex is formed as shown in Fig 2.6b, covering part of the blade suction side and the hub wall.

The second topology of corner stall is proposed by [Hah & Loellbach \(1999\)](#) (see Fig. 2.7). They numerically simulated two experiments by solving the Reynolds-averaged Navier-Stokes equations. One is the experiment of Schulz et al. ([1988](#); [1990a](#); [1990b](#)); the other one is the “blind test case” in 1994 ([Denton, 1997](#); [Strazisar & Denton, 1995](#); [Suder, 1996](#); [Suder & Celestina, 1996](#)), which is also the test case in CFD validation for propulsion system components in 1998 ([Dunham, 1998](#)). The dominant features of the hub corner stall appear to be two vortices. One is located near the suction surface at approximately 80 percent of the axial chord, and the other is located close to the trailing edge. These two counter-rotating vortices extend radially outward and connect outside the wall boundary layer. Thus, the vortices visualized on the hub wall are actually two legs of a single vortex. Because of the strong particle motion around this vortex, a reversed flow region and a limiting streamline are created on the suction surface.

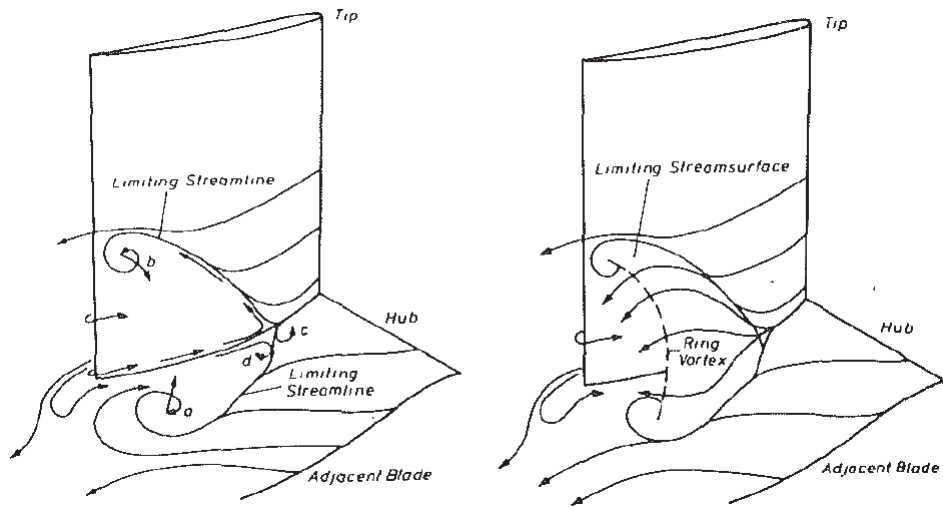


Figure 2.6: Topology of the corner stall, proposed by Schulz *et al.* (1990a).

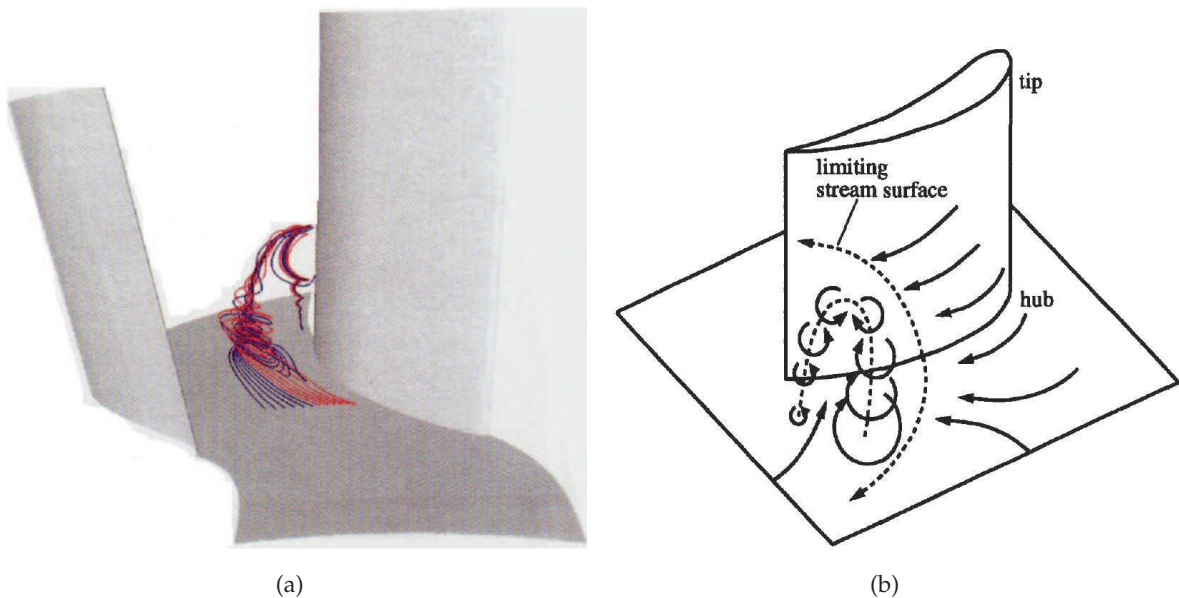


Figure 2.7: Topology of corner stall, proposed by Hah & Loellbach (1999).

2.4.3 Influencing factors

Incidence

The characteristic of the mid-span of a cascade with the incidence is similar to that of an airfoil that can be found in [Emery *et al.* \(1958\)](#). The stagnation point locates on suction side when incidence is negative, while the stagnation point locates on pressure side when incidence is positive. In addition, the stagnation point approaches progressively and then removes away from the leading edge, when incidence increases from negative to positive. The performance of cascade, for example lift coefficient and efficiency, firstly increases with incidence, and then drops at a critical incidence.

In the corner region, the losses and the extent of the corner separation increase monotonously with the incidence.

Reynolds number and free-stream turbulence

[Schreiber *et al.* \(2002\)](#) performed an experimental and analytical study of the effect of Reynolds number and free-stream turbulence on the location of transition on the suction surface of a controlled diffusion airfoil (CDA). The experiments were conducted in a linear cascade at Reynolds numbers in the range of $0.7 \sim 3.0 \times 10^6$ and turbulence intensities in the range of $0.7 \sim 4\%$. For small turbulence levels ($Tu < 3\%$) and all Reynolds numbers tested, the accelerated front portion of the blade is laminar and transition occurs within a laminar separation bubble shortly after the maximum velocity near 35-40 percent of chord. For high turbulence levels ($Tu > 3\%$) and high Reynolds numbers, the transition region moves upstream into the accelerated front portion. For those conditions, the sensitivity to surface roughness increases considerably; at $Tu = 4\%$, bypass transition is observed near $7 \sim 10\%$ of chord. They also claimed that the early bypass transition at high turbulence levels must alter the profile velocity distribution for compressor blades that are designed and optimized for high Reynolds numbers.

Mach number

[Bailie *et al.* \(2008\)](#) numerically investigated the corner stall in an axial compressor stage. They claimed that for the subsonic design inlet Mach number distribution (average of 0.72), the local acceleration creates a small leading edge shock and separation bubble for all incidence angles simulated and reducing the inlet Mach number at high incidence reduces the losses and eventually eliminates the corner stall.

Upstream rotor wake

Schulz *et al.* (1990a,b) carried out an experimental study of the 3D flow field in an annular compressor cascade in the presence of an upstream rotor. A clear corner separation was observed on the suction surface, which grew with the increase of incidence. They found that the upstream rotor wake has a major influence on the extent of separation as well as on aerodynamic losses, secondary flow, transition, laminar separation bubble and the 3D flow inside the passage.

Inlet boundary layer

The effect of the inlet boundary layer was studied by Gbadebo (2003) for a linear compressor cascade. He found that thickened boundary layer induces a reduction in blade loading and leads to an increase in deviation. Another significant effect of thickened boundary layer is the huge endwall loss. Gbadebo (2003) further claimed that the thickened boundary layer presumably leads to entrainment of high momentum fluid particles from the free-stream into the boundary layer, which consequently suppresses further growth of separation. In addition, the turbulent mixing within the boundary layer therefore generates the extra loss observed.

Tip clearance flow

Tip clearance flow is an inherent phenomenon in compressors. Gbadebo *et al.* (2007) numerically investigated the interaction of tip clearance flow and corner stall in a compressor cascade. They observed that the 3D separation on the blade suction surface was largely removed by the clearance flow at certain level of tip clearance. They claimed that the removal mechanism was associated with the suppression of the leading edge horseshoe vortex and the interaction of the tip clearance flow with the endwall boundary layer, which develops into a secondary flow as it is driven towards the blade suction surface.

Surface roughness effects

Surface roughness on a stator blade was found to have a major effect on the performance of compressor. Gbadebo *et al.* (2004) carried out a preliminary study to ascertain which part of the stator suction surface and at what operating condition the flow is most sensitive to roughness. They came to the conclusions that stage performance is extremely sensitive to surface roughness around the leading edge and peak-suction regions, particularly for flow rates corresponding to design and lower values. The size of the separation, in terms of spanwise and pitchwise extent, is increased with roughness present. Roughness produced the large 3D separation at design flow coefficient that is found for smooth blades nearer to stall.

Real geometries

Goodhand & Miller (2012) considered the effect of small variations in leading edge geometry, leading edge roughness, leading edge fillet and blade fillet geometry on the 3D separations in compressor blade passages. They found that any deviation that causes suction surface transition to move to the leading edge over the first 30% of span would cause a large growth in the size of the corner separation, doubling its impact on loss.

2.4.4 Criteria

2.4.4.1 Diffusion factor

Lieblein diffusion factor (DF) shows under what conditions the flow 2D blade separation occurs, derived by Lieblein (1959). For a simple 2D geometry diffusion factor reduces to

$$DF = 1 - \frac{V_2}{V_1} + \frac{\Delta V_\theta}{2\sigma V_1} \quad (2.22)$$

where V_1 and V_2 are the average velocities upstream and downstream of the a blade row in the frame of reference fixed to the blade, ΔV_θ is the change in circumferential velocity in the row and σ is the solidity. For incompressible flow with equal axial velocity upstream and downstream of the cascade, DF can also be expressed as

$$DF = \left(1 - \frac{\cos \beta_1}{\cos \beta_2}\right) + \frac{\cos \beta_1}{2\sigma} (\tan \beta_1 - \tan \beta_2) \quad (2.23)$$

where β_1 and β_2 are upstream flow angle and downstream flow angle, respectively. Values of DF excess of 0.6 are thought to indicate blade stall. However this criterion is valid only near nominal operating point.

Another equivalent diffusion factor DF_{eq} was then created that is valid also in the off-adaptation operation (Lieblein, 1959).

$$DF_{eq} = \frac{\cos \beta_2}{\cos \beta_1} \left[1.12 + \alpha |i - i^*|^{1.43} + 0.61 \frac{\cos^2 \beta_1}{\sigma} |\tan \beta_2 - \tan \beta_1| \right] \quad (2.24)$$

where $\alpha=0.0117$ for NACA 65 profiles, i^* is the optimum incidence. Values of DF_{eq} excess of 2 are thought to indicate blade stall. The limitation of DF_{eq} is that it is unreliable when $i < i^*$.

2.4.4.2 Lei's criterion

Lei(2006,2008) established a new criterion for estimating the size and strength of 3D hub-corner stall in rotors and shrouded stators of multi-stage axial compressors. They consider that the

basic processes governing the formation of hub-corner stall are:

- (1) the adverse pressure gradient in the blade passage,
- (2) the cross-flow from pressure to suction side due to the overturning of the fluid near the endwall inside the blade passage which brings low momentum fluid to the hub corner region, and
- (3) the condition and skew of the incoming endwall boundary layer flow which affects the strength of the cross-flow and the resistance to reversal.

Their criteria consist of

- (1) a stall indicator S , which quantifies the extent of the separated region via the local blade loading and thus indicates whether hub-corner stall occurs, and
- (2) a diffusion parameter D , which defines the diffusion limit for installed operation conditions.

The definitions of these two indicators are introduced below. The flow is assumed to be free of separation at mid-span, hence taking the local blade loading at mid-span as a reference. In order to avoid the influence of the flow turning effect due to the secondary flow, the nondimensional spanwise location z/c of 0.1 (which is near the endwall) is used in the calculation of the S indicator as

$$S = \left[\int_0^{c_x} \frac{p_{ps}(x) - p_{ss}(x)}{p_{t1} - p_1} \left(\frac{dx}{c_x} \right) \right]_{z/c=0.5AR} - \left[\int_0^{c_x} \frac{p_{ps}(x) - p_{ss}(x)}{p_{t1} - p_1} \left(\frac{dx}{c_x} \right) \right]_{z/c=0.1} \quad (2.25)$$

where c is the chord; p_{ps} , p_{ss} are the pressure on the pressure side and the pressure on the suction side, respectively; p_{t1} , p_t are the total pressure and the static pressure in the inlet, respectively. Introducing a modified Zweifel blade loading coefficient Ψ_z ,

$$\Psi_z = \int_0^{c_x} \frac{p_{ps}(x) - p_{ss}(x)}{p_{t1} - p_1} \left(\frac{dx}{c_x} \right) \quad (2.26)$$

which is defined as the ratio of actual blade loading to the ideal blade loading existing with isentropic diffusion to stagnation conditions, the stall indicator S can then be written as

$$S = \Psi_z|_{z/c=0.5AR} - \Psi_z|_{z/c=0.1} \quad (2.27)$$

where AR is the aspect ratio. The diffusion parameter D is based on preliminary design flow variables and geometry, and can be written as

$$D = \left[1 - \left(\frac{\cos(i + \gamma + \varphi/2)}{\cos(\gamma - \varphi/2)} \right)^2 \right] \frac{(i + \varphi - \Delta\eta)}{\sigma} \quad (2.28)$$

where γ is stagger angle; i is the incidence; φ is the blade camber angle; $\Delta\eta$ is the additional turning angle due to a skewed incoming endwall boundary layer.

After the definitions of these two indicators, a large number of numerical simulations (about 100 geometries) were initially carried out to assess whether a simple criterion would unify the

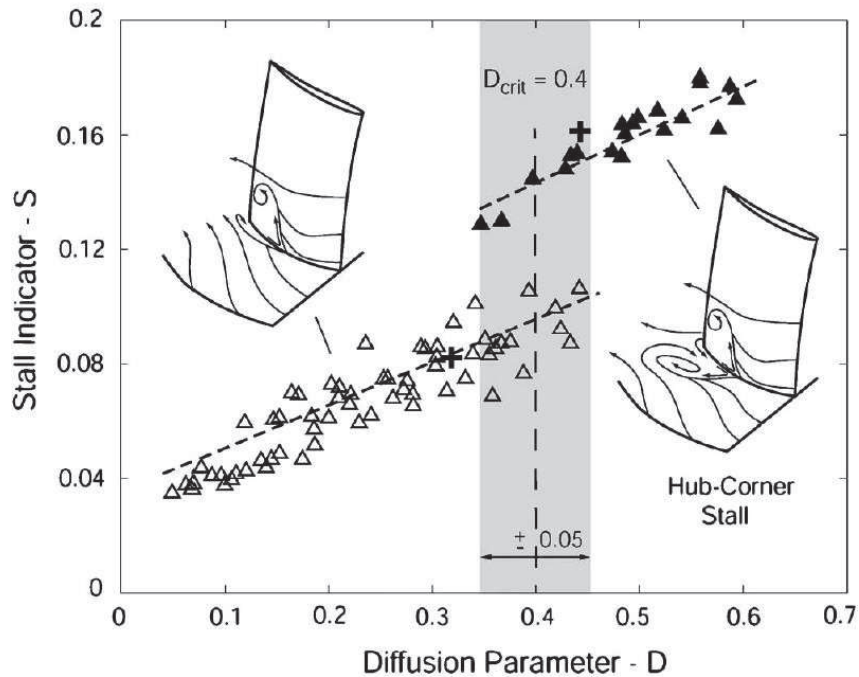


Figure 2.8: S and D , when Re , AR , δ/c are constant (Lei *et al.*, 2008).

description of hub stall onset for different compressors. The simulations were done with FLUENT using steady 3D RANS solver with the $k-\epsilon$ turbulence model. Linear blades with a modified NACA 65 thickness distribution on circular camber lines were used. For all these initial cases, the boundary layers were fully turbulent, the fixed Reynolds number $Re=2.5 \times 10^5$, the blade aspect ratio $AR=1.36$, and the incoming end wall boundary layer thickness $\delta/c=0.1$. The results for stall indicator S versus diffusion parameter D from all the initial simulations are shown in Fig. 2.8. Two distinct branches in S can be seen, with the condition for which hub-corner stall occurs defined by the diffusion parameter reaching critical value, $D_{crit} = 0.4 \pm 0.05$ ¹. On the lower branch, the magnitude of flow reversal is small at the hub endwall, although suction surface separation can occur in the manner indicated by the limiting streamlines. On the upper branch ($S > 0.12$), hub corner stall exists. There is a region of overlap of the upper and the lower branch in near this critical value. For the same D parameter (and different combinations of blade passage geometry and flow conditions) the stall indicator S can either yield low or high values. The effects responsible for this double-valued behaviour have not yet been identified.

Bailie *et al.* (2008) challenged Lei's criterion and they claimed that any compressibility and shock-related effects are certainly beyond the scope of Lei's formulation. Yu & Liu (2010) considered the factor of blade aspect ratio to Lei's criterion and proposed a modified diffusion parameter.

¹This number is different in Lei (2006) and Lei *et al.* (2008). Because for calculating D , the length unit is degree in the former while is radian in the latter. Of course, the latter is more reasonable.

2.5 Conclusions

Some issues of the linear cascade, the TBLs and the corner stall are reviewed in this chapter. These reviews (especially those influencing factors) have been used to guide not only the designs of set-ups but also the experimental operations. The main considerations are summarized below.

1. The familiar blade distribution NACA 65 will be used, in order to refer the abundant experimental and numerical results in the literature. In addition, Lei's criterion is established on the numerical results of NACA 65. Therefore, our experimental results can be used to assess this criterion.
2. In order to fix the position of the transition of the boundary layer and thus remove this difficulty in CFD, trips will be used on both the pressure and the suction sides of the blades in our cascade. The influences of trips will be investigated.
3. Incidence is one of the most important parameter. The setup of the experiment should permit to change this parameter.
4. In the experiments of this thesis, not all the inlet parameters (e.g. total pressure, static pressure, velocity, Reynolds number, free-stream intensity) will be changeable. However considering their importance, some careful selections and operations have been considered.
 - In order to obtain a Reynolds number as representative as possible as one could find in a real compressor (from 3.5×10^5 to 1×10^6), the inlet free-stream velocity will be as high as possible under the conditions allowed by the equipment in the laboratory.
 - The importance of the inlet conditions and especially the turbulent boundary layers that develop on the endwalls should be characterized accurately, if the experimental results are used for CFD (RANS and LES) validation.
5. The periodicity of the test section in the cascade is a crucial points.
6. The unsteady and intermittent feature of the flow is a key point. The measurement will have to quantify this aspect as close as possible to the surface.

Chapter 3

Experimental and numerical methods

Contents

3.1	Geometry of cascade	28
3.1.1	Blade	28
3.1.2	Cascade	29
3.1.3	Transition trips	29
3.1.4	Curvature of blade suction side	29
3.2	Experimental methods	34
3.2.1	Oil visualization	34
3.2.2	Temperature measurement system	34
3.2.3	Pressure measurement system	34
3.2.3.1	Pressure ports on the blade surface and endwall	34
3.2.3.2	Five-hole pressure probe	37
3.2.3.3	Pressure transducers	41
3.2.3.4	Uncertainty in static pressure on the blade and the endwall	42
3.2.3.5	Uncertainty in the results of the five-hole pressure probe	43
3.2.4	Hot-wire anemometry (HWA)	52
3.2.4.1	Introduction of HWA	52
3.2.4.2	Hot-wire probes	53
3.2.4.3	Probe mounting and positioning	54
3.2.4.4	Calibration	54
3.2.4.5	Data conversion	55
3.2.4.6	Uncertainty	56
3.2.5	Particle image velocimetry (PIV)	58
3.2.5.1	Set-up	58
3.2.5.2	Peak locking	60
3.2.5.3	Convergence statistics	61

3.2.5.4	Uncertainty in instantaneous velocity	62
3.2.5.5	Uncertainty in mean velocity	62
3.2.6	Laser Doppler anemometry (LDA)	64
3.2.6.1	Set-up	64
3.2.6.2	Data reduction procedure	68
3.2.6.3	Uncertainty of 2C LDA	69
3.2.7	Traverse system and facilities arrangement	73
3.3	Inlet reference parameters	73
3.4	Test procedure	74
3.5	Numerical method	76
3.5.1	Navier-Stokes equations	76
3.5.2	Reynolds-averaged Navier-Stokes equations	77
3.5.3	Turbulence model	78
3.5.4	Solver, grid and boundary conditions	79

3.1 Geometry of cascade

The investigation is carried out in a low speed cascade wind tunnel. The facility is powered by a 60 kW centrifugal blower and the test section is a rectangular duct with a cross section of 900 mm high by 370 mm wide. Figs. 3.1 and 3.2 show the cascade and the test section.

3.1.1 Blade

This low-speed cascade consists of 13 blades. The original thickness distribution of the blade is NACA 65-009. According to the naming convention for NACA airfoils, the first digit “6” simply represents the series name. The second digit “5” indicates, in the basic symmetrical airfoil version at the zero-lift position, that the pitchwise location of the airfoil’s minimum pressure is at 50% of the chord from the leading edge. The maximum airfoil thickness occurs at 40% chord and according to the final two digits “09”, the maximum airfoil thickness is 9% of the chord. The blade has rounded leading and trailing edges. The radii are 0.6183% and 0.3333% of the chord, respectively. The original thickness distribution of the blade is given in Table 3.1 and plotted in Fig. 3.3a. The mean camber line is a circular arc, as depicted in Fig. 3.3b, and the camber angle φ is 23.22° . Coordinates for the blade cross section are plotted in Fig. 3.3c.

3.1.2 Cascade

The notation used in describing this subsonic compressor cascade is shown in Fig. 3.4. The stagger angle of the cascade γ is 42.7° . From the relations between the angles, the designed inlet angle of the flow β'_1 is 54.31° ¹; and the designed outlet angle of the flow β'_2 is 31.09° . The chord length c , the span h and the spacing (or pitch) s of the blade are 150 mm, 370 mm and 134 mm, respectively. This implies that the aspect ratio and solidity σ are 2.47 and 1.12, respectively. The parameters of the cascade are summarized in Table 3.2.

3.1.3 Transition trips

The transition simulation is particularly complex to be carried out with CFD, thus the authors wanted to remove this difficulty and focus the study only on the development of the turbulent boundary layer and the corner stall region. To ensure and fix the location of the boundary layers transition that has large consequences on the corner zone separation, a sandpaper strip has been stuck at 6.0 mm from the leading edge on both suction side and pressure side of each blade in the cascade. The width in streamwise and thickness of the sandpaper are 3.0 mm and 0.3 mm, respectively. The grid size of the sandpapers is ISO P600 (average particle diameter is about $25.8 \mu\text{m}$). The sketch of trips is shown in Fig. 3.5. The influences of trips are introduced in Appendix C.

3.1.4 Curvature of blade suction side

The curvature of the blade suction side ($K=1/R$, with R the curvature radius), which can refer to the degree of bending, is one of the most important parameters. The curvature of the suction side is shown in Fig. 3.6, in which $s^*=s/L$ where s is the length of arc from the leading edge to the measurement location, L is the length of arc from the leading edge to the trailing edge. From the leading edge, K initially increases ($0 < s^* < 0.27$) and then slightly decreases ($0.27 < s^* < 0.47$), finally increases monotonically until the trailing edge ($0.47 < s^* < 1.00$). The K is equal to zero where $s^*=0.94$, smaller than zero where $0 < s^* < 0.94$, larger than zero where $0.94 < s^* < 1.00$. As a result, the blade suction side is convex where $0 < s^* < 0.94$, and is concave where $0.94 < s^* < 1.00$. Generally speaking, the magnitude of K are large relatively in the former part ($0 < s^* < 0.70$) and is small relatively in the latter part ($0.70 < s^* < 1.00$).

¹Not considering the optimum incidence $i^*=0.18^\circ$

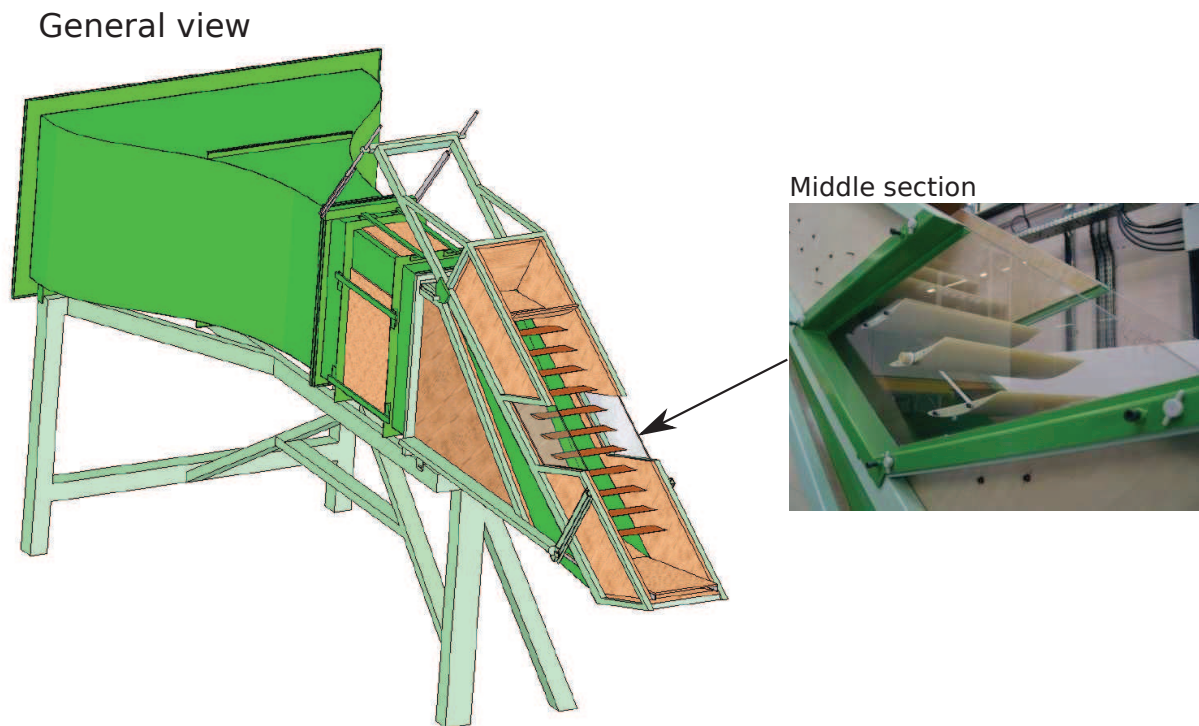


Figure 3.1: General view of the cascade in LMFA, Ecole Centrale de Lyon.

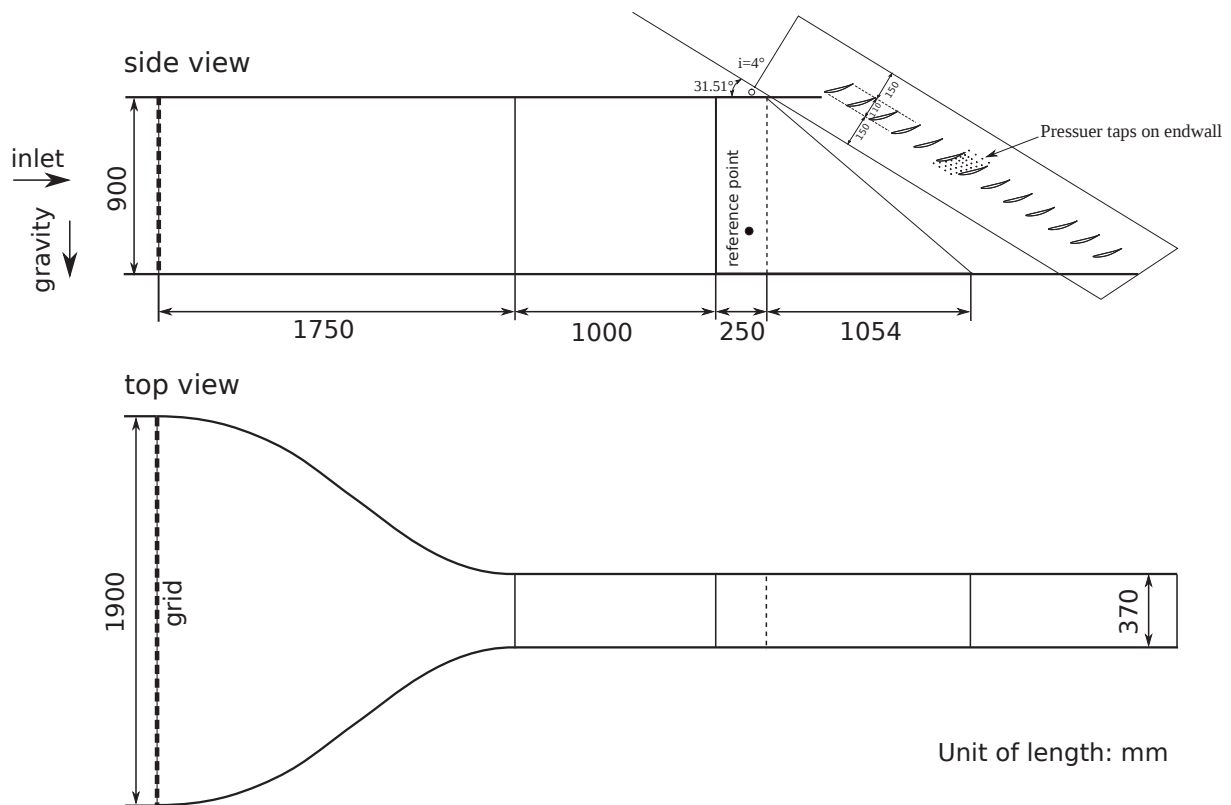


Figure 3.2: Side and top views of the cascade.

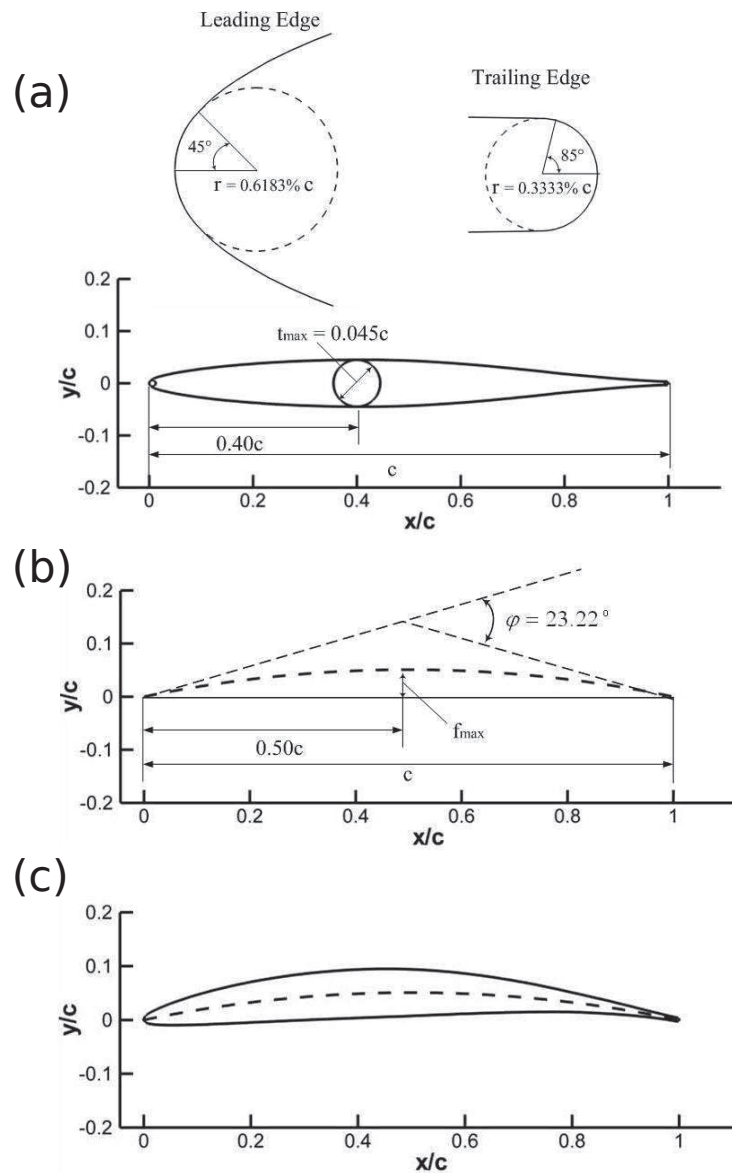


Figure 3.3: Parameters of blade: (a) original thickness; (b) mean camber line; (c) cross section, in the coordinates of blade.

Table 3.1: Half thickness of NACA 65-009 airfoils, in the coordinates of blade.

$x(\%c)$	$y(\%c)$	$x(\%c)$	$y(\%c)$	$x(\%c)$	$y(\%c)$	$x(\%c)$	$y(\%c)$
0	0	10	2.7360	45	4.4667	80	1.7883
0.5	0.6948	15	3.2994	50	4.3308	85	1.2465
0.75	0.8388	20	3.7287	55	4.0770	90	0.7290
1.25	1.0521	25	4.0527	60	3.7314	95	0.2754
2.5	1.4166	30	4.2840	65	3.3138	100	0
5.0	1.9593	35	4.4316	70	2.8404	L.E.R.	0.6183
7.5	2.3823	40	4.4964	75	2.3256	T.E.R.	0.3333

L.E.R, radius of leading edge; T.E.R, radius of trailing edge.

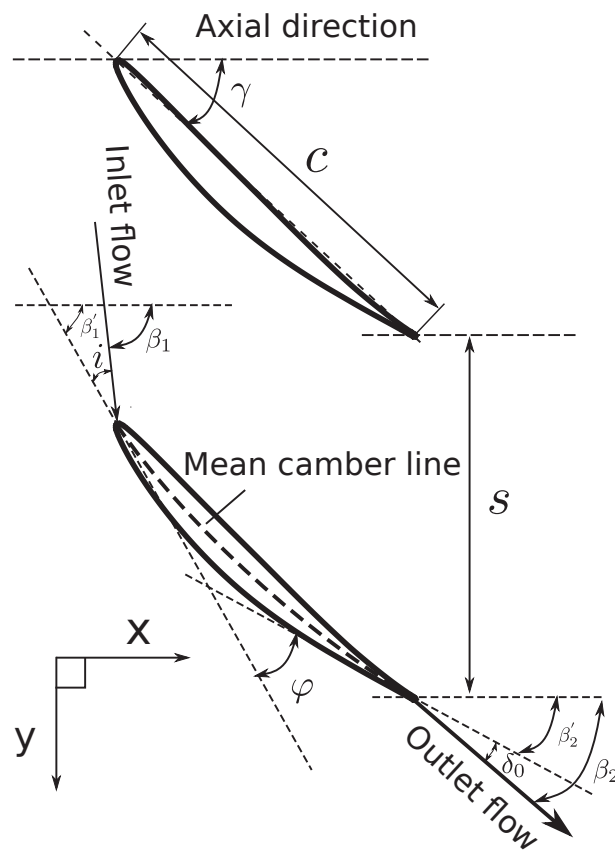


Figure 3.4: Notation for cascade, in the coordinates of cascade.

Table 3.2: Geometric parameters of the cascade.

Symbol	Name	Magnitude	Relations
c	chord	150.0 mm	
φ	camber angle	23.22°	$\varphi = \beta'_1 - \beta'_2$
γ	stagger angle	42.70°	
s	pitch/spacing	134.0 mm	
σ	solidity	1.12	$\sigma = c/s$
h	blade span	370.0 mm	
AR	aspect ratio	2.47	$AR = h/c$
i	incidence angle	$-5^\circ \sim 7^\circ$	
i^*	optimum incidence	0.18°	
β'_1	design upstream flow angle	54.31°	$\beta'_1 = \gamma + \varphi/2$
β_1	actual upstream flow angle		$\beta_1 = \beta'_1 + i + i^*$
β'_2	design downstream flow angle	31.09°	$\beta'_2 = \gamma - \varphi/2$
β_2	actual downstream flow angle		$\beta_2 = \beta'_2 + \delta^0$
δ^0	flow deviation angle		
θ	flow turning angle		$\theta = \beta_1 - \beta_2$ $= \varphi + i - \delta^0$

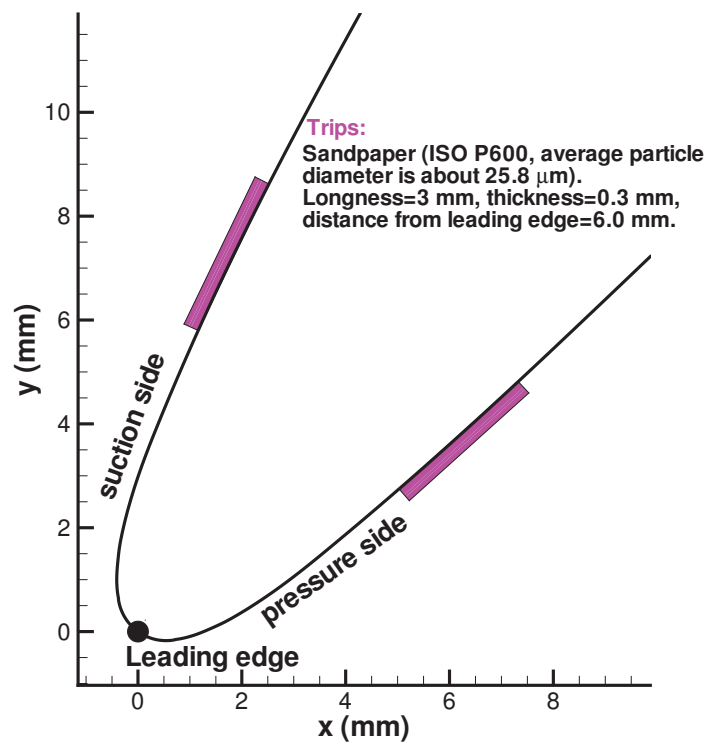


Figure 3.5: Sketch of trips.

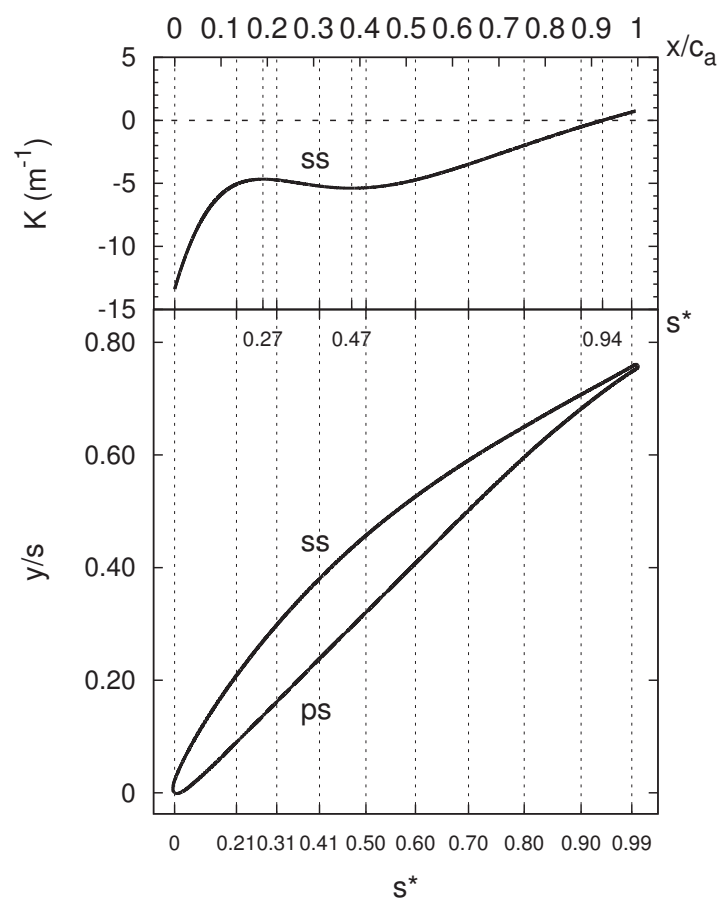


Figure 3.6: Curvature of the blade suction side.

3.2 Experimental methods

3.2.1 Oil visualization

Oil surface visualization is one of the oldest visualization techniques in fluid mechanics. This technique serves for visualizing the flow pattern close to the surface of a solid body exposed to airflow. The surface is coated with a specially prepared paint consisting of suitable oil and finely powdered pigment; due to frictional forces the air stream carries the oil with it. After much of the oil has evaporated, the persistent pattern of the pigment, which qualitatively represents the wall streamlines, gives information on the direction of flow (Merzkirch, 1987). The major advantage is the fact that it is inexpensive and easy to imply. The main disadvantage of this method is the fact that the mixture can be influenced by gravity, especially at low fluid velocities. Many instructions have been given in the literature on how to prepare an oil-pigment mixture, which is appropriate for specific test conditions (Settles & Teng, 1983). Perry & Chong (2000) summarized the interpretation of flow visualization results using critical point theory.

In this study because the inlet flow velocity is about 40 m/s, the ingredients are as follows: 100 ml Paraffin Oil; 3 ml Oleic Acid; 15 g Titanium Oxide.

3.2.2 Temperature measurement system

A thermocouple type K is used to measure the temperature, connected with the National Instruments thermocouple input module (NI¹ 9211). The output voltage is recorded by the National Instruments data acquisition card (NI cDAQ-9172). The uncertainty in the temperature is about 1°.

3.2.3 Pressure measurement system

3.2.3.1 Pressure ports on the blade surface and endwall

Forty pressure taps have been positioned at 34.2% span on the blade located in the middle of the test section (see Fig. 3.7). Twenty-five taps are located on the suction side while the other fifteen taps are located on the pressure side. The pressure taps on the blade are made by 1.6 mm diameter alloy steel tubes embedded into the blade surface, with a port of 0.8 mm opened to

¹<http://www.ni.com/>



Figure 3.7: Arrangement of the blade and the endwall.

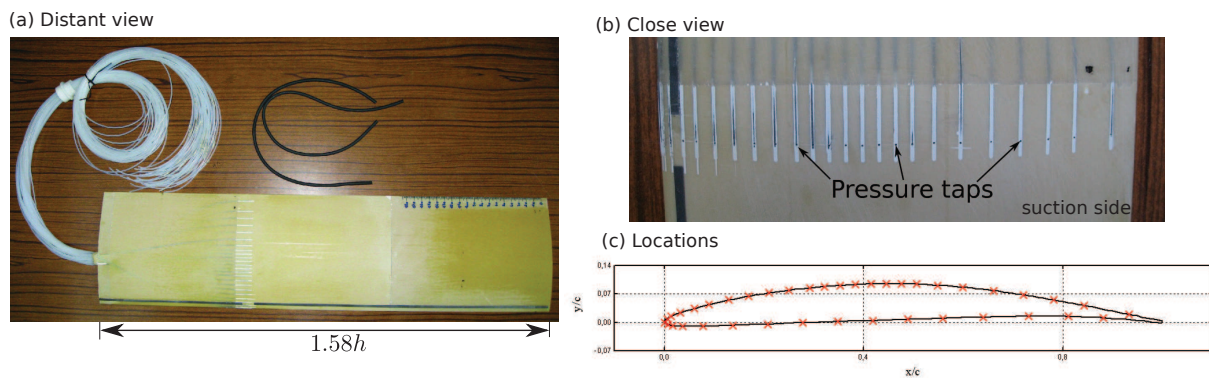


Figure 3.8: Pressure taps on the blade.

Table 3.3: The location of surface pressure ports on the blade, in the coordinates of blade.

Suction Side			Pressure Side					
NO.	x(mm)	y(mm)	NO.	x(mm)	y(mm)	NO.	x(mm)	y(mm)
1	0.00	0.00	16	66.81	14.24	1	132.23	1.62
2	1.00	1.56	17	71.45	14.22	2	121.67	2.16
3	2.00	2.16	18	76.08	14.07	3	109.60	2.22
4	4.75	3.47	19	82.24	13.69	4	96.03	1.93
5	9.07	5.14	20	89.93	12.95	5	83.97	1.50
6	13.48	6.58	21	99.11	11.72	6	73.42	1.07
7	19.43	8.23	22	108.24	10.14	7	62.87	0.68
8	25.44	9.66	23	117.31	8.26	8	52.31	0.28
9	31.50	10.88	24	126.36	6.23	9	41.76	-0.16
10	37.59	11.90	25	140.00	2.88	10	31.21	-0.65
11	43.71	12.73				11	20.66	-1.12
12	48.31	13.24				12	11.62	-1.41
13	52.93	13.65				13	5.59	-1.40
14	57.55	13.95				14	2.57	-1.23
15	62.18	14.15				15	1.10	-0.93

the flow. The span of the instrumented blade is $1.58h$, where h is the blade span of the cascade. This instrumented blade can slide in the spanwise direction through two slots (having the blade profile) on each side of the endwall. Leakage is prevented by O-rings around the profile. Static pressure can then be measured at any arbitrary section in the spanwise direction. The blade with pressure ports is shown in Fig. 3.8a and 3.8b. The locations of the pressure ports on the blade surface are listed in Table 3.3 and shown in Fig. 3.8c.

To measure the pressure on the endwall, 35 pressure ports are also planted on the endwall. The pressure ports on endwall are made using 1.6 mm diameter alloy steel tubes embedded into the blade surface with a port of 0.8 mm opened to the flow. The locations of the pressure ports on the blade surface are listed in Table 3.4 and shown in Fig. 3.9.

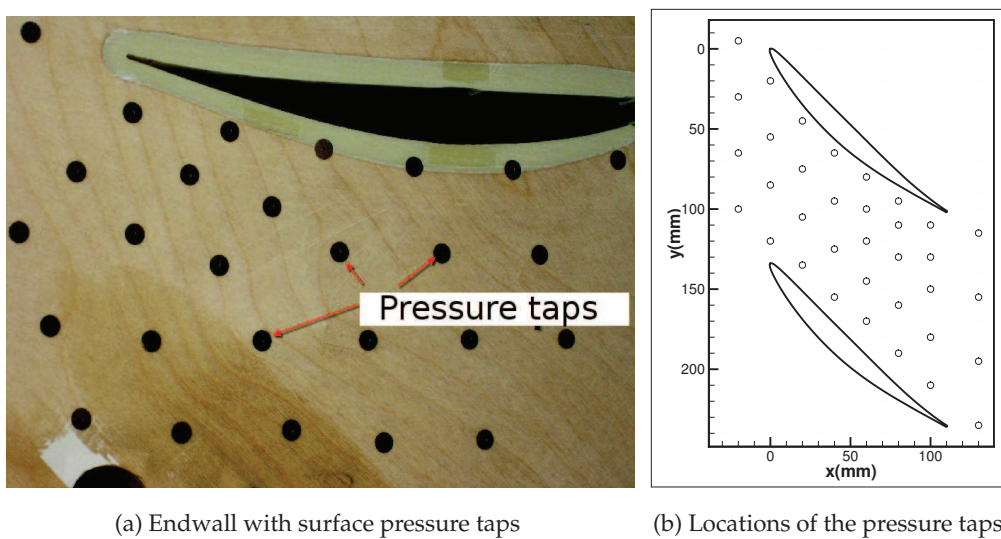


Figure 3.9: Pressure taps on the endwall.

Table 3.4: The location of surface pressure ports on endwall, in the coordinates of cascade.

NO.	x(mm)	y(mm)	NO.	x(mm)	y(mm)	NO.	x(mm)	y(mm)
1	-20.0	-5.0	13	40.0	65.0	25	80.0	160.0
2	-20.0	30.0	14	40.0	95.0	26	80.0	190.0
3	-20.0	65.0	15	40.0	125.0	27	100.0	110.0
4	-20.0	100.0	16	40.0	155.0	28	100.0	130.0
5	0.0	20.0	17	60.0	80.0	29	100.0	150.0
6	0.0	5.0	18	60.0	100.0	30	100.0	180.0
7	0.0	85.0	19	60.0	120.0	31	100.0	210.0
8	0.0	120.0	20	60.0	145.0	32	130.0	115.0
9	20.0	45.0	21	60.0	170.0	33	130.0	155.0
10	20.0	75.0	22	80.0	95.0	34	130.0	195.0
11	20.0	105.0	23	80.0	110.0	35	130.0	235.0
12	20.0	135.0	24	80.0	130.0			

3.2.3.2 Five-hole pressure probe

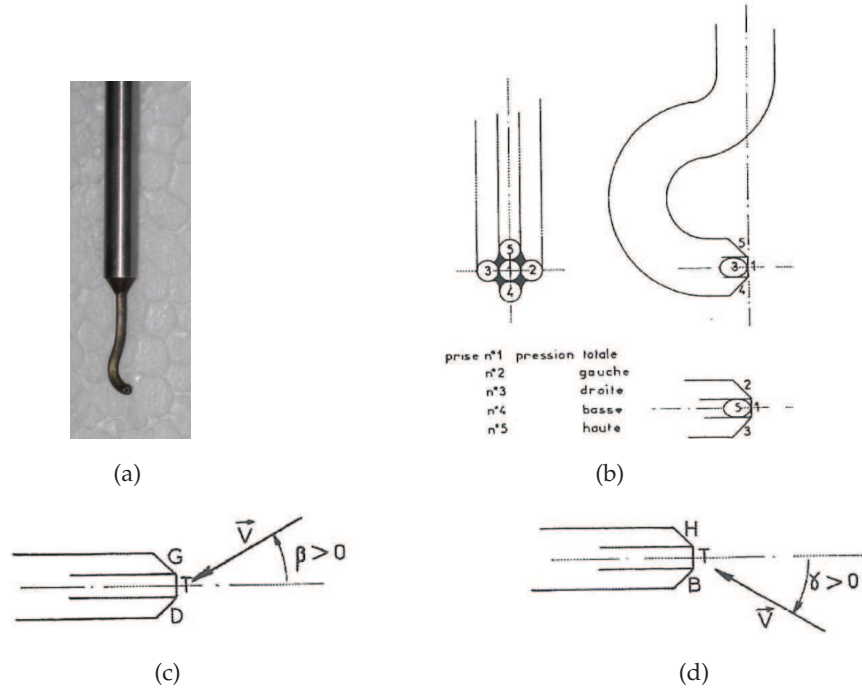


Figure 3.10: Photo and scheme of the five-hole pressure probe.

A five-hole pressure probe can measure abundant 3D information of a low speed flow, including static pressure, total pressure, the direction and the magnitude of the velocity. In our experiment, a five-hole pressure probe is used to measure the inlet flow and the outlet flow.

A. Parameters of pressure probe The scheme of the five-hole pressure probe and the direction of flow angle β and γ are shown in Fig. 3.10. The relations between the coefficients and the pressures are

$$P_{gd} = \frac{P_g + P_d}{2} \quad (3.1a)$$

$$C_\beta = \frac{P_g - P_d}{P_c - P_{gd}} \quad (3.1b)$$

$$C_\gamma = \frac{P_b - P_h}{P_c - P_{gd}} \quad (3.1c)$$

$$C_{P_t} = \frac{P_c - P_{tref}}{P_c - P_{gd}} \quad (3.1d)$$

$$C_{P_s} = \frac{P_{gd} - P_{sref}}{P_c - P_{gd}} \quad (3.1e)$$

where P_c , P_g , P_d , P_h and P_b are the pressure at center, left, right, top and bottom holes, respectively; C_β and C_γ are the angle coefficients of β and γ , respectively. The total pressure P_t and

the static pressure P_s can then be calculated by

$$P_t = P_c - C_{P_t}(P_c - P_{gd}) \quad (3.1f)$$

$$P_s = P_{gd} - C_{P_s}(P_c - P_{gd}) \quad (3.1g)$$

B. Processing of pressure probe In our experiment, the processing of the five-hole pressure probe can be presented as follow:

- **Step 1:** Calibrating the pressure probe and creating the calibration data. Because the velocity of inlet flow in the experiment is always about 40 m/s (i.e. Mach number is about 0.12), the calibration is done under just one Mach number of 0.12. In the calibration, the numbers of the angles β and γ are 25 and 20, respectively. In the process of calibration, P_b , P_h , P_g , P_d and P_c are measured at each β and γ . According to Eq. 3.1, C_{β} , C_{γ} , C_{P_t} , C_{P_s} are then calculated. It means that β , γ , C_{P_t} and C_{P_s} are functions of C_{β} , C_{γ} . The calibration data are shown in Fig. 3.11.
- **Step 2:** In the process of measurement, $P_b - P_h$, $P_g - P_d$, $P_c - P_d$ and P_c are measured.
- **Step 3:** According to Eqs. 3.1b and 3.1c, C_{β} , C_{γ} are calculated.
- **Step 4:** According to the calibration data, the MATLAB[®] interpolation function *griddata*¹ is used to calculate β , γ , C_{P_s} and C_{P_t} .
- **Step 5:** According to Eqs. 3.1f and 3.1g, P_t and P_s are calculated.

C. Correction according to total pressure gradient² Fig. 3.12 shows the sketch of the effects of total pressure gradient on the angle measured by a pressure probe. According to the Eq. 3.1b, the angle β depends on the difference of P_g and P_d . Usually in the calibration, there is not pressure gradient nor velocity gradient, so when $P_g = P_d$, $\beta = 0$ and $P_g \neq P_d$, $\beta \neq 0$. In the process of application, if $\beta_{real} = 0$ but a total pressure gradient exists, the measured P_g is not equal to P_d , and $\beta_{measured} \neq 0$. The effects of total pressure gradient can be represented by the gradient of P_c . Therefore the corrective equation can be expressed as

$$C'_{\beta} = \frac{P_g - P_d}{P_c - P'_{gd}} - \frac{P'_{c \rightarrow g} - P'_{c \rightarrow d}}{P_c - P'_{gd}}, \quad C'_{\gamma} = \frac{P_b - P_h}{P_c - P'_{gd}} - \frac{P'_{c \rightarrow b} - P'_{c \rightarrow h}}{P_c - P'_{gd}},$$

$$C'_{P_t} = \frac{P_c - P_{tref}}{P_c - P'_{gd}}, \quad C'_{P_s} = \frac{P_{gd} - P_{sref}}{P_c - P'_{gd}},$$

$$P'_{gd} = (P'_{g \rightarrow c} + P'_{d \rightarrow c})/2, \quad P'_t = P_c - C'_{P_t}(P_c - P'_{gd}), \quad P'_s = P'_{gd} - C'_{P_s}(P_c - P'_{gd}) \quad (3.2)$$

In Eq. 3.2, the parameters with superscript (') denote the corrective parameters corresponding to Eq. 3.1. The parameters with superscript (i) denote interpolated parameters. $P'_{c \rightarrow g}$, $P'_{c \rightarrow d}$, $P'_{c \rightarrow h}$ and $P'_{c \rightarrow b}$ are interpolated values of P_c at left, right, top and bottom holes, respectively. $P'_{g \rightarrow c}$, $P'_{d \rightarrow c}$ denote the interpolated values of P_g and P_d to the center hole.

¹<http://www.mathworks.com/access/helpdesk/help/techdoc/ref/griddata.html>

²See Appendix B

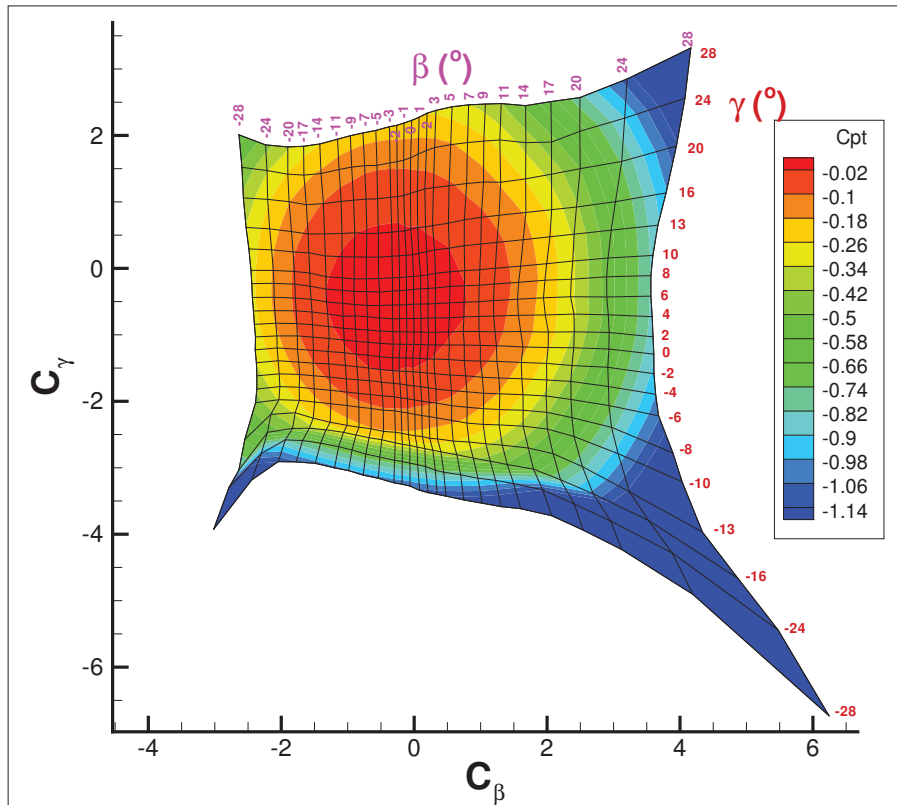
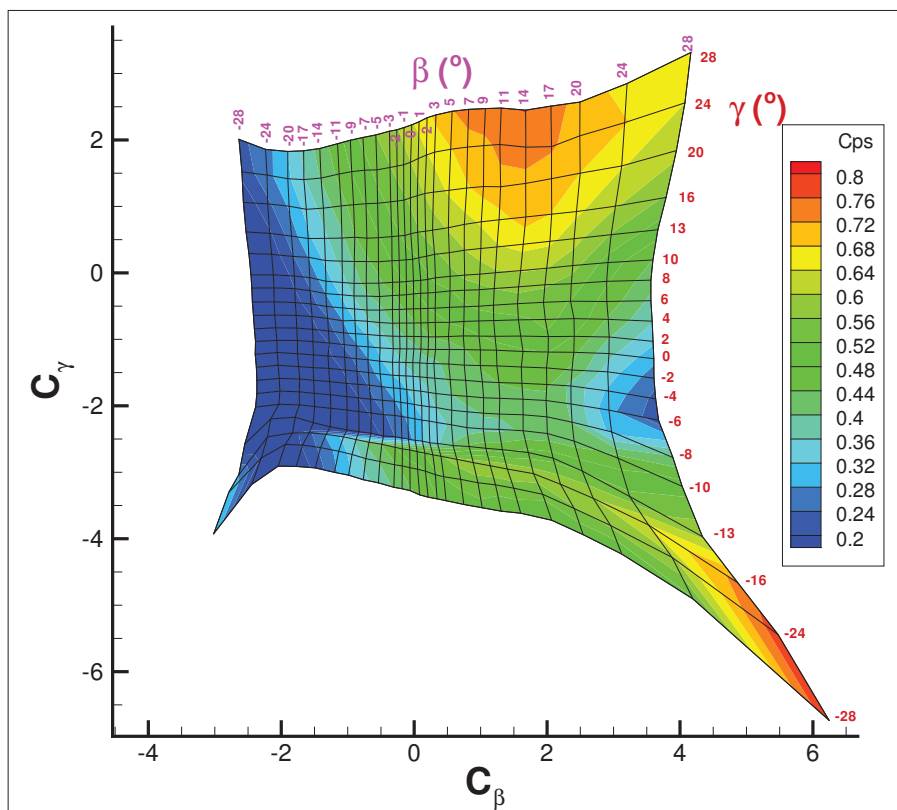
(a) β , γ , C_{P_t} as functions of C_β , C_γ (b) β , γ , C_{P_s} as functions of C_β , C_γ

Figure 3.11: Calibration data of the five-hole pressure probe.

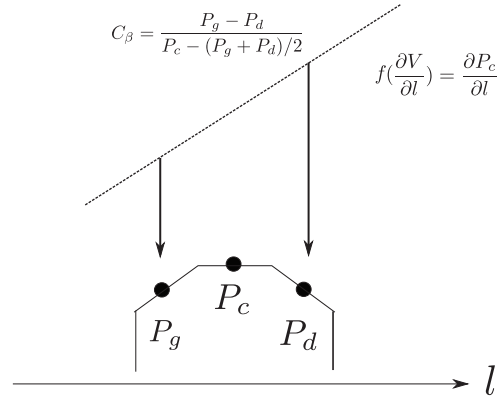


Figure 3.12: Sketch of the effects of total pressure gradient on the angle measured by a pressure probe.

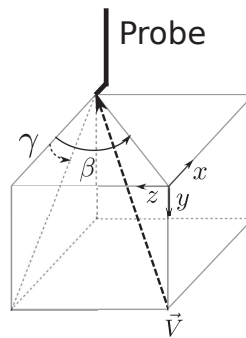


Figure 3.13: Coordinate of the five-hole pressure probe.

D. Velocity components with the pressure probe From the measurements of the pressure probe, including the static pressure P_s , the total pressure P_t and the two flow angles β and γ , the magnitude of the velocity can be calculated by

$$V = \sqrt{2(P_t - P_s)/\rho} \quad (3.3)$$

where ρ is the inlet flow mean density that are measured at the same time with pressures of the Pitot probe at the inlet of the cascade. After both the direction and the magnitude of the velocity are determined, the three component velocities can then be obtained. With the coordinates of the five-hole pressure probe shown in Fig. 3.13, the relations between the measured velocity \vec{V} and the three velocity components can be expressed as

$$u_x^2 + u_y^2 + u_z^2 = V^2, \quad u_y = -u_x \tan \gamma, \quad u_z = u_x \tan \beta \quad (3.4a)$$

where u_x , u_y and u_z are the velocity components in x , y , and z directions, respectively. These three velocity components can then be expressed as

$$\begin{aligned} u_x &= V \sqrt{\frac{1}{1 + \tan^2 \beta + \tan^2 \gamma}}, & u_y &= -V \tan \gamma \sqrt{\frac{1}{1 + \tan^2 \beta + \tan^2 \gamma}}, \\ u_z &= V \tan \beta \sqrt{\frac{1}{1 + \tan^2 \beta + \tan^2 \gamma}} \end{aligned} \quad (3.5)$$

E. Positions of pressure probe The arrangement of the pressure probe and the positions of the measurements are shown in Fig. 3.14 and Fig. 3.15.

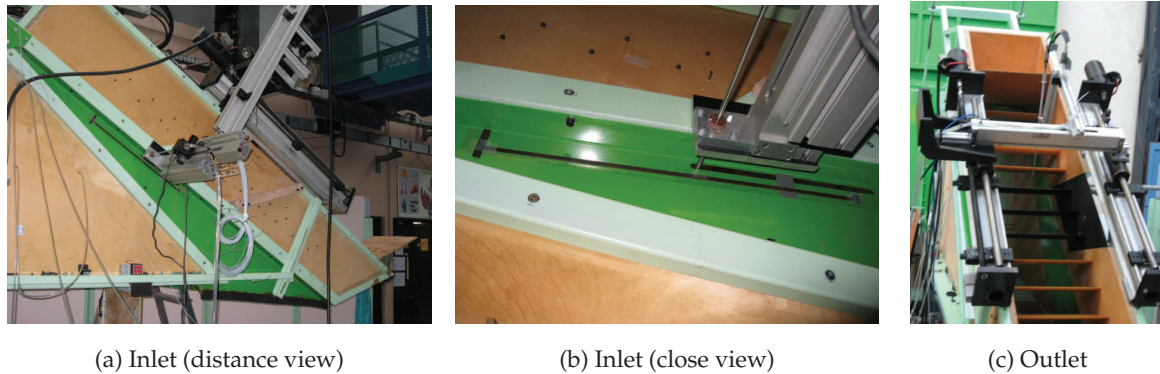


Figure 3.14: Arrangement of the five-hole pressure probe.

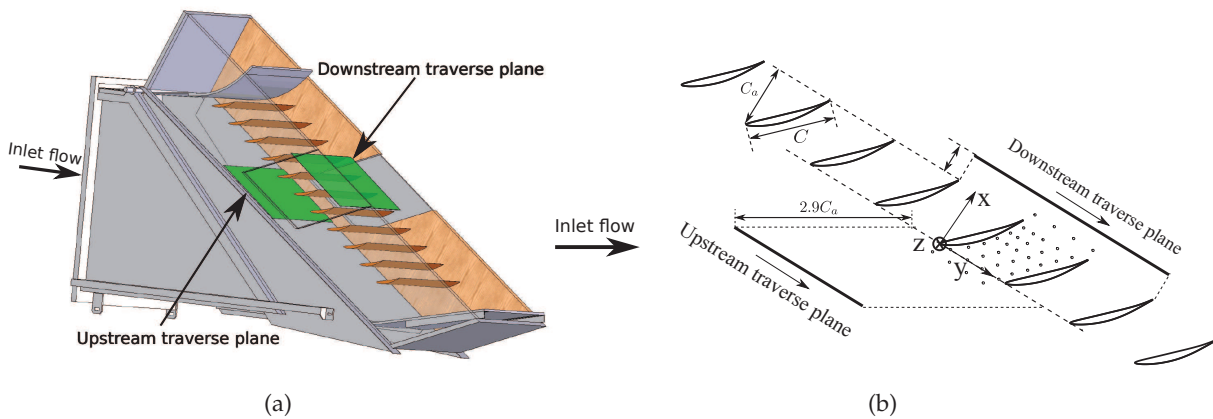


Figure 3.15: Measurement positions of the five-hole pressure probe.

3.2.3.3 Pressure transducers

The pressure taps on the blade are connected to a Scanivalve. Using plastic tubes, both the pressure probe and the Scanivalve are attached to a VALIDYNE¹ Model DP45- $\times\times$ (the number after the dash " $\times\times$ " indicates the correct range according to the DP45 data sheet) electronic pressure transducers. Then the pressures are monitored using Carrier Demodulators, which have an output voltage range of -10 V~10 V. The transducer output voltage is recorded by a NI cDAQ-9172 data acquisition system through a NI 9205. All the data are acquired and controlled by a PC with LabVIEW².

¹<http://www.validyne.com/>

²<http://www.ni.com/labview/>

3.2.3.4 Uncertainty in static pressure on the blade and the endwall

The uncertainty in the static pressure on the blade and the endwall are determined according to the basic definitions of uncertainty analysis, introduced in Appendix A. The formula of coefficient of static pressure is

$$C_p = \frac{P_s - P_s^\infty}{P_t^\infty - P_s^\infty} = \frac{P_{s-a} - P_{s-a}^\infty}{P_{t-a}^\infty - P_{s-a}^\infty} \quad (3.6)$$

Thus the uncertainty in C_p , U_{C_p} , can be expressed as

$$U_{C_p}^2 = \left(\frac{\partial C_p}{\partial P_{s-a}} 2\sigma_{P_{s-a}} \right)^2 + \left(\frac{\partial C_p}{\partial P_{s-a}^\infty} 2\sigma_{P_{s-a}^\infty} \right)^2 + \left(\frac{\partial C_p}{\partial P_{t-a}^\infty} 2\sigma_{P_{t-a}^\infty} \right)^2 \quad (3.7a)$$

with

$$\frac{\partial C_p}{\partial P_{s-a}} = \frac{1}{P_{t-a}^\infty - P_{s-a}^\infty}, \quad \frac{\partial C_p}{\partial P_{s-a}^\infty} = \frac{P_{s-a} - P_{t-a}^\infty}{(P_{t-a}^\infty - P_{s-a}^\infty)^2}, \quad \frac{\partial C_p}{\partial P_{t-a}^\infty} = -\frac{P_{s-a} - P_{s-a}^\infty}{(P_{t-a}^\infty - P_{s-a}^\infty)^2} \quad (3.7b)$$

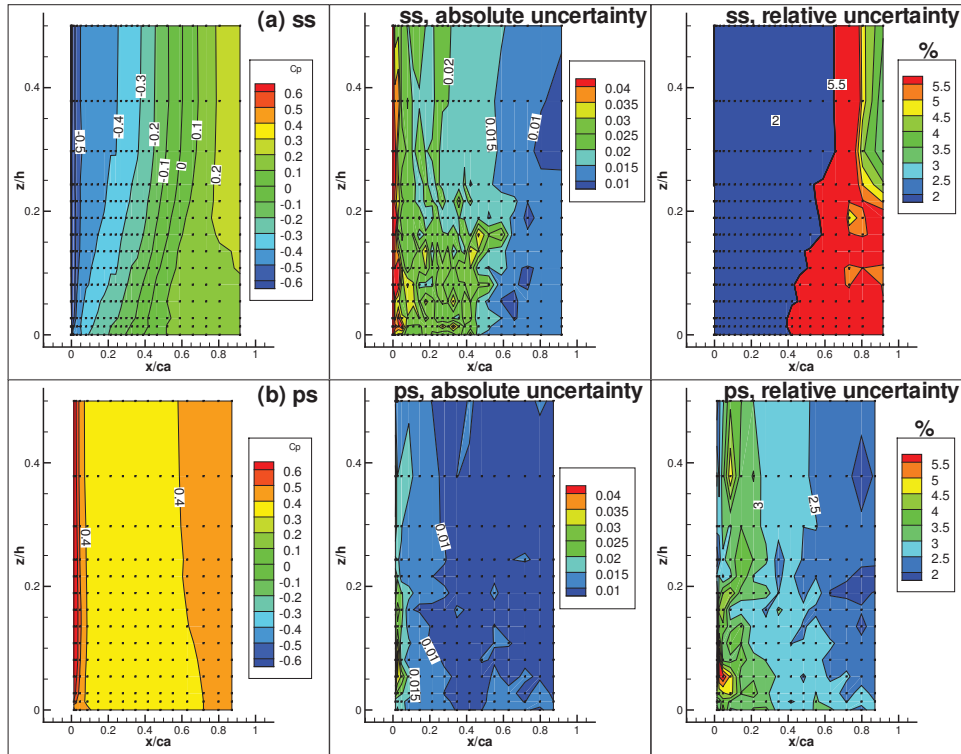


Figure 3.16: An example ($i=4^\circ$) of absolute and relative uncertainties of static pressure on the blade. Markers indicate the measurement positions.

Fig. 3.16 shows typical results of absolute and relative uncertainties of static pressure coefficient C_p on the blade. On the suction side, its absolute value decreases from the leading edge to the trailing edge, and is about 0.02 in the middle region. The corresponding relative value is about 2% in the former region, and increases dramatically in the latter region where the magnitude of C_p is very small. On the pressure side, the absolute uncertainty decreases from the

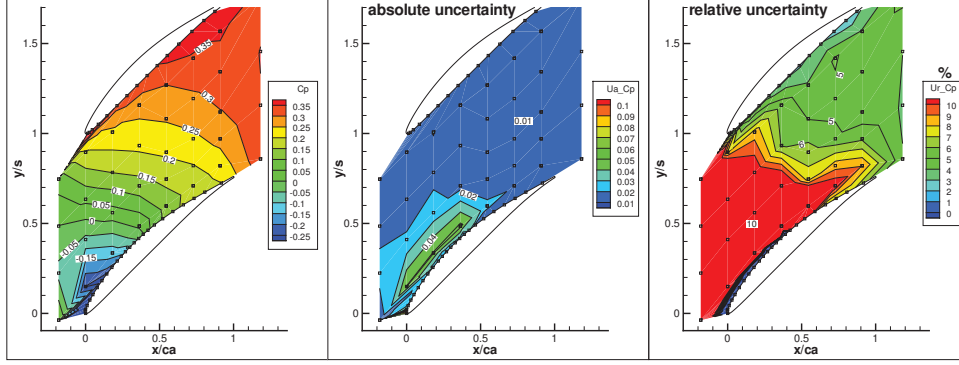


Figure 3.17: An example ($i=4^\circ$) of absolute and relative uncertainties of static pressure on the endwall. Markers indicate the measurement positions.

leading edge to the trailing edge, and is about 0.01 in the middle region. The corresponding relative uncertainty is about 3% in the middle region.

Fig. 3.17 shows typical results of absolute and relative uncertainties of static pressure coefficient C_p on the endwall. The absolute value is about 0.01 except the region near the leading edge and near the suction side. The relative value is very high in the former part where the magnitude of C_p is very small, and is about 5% in the latter part.

3.2.3.5 Uncertainty in the results of the five-hole pressure probe

The uncertainty in the results of the five-hole Pitot probe are determined according to the basic definitions of uncertainty analysis introduced in Appendix A. In the experiment, $P_{b-h} = P_b - P_h$, $P_{g-d} = P_g - P_d$, $P_{c-d} = P_c - P_d$ and $P_{c-a} = P_c - P_{atmo}$ are measured $N=5000$ times and their standard deviation are obtained at the same time, i.e. $\sigma_{P_{b-h}}$, $\sigma_{P_{g-d}}$, $\sigma_{P_{c-d}}$, $\sigma_{P_{c-a}}$. The atmosphere pressure is read from a pressure calibrator with uncertainty of 25 Pa, i.e. the bias limit of atmosphere pressure $B_{P_{atmo}}=25$ Pa. Because of $N>31$ in the experiment, $t=2$ in the Eq. A.13. Using the parameters measured directly, the pressures that will be used can be expressed as

$$P_c = P_{c-a} + P_{atmo} \quad (3.8a)$$

$$P_d = P_c - P_{c-d} = P_{c-a} + P_{atmo} - P_{c-d} \quad (3.8b)$$

$$P_g = P_{g-d} + P_d = P_{g-d} + P_{c-a} + P_{atmo} - P_{c-d} \quad (3.8c)$$

$$\begin{aligned} P_c - P_{gd} &= P_c - (P_g + P_d)/2 = (P_{c-a} + P_{atmo}) - [P_{g-d} + 2(P_{c-a} + P_{atmo} - P_{c-d})]/2 \\ &= P_{c-d} - P_{g-d}/2 \end{aligned} \quad (3.8d)$$

Precision limit of C_{β} , $P_{C_{\beta}}$ From the formula of pressure coefficient C_{β} ,

$$C_{\beta} = \frac{P_g - P_d}{P_c - P_{gd}} = \frac{P_{g-d}}{P_{c-d} - P_{g-d}/2} \quad (3.9a)$$

the precision limit of C_β, P_{C_β} , can be expressed as,

$$P_{C_\beta}^2 = \left(\frac{\partial C_\beta}{\partial P_{g-d}} 2\sigma_{P_{g-d}} \right)^2 + \left(\frac{\partial C_\beta}{\partial P_{c-d}} 2\sigma_{P_{c-d}} \right)^2 + \left(2\sigma_{C_\beta}^e \right)^2 \quad (3.9b)$$

where $\sigma_{C_\beta}^e$ is the uncertainty in C_β in the processing of calibration, and

$$\frac{\partial C_\beta}{\partial P_{g-d}} = \frac{P_{c-d}}{(P_{c-d} - P_{g-d}/2)^2}, \quad \frac{\partial C_\beta}{\partial P_{c-d}} = \frac{-P_{g-d}}{(P_{c-d} - P_{g-d}/2)^2} \quad (3.9c)$$

Precision limit of C_γ, P_{C_γ} From the formula of pressure coefficient C_γ ,

$$C_\gamma = \frac{P_b - P_h}{P_c - P_{gd}} = \frac{P_{b-h}}{P_{c-d} - P_{g-d}/2} \quad (3.10a)$$

the precision limit of C_γ from measurement, P_{C_γ} , can be expressed as,

$$P_{C_\gamma}^2 = \left(\frac{\partial C_\gamma}{\partial P_{b-h}} 2\sigma_{P_{b-h}} \right)^2 + \left(\frac{\partial C_\gamma}{\partial P_{g-d}} 2\sigma_{P_{g-d}} \right)^2 + \left(\frac{\partial C_\gamma}{\partial P_{c-d}} 2\sigma_{P_{c-d}} \right)^2 + \left(2\sigma_{C_\gamma}^e \right)^2 \quad (3.10b)$$

where $\sigma_{C_\gamma}^e$ is the uncertainty in C_γ in the processing of calibration, and

$$\frac{\partial C_\gamma}{\partial P_{b-h}} = \frac{1}{P_{c-d} - P_{g-d}/2}, \quad \frac{\partial C_\gamma}{\partial P_{g-d}} = \frac{P_{b-h}/2}{(P_{c-d} - P_{g-d}/2)^2}, \quad \frac{\partial C_\gamma}{\partial P_{c-d}} = \frac{-P_{b-h}}{(P_{c-d} - P_{g-d}/2)^2} \quad (3.10c)$$

Precision limit of $C_{P_t}, P_{C_{P_t}}$

$$P_{C_{P_t}}^2 = \left(\frac{\partial C_{P_t}}{\partial C_\beta} P_{C_\beta} \right)^2 + \left(\frac{\partial C_{P_t}}{\partial C_\gamma} P_{C_\gamma} \right)^2 + \left(2\sigma_{C_{P_t}}^e \right)^2 \quad (3.11)$$

where $\sigma_{C_{P_t}}^e$ is the uncertainty in C_{P_t} in the processing of calibration.

Precision limit of $C_{P_s}, P_{C_{P_s}}$

$$P_{C_{P_s}} = \left(\frac{\partial C_{P_s}}{\partial C_\beta} P_{C_\beta} \right)^2 + \left(\frac{\partial C_{P_s}}{\partial C_\gamma} P_{C_\gamma} \right)^2 + \left(2\sigma_{C_{P_s}}^e \right)^2 \quad (3.12)$$

where $\sigma_{C_{P_s}}^e$ is the uncertainty in C_{P_s} in the processing of calibration.

Parameters $\partial y_j / \partial x_i$ ($y_j = \beta, \gamma, C_{P_t}, C_{P_s}$; $x_i = C_\beta, C_\gamma$) In the data processing of Pitot probe, β, γ, C_{P_t} and C_{P_s} are calculated from C_β and C_γ using the MATLAB[®] interpolation function according the calibration data. The partial parameter $\partial y_i / \partial x_j$ ($y_i = \beta, \gamma, C_{P_t}, C_{P_s}$; $x_j = C_\beta, C_\gamma$) can

also be determined by

$$\frac{\partial \beta}{\partial C_\beta}(C_\beta, C_\gamma) = [\beta(C_\beta + \eta, C_\gamma) - \beta(C_\beta, C_\gamma)]/\eta \quad (3.13a)$$

$$\frac{\partial \beta}{\partial C_\gamma}(C_\beta, C_\gamma) = [\beta(C_\beta, C_\gamma + \eta) - \beta(C_\beta, C_\gamma)]/\eta \quad (3.13b)$$

$$\frac{\partial \gamma}{\partial C_\beta}(C_\beta, C_\gamma) = [\gamma(C_\beta + \eta, C_\gamma) - \gamma(C_\beta, C_\gamma)]/\eta \quad (3.13c)$$

$$\frac{\partial \gamma}{\partial C_\gamma}(C_\beta, C_\gamma) = [\gamma(C_\beta, C_\gamma + \eta) - \gamma(C_\beta, C_\gamma)]/\eta \quad (3.13d)$$

$$\frac{\partial C_{P_t}}{\partial C_\beta}(C_\beta, C_\gamma) = [C_{P_t}(C_\beta + \eta, C_\gamma) - C_{P_t}(C_\beta, C_\gamma)]/\eta \quad (3.13e)$$

$$\frac{\partial C_{P_t}}{\partial C_\gamma}(C_\beta, C_\gamma) = [C_{P_t}(C_\beta, C_\gamma + \eta) - C_{P_t}(C_\beta, C_\gamma)]/\eta \quad (3.13f)$$

$$\frac{\partial C_{P_s}}{\partial C_\beta}(C_\beta, C_\gamma) = [C_{P_s}(C_\beta + \eta, C_\gamma) - C_{P_s}(C_\beta, C_\gamma)]/\eta \quad (3.13g)$$

$$\frac{\partial C_{P_s}}{\partial C_\gamma}(C_\beta, C_\gamma) = [C_{P_s}(C_\beta, C_\gamma + \eta) - C_{P_s}(C_\beta, C_\gamma)]/\eta \quad (3.13h)$$

where η is a small value, for instance $\eta = 0.01$.

1. Uncertainty in angle β relative to probe, U_β

The total uncertainty in angle β relative to probe, U_β , can be expressed as

$$U_\beta^2 = B_\beta^2 + P_\beta^2 \quad (3.14)$$

where B_β and P_β are bias limit and precision limit of β , respectively. P_β , can be expressed as

$$P_\beta^2 = \left(\frac{\partial \beta}{\partial C_\beta} P_{C_\beta} \right)^2 + \left(\frac{\partial \beta}{\partial C_\gamma} P_{C_\gamma} \right)^2 \quad (3.15a)$$

where P_{C_β} and P_{C_γ} are the precision limit of C_β and C_γ from measurement, respectively.

2. Uncertainty in angle γ relative to probe, U_γ

The total uncertainty in angle γ relative to probe, U_γ , can be expressed as

$$U_\gamma^2 = B_\gamma^2 + P_\gamma^2 \quad (3.16)$$

where B_γ and P_γ are bias limit and precision limit of γ , respectively. P_γ , can be expressed as

$$P_\gamma^2 = \left(\frac{\partial \gamma}{\partial C_\beta} P_{C_\beta} \right)^2 + \left(\frac{\partial \gamma}{\partial C_\gamma} P_{C_\gamma} \right)^2 \quad (3.17a)$$

where P_{C_β} and P_{C_γ} are the precision limit of C_β and C_γ from measurement, respectively.

3. Uncertainty in total pressure P_t , U_{P_t}

The total uncertainty in total pressure, U_{P_t} , can be expressed as

$$U_{P_t}^2 = B_{P_t}^2 + P_{P_t}^2 \quad (3.18)$$

where B_{P_t} and P_{P_t} are bias limit and precision limit of P_t , respectively. The formula of total pressure P_t is

$$P_t = P_c - C_{P_t}(P_c - P_{gd}) = P_{c-a} + P_{atmo} - C_{P_t} \left(P_{c-d} - \frac{P_{g-d}}{2} \right) \quad (3.19a)$$

The bias limit and precision limit of total pressure B_{P_t} and P_{P_t} can be expressed as

$$B_{P_t}^2 = \left(\frac{\partial P_t}{\partial P_{atmo}} B_{P_{atmo}} \right)^2, \quad P_{P_t}^2 = \left(\frac{\partial P_t}{\partial P_{g-d}} P_{P_{g-d}} \right)^2 + \left(\frac{\partial P_t}{\partial P_{c-a}} P_{P_{c-a}} \right)^2 + \left(\frac{\partial P_t}{\partial P_{c-d}} P_{P_{c-d}} \right)^2 + \left(\frac{\partial P_t}{\partial C_{P_t}} P_{C_{P_t}} \right)^2 \quad (3.19b)$$

$$\frac{\partial P_t}{\partial P_{g-d}} = \frac{C_{P_t}}{2}, \quad \frac{\partial P_t}{\partial P_{c-a}} = 1, \quad \frac{\partial P_t}{\partial P_{c-d}} = -C_{P_t}, \quad \frac{\partial P_t}{\partial C_{P_t}} = -(P_{c-d} - \frac{P_{g-d}}{2}), \quad \frac{\partial P_t}{\partial P_{atmo}} = 1 \quad (3.19c)$$

$$B_{P_{atmo}} = 25\text{Pa}, \quad P_{P_{g-d}} = 2\sigma_{P_{g-d}}, \quad P_{P_{c-a}} = 2\sigma_{P_{c-a}}, \quad P_{P_{c-d}} = 2\sigma_{P_{c-d}} \quad (3.19d)$$

4. Uncertainty in static pressure P_s , U_{P_s}

The total uncertainty in static pressure, U_{P_s} , can be expressed as

$$U_{P_s}^2 = B_{P_s}^2 + P_{P_s}^2 \quad (3.20)$$

where B_{P_s} and P_{P_s} are precision bias and precision limit of P_s , respectively. The formula of total pressure P_s is

$$P_s = P_{gd} - C_{P_s}(P_c - P_{gd}) = P_{c-a} + P_{atmo} - P_{c-d} + P_{g-d}/2 - C_{P_s} (P_{c-d} - P_{g-d}/2) \quad (3.21a)$$

The bias limit and precision limit of static pressure B_{P_s} and P_{P_s} can be expressed as

$$B_{P_s}^2 = \left(\frac{\partial P_s}{\partial P_{atmo}} B_{P_{atmo}} \right)^2, \quad P_{P_s}^2 = \left(\frac{\partial P_s}{\partial P_{g-d}} P_{P_{g-d}} \right)^2 + \left(\frac{\partial P_s}{\partial P_{c-a}} P_{P_{c-a}} \right)^2 + \left(\frac{\partial P_s}{\partial P_{c-d}} P_{P_{c-d}} \right)^2 + \left(\frac{\partial P_s}{\partial C_{P_s}} P_{C_{P_s}} \right)^2 \quad (3.21b)$$

$$\frac{\partial P_s}{\partial P_{g-d}} = 1 + \frac{C_{P_s}}{2}, \quad \frac{\partial P_s}{\partial P_{c-a}} = 1, \quad \frac{\partial P_s}{\partial P_{c-d}} = -1 - C_{P_s}, \quad \frac{\partial P_s}{\partial C_{P_s}} = -(P_{c-d} - \frac{P_{g-d}}{2}), \quad \frac{\partial P_s}{\partial P_{atmo}} = 1 \quad (3.21c)$$

$$B_{P_{atmo}} = 25\text{Pa}, \quad P_{P_{g-d}} = 2\sigma_{P_{g-d}}, \quad P_{P_{c-a}} = 2\sigma_{P_{c-a}}, \quad P_{P_{c-d}} = 2\sigma_{P_{c-d}} \quad (3.21d)$$

5. Uncertainty in total losses coefficient ω , U_ω

The formula of total losses coefficient ω is

$$\omega = \frac{P_t^\infty - P_t}{P_t^\infty - P_s^\infty} = \frac{P_{t-a}^\infty - [P_{c-a} - C_{P_t}(P_{c-d} - P_{g-d}/2)]}{P_{t-a}^\infty - P_{s-a}^\infty} \quad (3.22)$$

The uncertainty in ω , U_ω

$$U_\omega^2 = \left(\frac{\partial \omega}{\partial P_{t-a}^\infty} 2\sigma_{P_{t-a}^\infty} \right)^2 + \left(\frac{\partial \omega}{\partial P_{s-a}^\infty} 2\sigma_{P_{s-a}^\infty} \right)^2 + \left(\frac{\partial \omega}{\partial P_{g-d}} 2\sigma_{P_{g-d}} \right)^2 + \left(\frac{\partial \omega}{\partial P_{c-a}} 2\sigma_{P_{c-a}} \right)^2 + \left(\frac{\partial \omega}{\partial P_{c-d}} 2\sigma_{P_{c-d}} \right)^2 + \left(\frac{\partial \omega}{\partial C_{P_t}} P_{C_{P_t}} \right)^2 \quad (3.23a)$$

$$\frac{\partial \omega}{\partial P_{t-a}^\infty} = \frac{-P_{s-a}^\infty + P_{c-a} + C_{P_t}(P_{c-d} - P_{g-d}/2)}{(P_{t-a}^\infty - P_{s-a}^\infty)^2} \quad (3.23b)$$

$$\frac{\partial \omega}{\partial P_{s-a}^\infty} = \frac{P_{t-a}^\infty - (P_{c-a} - C_{P_t}(P_{c-d} - P_{g-d}/2))}{(P_{t-a}^\infty - P_{s-a}^\infty)^2} \quad (3.23c)$$

$$\frac{\partial \omega}{\partial P_{g-d}} = \frac{-C_{P_t}/2}{P_{t-a}^\infty - P_{s-a}^\infty}, \quad \frac{\partial \omega}{\partial P_{c-a}} = \frac{-1}{P_{t-a}^\infty - P_{s-a}^\infty}, \quad \frac{\partial \omega}{\partial P_{c-d}} = \frac{C_{P_t}}{P_{t-a}^\infty - P_{s-a}^\infty}, \quad \frac{\partial \omega}{\partial C_{P_t}} = \frac{P_{c-d} - P_{g-d}/2}{P_{t-a}^\infty - P_{s-a}^\infty} \quad (3.23d)$$

6. Uncertainty in magnitude of density ρ , U_ρ

The formula of density ρ is

$$\rho = \frac{P_{s-a}^\infty + P_{atmo}}{RT_t \left(\frac{P_{t-a}^\infty + P_{atmo}}{P_{s-a}^\infty + P_{atmo}} \right)^{-(k-1)/k}} \quad (3.24)$$

where $k = 1.4$ and $R = 287.06 \text{ J}/(\text{kg} \cdot \text{K})$. The uncertainty in density ρ , U_ρ is

$$U_\rho = \left(\frac{\partial \rho}{\partial P_{s-a}^\infty} 2\sigma_{P_{s-a}^\infty} \right)^2 + \left(\frac{\partial \rho}{\partial P_{t-a}^\infty} 2\sigma_{P_{t-a}^\infty} \right)^2 + \left(\frac{\partial \rho}{\partial P_{atmo}} B_{P_{atmo}} \right)^2 + \left(\frac{\partial \rho}{\partial T_t} U_{T_t} \right)^2 \quad (3.25a)$$

$$\frac{\partial \rho}{\partial P_{s-a}^\infty} = \frac{1}{kRT_t} \left(\frac{P_{t-a}^\infty + P_{atmo}}{P_{s-a}^\infty + P_{atmo}} \right)^{(k-1)/k} \quad (3.25b)$$

$$\frac{\partial \rho}{\partial P_{t-a}^\infty} = \frac{k-1}{kRT_t} \left(\frac{P_{t-a}^\infty + P_{atmo}}{P_{s-a}^\infty + P_{atmo}} \right)^{-1/k} \quad (3.25c)$$

$$\frac{\partial \rho}{\partial P_{atmo}} = \frac{1}{RT_t} \left(1 - \frac{k-1}{k} \frac{P_{t-a}^\infty - P_{s-a}^\infty}{P_{t-a}^\infty + P_{atmo}} \right) \left(\frac{P_{t-a}^\infty + P_{atmo}}{P_{s-a}^\infty + P_{atmo}} \right)^{(k-1)/k} \quad (3.25d)$$

$$\frac{\partial \rho}{\partial T_t} = -\frac{P_{s-a}^\infty + P_{atmo}}{RT_t^2} \left(\frac{P_{t-a}^\infty + P_{atmo}}{P_{s-a}^\infty + P_{atmo}} \right)^{(k-1)/k} \quad (3.25e)$$

7. Uncertainty in magnitude of velocity V , U_V

The formula of magnitude of velocity V is

$$V = \sqrt{2(P_t - P_s)/\rho} = \sqrt{2/\rho(1 + C_{P_s} - C_{P_t})(P_{c-d} - P_{g-d}/2)} \quad (3.26)$$

The uncertainty in magnitude of velocity V , U_V

$$U_V^2 = \left(\frac{\partial V}{\partial P_{c-d}} 2\sigma_{P_{c-d}} \right)^2 + \left(\frac{\partial V}{\partial P_{g-d}} 2\sigma_{P_{g-d}} \right)^2 + \left(\frac{\partial V}{\partial C_{P_t}} P_{C_{P_t}} \right)^2 + \left(\frac{\partial V}{\partial C_{P_s}} P_{C_{P_s}} \right)^2 + \left(\frac{\partial V}{\partial \rho} U_\rho \right)^2 \quad (3.27a)$$

$$\frac{\partial V}{\partial P_{c-d}} = \frac{1}{\rho} (1 + C_{P_s} - C_{P_t}) \left(\frac{2}{\rho} (1 + C_{P_s} - C_{P_t}) (P_{c-d} - \frac{P_{g-d}}{2}) \right)^{-1/2} \quad (3.27b)$$

$$\frac{\partial V}{\partial P_{g-d}} = -\frac{1}{2\rho} (1 + C_{P_s} - C_{P_t}) \left(\frac{2}{\rho} (1 + C_{P_s} - C_{P_t}) (P_{c-d} - \frac{P_{g-d}}{2}) \right)^{-1/2} \quad (3.27c)$$

$$\frac{\partial V}{\partial C_{P_t}} = -\frac{1}{\rho} (P_{c-d} - \frac{P_{g-d}}{2}) \left(\frac{2}{\rho} (1 + C_{P_s} - C_{P_t}) (P_{c-d} - \frac{P_{g-d}}{2}) \right)^{-1/2} \quad (3.27d)$$

$$\frac{\partial V}{\partial C_{P_s}} = \frac{1}{\rho} (P_{c-d} - \frac{P_{g-d}}{2}) \left(\frac{2}{\rho} (1 + C_{P_s} - C_{P_t}) (P_{c-d} - \frac{P_{g-d}}{2}) \right)^{-1/2} \quad (3.27e)$$

$$\frac{\partial V}{\partial \rho} = -\frac{1}{\rho^{3/2} 2^{1/2}} \left((1 + C_{P_s} - C_{P_t}) (P_{c-d} - \frac{P_{g-d}}{2}) \right)^{1/2} \quad (3.27f)$$

8. Uncertainty in u_x in probe coordinate, U_{u_x}

The formula of u_x in probe coordinate is

$$u_x = V \sqrt{1 / (1 + \tan^2 \beta + \tan^2 \gamma)} \quad (3.28)$$

The uncertainty in u_x in probe coordinate, U_{u_x}

$$U_{u_x}^2 = \left(\frac{\partial u_x}{\partial V} U_V \right)^2 + \left(\frac{\partial u_x}{\partial \beta} U_\beta \right)^2 + \left(\frac{\partial u_x}{\partial \gamma} U_\gamma \right)^2 \quad (3.29a)$$

$$\frac{\partial u_x}{\partial V} = (1 + \tan^2 \beta + \tan^2 \gamma)^{-1/2} \quad (3.29b)$$

$$\frac{\partial u_x}{\partial \beta} = -\frac{V \tan \beta}{\cos^2 \beta} (1 + \tan^2 \beta + \tan^2 \gamma)^{-3/2} \quad (3.29c)$$

$$\frac{\partial u_x}{\partial \gamma} = -\frac{V \tan \gamma}{\cos^2 \gamma} (1 + \tan^2 \beta + \tan^2 \gamma)^{-3/2} \quad (3.29d)$$

9. Uncertainty in u_y in probe coordinate, U_{u_y}

The formula of u_y in probe coordinate is

$$u_y = -V \tan \gamma \sqrt{1 / (1 + \tan^2 \beta + \tan^2 \gamma)} \quad (3.30)$$

The uncertainty in u_y in probe coordinate, U_{u_y}

$$U_{u_y}^2 = \left(\frac{\partial u_y}{\partial V} U_V \right)^2 + \left(\frac{\partial u_y}{\partial \beta} U_\beta \right)^2 + \left(\frac{\partial u_y}{\partial \gamma} U_\gamma \right)^2 \quad (3.31a)$$

$$\frac{\partial u_y}{\partial V} = -\tan \gamma (1 + \tan^2 \beta + \tan^2 \gamma)^{-1/2} \quad (3.31b)$$

$$\frac{\partial u_y}{\partial \beta} = \frac{V \tan \beta \tan \gamma}{\cos^2 \beta} (1 + \tan^2 \beta + \tan^2 \gamma)^{-3/2} \quad (3.31c)$$

$$\frac{\partial u_y}{\partial \gamma} = -\frac{V}{\cos^2 \gamma} (1 + \tan^2 \beta + \tan^2 \gamma)^{-1/2} + \frac{V \tan^2 \gamma}{\cos^2 \gamma} (1 + \tan^2 \beta + \tan^2 \gamma)^{-3/2} \quad (3.31d)$$

10. Uncertainty in u_z in probe coordinate, U_{u_z}

The formula of u_z in probe coordinate is

$$u_z = V \tan \beta \sqrt{1/(1 + \tan^2 \beta + \tan^2 \gamma)} \quad (3.32)$$

The uncertainty in u_z in probe coordinate, U_{u_z}

$$U_{u_z}^2 = \left(\frac{\partial u_z}{\partial V} U_V \right)^2 + \left(\frac{\partial u_z}{\partial \beta} U_\beta \right)^2 + \left(\frac{\partial u_z}{\partial \gamma} U_\gamma \right)^2 \quad (3.33a)$$

$$\frac{\partial u_z}{\partial V} = \tan \beta (1 + \tan^2 \beta + \tan^2 \gamma)^{-1/2} \quad (3.33b)$$

$$\frac{\partial u_z}{\partial \beta} = \frac{V}{\cos^2 \beta} (1 + \tan^2 \beta + \tan^2 \gamma)^{-1/2} - \frac{V \tan^2 \beta}{\cos^2 \beta} (1 + \tan^2 \beta + \tan^2 \gamma)^{-3/2} \quad (3.33c)$$

$$\frac{\partial u_z}{\partial \gamma} = -\frac{V \tan \beta \tan \gamma}{\cos^2 \gamma} (1 + \tan^2 \beta + \tan^2 \gamma)^{-3/2} \quad (3.33d)$$

11. Uncertainty in angle β' in cascade coordinate, $U_{\beta'}$

The formula of β', γ' in cascade coordinate are

$$\beta' = \arctan \frac{\tan \beta}{\cos \theta_{xy} - \tan \gamma \sin \theta_{xy}} + \theta_{xz} \quad (3.34)$$

where the θ_{xy} and θ_{xz} are the shift angles from probe coordinate to cascade coordinate in x - y and x - z plans, respectively. The uncertainty in angle β' in cascade coordinate, $U_{\beta'}$,

$$U_{\beta'}^2 = \left(\frac{\partial \beta'}{\partial \beta} U_\beta \right)^2 + \left(\frac{\partial \beta'}{\partial \gamma} U_\gamma \right)^2 + \left(\frac{\partial \beta'}{\partial \theta_{xy}} U_{\theta_{xy}} \right)^2 + \left(\frac{\partial \beta'}{\partial \theta_{xz}} U_{\theta_{xz}} \right)^2 \quad (3.35a)$$

$$\frac{\partial \beta'}{\partial \beta} = \frac{1}{1 + \left(\frac{\tan \beta}{\cos \theta_{xy} - \tan \gamma \sin \theta} \right)^2} \frac{1}{\cos \theta_{xy} - \tan \gamma \sin \theta_{xy}} \frac{1}{\cos^2 \beta} \quad (3.35b)$$

$$\frac{\partial \beta'}{\partial \gamma} = \frac{1}{1 + \left(\frac{\tan \beta}{\cos \theta_{xy} - \tan \gamma \sin \theta} \right)^2} \frac{\tan \beta \sin \theta_{xy}}{(\cos \theta_{xy} - \tan \gamma \sin \theta_{xy})^2} \frac{1}{\cos^2 \gamma} \quad (3.35c)$$

$$\frac{\partial \beta'}{\partial \theta_{xy}} = \frac{1}{1 + \left(\frac{\tan \beta}{\cos \theta_{xy} - \tan \gamma \sin \theta} \right)^2} \frac{\tan \beta (\sin \theta_{xy} + \tan \gamma \cos \theta_{xy})}{(\cos \theta_{xy} - \tan \gamma \sin \theta_{xy})^2} \quad (3.35d)$$

$$\frac{\partial \beta'}{\partial \theta_{xz}} = 1 \quad (3.35e)$$

In the experiment, $U_{\theta_{xy}} = 0.2^\circ, U_{\theta_{xz}} = 0.2^\circ$.

12. Uncertainty in angle γ' in cascade coordinate, $U_{\gamma'}$

The formula of γ' in cascade coordinate is

$$\gamma' = \gamma + \theta_{xy} \quad (3.36)$$

where the θ_{xy} and θ_{xz} are the shift angles from probe coordinate to cascade coordinate in x - y and x - z plans, respectively. The uncertainty in angle γ' in cascade coordinate, $U_{\gamma'}$,

$$U_{\gamma'}^2 = \left(\frac{\partial \gamma'}{\partial \gamma} U_{\gamma} \right)^2 + \left(\frac{\partial \gamma'}{\partial \theta_{xy}} U_{\theta_{xy}} \right)^2, \quad \frac{\partial \gamma'}{\partial \gamma} = 1, \quad \frac{\partial \gamma'}{\partial \theta_{xy}} = 1 \quad (3.37a)$$

In the experiment, $U_{\theta_{xy}} = 0.2^\circ$.

13. Uncertainty in u'_x in cascade coordinate, $U_{u'_x}$

The formula of u'_x in probe coordinate is

$$u'_x = V \sqrt{1/(1 + \tan^2 \beta' + \tan^2 \gamma')} \quad (3.38)$$

The uncertainty in u'_x in probe coordinate, $U_{u'_x}$

$$U_{u'_x}^2 = \left(\frac{\partial u'_x}{\partial V} U_V \right)^2 + \left(\frac{\partial u'_x}{\partial \beta'} U_{\beta'} \right)^2 + \left(\frac{\partial u'_x}{\partial \gamma'} U_{\gamma'} \right)^2 \quad (3.39a)$$

$$\frac{\partial u'_x}{\partial V} = (1 + \tan^2 \beta' + \tan^2 \gamma')^{-1/2} \quad (3.39b)$$

$$\frac{\partial u'_x}{\partial \beta'} = -\frac{V \tan \beta'}{\cos^2 \beta'} (1 + \tan^2 \beta' + \tan^2 \gamma')^{-3/2} \quad (3.39c)$$

$$\frac{\partial u'_x}{\partial \gamma'} = -\frac{V \tan \gamma'}{\cos^2 \gamma'} (1 + \tan^2 \beta' + \tan^2 \gamma')^{-3/2} \quad (3.39d)$$

14. Uncertainty in u'_y in probe coordinate, $U_{u'_y}$

The formula of u'_y in probe coordinate is

$$u'_y = -V \tan \gamma' \sqrt{1/(1 + \tan^2 \beta' + \tan^2 \gamma')} \quad (3.40)$$

The uncertainty in u'_y in probe coordinate, $U_{u'_y}$

$$U_{u'_y}^2 = \left(\frac{\partial u'_y}{\partial V} U_V \right)^2 + \left(\frac{\partial u'_y}{\partial \beta'} U_{\beta'} \right)^2 + \left(\frac{\partial u'_y}{\partial \gamma'} U_{\gamma'} \right)^2 \quad (3.41a)$$

$$\frac{\partial u'_y}{\partial V} = -\tan \gamma' (1 + \tan^2 \beta' + \tan^2 \gamma')^{-1/2} \quad (3.41b)$$

$$\frac{\partial u'_y}{\partial \beta'} = \frac{V \tan \beta' \tan \gamma'}{\cos^2 \beta'} (1 + \tan^2 \beta' + \tan^2 \gamma')^{-3/2} \quad (3.41c)$$

$$\frac{\partial u'_y}{\partial \gamma'} = -\frac{V}{\cos^2 \gamma'} (1 + \tan^2 \beta' + \tan^2 \gamma')^{-1/2} + \frac{V \tan^2 \gamma'}{\cos^2 \gamma'} (1 + \tan^2 \beta' + \tan^2 \gamma')^{-3/2} \quad (3.41d)$$

15. Uncertainty in u'_z in probe coordinate, $U_{u'_z}$

The formula of u'_z in probe coordinate is

$$u'_z = V \tan \beta' \sqrt{1/(1 + \tan^2 \beta' + \tan^2 \gamma')} \quad (3.42)$$

The uncertainty in u'_z in probe coordinate, $U_{u'_z}$

$$U_{u'_x}^2 = \left(\frac{\partial u'_z}{\partial V} U_V \right)^2 + \left(\frac{\partial u'_z}{\partial \beta'} U_{\beta'} \right)^2 + \left(\frac{\partial u'_z}{\partial \gamma'} U_{\gamma'} \right)^2 \quad (3.43a)$$

$$\frac{\partial u'_z}{\partial V} = \tan \beta' (1 + \tan^2 \beta' + \tan^2 \gamma')^{-1/2} \quad (3.43b)$$

$$\frac{\partial u'_z}{\partial \beta'} = \frac{V}{\cos^2 \beta'} (1 + \tan^2 \beta' + \tan^2 \gamma')^{-1/2} - \frac{V \tan^2 \beta'}{\cos^2 \beta'} (1 + \tan^2 \beta' + \tan^2 \gamma')^{-3/2} \quad (3.43c)$$

$$\frac{\partial u'_z}{\partial \gamma'} = -\frac{V \tan \beta' \tan \gamma'}{\cos^2 \gamma'} (1 + \tan^2 \beta' + \tan^2 \gamma')^{-3/2} \quad (3.43d)$$

Attention: $U_{\beta'}$, $U_{\gamma'}$ in Eqs. 3.29a, 3.31a, 3.33a, 3.39a, 3.41a and 3.43a are in radians.

Example In the measurement, the original position of the five-hole pressure probe is adjusted for measuring the corner region with small uncertainty. Fig. 3.16 shows typical results of absolute and relative uncertainties of the results measured by the five-hole pressure probe. For the total losses coefficient ω (see Fig. 3.16a), its relative value is about 0.03, and its corresponding relative value is about 3% in the corner region and increases in the other region where the magnitude of ω is very small. For the nondimensional magnitude of velocity (see Fig. 3.16b), its relative value is about 0.04, and increases in the corner region. The corresponding relative value is very high in the corner region where the magnitude of velocity is very small, and is about 5% in the other region.

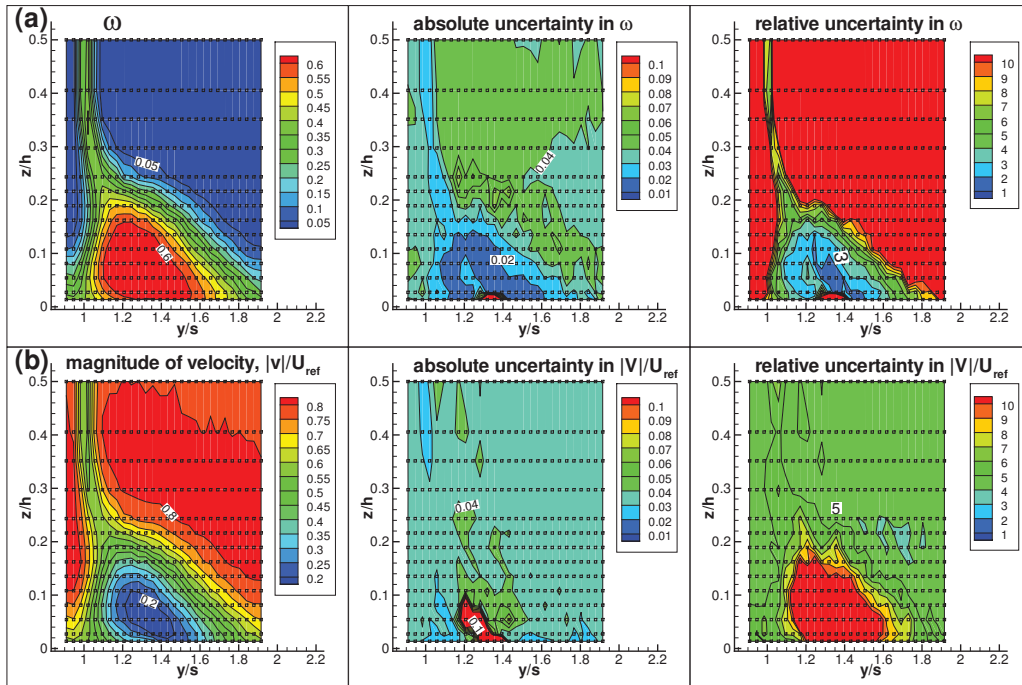


Figure 3.18: An example ($i=4^\circ$, outlet Section 1) of absolute and relative uncertainties in results measured by the five-hole pressure probe: (a) total losses coefficient; (b) magnitude of velocity. Markers indicate the measurement positions.

3.2.4 Hot-wire anemometry (HWA)

3.2.4.1 Introduction of HWA

The history of HWA goes back to the beginning of 20th century, and a major breakthrough was made in the 1950s. By using very fine wire sensors placed in the fluid and electronics with servo-loop technique, the HWA can provide reliable information on the fluctuating flow component in both the space and time domains. As a flow measurement device, the HWA has a number of positive attributes. It has extremely high frequency-response and fine spatial resolution, provides a continuous signal, produces an almost “local” spatial measurement, can be used over a large range of velocities and can be used in gases, bubbly mixtures and opaque liquids. But like all sensors, HWA has its disadvantages, for example it intrudes into the flow and it is not well suited to reversing flows. There are a lot of references in the literature, for example [Bruun \(1995\)](#) and [Comte-Bellot \(1998\)](#).

The hot wire is heated by an electric current (Joule effect) and simultaneously cooled by the convective heat transfer induced by the lower-temperature of the incident flow. The electrical resistance of the hot wire depends on its temperature. There is a relation between these parameters, for example, King’s law ([King, 1914](#)) suggested a relation for subsonic incompressible flows as:

$$\frac{R_w I_w^2}{R_w - R_{ref}} = A + BU^{0.5} \quad (3.44)$$

where R_w is the sensor resistance at the operating temperature T_w during the calibration, R_{ref} is the resistance at the ambient (reference) temperature T_{ref} during the calibration and I_w is the electrical current passing through the hot wire.

Depending on the electronic system in which the sensor is included, there are three types of anemometers, constant-current anemometer (CCA), constant-temperature anemometer (CTA) and constant-voltage anemometer (CVA). Because CTA is easy to use and has high frequency response and low noise, it is the most attractive type and has been chosen in our experiment.

A basic circuit for the CTA is illustrated in [Fig. 3.19](#). The hot-wire probe is placed in a Wheatstone bridge. As the flow conditions vary the error voltage $e_2 - e_1$ will be a measure of the corresponding change in the wire resistance. These two voltages form the input to the operational amplifier. The selected amplifier has an output current, i , which is inversely proportional to the resistance change in the hot-wire sensor. Feeding this current back to the top of the bridge will restore the sensor’s resistance to its original value.

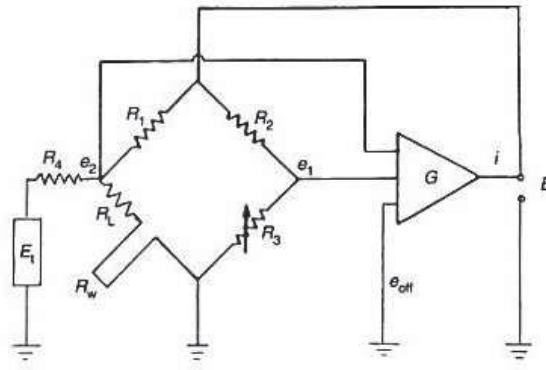


Figure 3.19: A basic CTA circuit, containing a Wheatstone bridge, a feedback amplifier and a electronic-testing subcircuit, (Bruun, 1995, pp.46).

The relation between the bridge voltage E and the velocity U may be described as an exponential function

$$U = (E^2/B - A)^{1/n} \quad (3.45)$$

where A , B and n are the calibration constants, or as a polynomial

$$U = C_0 + C_1E + C_2E^2 + C_3E^3 + C_4E^4 \quad (3.46)$$

where C_0 to C_4 are the calibration constants. Because the polynomial is simpler and more accurate, it is used in our experiment.

3.2.4.2 Hot-wire probes

In this work, the Dantec¹ 55P05 probes are used, shown in Fig. 3.20 The prongs of the sensor are perpendicular to the probe axis. This probe is designed for using in boundary layers. The shape of the prongs permits measurements close to a solid wall without disturbance from the probe body, which is out of the boundary layer. The probe is mounted with the probe axis parallel to the direction of flow.

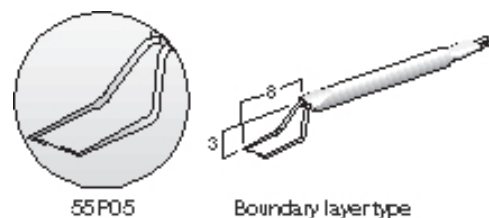


Figure 3.20: Dantec probe (from the web of Dantec). The dimensions are in millimeters.

¹<http://www.dantecdynamics.com>

3.2.4.3 Probe mounting and positioning

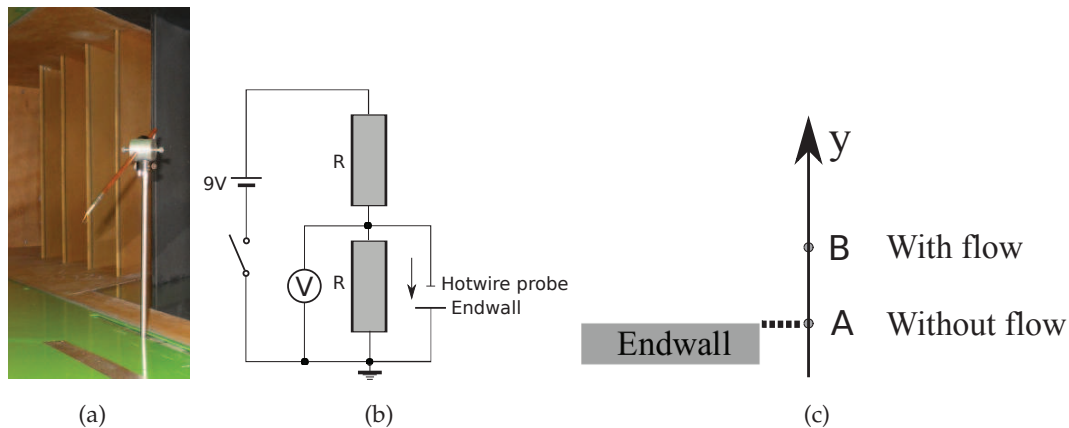


Figure 3.21: Hot-wire probe mounting and positioning: (a) a snap in the experiment; (b) circuit diagram for probe positioning; (c) position of hot-wire and influences of vibration.

Probes are introduced into the flow through slots cut through the endwall, using the same method as the five-hole pressure probe (see Fig. 3.21a). The probes are positioned in the measurement plane by means of a computer controlled traverse system. The resolution of the programmable traverse movement is 0.05 mm.

The circuit diagram (Ottavy & Hodson, 2000) as shown in Fig. 3.21b is used to observe the situation when the distance between hotwire probe and endwall is zero. In the beginning, the voltage measured by the voltmeter is half of battery voltage V , indicating hotwire probe does not touch the endwall. The hotwire probe is then moved towards the endwall. This process is controlled by the traverse system step by step, until the voltage measured by the voltmeter reaches zero, implying that the hot-wire probe touches the endwall. Because of the vibration and the hotwire probe fragility, during the experiment the velocity of the probe approaching the endwall is set to 0.02 mm/step. We then measured two positions y_A and y_B , illustrated in Fig. 3.21c. y_B is the distance with inlet flow and when the mean voltage measured during 1s is smaller than 90% V , while y_A is the distance without inlet flow and when the mean voltage measured during 1s is smaller than 20% V . The distance $y_B - y_A$ is used to determine the original measurement positions.

3.2.4.4 Calibration

The hot-wire calibration is achieved in LMFA (Fig. 3.22). Square wave test is used to optimize the bandwidth of the combined sensor/anemometer circuit. The bandwidth of the probe/anemometer system (or cut-off frequency) with a one-dimension hotwire in our experiment is about 60 kHz. According to the Nyquist sampling criteria, sampling rate has to be

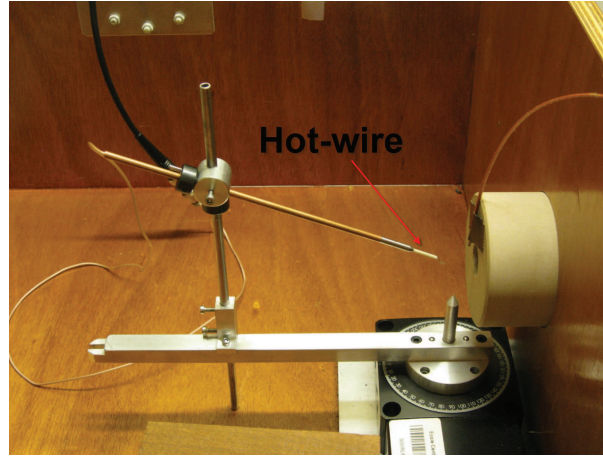


Figure 3.22: Hotwire calibration.

greater than 120 kHz; here the sampling rate is 200 kHz. The number of samples obtained is set to 10^6 .

3.2.4.5 Data conversion

Step 1: Re-scaling of CTA-signals Calculation of the re-scaled voltage E from the acquired voltage E_a :

$$E = \frac{E_a}{Gain} - E_{offset} \quad (3.47)$$

In our experiment, $Gain=4.0$ and $E_{offset}=2.0$.

Step 2: Temperature correction The bridge voltage depends on both the velocity and the temperature. The voltage may be corrected before the linearization, using the ratio between the over-temperatures during the calibration and the measurement. The fluid temperature T_a needs then to be acquired along with the CTA voltage E_a . The corrected CTA voltage E_{corr} can be calculated as:

$$E_{corr} = E_a \left(\frac{T_w - T_{ref}}{T_w - T_a} \right)^{0.5} \quad (3.48)$$

in which,

$$T_w = T_{ref} + \frac{a}{\alpha_0} \quad (3.49)$$

$$a = \frac{R_w - R_{ref}}{R_{ref}} \quad (3.50)$$

where a is the overheat ratio ($a=0.8$ in our experiment), R_w is the sensor resistance at operating temperature T_w during the calibration, R_{ref} is the resistance at the ambient (reference) temperature T_{ref} during the calibration, α_0 is the sensor temperature coefficient of the resistance at the ambient(reference) temperature T_{ref} , the values stated on the probe container are used, for

example $\alpha_0 = \alpha_{20^\circ\text{C}} = 0.36\%$ for the boundary layer probe 55P05. In practice, the ambient temperature T_{ref} is measured and saved during the calibration, while it is read in the saved file during the measurement. T_w is calculated according to Eq. 3.49, and the temperature correction is then carried out according to Eq. 3.48.

Step 3: Conversion into velocities The CTA voltages are converted into velocities by inserting the acquired voltages into the calibration transfer functions. The four-order polynomial is used as a transfer function between bridge voltage and velocity.

$$U = C_0 + C_1 E_{corr} + C_2 E_{corr}^2 + C_3 E_{corr}^3 + C_4 E_{corr}^4 \quad (3.51)$$

where C_0 to C_4 are the calibrated constants. A typical fitting line as well as the original calibration data is shown in Fig. 3.23.

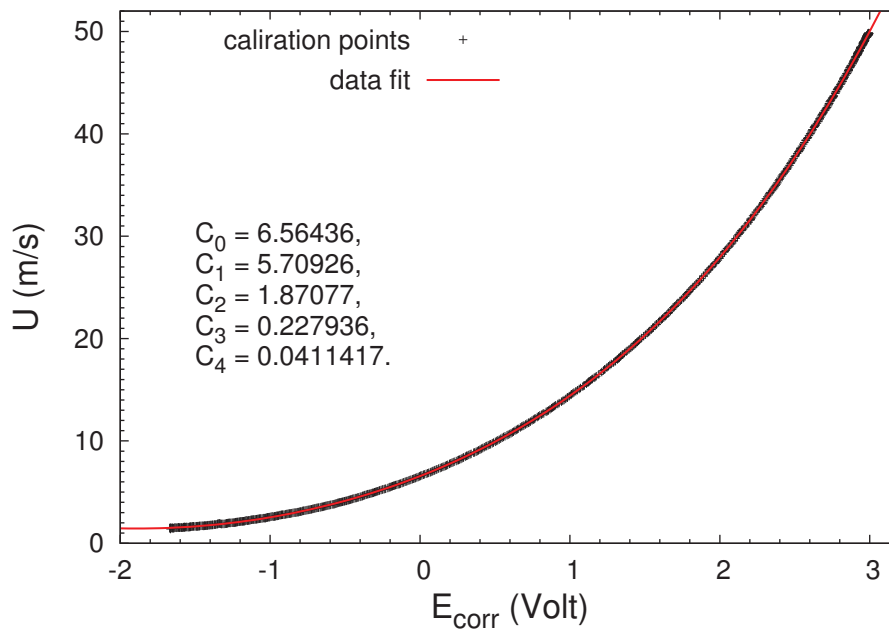


Figure 3.23: Transfer function between bridge voltage and velocity.

3.2.4.6 Uncertainty

The method, to determine the uncertainties in the velocity measurements by 1D hot-wire, refers to (Jorgensen, 2002). The resources of uncertainty are listed in Table 3.5.

In our experiment a typical inlet boundary layer is shown in Fig. 3.24, including the mean velocity and its absolute and relative uncertainties.

Outside the boundary layer, the typical input data are: $T_w - T_0 = 225^\circ\text{C}$, $U = 40 \text{ m/s}$, $\partial U / \partial E = 40.0 \text{ m/(s}\cdot\text{Volt)}$. The corresponding relative output uncertainties are also listed in Table 3.5. The

total relative uncertainty in the mean velocity U is then about $2 \cdot \sqrt{\sum (\epsilon_i)^2} \approx 0.02 = 2\%$. Additionally, the absolute uncertainty in the mean velocity U is about 0.8 m/s.

In the boundary layer, the absolute uncertainty in the mean velocity is also about 1 m/s; About the relative uncertainty, it increases gradually when the distance to the wall surface decreases.

Using the same method, the total relative uncertainty in Reynolds stress $\overline{u^2}$ outside the boundary layer is about 4%. In the boundary layer, this value increases gradually when the distance to the wall surface decreases.

Table 3.5: Uncertainties of 1D hot-wire outside the boundary layer.

Source of uncertainty	Input variants	Typical value	Relative output variants	Relative output uncertainty (ϵ_i)
Calibrator	ΔU_{cal}	0.5%	$\text{RMS}(100 \cdot \Delta U_{cal})$	0.005
Linearisation	ΔU_{fit}	0.5%	$\text{RMS}(100 \cdot \Delta U_{fit})$	0.005
A/D resolution	E_{AD} n	10 Volts 12 bit	$\frac{1}{\sqrt{3}} \cdot \frac{1}{U} \cdot \frac{E_{AD}}{2^n} \cdot \frac{\partial U}{\partial E}$	0.0006
Probe positioning	θ	1°	$\frac{1}{\sqrt{3}} \cdot (1 - \cos\theta)$	≈ 0
Temperature variations	ΔT	1°	$\frac{2}{\sqrt{3}} \cdot \frac{\Delta T}{273}$	0.004
Ambient pressure	ΔP	10 kPa	$\frac{1}{\sqrt{3}} \cdot \frac{P_0}{P_0 + \Delta P}$	0.006
Humidity	ΔP_{wv}	1 kPa	$\frac{1}{\sqrt{3}} \cdot \frac{1}{U} \cdot \frac{\partial U}{\partial P_{wv}} \cdot \Delta P_{wv}$	≈ 0

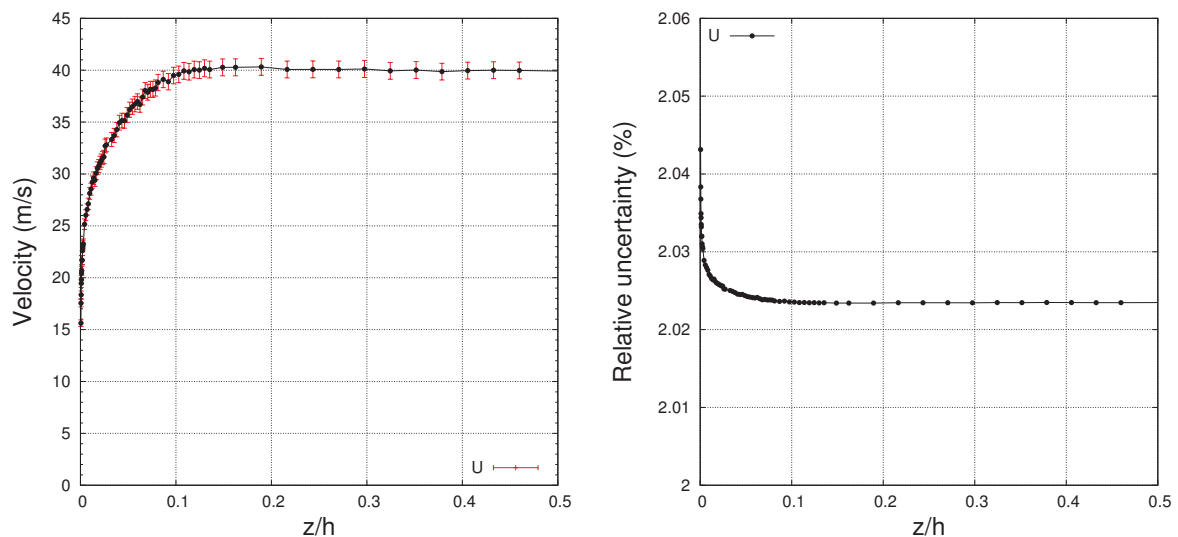


Figure 3.24: Absolute and relative errors of mean velocity measured by HWA.

3.2.5 Particle image velocimetry (PIV)

3.2.5.1 Set-up

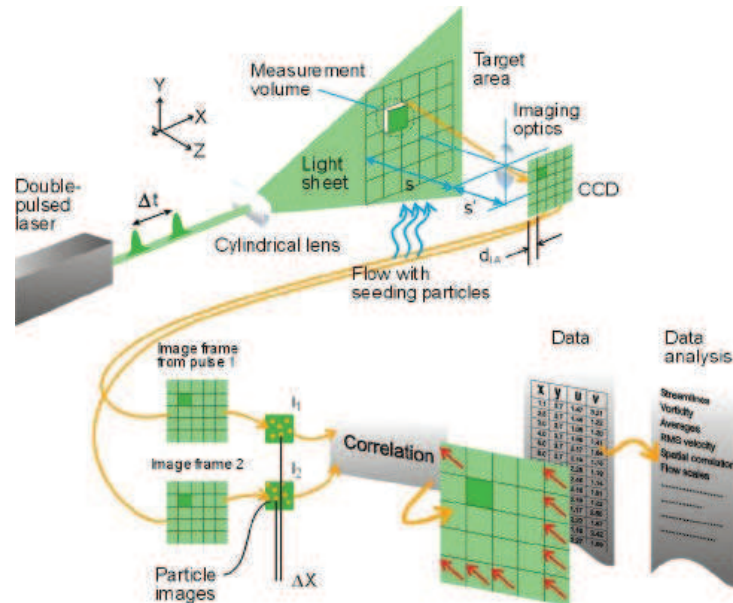


Figure 3.25: PIV principle, adopted from Dantec.

PIV can measure the whole velocity field in a plane. Fig. 3.25 briefly shows a sketch of the PIV principle. Small tracer particles are added to the flow. A plane within the flow is illuminated twice by means of a laser. It is assumed that the tracer particles move with local flow velocity between the two illuminations. The light scattered by the tracer particles is recorded via a digital camera and transferred to the memory of a computer directly. For evaluation, the digital PIV recording is divided into interrogation areas. It is assumed that all particles within one interrogation area have moved homogeneously between the two illuminations. The local displacement vector in each interrogation area is determined by statistical methods (inter-correlation). The 2C velocity vector in the plane of the light sheet is calculated by taking into account the time delay between the two illuminations and the magnification at imaging. A detailed introduction can be found in the book of Raffel *et al.* (2007).

In our experiment, a CCD camera of 1280×1024 pixels is used. The light source is a dual cavity Nd:YAG laser, developed by Quantel¹, the maximum illumination energy is 150 mJ/pulse. The used generator of particle is the commercial Safex Nebelgerät², in which the particles are generated by spraying a mixture of water and glycerol. The particle diameter is of the order of micrometer. The commercial Lavision program DAVIS is used for the acquisition and the post-processing. The frequency of the images acquisition is 4 Hz, and the time delay between

¹<http://www.quantel-laser.com>

²<http://www.safex.de>

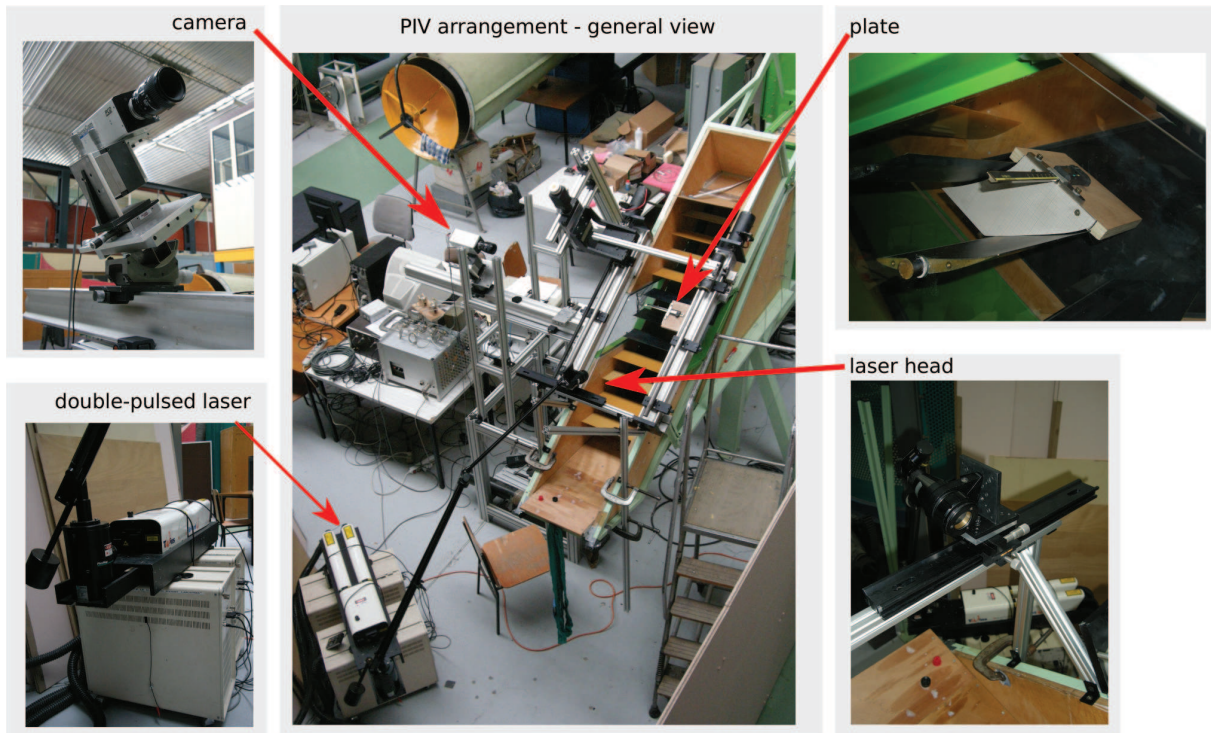


Figure 3.26: Set-up of PIV.

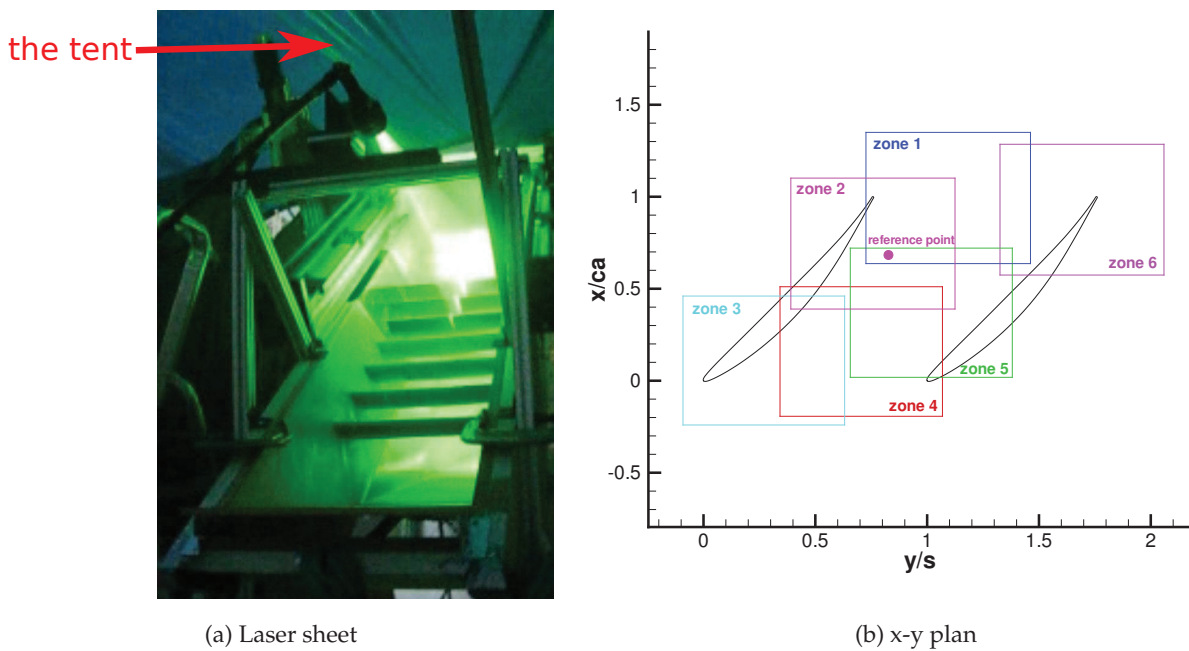


Figure 3.27: PIV measurement sections (perpendicular to the spanwise direction).

two frames is $10 \mu\text{s}$. The experimental setup has been built for 2D PIV, as shown in Fig. 3.26, in which the measurement planes are perpendicular to the spanwise direction (see Fig. 3.27a). According to the position of the laser and the camera shot size which guarantees enough spatial resolution, fourteen sections were measured and each section was divided into 6 zones ($100 \text{ mm} \times 80 \text{ mm}$), as shown in Fig. 3.27b.

The multi-pass interrogation is used. The particle-image displacement is firstly estimated by using a 64×64 pixels interrogation window, and then by a 32×32 pixels interrogation window with 50% overlap. As a result, the final spatial resolution of the grid for the velocity vector is about 1.25 mm.

3.2.5.2 Peak locking

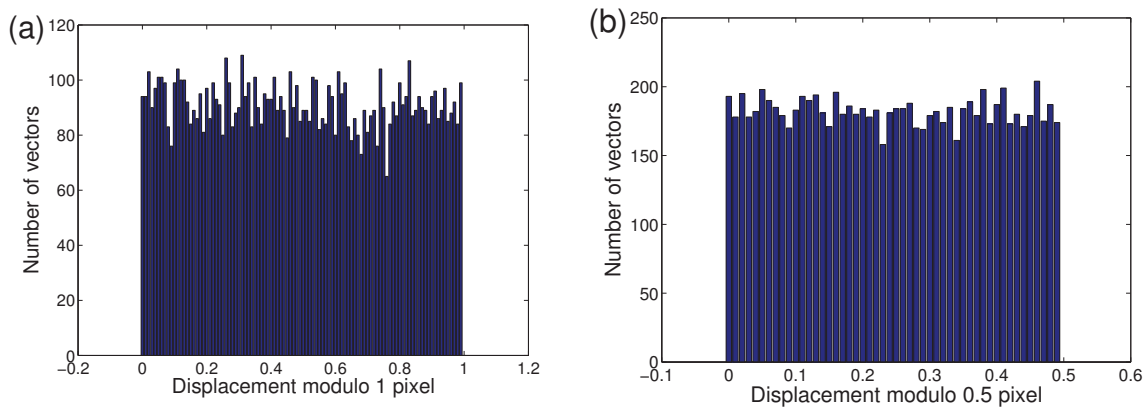


Figure 3.28: Displacement histogram of a typical flow field.

The peak locking occurs when the used seeding particles are too small and their produce particle images on the CCD are less than one pixel in diameter (Westerweel, 1998). When peak locking occurs, the velocity field computation has a bias toward integer velocity values. Therefore, a displacement histogram can be used to check whether the peak locking occurs. In our experiment, two typical displacement histograms of a flow field are shown in Fig. 3.28, including modulo 1 pixel and 0.5 pixel. From this figure, we know that the peak locking does not occur.

In order to quantitatively indicate the effect of peak locking, a parameter named as “*PeakLock*” can be used (LaVision, 2007, p.26). The *PeakLock* is calculated from the center of mass of the modulo 0.5 pixel histogram, expressed as

$$PeakLock = 4 \times (0.25 - \text{center of mass}) \quad (3.52)$$

Since there is more or less an equipartition of the decimal places the center of mass should be close to 0.25, when there is a high peak locking effect due to small particles etc. the center

of mass is shifted to zero. The value of *PeakLock* allows estimating the peak locking effect, summarized as

$$PeakLock = \begin{cases} 0 : & \text{indicates no peak locking effect,} \\ 1 : & \text{indicates a strong peak locking effect,} \\ < 0.1 : & \text{indicates that the peak locking effect is acceptable.} \end{cases}$$

In our experiment, the values of *PeakLock* are always smaller than 0.1. For example, the *PeakLock* is about 0.081 for the displacement histogram in Fig. 3.28b. This also indicates that the peak locking effect is acceptable in our experiment.

3.2.5.3 Convergence statistics

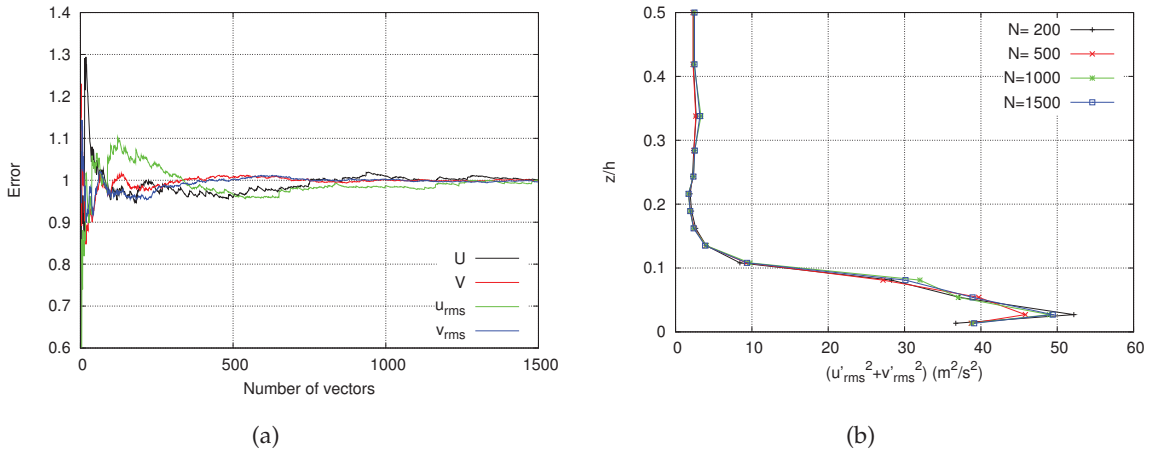


Figure 3.29: Convergence statistics at the reference points, $x/c_a=0.683$ and $y/s=0.827$. (a) Convergence statistics at $z=10$ mm; (b) convergence of turbulence intensity in spanwise direction.

In our experiment, a sequence of 2000 pairs of images is acquired at each operation condition. At each instantaneous flow field after the vector is calculated at each interrogation window, the percent of interrogation window with wrong vector can then be counted. If this percent is larger than 5% mainly due to the lack of seeding particles, this instantaneous flow field is abandoned. After that the number of the acceptable instantaneous flow field at each operation condition is more than 1500.

Fig. 3.29a shows the convergence statistics at one reference point in the middle of corner stall, where

$$Error(i) = \frac{\sum_{n=1}^i Para_n}{\sum_{n=1}^N Para_n} \quad (3.53)$$

The “Para” in Eq. 3.53 refers to the parameters, for example velocities, turbulence intensity or shear stresses. This reference point is in the zone 2, as illustrated in Fig. 3.27b. The distance between this reference and the endwall is 10 mm. This reference point is thus in the region of corner separation, so it is more difficult to converge than other points. At this reference

point, the velocity u is more difficult than v to converge. The mean velocity U converges when the number of flow field is about 800, while the root-mean-square of u' converges when the number of flow field is about 1200.

The turbulence intensity convergence statistics at the reference points in the spanwise direction is shown in Fig. 3.29b. From the convergence statistics, we can come to the conclusion that the flow field is highly unsteady, especially in the separation region.

3.2.5.4 Uncertainty in instantaneous velocity

The sources of error of the instantaneous PIV result include random errors and bias errors. Both of these two types of errors are very complex and have been investigated in detail by a lot of researchers (e.g. Boillot & Prasad, 1996; Westerweel, 1997, 2000). The random errors can be minimized with care during the experiment and post-processing. According to Section 3.2.5.2, the bias error caused by peak locking has been mostly eliminated in our experiment. According to Westerweel (1997, 2000) and Stanislas *et al.* (2008), the displacement error is between 0.04 and 0.1 pixels. Taking into account other uncertainties (e.g. individual variations of particle image intensities, researched by Nobach & Bodenschatz (2009)), we consider the displacement error of about 0.1 pixels. Thus the accuracy in the instantaneous velocity is

$$\epsilon_V = \frac{\alpha \cdot \text{Pixel}}{\Delta T} \quad (3.54)$$

where $\alpha=0.1$. In our experiment, one pixel is about 0.077 mm and $\Delta T=10 \mu\text{s}$, thus

$$\epsilon_V = 0.77 \text{ m/s} \quad (3.55)$$

and

$$\frac{\epsilon_V}{U_\infty} = 0.019 \quad (3.56)$$

where U_∞ is the inlet reference velocity and $U_\infty=40 \text{ m/s}$.

3.2.5.5 Uncertainty in mean velocity

The uncertainties in the mean velocity contain both the statistical factor (type A uncertainty) and the factors unrelated with the statistical analysis (type B uncertainty). In this subsection, the methods to estimate the uncertainties are adopted from Liu *et al.* (2006). Taking the u -component velocity as an example. The v -component velocity is similar to that of u -component.

Type A uncertainty can be estimated as

$$U_{\bar{u}}^A = \sqrt{\frac{1}{N(N-1)} \sum_{i=1}^N (u_i - \bar{u})^2} \quad (3.57)$$

where \bar{u} is the u-component of the mean velocity at a grid node, u_i is the corresponding instantaneous velocity in the i th instantaneous vector map.

In our experiment, the type B uncertainty mainly comes from the deviations of the instantaneous velocity,

$$\langle U_{\bar{u}}^B \rangle = \sigma_u \bar{u} / K \quad (3.58)$$

where σ_u is the relative measurement accuracy of instantaneous velocity ($\sigma_u = \frac{0.77 \text{ m/s}}{\bar{u}}$), K is the coverage factor. Because the sample size is large enough ($N > 1500$), $K = 2.576$ is selected for a 99% confidence interval. The combined standard uncertainty in the mean velocity is

$$U_{\bar{u}} = \sqrt{(U_{\bar{u}}^A)^2 + \langle U_{\bar{u}}^B \rangle^2} \quad (3.59)$$

The relative uncertainty in the mean velocity can be expressed as

$$\sigma_{\bar{u}} = U_{\bar{u}} / \bar{u} \quad (3.60)$$

The accuracy analysis of the Reynolds stresses are the same as that as mean velocity. In order to keep the thesis more concise, the accuracy analysis of the Reynolds stresses are not presented here.

Example A typical result of absolute and relative uncertainties for the magnitude of the mean velocity is shown in Fig. 3.30. The absolute uncertainty (in Fig. 3.30a) is about 0.4 m/s in the corner region, and about 0.3 m/s in the other region. The relative uncertainty (in Fig. 3.30b) is about 2% in the main flow, and increases in the corner region and are larger than 10%, mainly because the velocities are relatively smaller in this region.

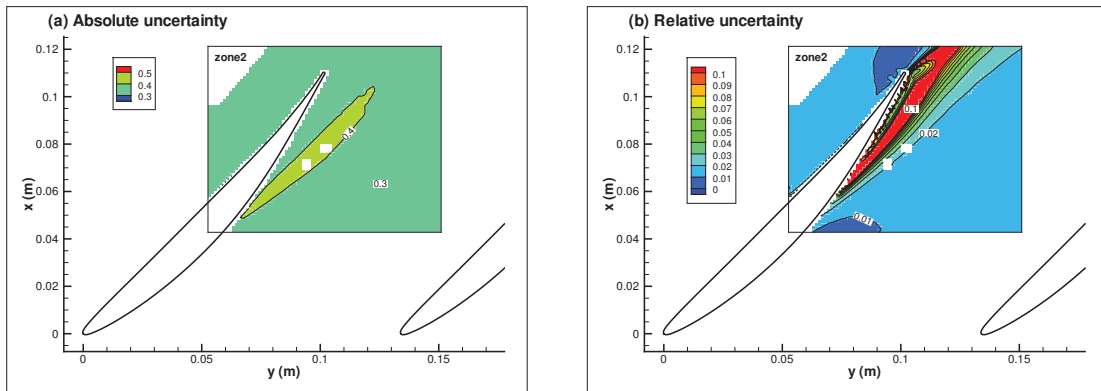


Figure 3.30: Absolute and relative uncertainty for the magnitude of the velocity $\sqrt{U_x^2 + U_y^2}$.

3.2.6 Laser Doppler anemometry (LDA)

3.2.6.1 Set-up

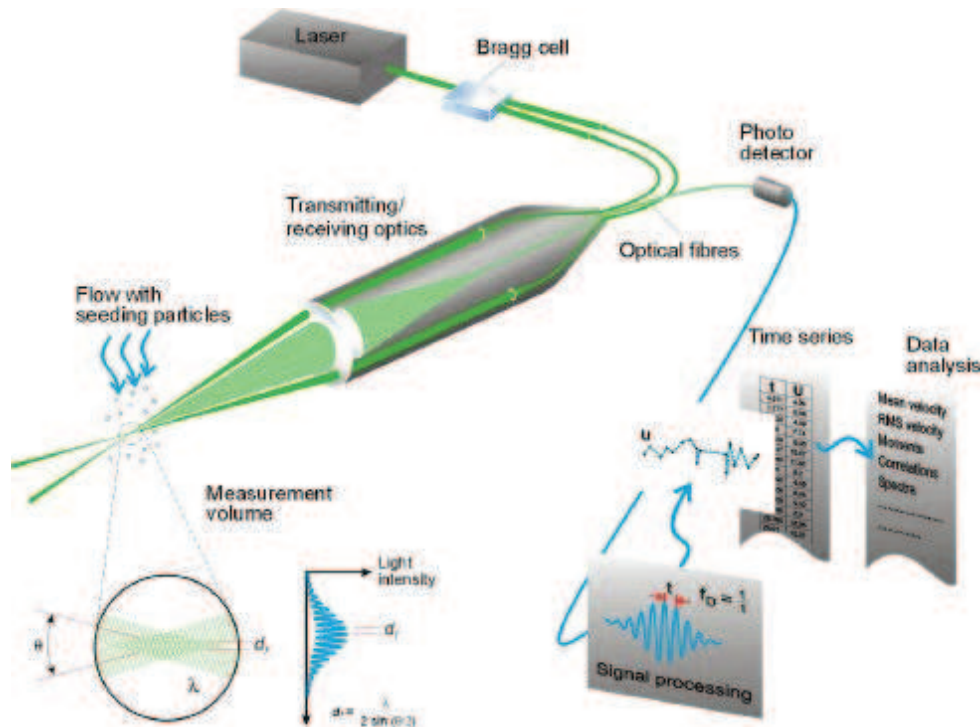


Figure 3.31: LDA principle from Dantec.

LDA, also known as laser Doppler velocimetry (LDV), is a single point optical technique for measuring the velocity vector of fluids like air and water. In its simplest form, LDA crosses two beams of collimated, monochromatic, and coherent laser light in the flow of the fluid being measured. The two beams are usually obtained by splitting a single beam, thus ensuring coherency between the two. The two beams are made to intersect at their waists (the focal point of a laser beam), where they interfere and generate a set of straight fringes. As particles pass through the fringes, they scatter light (only from the regions of constructive interference) into a photo detector. As particles cross the fringes, the intensity of the scattered light is modulated at a rate directly proportional to the velocity (see Fig. 3.31). The instantaneous velocity is

$$u = d_F \cdot f_D \quad (3.61)$$

where

$$d_F = \frac{\lambda}{2 \cdot \sin(\theta/2)} \quad (3.62)$$

where d_F is the distance between the fringes, f_D is the frequency measured. LDA systems with frequency shift are used to distinguish the flow direction and measure zero velocity. Main features of LDA include: non intrusive, no calibration required, velocity modulus range from 0

to supersonic, one, two or three velocity components measured simultaneously, measurement distance from centimeters to meters, flow reversals can be measured, high spatial and temporal resolution, instantaneous and time averaged. The basic configuration of an LDA consists of: a continuous wave laser, transmitting optics, including a beam splitter and a focusing lens, receiving optics, comprising a focusing lens, an interference filter and a photo detector, a signal conditioner and a signal processor. A more intuitive explanation of this formula using fringe patterns of LDA can be found in the book of [Albrecht *et al.* \(2003\)](#). Compared with PIV, LDA can measure the flow field closer to the blade surface. Compared with HWA, LDA can measure the reverse flow but without continuous signal.

In our experiment, the LDA set-up is shown in Fig. 3.32. The facilities include Spectra-Physics Stability 2017 Laser beam, Dantec FiberFlow 60×41 transmitter, Dantec FiberFlow 60×24 manipulator, Dantec FiberFlow 60×61 2D probe, and Dantec BAS-F80 signal processor. The commercial Dantec Dynamics BSA Flow Software for LDA version 4.11.00 is used for acquisition and post processing. The response of the photo detector is used to find the point where the distance to the blade surface or the endwall is zero. The measurement volume is on the wall when the anode current of the photo detector is maximum. The specification of LDA sensor is listed in Table 3.6. The generator of particle is the same as the one used in PIV. The particle diameter is of the order of micrometer.

In the experiment the velocity in the axial direction u_x and the velocity in the pitchwise direction u_y are measured directly (see Fig. 3.33). In each cross section in the spanwise direction, the measurement stations are in the normal direction of the point located on blade suction side, as shown in Fig. 3.34. In this figure, \vec{s} and \vec{n} are the unit vectors in tangential direction and normal direction of the point A , respectively. The measured velocity \vec{u} can be decomposed into the velocity along normal direction \vec{u}_n and the velocity along tangential direction \vec{u}_s . The velocity formula can be expressed as,

$$\vec{u} = \vec{u}_x + \vec{u}_y = \vec{u}_n + \vec{u}_s \quad (3.63)$$

Most of the results are presented in the (s, n) coordinate system instead of the Cartesian (x, y) system. The location of the measurement stations on the suction side are shown in Fig. 3.35. In order to show the actual travelled distance of the fluid over the blade suction side surface, a normalized parameter is used to indicate the positions of measurement stations, defined as

$$s^* = \frac{s}{L} \quad (3.64)$$

where s is the length of arc from the leading edge to the measurement location, L is the length of arc from leading edge to the trailing edge.



Figure 3.32: Set-up of LDA.

Table 3.6: Parameters of LDA sensor.

Property	Optical LDA- U_y	Optical LDA- U_x
Wavelength λ (nm)	514.5	488
Beam diameter (mm)	2.2	2.2
Expander ratio	1	1
Beam spacing (mm)	39.03	39.2
Frequency shift (MHz)	40	40
Number of fringes	22	22
Fringe spacing d_F (μm)	3.306	3.122
Beam half-angle $\theta/2$ ($^\circ$)	4.463	4.483
Probe volume dX (mm)	0.07467	0.07082
Probe volume dY (mm)	0.07444	0.07061
Probe volume dZ (mm)	0.9565	0.9034

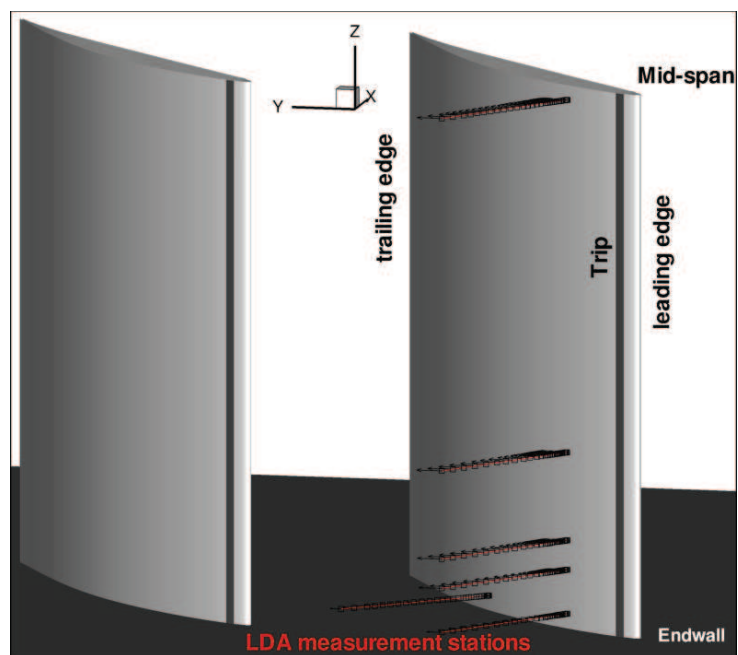


Figure 3.33: Examples of measurement stations.

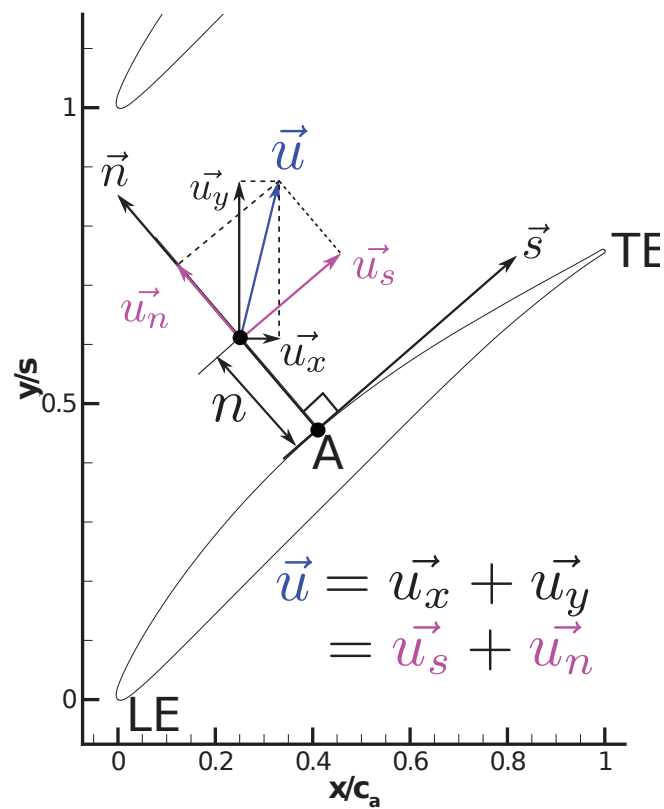


Figure 3.34: Velocity decomposition.

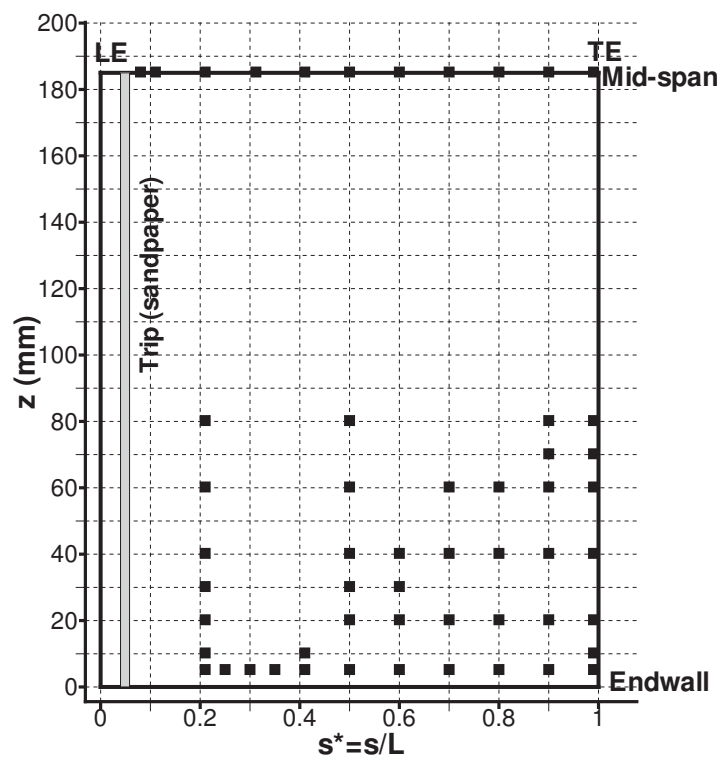


Figure 3.35: LDA measurement stations. Squares, starting points of the measurement stations.

3.2.6.2 Data reduction procedure

In our experiment, the 2D velocity $\vec{u} = \vec{u}_s + \vec{u}_n$ takes random values from a finite data set $u_{s1}, u_{n1}; u_{s2}, u_{n2}; \dots; u_{sN}, u_{nN}$, in tangential and normal directions, with each value having the same probability. Parameters $A_s, A_n, B_s, B_n, C_s, C_n$ are used and defined as,

$$A_{u_s} = \langle (u'_s)^2 \rangle = \frac{1}{N} \sum_{i=1}^N (u'_{si})^2, A_{u_n} = \langle (u'_n)^2 \rangle = \frac{1}{N} \sum_{i=1}^N (u'_{ni})^2 \quad (3.65)$$

$$B_{u_s} = \langle (u'_s)^3 \rangle = \frac{1}{N} \sum_{i=1}^N (u'_{si})^3, B_{u_n} = \langle (u'_n)^3 \rangle = \frac{1}{N} \sum_{i=1}^N (u'_{ni})^3 \quad (3.66)$$

$$C_{u_s} = \langle (u'_s)^4 \rangle = \frac{1}{N} \sum_{i=1}^N (u'_{si})^4, C_{u_n} = \langle (u'_n)^4 \rangle = \frac{1}{N} \sum_{i=1}^N (u'_{ni})^4 \quad (3.67)$$

where the fluctuation and mean velocities are

$$u'_{si} = u_{si} - \langle u_s \rangle = u_{si} - \bar{u}_s, u'_{ni} = u_{ni} - \langle u_n \rangle = u_{ni} - \bar{u}_n \quad (3.68)$$

$$\langle u_s \rangle = \bar{u}_s = \frac{1}{N} \sum_{i=1}^N u_{si}, \langle u_n \rangle = \bar{u}_n = \frac{1}{N} \sum_{i=1}^N u_{ni} \quad (3.69)$$

then (1) RMS $\sigma_{u_s}, \sigma_{u_n}$

$$\sigma_{u_s} = (A_{u_s})^{1/2}, \sigma_{u_n} = (A_{u_n})^{1/2} \quad (3.70)$$

(2) Skewness Sk_{u_s}, Sk_{u_n}

$$Sk_{u_s} = \frac{\langle (u'_s)^3 \rangle}{\langle (u'_s)^2 \rangle^{3/2}} = \frac{B_{u_s}}{(A_{u_s})^{3/2}}, Sk_{u_n} = \frac{\langle (u'_n)^3 \rangle}{\langle (u'_n)^2 \rangle^{3/2}} = \frac{B_{u_n}}{(A_{u_n})^{3/2}} \quad (3.71)$$

(3) Flatness Fl_{u_s}, Fl_{u_n}

$$Fl_{u_s} = \frac{\langle (u'_s)^4 \rangle}{\langle (u'_s)^2 \rangle^2} = \frac{C_{u_s}}{(A_{u_s})^2}, Fl_{u_n} = \frac{\langle (u'_n)^4 \rangle}{\langle (u'_n)^2 \rangle^2} = \frac{C_{u_n}}{(A_{u_n})^2} \quad (3.72)$$

(4) Local turbulence intensity Tu_{local}

$$Tu_{local} = \frac{\sqrt{\frac{1}{2}(A_{u_s} + A_{u_n})}}{\sqrt{\bar{u}_s^2 + \bar{u}_n^2}} = \frac{\sqrt{\frac{1}{2}(\sigma_{u_s}^2 + \sigma_{u_n}^2)}}{\sqrt{\bar{u}_s^2 + \bar{u}_n^2}} \quad (3.73)$$

(5) Turbulence intensity Tu

$$Tu = \frac{1}{U_\infty} \sqrt{\frac{1}{2}(A_{u_s} + A_{u_n})} = \frac{1}{U_\infty} \sqrt{\frac{1}{2}(\sigma_{u_s}^2 + \sigma_{u_n}^2)} \quad (3.74)$$

where U_∞ is the inlet reference velocity.

(6) Reynolds stresses

$$\langle u'_s u'_s \rangle = \overline{u'_s u'_s} = \frac{1}{N} \sum_{i=1}^N (u'_{si} u'_{si}) \quad (3.75)$$

$$\langle u'_n u'_n \rangle = \overline{u'_n u'_n} = \frac{1}{N} \sum_{i=1}^N (u'_{ni} u'_{ni}) \quad (3.76)$$

$$\langle u'_s u'_n \rangle = \overline{u'_s u'_n} = \frac{1}{N} \sum_{i=1}^N (u'_{si} u'_{ni}) \quad (3.77)$$

(7) The first backflow percent coefficient η_1 is defined as the portion of the measured velocity distribution that includes negative velocities

$$\eta_1 = N^- / N \quad (3.78)$$

where N is the sample number and N^- is the sample number with negative velocity.

(8) The second backflow percent coefficient η_2 , defined as the ratio of the magnitude of the sum of negative velocities to the sum of positive velocities,

$$\eta_2 = \frac{\sum_1^{N^-} |u_s^{neg}|}{\sum_1^{N^+} u_s^{pos}} \quad (3.79)$$

where N^+ is the sample number with positive velocity, thus $N^+ = N - N^-$. When $\eta_2 > 1$, the mean velocity is negative; when $\eta_2 = 1$, then the mean velocity is zero; when $\eta_2 < 1$ then the mean velocity is positive.

3.2.6.3 Uncertainty of 2C LDA

The absolute measurement error, ϵ_{tot} , can be decomposed into a bias error, ϵ_{bias} , and a random error, ϵ_{rms} (ISO, 1999). According to Godard (2010), In LDA the ϵ_{bias} is the sum of the error of calibration and sampling, ϵ_e , and the error of position, ϵ_p . Thus the total error can be expressed as

$$\epsilon_{tot}^2 = \epsilon_{bias}^2 + \epsilon_{rms}^2 = \epsilon_e^2 + \epsilon_p^2 + \epsilon_{rms}^2 \quad (3.80)$$

In the following part, ϵ_e , ϵ_p and ϵ_{rms} in our experiment will be introduced, respectively.

Error of calibration and sampling, ϵ_e If the measurement volume is fixed, according to Eq. 3.61, then (U presents U_x or U_y)

$$\left[\frac{\epsilon_e(U)}{U} \right]^2 = \left[\frac{\partial U}{\partial d_F} \epsilon_e(d_F) \right]^2 + \left[\frac{\partial U}{\partial f_D} \epsilon_e(f_D) \right]^2 = \left[\frac{\epsilon_e(d_F)}{d_F} \right]^2 + \left[\frac{\epsilon_e(f_D)}{f_D} \right]^2 \quad (3.81)$$

where $\epsilon_e(d_F)$ is the error of calibration of the LDA sensor. It represents the error on the value of the fringe distance, due to the fact that the angle of intersection of the laser beams forming the measurement volume, does not necessarily correspond to that specified in Table 3.6. During calibration, the laser beams associated with each component are projected onto a screen located at great distance from the measurement volume (about ten times the focal length of the probe). The intersection angles θ associated with each component are then calculated by measuring the distance of the beams corresponding tasks on the screen. Using this method, the relative error in d_F is about 1%, e.g.

$$\frac{\epsilon_e(d_F)}{d_F} = 1\% \quad (3.82)$$

The term $\epsilon_e(f_D)$ in Eq. 3.81 is the error of sampling when the signal of Doppler is analyzed. At each frequency f_e , the Doppler frequency f_D is calculated by fast Fourier transform (FFT) of Doppler signal, performed on N samples of signal. According to Ibrahim *et al.* (1994), the relative error in f_D is

$$\frac{\epsilon_e(f_D)}{f_D} = \sqrt{\frac{12}{(2\pi)^2 \cdot SNR \cdot N_e \cdot (N_e^2 - 1)}} \cdot \frac{f_e}{f_D} \quad (3.83)$$

where SNR is the signal-to-noise ratio. In the worst situation, SNR is about 2dB. In the experiment, the sample number is 64 for both two components. We consider that f_e/f_D is about 5 in our experiment, so

$$\frac{\epsilon_e(f_D)}{f_D} = 0.4\% \quad (3.84)$$

Substituting Eqs. 3.82 and 3.84 in to Eq. 3.81, then

$$\frac{\epsilon_e(U)}{U} = 1.1\% \quad (3.85)$$

Error of position, ϵ_p By applying the law of propagation of uncertainties, we obtain

$$\epsilon_p^2(U) = \left[\frac{\partial U}{\partial x} \cdot \epsilon_p(x) \right]^2 + \left[\frac{\partial U}{\partial y} \cdot \epsilon_p(y) \right]^2 + \left[\frac{\partial U}{\partial z} \cdot \epsilon_p(z) \right]^2 \quad (3.86)$$

This formula shows clearly the influence of velocity gradient at the measurement point. The initial positioning of the measurement volume is performed using a calliper, which has an accuracy of 0.1 mm. Therefore the initial error of position is also 0.1 mm, e.g.

$$\epsilon_{initial}(x) = \epsilon_{relative}(z) = \epsilon_{relative}(z) = 0.1 \text{ mm}. \quad (3.87)$$

In the measurement, the error of position comes from the error of traverse system. In our experiment,

$$\epsilon_{relative}(x) = 0.06 \text{ mm}, \quad \epsilon_{relative}(y) = 0.06 \text{ mm}, \quad \epsilon_{relative}(z) = 0.01 \text{ mm} \quad (3.88)$$

According to Eqs. 3.87 and 3.88, the total errors of position in three directions are

$$\begin{aligned} \epsilon_p(x) &= \sqrt{\epsilon_{initial}^2(x) + \epsilon_{relative}^2(x)} = 0.12 \text{ mm} \\ \epsilon_p(y) &= \sqrt{\epsilon_{initial}^2(y) + \epsilon_{relative}^2(y)} = 0.12 \text{ mm} \\ \epsilon_p(z) &= \sqrt{\epsilon_{initial}^2(z) + \epsilon_{relative}^2(z)} = 0.11 \text{ mm} \end{aligned} \quad (3.89)$$

Random error, ϵ_{rms} The random error can be calculated by

$$\epsilon_{rms}(U) = \frac{2 \cdot U_{rms}}{\sqrt{N}} \quad (3.90)$$

where N is the number of measurement. Because $N > 31$, so the constant 2 is used in Eq. 3.90. There is a 95% probability that the true value lies within the range of $[U - \epsilon_{rms}(U), U + \epsilon_{rms}(U)]$.

In this thesis, most of the results are presented in the streamline-normal coordinate system (s, n, z) instead of the Cartesian (x, y, z) system. Therefore the errors in the parameters in the streamline-normal coordinates system will be estimated. The error of calibration and sampling in the U_s and U_n are the same as that in the U_x and U_y , thus

$$\frac{\epsilon_e(U_s)}{U_s} = 1.1\%, \quad \frac{\epsilon_e(U_n)}{U_n} = 1.1\% \quad (3.91)$$

For the error of position, it is very difficult to estimate the velocity gradients in the s and z directions, thus they are approximated as the velocity gradient in the n direction. Thus we have

$$\frac{\epsilon_p(U_s)}{U_s} = \frac{\sqrt{3}}{U_s} \cdot \frac{\partial U_s}{\partial n} \cdot \epsilon_p(n), \quad \frac{\epsilon_p(U_n)}{U_n} = \frac{\sqrt{3}}{U_n} \cdot \frac{\partial U_n}{\partial n} \cdot \epsilon_p(n) \quad (3.92)$$

where $\epsilon_p(n) = 0.15$ mm. The random error in the U_s and U_n are the same as that in the U_x and U_y , thus

$$\frac{\epsilon_{rms}(U_s)}{U_s} = \frac{2 \cdot (U_s)_{rms}}{U_s \cdot \sqrt{N}}, \quad \frac{\epsilon_{rms}(U_n)}{U_n} = \frac{2 \cdot (U_n)_{rms}}{U_n \cdot \sqrt{N}} \quad (3.93)$$

Example Typical LDA measurement results of U_s and U_n and their absolute errors are shown in Fig. 3.36a. The corresponding relative errors are shown in Fig. 3.36b. Generally speaking, the errors are larger in the boundary layer than that in the region far from the wall.

In the region far from the wall, the average sampling rate is approximately 10 kHz and the sampling number is more than 500 000. The corresponding relative uncertainty in the magnitude of mean velocity is less than 2% (listed in Table 3.7). The accuracy analysis of the Reynolds stresses are the same as that of the mean velocity, and the uncertainties of Reynolds stresses are also listed in Table 3.7.

In the boundary layer (near the endwall), the data acquisition frequency decreases dramatically. In order to minimize the statistical uncertainty due to sampling number, we extended the acquisition time to 2 minutes. However the sampling number is very low, about 20 000. In this region the statistical uncertainty was high.

Since the local values approach zero in the region near the wall, the relative error is extremely large.

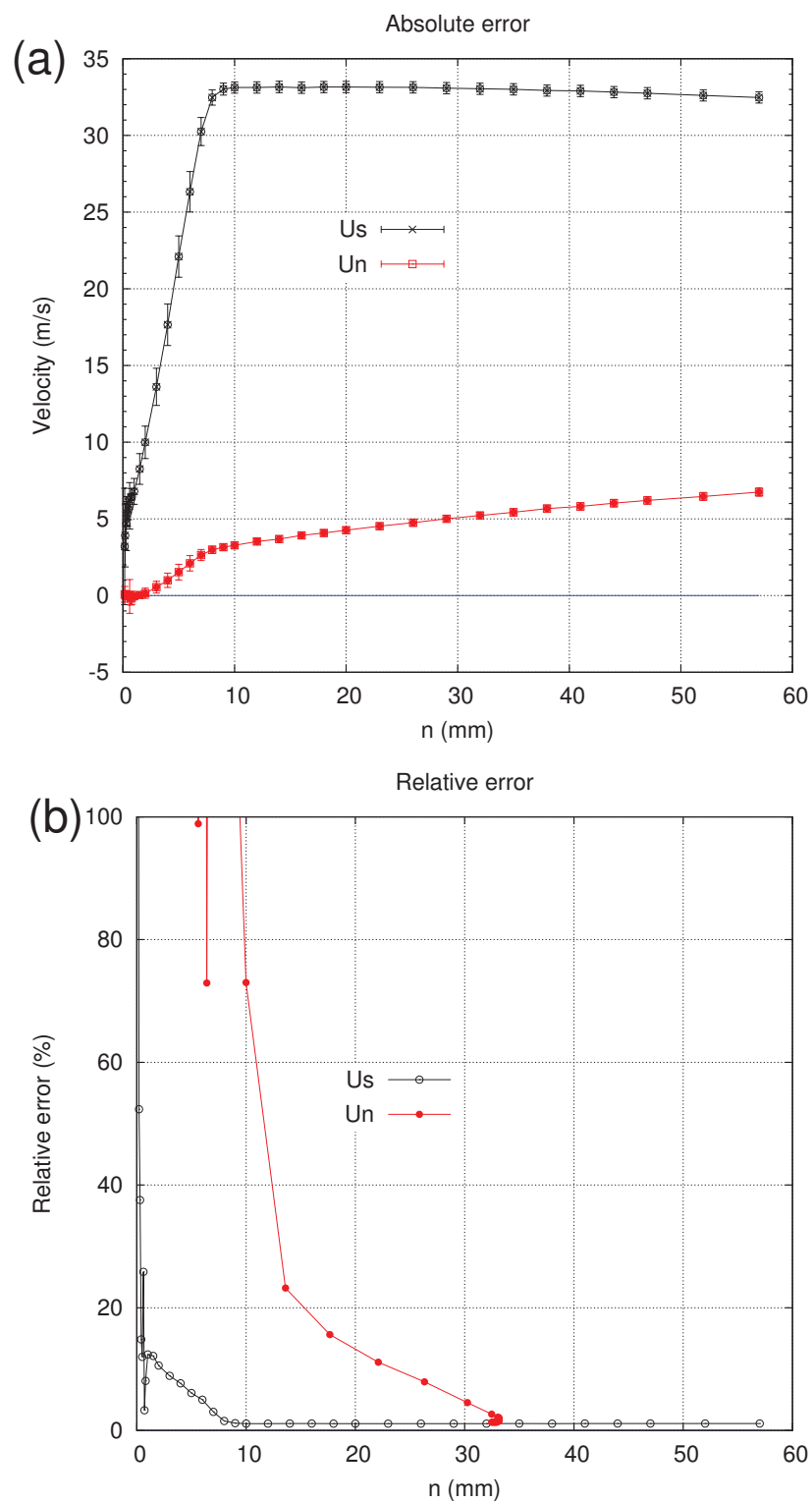


Figure 3.36: Absolute and relative errors of mean velocity measured by LDA.

Table 3.7: Relative errors of parameters measured by LDA in the region far from the wall.

Parameter	\bar{u}_s	\bar{u}_n	$\overline{u'_s u'_s}$	$\overline{u'_n u'_n}$	$\overline{u'_s u'_n}$
Relative error	1.2%	1.8%	3%	4%	5%

3.2.7 Traverse system and facilities arrangement

Three traverse systems are used connected to a PC using the serial ports. They are MM4005, RHOCM and ITL09, who traverse along the direction of pitchwise, spanwise and gravity, respectively. The resolutions of the programmable traverse movements are 0.05 mm, 0.07 mm and 0.01 mm, respectively.

3.3 Inlet reference parameters

Inlet reference parameters are measured at the reference point, shown in Fig. 3.2. The total pressure $P_{t\infty}$ and static pressure $P_{s\infty}$ are measured by a Pitot probe. The total temperature $T_{t\infty}$ is measured by a thermocouple. Other parameters can then be calculated from these three reference parameters.

(1) Static temperature

$$T_{s\infty} = T_{t\infty} \left(\frac{P_{t\infty}}{P_{s\infty}} \right)^{-\frac{k-1}{k}} \quad (3.94)$$

where the air specific heat ratio $k=1.4$.

(2) Mach number

$$Ma_{\infty} = \sqrt{\frac{2}{k-1} \left[\left(\frac{P_{t\infty}}{P_{s\infty}} \right)^{(k-1)/k} - 1 \right]} \quad (3.95)$$

(3) Velocity of sound

$$c_{\infty} = \sqrt{k \cdot R \cdot T_{s\infty}} \quad (3.96)$$

where ideal gas constant $R=287.06 \text{ J}/(\text{kg}\cdot\text{K})$.

(4) Velocity

$$U_{\infty} = Ma_{\infty} \cdot c_{\infty} \quad (3.97)$$

(5) Density

$$\rho_{\infty} = \frac{P_{s\infty}}{R \cdot T_{s\infty}} \quad (3.98)$$

(6) Viscosity (Sutherland formula)

$$\mu_{\infty} = 1.7161 \times 10^{-5} \cdot \left(\frac{T_{s\infty}}{273.16} \right)^{1.5} \left(\frac{273.16 + 124.0}{T_{s\infty} + 124.0} \right) \quad (3.99)$$

(7) Reynolds number

$$\text{Re}_{\infty} = \frac{\rho_{\infty} \cdot U_{\infty} \cdot L}{\mu_{\infty}} \quad (3.100)$$

3.4 Test procedure

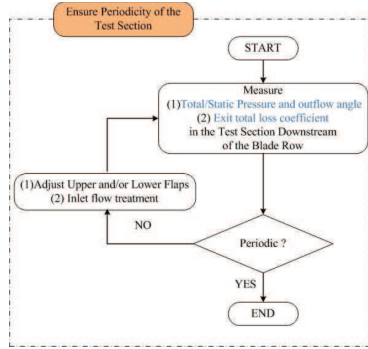


Figure 3.37: Test procedure.

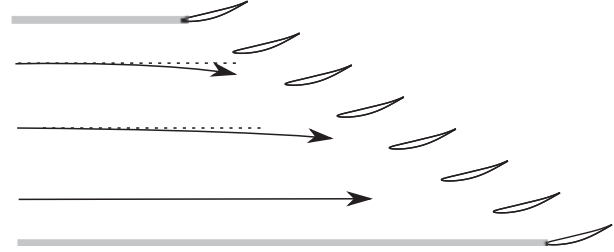


Figure 3.38: Skewness of inflow.

Using linear cascade flow to simulate real internal compressor flow, it is necessary to ensure the spatial periodicity in the pitchwise direction of the test section. In our experiment, the procedure to ensure the periodicity of the test section is shown in Fig. 3.37. Three indicators are used to show the periodicity of the cascade especially near the region under investigation:

(1) Total and static pressure coefficients,

$$C_p = \frac{p_s - p_{s\infty}}{p_{t\infty} - p_{s\infty}} = \frac{p_s - p_{s\infty}}{\frac{1}{2}\rho_\infty U_\infty^2} \quad (3.101)$$

$$C_{p_t} = \frac{p_t - p_{s\infty}}{p_{t\infty} - p_{s\infty}} = \frac{p_t - p_{s\infty}}{\frac{1}{2}\rho_\infty U_\infty^2} \quad (3.102)$$

where $p_{t\infty}$, $p_{s\infty}$ are the reference inlet total and static pressures, respectively; ρ_∞ is the reference density; p_t , p_s are the total and static pressures at the desired point, respectively. According to Eqs. 3.101 and 3.102,

$$C_{p_t} - C_p = \frac{p_t - p_s}{p_{t\infty} - p_{s\infty}} = \frac{\frac{1}{2}\rho U^2}{\frac{1}{2}\rho_\infty U_\infty^2} \quad (3.103)$$

in our experiment $Ma < 0.3$, $\rho = \rho_\infty$, therefore another indicator, the normalized magnitude of velocity, can express as

$$U/U_\infty = \sqrt{C_{p_t} - C_p} \quad (3.104)$$

(2) Relative angle γ , which indicates the angle between the outlet flow and reference direction of the five-hole pressure probe in the section perpendicular to the spanwise direction.

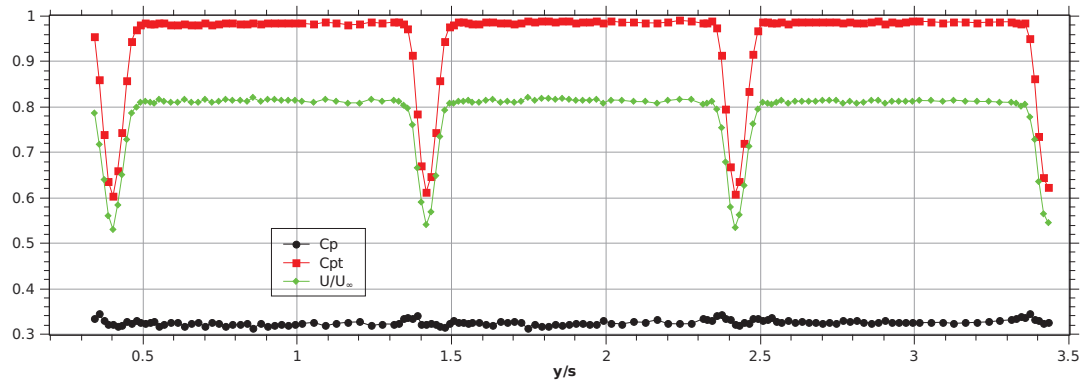
(3) Exit total loss coefficient,

$$\omega = \frac{p_{t\infty} - p_t}{p_{t\infty} - p_{s\infty}} = \frac{p_{t\infty} - p_t}{\frac{1}{2}\rho_\infty U_\infty^2} \quad (3.105)$$

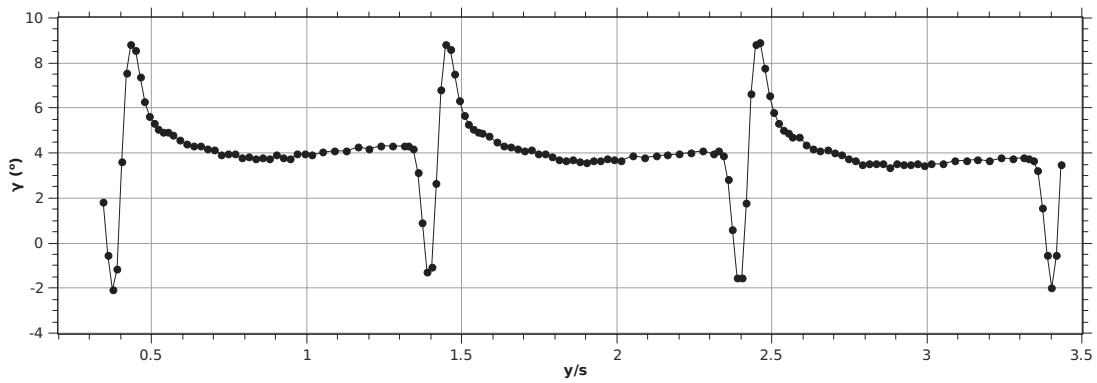
If the periodicity is not sufficient, some adjustments are used:

- (1) adjustment the upper/lower flaps of the cascade,
- (2) using inlet flow treatment (importance of the incoming boundary layers).

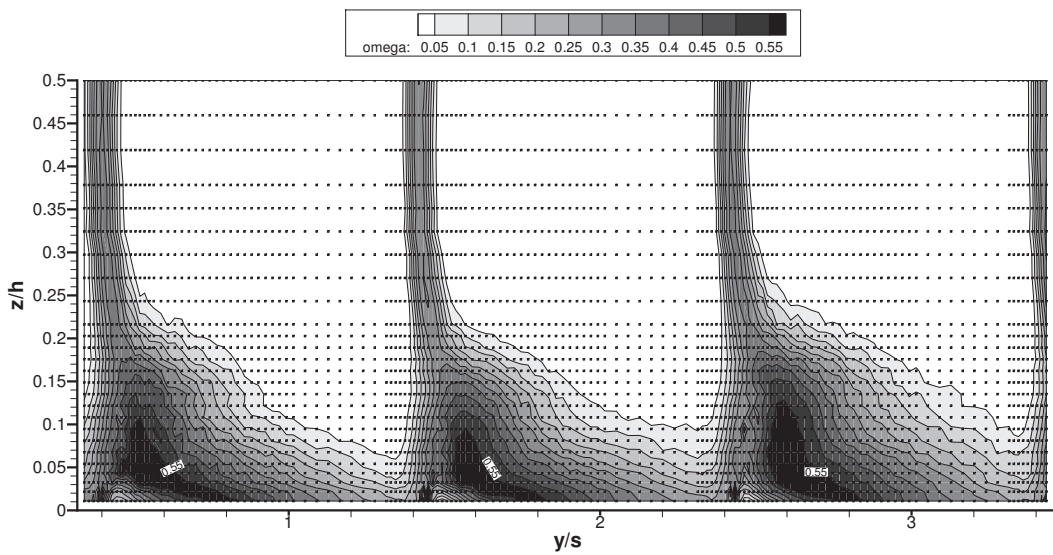
At last our cascade was in a perfect periodical state, typical results of the indicators are shown in Fig. 3.39.



(a) Pressure distribution at mid-span



(b) γ distribution at mid-span



(c) Contour of total pressure loss coefficient, scatters indicate the positions of measurement points

Figure 3.39: Periodicity of the test section at outlet.

3.5 Numerical method

The numerical method is introduced in this section. First of all the basic equations are presented. And then the solver, grid and boundary conditions are introduced.

3.5.1 Navier-Stokes equations

The Navier-Stokes equations can describe the motion of a fluid in space and time. It is believed that an explanation and the prediction of both the breeze and the turbulence can be found through an understanding of the solutions to the Navier-Stokes equations. The Navier-Stokes equations are derived from the laws of conservations of mass, momentum and energy, and expressed as

$$\frac{\partial \rho}{\partial t} + \frac{\partial(\rho u_i)}{\partial x_i} = 0 \quad (3.106)$$

$$\frac{\partial(\rho u_i)}{\partial t} + \frac{\partial(\rho u_i u_j)}{\partial x_j} = \frac{\partial \tau_{ij}}{\partial x_j} - \frac{\partial p}{\partial x_i} \quad (3.107)$$

$$\frac{\partial(\rho E)}{\partial t} + \frac{\partial[(\rho E + p)u_i]}{\partial x_i} = \frac{\partial(u_i \tau_{ij})}{\partial x_j} - \frac{\partial q_i}{\partial x_i} \quad (3.108)$$

where the viscous stress tensor is

$$\tau_{ij} = \mu \left(\frac{\partial u_i}{\partial x_j} + \frac{\partial u_j}{\partial x_i} - \frac{2}{3} \delta_{ij} \frac{\partial u_k}{\partial x_k} \right) \quad (3.109)$$

where δ_{ij} is the Kronecker delta,

$$\delta_{ij} = \begin{cases} 1 & i = j \\ 0 & i \neq j \end{cases}$$

The dynamic viscosity of an ideal gas can be derived by the Sutherland's formula,

$$\frac{\mu}{\mu_0} = \left(\frac{T}{T_0} \right)^{1.5} \left(\frac{T_0 + T_s}{T + T_s} \right) \quad (3.110)$$

where T_s , T_0 and μ_0 are constant. According to the Fourier's Law of Conduction,

$$q_i = -\lambda \frac{\partial T}{\partial x_i} \quad (3.111)$$

where λ is the thermal conductivity of the air,

$$\lambda = \frac{\mu c_p}{Pr} \quad (3.112)$$

where Pr is the number of Prandtl, c_p is the heat capacity at constant pressure. According to the ideal gas law

$$p = \rho RT \quad (3.113)$$

where R is the gas constant, the total energy can be expressed as

$$E = \frac{p}{\rho(\gamma - 1)} + \frac{1}{2}u_i^2 \quad (3.114)$$

where γ is the heat capacity ratio.

Although the Navier-Stokes equations were found in the 19th century, mathematicians have not yet proved that smooth solutions always exist, or that if they do exist they do not contain any infinities, singularities or discontinuities (Doering, 2009). These are called the Navier-Stokes existence and smoothness problems. The Clay Mathematics Institute has called this one of the seven most important open problems in mathematics, and offered a US \$10⁶ prize for a solution or a counter-example¹.

3.5.2 Reynolds-averaged Navier-Stokes equations

The numerical solutions of averaged Navier-Stokes equations are used in engineering applications, with a gradual increase in computing power. The most famous averaged Navier-Stokes equations are Reynolds-averaged Navier-Stokes equations, in which the Navier-Stokes equations (Eqs. 3.106~3.108) are averaged by Reynolds decomposition. At the same time, Favre decomposition is also used, in order to take into account the compressibility. Neglecting the switching errors of the mean of Favre with the derivatives space (Smati, 1997), we have

$$\frac{\partial \bar{\rho}}{\partial t} + \frac{\partial(\bar{\rho}\tilde{u}_i)}{\partial x_i} = 0 \quad (3.115)$$

$$\frac{\partial(\bar{\rho}\tilde{u}_i)}{\partial t} + \frac{\partial(\bar{\rho}\tilde{u}_i\tilde{u}_j)}{\partial x_j} = \frac{\partial(\bar{\tau}_{ij} - \overline{\rho u'_i u'_j})}{\partial x_j} - \frac{\partial \bar{p}}{\partial x_i} \quad (3.116)$$

$$\frac{\partial(\bar{\rho}\tilde{E})}{\partial t} + \frac{\partial[(\bar{\rho}\tilde{E} + \bar{p})\tilde{u}_i]}{\partial x_i} = \frac{\partial[\overline{u_i \tau_{ij}} - (\overline{\rho E + p})u'_j]}{\partial x_j} - \frac{\partial}{\partial x_i} \left(\frac{\gamma \bar{\mu}}{Pr} \frac{\partial \tilde{e}}{\partial x_i} \right) \quad (3.117)$$

with

$$\bar{\tau}_{ij} = \bar{\mu} \left(\frac{\partial \tilde{u}_i}{\partial x_j} + \frac{\partial \tilde{u}_j}{\partial x_i} - \frac{2}{3} \delta_{ij} \frac{\partial \tilde{u}_k}{\partial x_k} \right) \quad (3.118)$$

$$\bar{p} = \bar{\rho}(\gamma - 1) \left[\tilde{E} - \frac{1}{2}(\tilde{u}_i^2 + \tilde{u}_i'^2) \right] \quad (3.119)$$

¹<http://www.claymath.org/millennium/>

3.5.3 Turbulence model

The Reynolds stresses $-\overline{\rho u'_i u'_j}$ in Eq. 3.116 are due to the fluctuating velocity field. This non-linear term requires additional modelling to close the RANS equation for solving. In 1887, Boussinesq proposed relating the turbulent stresses to the mean flow to close the system of equations. The Boussinesq hypothesis is applied to model the Reynolds stress term.

$$-\overline{\rho u'_i u'_j} = \mu_t \left(\frac{\partial \tilde{u}_i}{\partial x_j} + \frac{\partial \tilde{u}_j}{\partial x_i} - \frac{2}{3} \delta_{ij} \frac{\partial \tilde{u}_k}{\partial x_k} \right) - \frac{2}{3} \tilde{\rho} k \delta_{ij} \quad (3.120)$$

where k is the turbulence kinetic energy, $k = 1/2 u_i'^2$.

Turbulence models are used to calculate the turbulent eddy viscosity μ_t . In the text, we only use the S-A turbulence model (Spalart & Allmaras (1992, 1994)), one of the widely used turbulence models in the industry. The computational requirements of this turbulence model is about half of that of other two-equations turbulence models (e.g. k - ϵ and k - ω turbulence models), and the accuracy of these models are nearly the same.

Spalart & Allmaras (1992) proposed an equation of turbulent eddy viscosity by experience and dimensional analysis. This model was gradually derived for the isotropic turbulence to the low Reynolds number near wall flows. Later Spalart & Allmaras (1994) modified the values of two constants in the equations.

The turbulent eddy viscosity is calculated by

$$\mu_t = \rho \tilde{\nu} \cdot f_{v1} \quad (3.121)$$

The empirical equation for $\tilde{\nu}$ is

$$\frac{\partial \tilde{\nu}}{\partial t} + u_j \frac{\partial \tilde{\nu}}{\partial x_j} = C_{b1} (1 - f_{t2}) \tilde{S} \tilde{\nu} + \frac{1}{\sigma} (\nabla \cdot [(v + \tilde{\nu}) \nabla \tilde{\nu}] + C_{b2} |\nabla v|^2) - \left[C_{w1} f_w - \frac{C_{b1}}{k^2} \right] \left(\frac{\tilde{\nu}}{d} \right)^2 + f_{t1} (\Delta U)^2 \quad (3.122)$$

with

$$\begin{aligned} \tilde{S} &\equiv S + \frac{\tilde{\nu}}{k^2 d^2} f_{v2}, \quad f_{v2} = 1 - \frac{\chi}{1 + \chi f_{v1}}, \\ f_w &= g \left[\frac{1 + C_{w3}^6}{g^6 + C_{w3}^6} \right]^{1/6}, \quad g = r + C_{w2} (r^6 - r), \quad r \equiv \frac{\tilde{\nu}}{\tilde{S} k^2 d^2}, \\ f_{t1} &= C_{t1} g_t \exp \left(-C_{t2} \frac{\omega_t^2}{\Delta U^2} (d^2 + g_t^2 d_t^2) \right), \quad g_t = \min \left(0.1, \frac{\Delta U}{\omega_t \Delta x_t} \right), \\ f_{t2} &= C_{t3} \exp(-C_{t4} \chi^2), \quad S = \sqrt{2 \Omega_{ij} \Omega_{ij}}, \quad \Omega_{ij} = \frac{1}{2} \left(\frac{\partial u_i}{\partial x_j} - \frac{\partial u_j}{\partial x_i} \right) \end{aligned} \quad (3.123)$$

The constants are

$$\begin{aligned} \sigma &= 2/3, \quad C_{b1} = 0.1355, \quad C_{b2} = 0.622, \quad k = 0.41, \quad C_{w1} = C_{b1}/k^2 + (1 + C_{b2})/\sigma, \\ C_{w2} &= 0.3, \quad C_{v1} = 7.1, \quad C_{t1} = 1, \quad C_{t2} = 2, \quad C_{t3} = 1.2, \quad C_{t4} = 0.5 \end{aligned} \quad (3.124)$$

In order to improve the accuracy of simulating strong non-equilibrium turbulent, the S-A turbulence model is adopted to study the modification method based on the analysis of turbulence transport nature by [Ma et al. \(2008\)](#) and [Wang et al. \(2009\)](#). On of the purpose of this thesis is to provide experimental data, which can be used to continue the modification of S-A turbulence model. Therefore the numerical results of the S-A turbulence model are used in the main body of this thesis, to compare with the experimental results and help to understand the physics. Some numerical results of other turbulence models are presented in Appendix D.

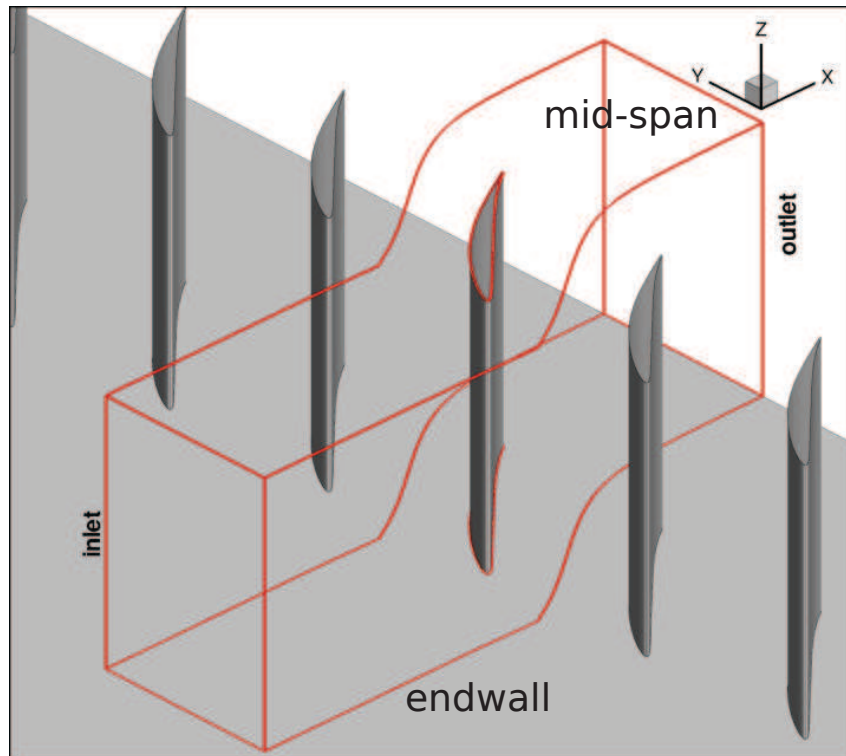
3.5.4 Solver, grid and boundary conditions

The commercial computational fluid dynamics software packages FLUENT ([ANSYS, 2006](#)) is used. The convergence requires that the scaled residuals decrease to 1.0×10^{-11} for all equations.

The computational grid used in the current investigation is generated by AutoGrid5^{TM1}, a commercial software package. The multi-block method is used to ensure the grid quality, as well as the matching periodicity strategy. Three meshes with different grid densities are tested to check the grid independence of the solutions. Finally the grid with about 2.27×10^6 cells is chosen for this numerical work. The first cell width from the surface of the blade and endwall is set to $n^+ = \frac{nu_\tau}{\nu} \sim 1$, where n is the distance from the cell to the surface of the blade and the endwall, u_τ is the local friction velocity. To be able to compare these results with the experimental results, the inlet and the exit of the computational domain are placed at 2.16 axial chords upstream of the leading edge and 1.36 axial chords downstream of the trailing edge of the blade, respectively. The grid distribution in the plane perpendicular to spanwise is shown in Fig. 3.40.

In the computation the flow is assumed to be steady and fully turbulent. The inlet velocity profile is obtained from the hotwire in the experiment and the incidence angle is specified for the inlet boundary. The static pressure is used for the outlet boundary. The turbulent viscosity of 0.8% is specified for inlet boundary, in accordance with the present experimental values (see Section 4.2). The eddy viscosity ratio $\frac{\mu_t}{\mu}$ is not measured in the experiment, here we assume $\frac{\mu_t}{\mu} = 50$. Furthermore, nonslip and adiabatic conditions are adopted for all of the solid walls. Periodic conditions are imposed along the pitchwise boundaries.

¹<http://www.numeca.com>



(a) Global view of computational region

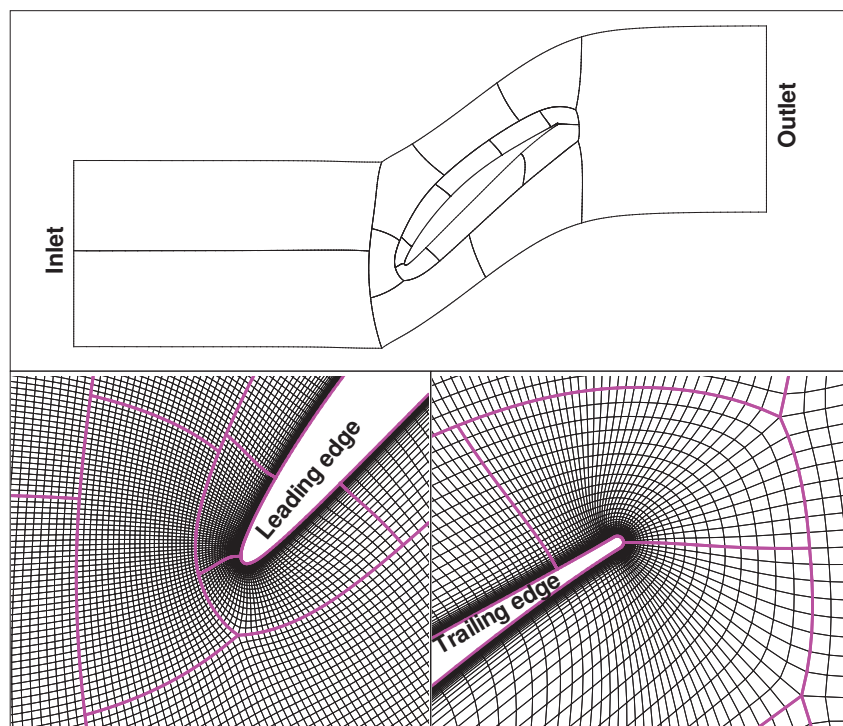
(b) Top: multi-block of grid in x - y plane; bottom: detailed grids at the leading edge and trailing edge

Figure 3.40: Grid distribution.

Chapter 4

Cascade performance

Contents

4.1	Introduction	82
4.2	Inlet flow conditions	84
4.2.1	Mean velocity	84
4.2.2	Streamwise normal stress	86
4.2.3	Spectrum	86
4.2.4	Evolution of boundary layer in the streamwise direction	88
4.3	Effects of incidence	89
4.3.1	Static pressure on the blade	89
4.3.2	Static pressure on the endwall	96
4.3.3	Total pressure losses of the outlet flow	97
4.4	Development of outlet flow	98
4.4.1	Total pressure losses	98
4.4.2	Velocity vector and secondary flow vector	100
4.4.3	Two typical sections in the spanwise direction	102
4.5	Conclusions	105

4.1 Introduction

After the introduction of the experimental and numerical methods in Chapter 3, the configuration of the cascade will be presented in this chapter. The measurements used in this chapter are illustrated in Fig. 4.1 and summarized in Table 4.1. Besides the experimental results, some numerical results of the S-A turbulence model are also presented and used to understand the physics. Other numerical results are presented in Appendix D.

Firstly, the inlet flow conditions are presented in this chapter. This is because the inlet flow conditions present the initial state of the experiment, and can provide the boundary conditions for the numerical simulations. The inlet boundary layers are measured by 1D hot-wires. The measurement region in the spanwise direction is from the endwall to the mid-span. In order to minimize the influences of incidence, five measurement stations are located at $4.13c_a$ upstream of the blade leading edge. The measurement station 2 is just upstream of the leading edge of the blade 6. Additionally, the spacing between measurement stations is $0.5s$, where s is the blade pitch. Another measurement station (L6) is located at $8.3c_a$ upstream of the blade leading edge and just upstream of the leading edge of the blade 5.

Secondly, the effects of incidence on the flow behaviour and the overall performance of the cascade are investigated, using the measurements carried out at five incidences in a range of $i=-2^\circ\sim 6^\circ$. The measurements include the static pressures on the blade and the endwall, and the total losses of the outlet flow. The static pressures on the blade are measured by the pressure taps on the blade 6. The static pressures on the endwall are measured by the pressure taps on the endwall. The total losses of the outlet flows are measured by a five-hole pressure probe at the outlet section 1.

Finally, the development of the outlet flow is discussed using the outlet flow measured at the outlet sections 1~3 at $i=4^\circ$. These outlet flows at the outlet sections are measured by a five-hole pressure probe. The measurement sections 1~3 are located at 40.00 mm, 70.00 mm and 100.00 mm (i.e. $0.363c_a$, $0.635c_a$ and $0.907c_a$) downstream of the blade trailing edge, respectively. In spanwise direction, the extent of each measurement section is from the endwall to the mid-span.

4.2 Inlet flow conditions

In the experiment, inflow reference velocity U_∞ is always 40.0 m/s, corresponding to a Reynolds number of 3.82×10^5 according to the chord and the inflow velocity. The inlet boundary layers are measured by 1D hot-wires. The parameters of the hot-wires are listed in Table 4.2, in which l and d are the active length and the diameter of a probe, respectively. To avoid conduction errors, all of the l/d of the hot-wire probes are greater than 200.

4.2.1 Mean velocity

Fig. 4.2a shows the experimental profiles of the mean velocity. They are similar to each other. Based on the mean velocity profiles, various parameters of boundary layer can be calculated, as listed in Table 4.3. In this table, "LA-PB" is a label for the results of station "A" using the number "B" hot-wire probe. For example, "L1-P2" is a label for the results of station "1" using the number "2" hot-wire probe. The thickness of boundary layer δ is defined as the distance from the wall where the velocity reaches 99% of the outer velocity U_e . The displacement thickness δ^* , momentum thickness θ and energy thickness δ_3 are calculated respectively by

$$\delta^* = \int_0^\delta \left(1 - \frac{U}{U_e}\right) dz, \quad (4.1)$$

$$\theta = \int_0^\delta \frac{U}{U_e} \left(1 - \frac{U}{U_e}\right) dz, \quad (4.2)$$

$$\delta_3 = \int_0^\delta \frac{U}{U_e} \left(1 - \frac{U^2}{U_e^2}\right) dz \quad (4.3)$$

The shape factor is defined as

$$H_{12} = \delta^* / \theta \quad (4.4)$$

The difference in U_e is less than 2%, which is nearly equal to the uncertainty of mean velocity measured by HWA (introduced in Section 3.2.4.6). Thus the inlet flow is nearly uniform. The shape factor is about 1.3, which is equal to the typical value for fully developed TBL, thus the inlet flow boundary layer is fully turbulent.

In our experiment, the friction velocity u_τ is not measured directly. However, it is determined indirectly from a least-square fit to the van Driest formula (Eq. 2.6) between $z^+ = 10 \sim 50$, as listed in Table 4.3. Then the mean velocity profiles in inner variables are obtained, as shown in Fig. 4.2b. The closest distance to the wall is $z^+ \approx 14$, in the buffer layer and outside of the region of $z^+ < 4$ where the wall affects considerably the measurement results confirmed by [Durst et al. \(2001\)](#).

Table 4.2: Parameters of 1D hotwire probes.

NO.	$l(\text{mm})$	$d(\mu\text{m})$	NO.	$l(\text{mm})$	$d(\mu\text{m})$	NO.	$l(\text{mm})$	$d(\mu\text{m})$
P0	1.25	5	P1	0.82	4	P2	1.00	4

Table 4.3: Parameters of inlet boundary layers measured by HWA.

NO.	U_e/U_∞	δ_{99} (mm)	δ^* (mm)	θ (mm)	δ_3 (mm)	H_{12} $= \delta^*/\theta$	u_τ (m/s)	τ_w (kg/ms^{-2})	l^+ $= lu_\tau/\nu$	Re_θ $= U_e\theta/\nu$
L1-P0	0.996	30.1	3.7	2.9	5.2	1.29	1.46	2.494	116	7359
L2-P0	0.998	29.1	3.8	2.9	5.3	1.28	1.46	2.494	116	7374
L3-P0	1.008	30.1	4.0	3.1	5.6	1.29	1.46	2.494	116	7961
L3-P2	1.004	30.1	4.0	3.1	5.8	1.29	1.44	2.426	92	7930
L4-P0	1.013	32.1	4.5	3.5	6.3	1.28	1.46	2.494	116	9033
L4-P1	1.008	31.1	4.8	3.7	6.7	1.30	1.43	2.393	75	9502
L5-P1	1.016	30.1	4.1	3.2	5.7	1.28	1.45	2.494	76	8283

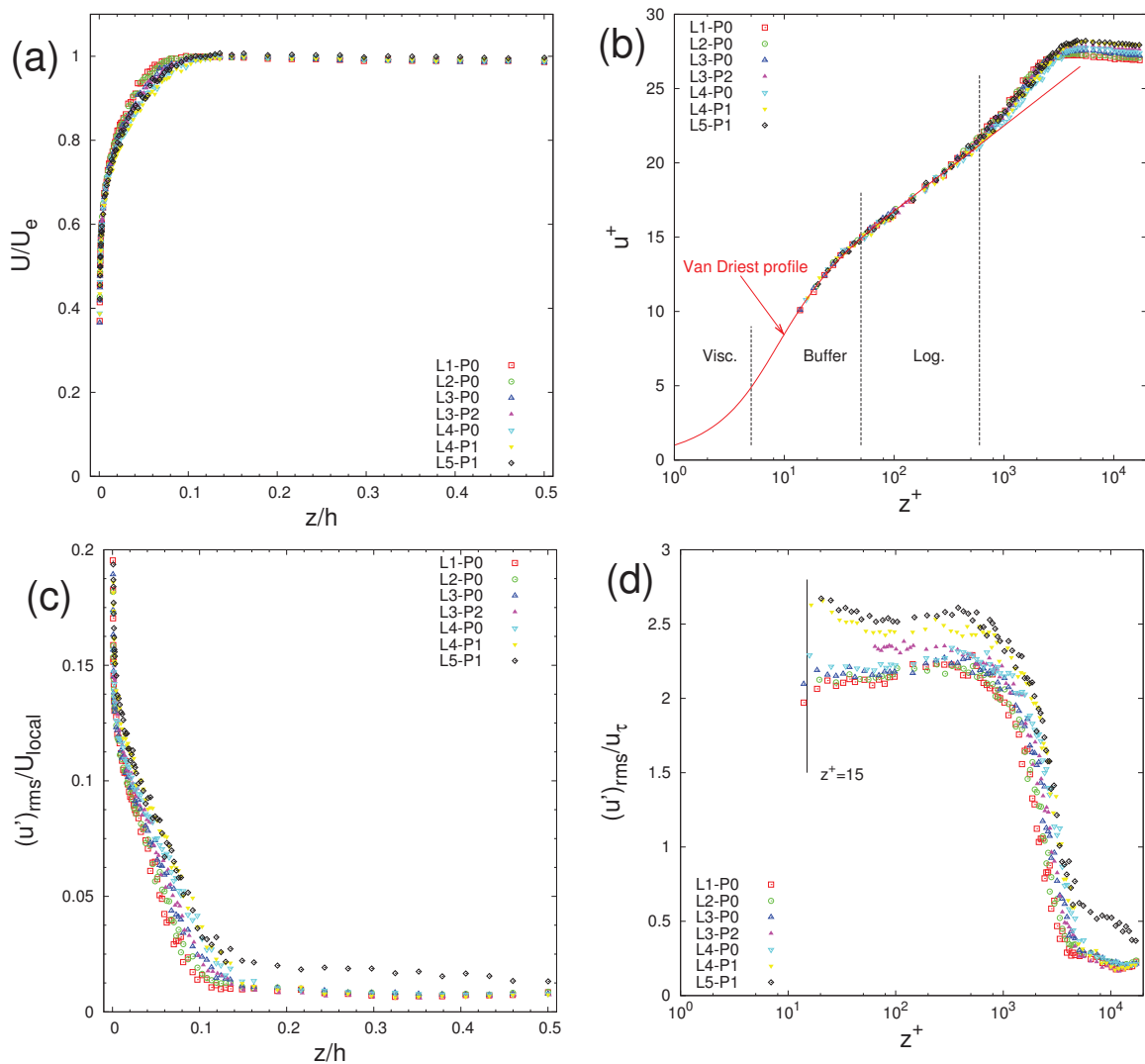


Figure 4.2: Experimental results of inlet boundary layer, measured by HWA.

4.2.2 Streamwise normal stress

The profiles of Reynolds normal stress are shown in Fig. 4.2c. These profiles are similar from station 1 to station 4, except station 5 where the value is a little larger than others at the same distance to the endwall. This shows that the uniformity of inlet flow is acceptable from station 1 to station 4. Outside of the boundary layer, the local turbulence intensity $Tu_{local} \approx 0.8\%$ for most of the inlet flow (from station 1 to station 4).

For the Reynolds normal stresses in inner variables $\sqrt{u'^2}/u_\tau$, a widely acceptable conclusion is that the profile of $\sqrt{u'^2}/u_\tau$ in a TBL with ZPG shows a peak very close to the wall where $z^+ \approx 15$. Additionally, the value of the peak is about 2.7, although it increases slowly with Re_θ .

Our experimental profiles of $\sqrt{u'^2}/u_\tau$ are shown in Fig. 4.2d. At each measurement station, the profile of Reynolds normal stress shows a peak near $z^+ \approx 15$, consistent with that in a TBL with ZPG; however the value at the peak is not always equal to 2.7, the value in a TBL with ZPG. Moreover, there are obvious differences between the experimental results obtained with the different hot-wire probes; this is consistent with a lot of results measured by hot-wires in the literature. For example at the same measurement station 3, the $(\sqrt{u'^2}/u_\tau)_{max}$ reaches 2.3 with the P0, whereas 2.7 with the P2. Besides the uncertainty of measurement, we can associate this variation with the difference in l^+ of the hot-wire probes according to [Fernholz & Finley \(1996\)](#). Since a hot wire measures the average heat transfer rate over its length, it will weaken the measured velocity fluctuation if that fluctuation occurs over a length-scale smaller than the length of the hot wire. If it's assumed that the characteristic eddy size is taken by the distance to the wall, and that a non-negligible fraction of the turbulent kinetic energy is carried by eddies with this characteristic size, then a hot wire will significantly weaken the measured turbulence intensity when it is positioned close to the wall. Therefore the experimental results of the probe "P1" are more accurate than other probes.

4.2.3 Spectrum

From the instantaneous velocity measured by HWA, frequency spectrum can be obtained directly using the operation of fast Fourier transform (FFT). According to the Taylor hypothesis ([Pope, 2000](#)), e.g. the turbulent structures transfer by the mean flow, the frequency spectrum can be transformed to the spatial spectrum

$$E_{11}(K) = \frac{U}{2\pi} \cdot E(f) \quad (4.5)$$

where K is the wave number

$$K = \frac{2\pi}{U} \cdot f \quad (4.6)$$

and U is the mean velocity at the measurement point. Compared with the frequency spectrum, the spatial spectrum just shifts in the log-log coordinates according to Eqs. 4.5 and 4.6.

Both frequency spectrum and spatial spectrum at a point, where $z=0.17$ mm and $z^+=15.9$, are shown in Fig. 4.3. This point is located at measurement station L4, where the Reynolds number is $Re_\theta=9502$. In the frequency spectrum (Fig. 4.3a), the maximum frequency is 100 kHz, because the sampling rate is 200 kHz in the experiment. The lifting exists in the high frequency region due to the effect of noise. For spatial spectrum, two other experimental near-wall turbulence spectra from Metzger *et al.* (2001) are also shown in Fig. 4.3b. One is at $z^+=20.6$ with low Reynolds number $Re_\theta=2000$. The other one is at $z^+=16.9$ with very high Reynolds number $Re_\theta \approx 5 \times 10^6$. These three spectra are similar; and the difference can be interpreted as the influence of Reynolds number. Therefore our experimental results are reliable.

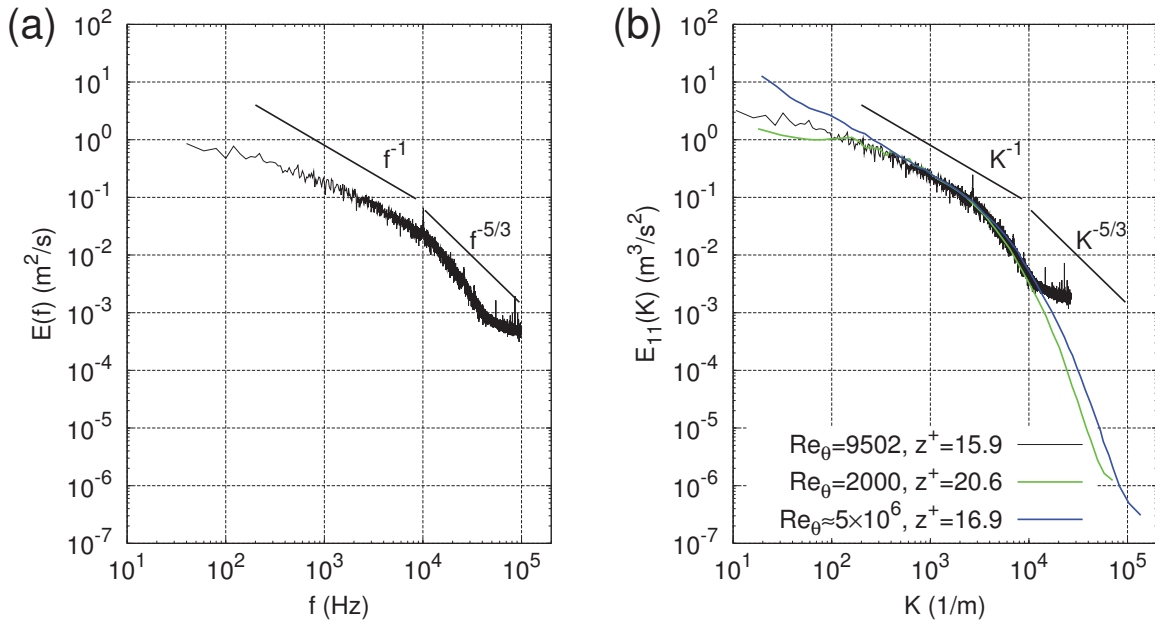


Figure 4.3: Spectra of streamwise velocity at the point where $z=0.17$ mm and $z^+=15.9$, measured by HWA. (a) Frequency spectrum. (b) Spatial spectrum, green and blue lines show the experimental spectra from Metzger *et al.* (2001).

4.2.4 Evolution of boundary layer in the streamwise direction

To observe the evolution of the boundary layer in the streamwise direction, the boundary layer is also measured in the line 6, much upstream of the other measurement stations. However measurements have been operated only at four points in this line, because of the limitation of our experimental setup.

The comparisons between the station 3 and the station 6 are shown in Fig. 4.4. In order to show the differences more clearly, the experimental results in the station 3 are shown with lines. We can come to the conclusion that the boundary layer is obviously gradually thicken in streamwise direction, as illustrated in Fig. 4.5. However, the measurement accuracy does not permit to calculate the evolution of some quantities such as the decrease in the turbulent kinetic energy.

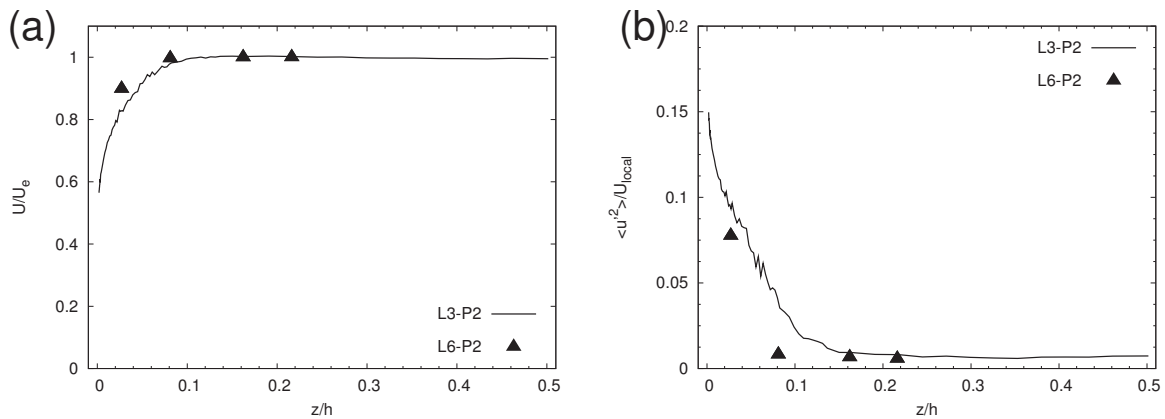


Figure 4.4: Evolution of boundary layer in streamwise direction.

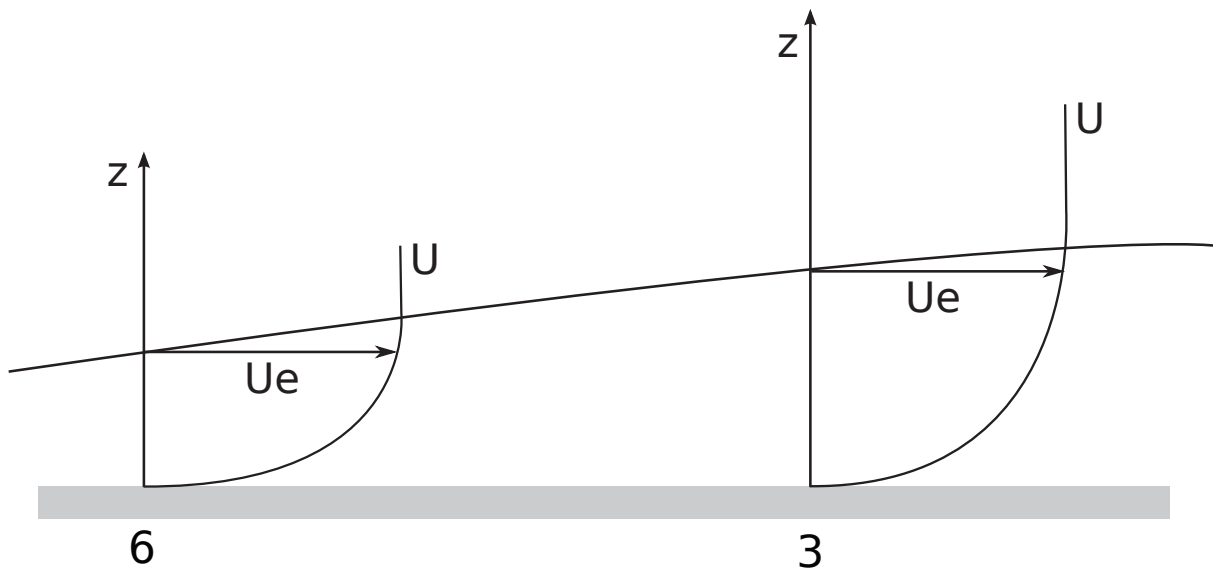


Figure 4.5: Sketch of evolution of boundary layer in streamwise direction.

4.3 Effects of incidence

Incidence is one of the most important factors of corner stall. To assess the effects of incidence on the flow behaviour and the overall performance of the cascade, measurements have been carried out at five incidences in a range of $i=-2^\circ\sim 6^\circ$. The measurements include the static pressure on the blade and the endwall measured by pressure taps, and the total pressure losses of the outlet flow at outlet section 1 measured by a five-hole pressure probe.

4.3.1 Static pressure on the blade

The global view of the experimental distribution of static pressure on the blade is shown in Fig. 4.6, in which the markers indicate the measurement positions. In order to show more accurately their evolutions, Fig. 4.7 shows a representative experimental distribution of the static pressure ($i=4^\circ$). Fig. 4.8 shows the numerical results of static pressure and streamlines on the blade.

Firstly, the experimental and numerical results at $i=4^\circ$ are used to show the characteristics of the static pressure distribution at a given incidence. On the pressure side near the leading edge, the static pressure near the endwall is smaller than that far from the endwall. In contrast, on the suction side near the leading edge, the static pressure near the endwall is larger than that far from the endwall. This is due to the existence of inlet flow boundary layer. The oblique of the contours close to the endwall on both the pressure and suction sides are caused by the blockage of corner separation.

Secondly, the experimental and numerical results at five incidences are used to investigate the effects of incidence. The effects of incidence mainly come through the effects on two typical regions. One is the region where $C_p > 0.3$ on the pressure side; the other one is the region where $C_p < -0.3$ on the suction side. When the incidence increases, the location of the first region moves upstream and its extent enlarges; the location of the second region moves also upstream but its extent reduces.

After the global view, the distributions of static pressure at two representative sections are discussed, as shown in Fig. 4.9. The first section is at mid-span ($z/h=50.0\%$); the second one is near the endwall and in the region of corner stall ($z/h=5.4\%$).

Besides the experimental results, the numerical results are used to help to understand the physics, and also shown in Fig. 4.9. The numerical results reproduce properly the pressure distributions on the blade at mid-span. However, the numerical results fail to reproduce the pressure distributions near the endwall where the 3D separations occur. This behavior is mainly

due to the numerical results overestimate the separation region.

At mid-span on the suction side, the static pressure firstly decreases rapidly and then increases slowly until just upstream of the trailing edge, at last decreases slightly until the trailing edge. This is a typical point on the blade suction side, noted as "B" in Fig. 4.9. The static pressure decreases versus incidence from the leading edge to the point B, while the static pressure increases versus incidence from the point B to the trailing edge. The experimental and numerical locations of the point B are in very good agreement, and locate at $x/c_a=0.21$. In addition, the static pressure on the pressure side increases with incidence.

The results at the section near the endwall are then discussed. At this section, some specific phenomena related to flow separation are observed. The pressure evolutions reach constant value after a specific axial position; this phenomenon can be used to indicate the location of the separation point and the extent of flow separation. At this section, the separation point moves upstream when the incidence increases. The separation occurs at this section around $x/c_a=0.6$ for instance at $i=4^\circ$. Considering again Fig. 4.6, a strong inclination of the C_p isoline for $z/h<0.3$ is also observed; this is the direct consequence of the blockage effect due to the existence of corner separation which induces curvature in the flow up to the leading edge (see also Bario *et al.*, 1982). About the location of the point B in this section, the experimental result is very different with the numerical result. The experimental result is $x/c_a=0.14$, however the numerical result is $x/c_a=0.03$.

The phenomenon near the leading edge is investigated. A typical phenomenon near the leading edge is the existence of a stagnation point. According to the definition, the stagnation point locates at the point where the static pressure reaches a maximum value. The position of the stagnation point cannot be determined by the experimental results, because of the limited number of the experimental points. Therefore the numerical results are used instead. From the enlarged figures of the region near the leading edge (Fig. 4.9), the C_p at the stagnation points are approximately 1.0 at mid-span, and smaller than 1.0 near the endwall. This is mainly caused by the inlet velocity profile imposed in the CFD, which includes the boundary layer. Therefore the dynamic pressure in the region near the endwall is smaller than that at mid-span. In addition, the dynamic pressure used to calculate the pressure coefficient C_p is the dynamic pressure at mid-span. At mid-span, the stagnation point is on the suction side at the negative incidence ($i=-2^\circ$), whereas is on the pressure side at other incidences ($i=0^\circ, 2^\circ, 4^\circ$ and 6°). At the same time, the stagnation point moves downstream when incidence increases from 0° to 6° . Similar as that at mid-span, the stagnation points near the endwall moves also downstream at an increasing incidence. This means that the incidence increases from the endwall to the mid-span, mainly due to the influence of inlet boundary layer and the blockage of the corner stall.

Besides near the leading edge, the phenomenon near the trailing edge is also investigated

using numerical results (see the enlarged figures of trailing edge in Fig. 4.9). The static pressure on the pressure side decreases then increases very near the trailing edge where $0.99 < x/c_a < 1$. This is similar to the pressure distribution predicted by usual potential-flow theory (Pinkerton, 1936), because the flow accelerates in this region.

The comparison between experimental and numerical results at mid-span can also be used to show the reliability of the experimental set-up. The reliability of the experimental set-up is very different to assess mainly because of the difficulty to obtain specific value of incidence in the experiment, mainly due to two issues. The first issue is that it is difficult to keep the incidence constant in the pitchwise direction (i.e. to ensure the periodicity of the cascade), because of the skewness of test rig. The second issue is that it is difficult to measure the incidence accurately, because the measurement uncertainty in the angle may be larger than 1° . The incidence is controlled directly by the cascade orientation (angle position). The agreement between the experimental and numerical results at mid-span partly means that the experimental set-up and the control of the incidence are reliable. Moreover, the inlet conditions measured in the experiment and used in the CFD are also reliable. This may be due to that no separation occurs at mid-span, and the C_p distribution is not directly influenced by the turbulence modelling at mid-span. The agreement does not exist anymore near the endwall where the 3D separation exists. The 3D separation causes the blockage in the passage. The different of the experimental and numerical blockage may explain the small differences in the C_p at mid-span.

To assess the effects of the incidence on the flow behaviour and the overall performance, four pressure force parameters are used:

$$F_x(z) = \frac{1}{c_a} \oint C_p \vec{n} \cdot \vec{i} dl, \quad F_y(z) = \frac{1}{c_a} \oint C_p \vec{n} \cdot \vec{j} dl \quad (4.7)$$

$$F_x^* = \frac{1}{c_a h/2} \int_0^{h/2} \oint C_p z \vec{n} \cdot \vec{i} dl dz, \quad F_y^* = \frac{1}{c_a h/2} \int_0^{h/2} \oint C_p z \vec{n} \cdot \vec{j} dl dz \quad (4.8)$$

where \vec{n} , \vec{i} and \vec{j} are the unit normal vectors of blade surface, x axis and y axis, respectively. Subscripts x and y denote the direction of the force in x axis and y axis, respectively. For a given C_p distribution, F_x^* and F_y^* have unique values respectively, while F_x and F_y are functions of the distance from the endwall. The experimental and numerical F_x and F_y are shown in Fig. 4.10.

The experimental F_x and F_y increase in spanwise direction for all incidences, and increase also with incidence, except when $i=6^\circ$ or $z/h < 0.2$. We can infer that there are stronger separations at $i=6^\circ$ than at other incidences, and this will be confirmed by the experimental total pressure losses in the exit plane as discussed in Section 4.3.3. From the comparisons between experimental and numerical results, the differences are generally larger in the corner region ($0 < z/h < 0.3$) than that in the outer region ($0.3 < z/h < 0.5$), because the CFD tools simulate less

accurately in the corner region.

The experimental and numerical F_x^* and F_y^* are shown in Fig. 4.11. Their magnitude increase, when the incidence increases. The ratio of F_y^* to F_x^* decreases, with the incidence increasing. This means that F_x^* increases faster than F_y^* . From the comparisons of experimental and numerical results, CFD tools can simulate very well the trend of these two pressure force parameters but underestimate the magnitude of these forces. This is obviously because of the overestimation of the corner separation.

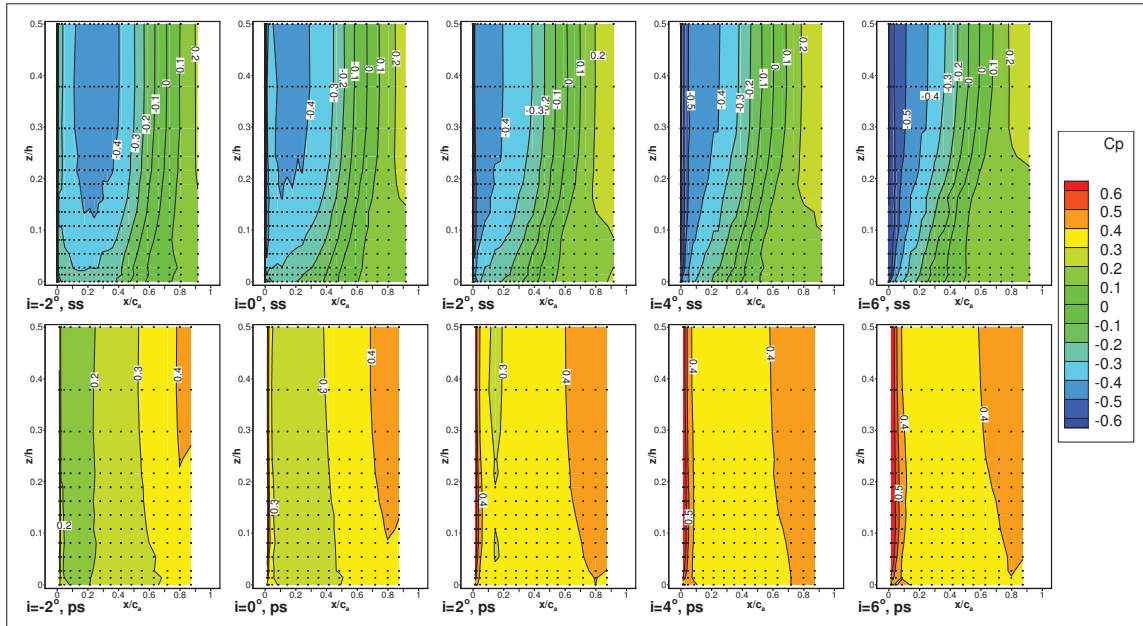


Figure 4.6: Experimental distribution of C_p on the blade at five incidences. Markers indicate the measurement positions.

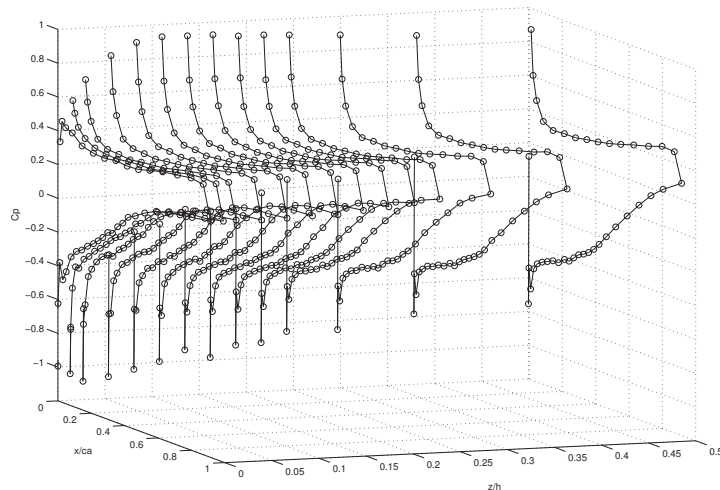


Figure 4.7: Experimental distribution of C_p on the blade at $i=4^\circ$. Lines for visual aid only.

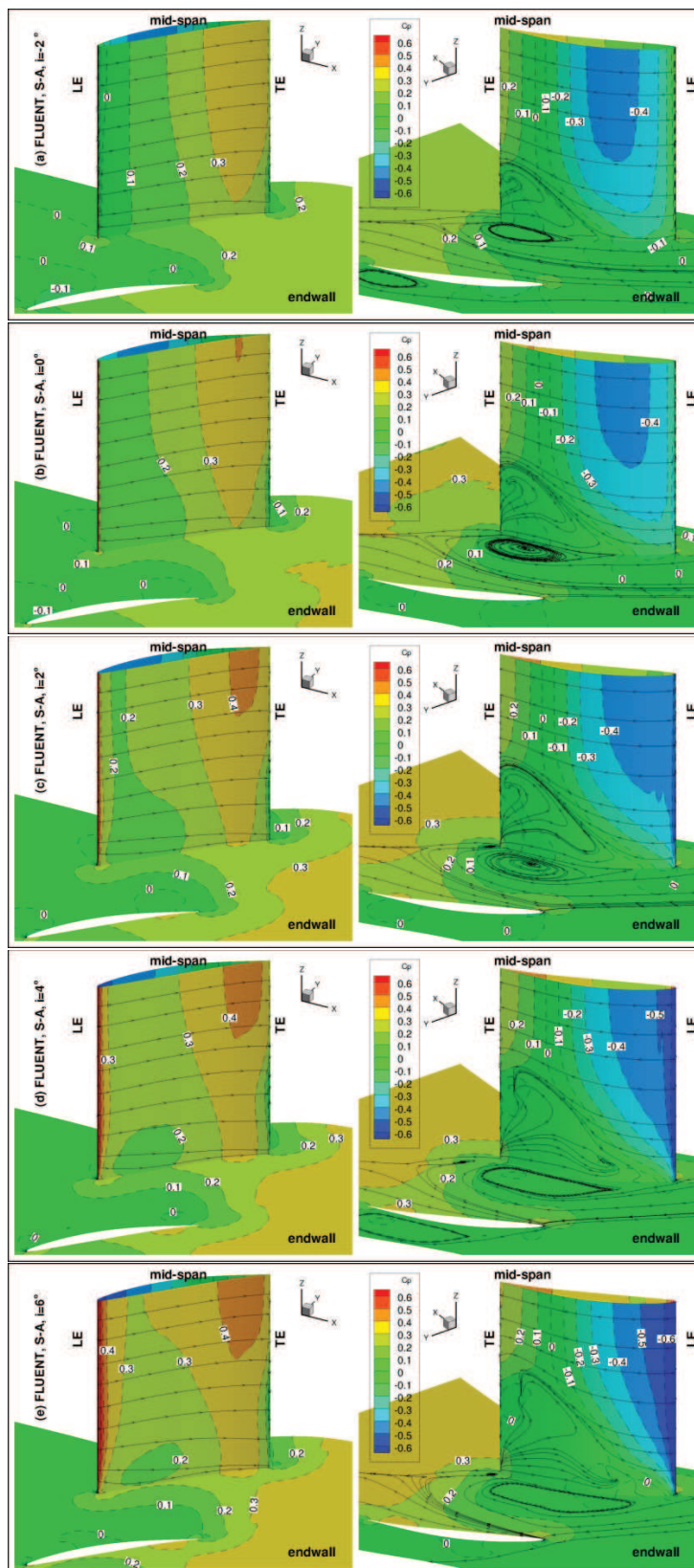


Figure 4.8: Numerical results of static pressure and streamlines on the blade and endwall at five incidences.

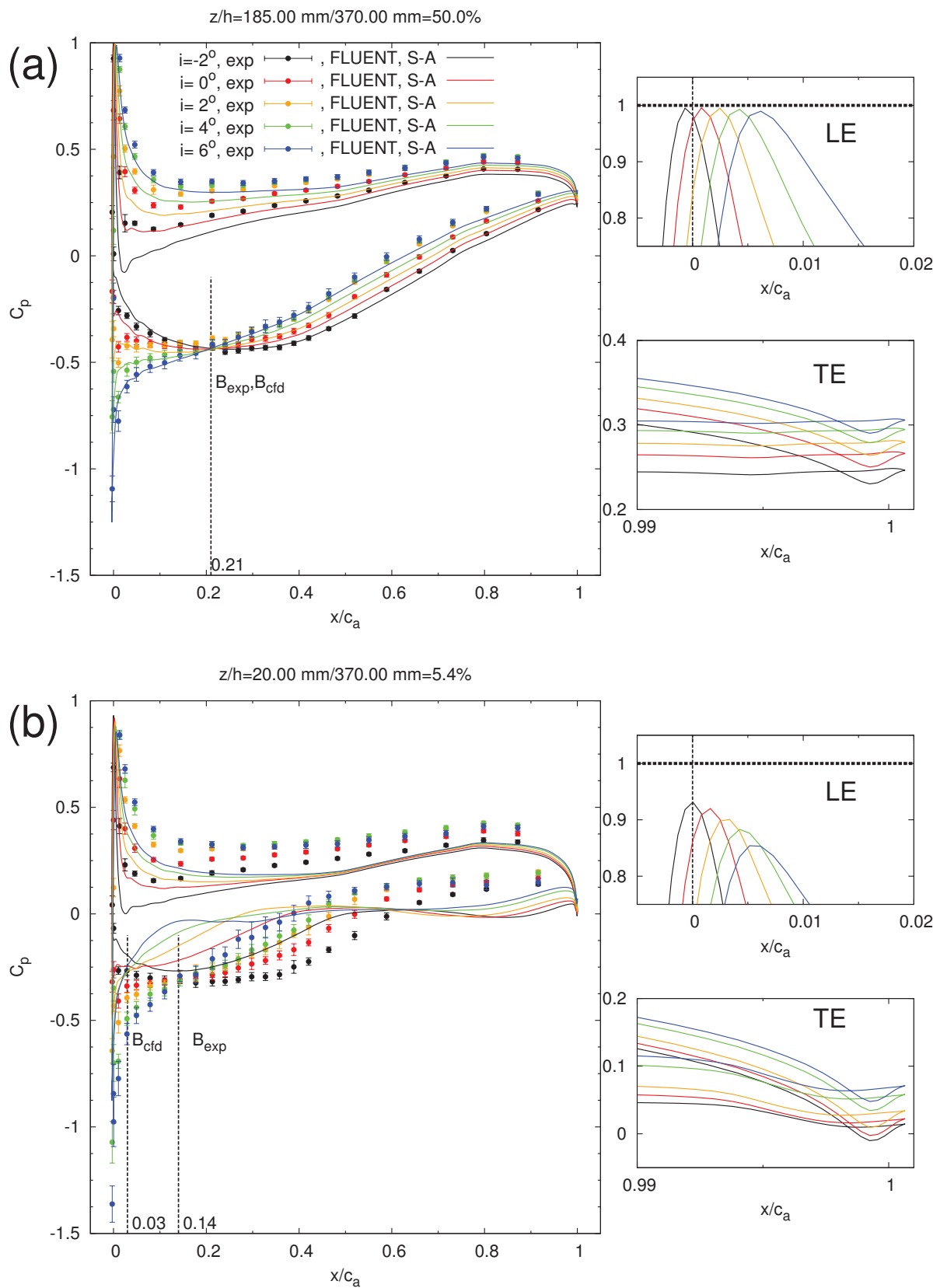


Figure 4.9: Experimental and numerical results of static pressure on the blade at five incidences. (a) The mid-span; (b) the section near endwall.

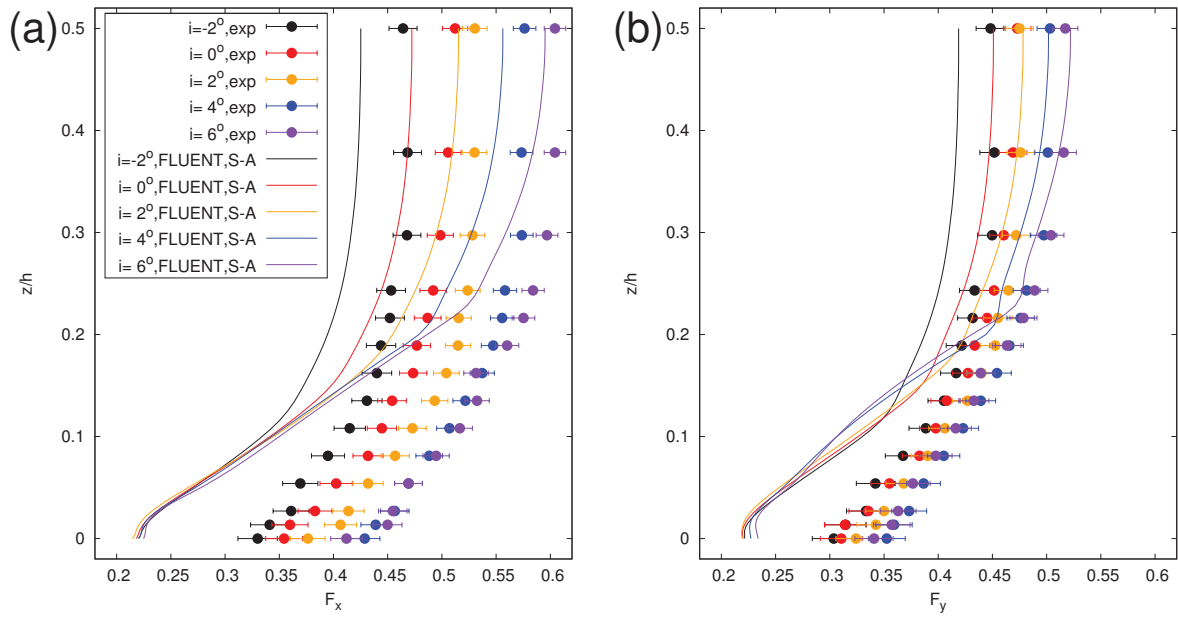


Figure 4.10: Experimental and numerical F_x and F_y at five incidences.

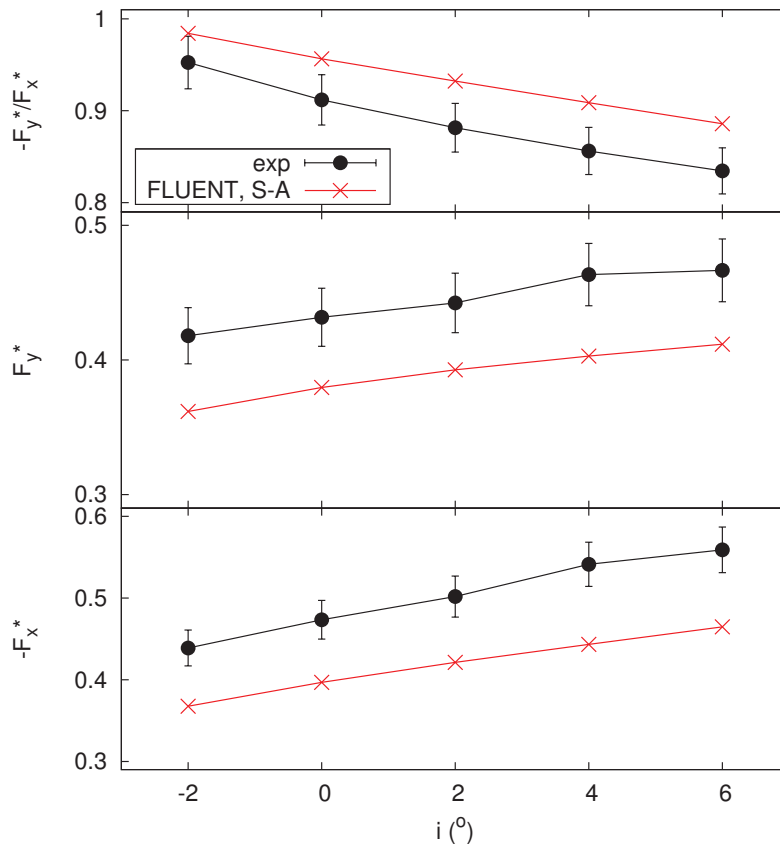


Figure 4.11: Experimental and numerical F_x^* , F_y^* and F_y^*/F_x^* .

4.3.2 Static pressure on the endwall

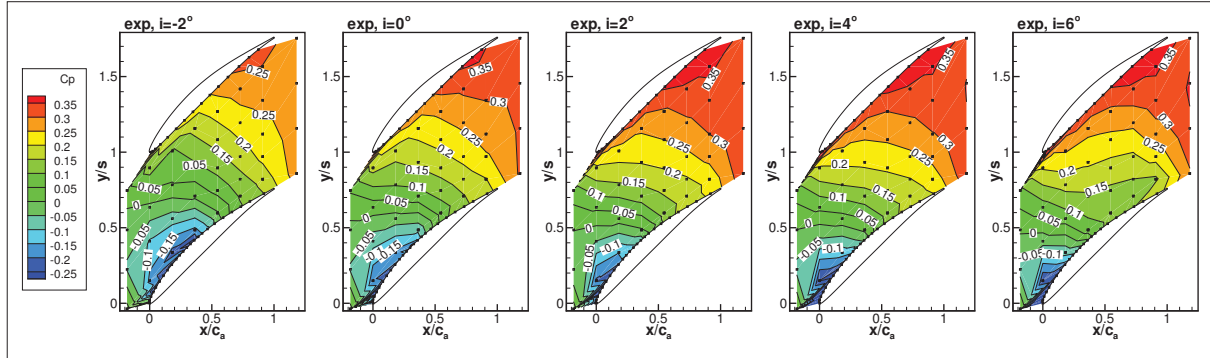


Figure 4.12: Experimental static pressure coefficients on the endwall at five incidences. Markers indicate the measurement positions.

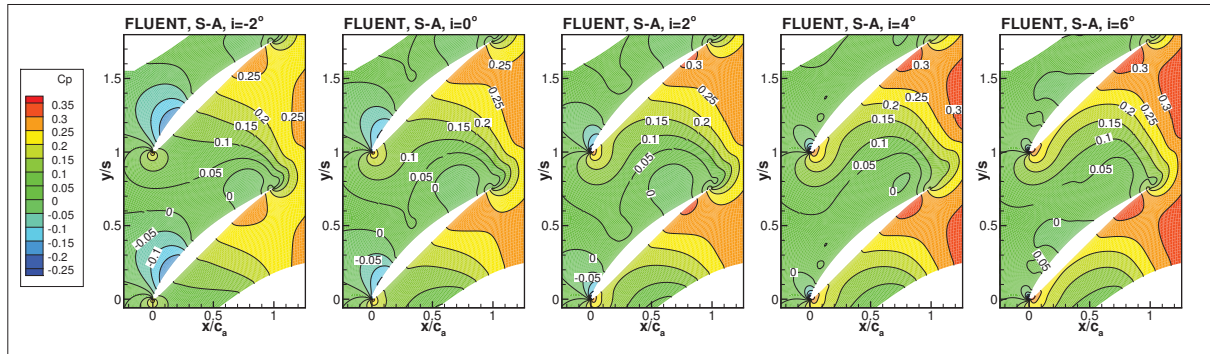


Figure 4.13: Numerical static pressure coefficients on the endwall at five incidences.

The experimental static pressure coefficients C_p on the endwall at five incidences are shown in Fig. 4.12, including the experimental results on the blade measured by an instrumented blade that can slide in the spanwise direction through two holes on the endwall. The extent of the region where the flow accelerates from the leading edge progressively narrows with incidence; this is consistent with the experimental surface static pressure on the blade, discussed in Section 4.3.1. With increasing incidence, the location of separation point gradually moves upstream and the extent of the corner separation expands; at the same time, the ratio of the outlet pressure to the inlet pressure in the passage increases.

In comparison with the experimental results, the numerical results (shown in Figs. 4.8 and 4.13) are quite different, especially for the contours of C_p . The limitations of the experimental results must be taken into account, such as the limited number of the measurement points and the distribution of those measurement points. Thus the numerical results are to be used to understand the physics. From the relation between the distribution of static pressure coefficient and the streamlines on the endwall, the patterns of the contour lines near the suction side correspond to the extent of the separation vortex in the corner. Therefore, the extent to the separation vortex in the corner increases with incidence.

4.3.3 Total pressure losses of the outlet flow

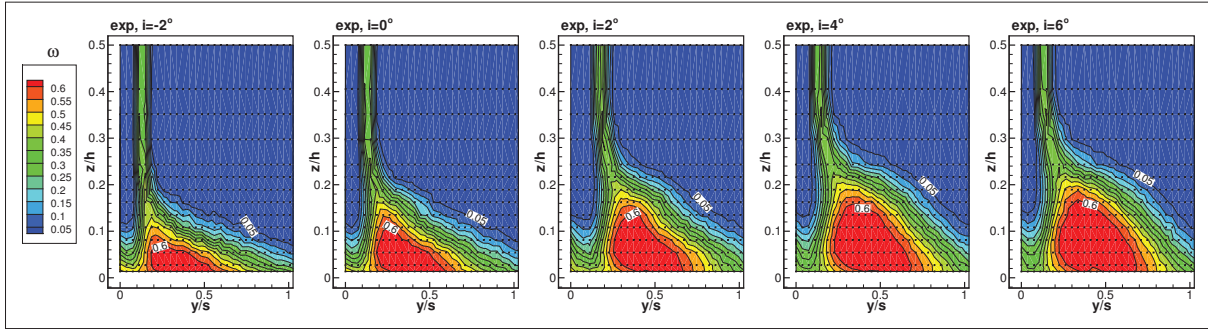


Figure 4.14: Experimental exit total pressure loss coefficient at the outlet section 1 at five incidences. Markers indicate the measurement positions.

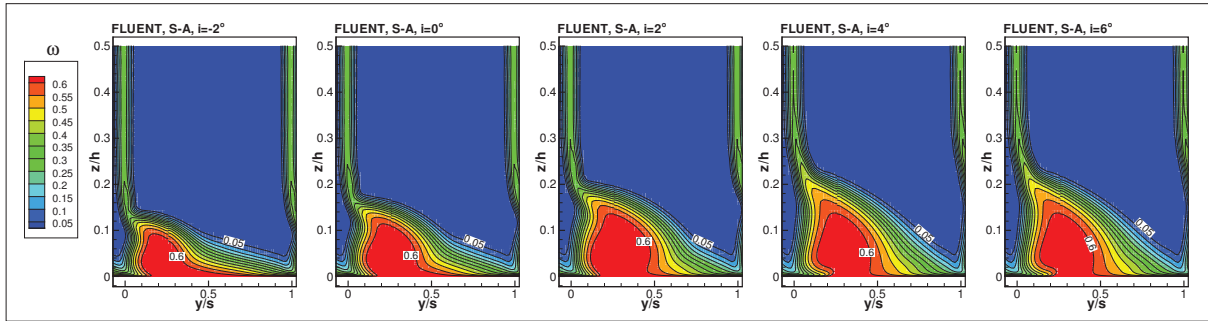


Figure 4.15: Numerical exit total pressure loss coefficient at the outlet section 1 at five incidences.

The experimental and numerical exit total pressure loss coefficient ω at the outlet section 1 (see Fig. 4.1) are shown in Figs. 4.14 and 4.15, respectively. At a given incidence, the losses increase in the spanwise direction from the mid-span to the endwall due to the corner separation. When the incidence increases, the extent of high losses (i.e. where $\omega > 0.05$) increases.

To quantify the global effects of the total pressure loss at the cascade outlet, two parameters are used. The first one is the pitchwise-mass-averaged total pressure loss coefficient ω^* . The second one is the mass-averaged total pressure loss coefficient ω' . They are defined as

$$\omega^*(z) = \frac{\int_0^s \omega(y, z) u_x(y, z) dy}{\int_0^s u_x(y, z) dy} \quad (4.9)$$

$$\omega' = \frac{\int_0^s \int_0^{h/2} \omega(y, z) u_x(y, z) dy dz}{\int_0^s \int_0^{h/2} u_x(y, z) dy dz} \quad (4.10)$$

where u_x is the axial velocity of outlet flow. From its definition, ω^* is a function of the spanwise distance from the endwall, while ω' only depends on a given plane. The experimental and numerical ω^* and ω' are shown in Fig. 4.16. They have the same trend, but not the same levels.

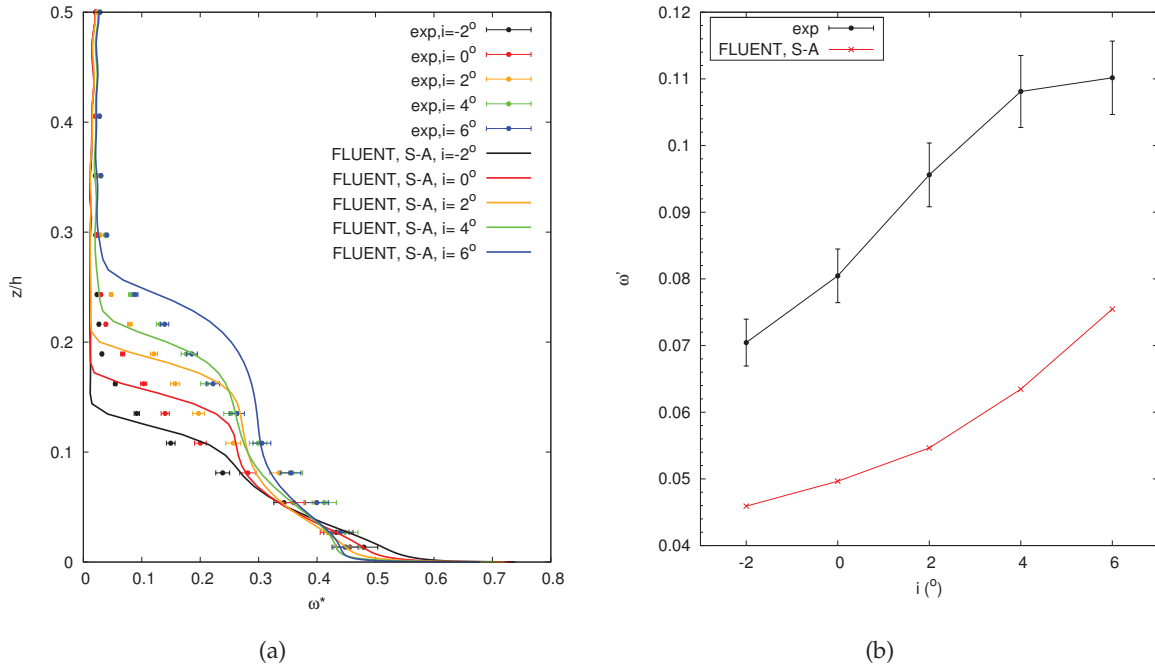


Figure 4.16: Experimental and numerical (a) ω^* at the outlet section 1, (b) ω' versus incidence.

4.4 Development of outlet flow

4.4.1 Total pressure losses

In this subsection, the development of the outlet flow is discussed using the outlet flow measured at sections 1~3. The trends of the results at $i=0^\circ$ are similar to that at $i=4^\circ$. Therefore, only the results at $i=4^\circ$ are presented and discussed in this subsection, in order to keep the thesis more concise.

The experimental distributions of ω are shown in Fig. 4.17. From the first to the third measurement section, the extents of losses (where $\omega > 0.05$) increase; in contrast, the extents of the high losses (where $\omega > 0.60$) decrease.

The experimental and numerical ω^* (Ref. Eq. 4.9) and ω' (Ref. Eq. 4.10) are shown in Fig. 4.18a and Fig. 4.18b, respectively. In the spanwise direction from the first to the third measurement section, the development of ω^* can be divided into three parts. In the first part $0.3 < z/h < 0.5$, ω^* in the second and third section are nearly the same and a little smaller than that in the first section. In the second part $0.08 < z/h < 0.3$, ω^* increases slowly from the first section to the third section. In the third part $0 < z/h < 0.08$, ω^* drops in the second and third sections. According to the corresponding ω' , which increases obviously from the first to the third measurement section, there are additional losses in the process of development.

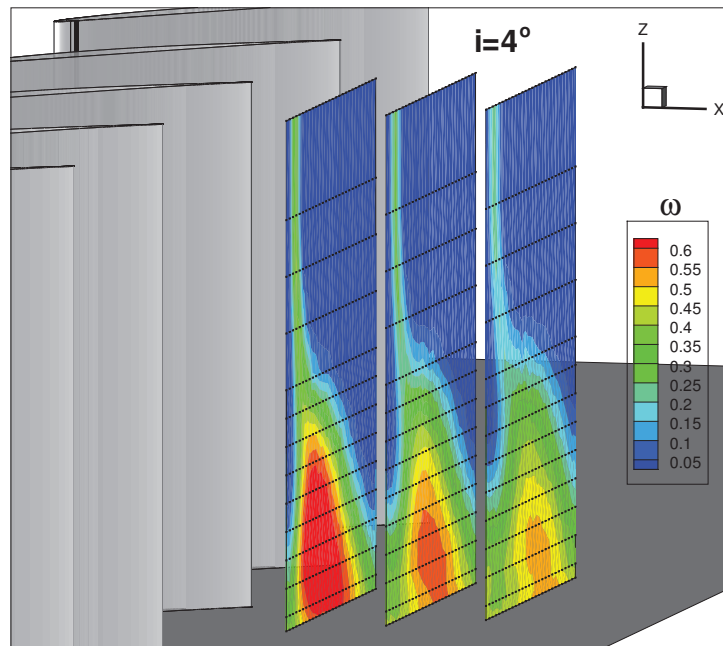


Figure 4.17: Experimental results of the total pressure losses coefficient distributions at measurement sections downstream the cascade, $i=4^\circ$. Markers indicate the measurement positions.

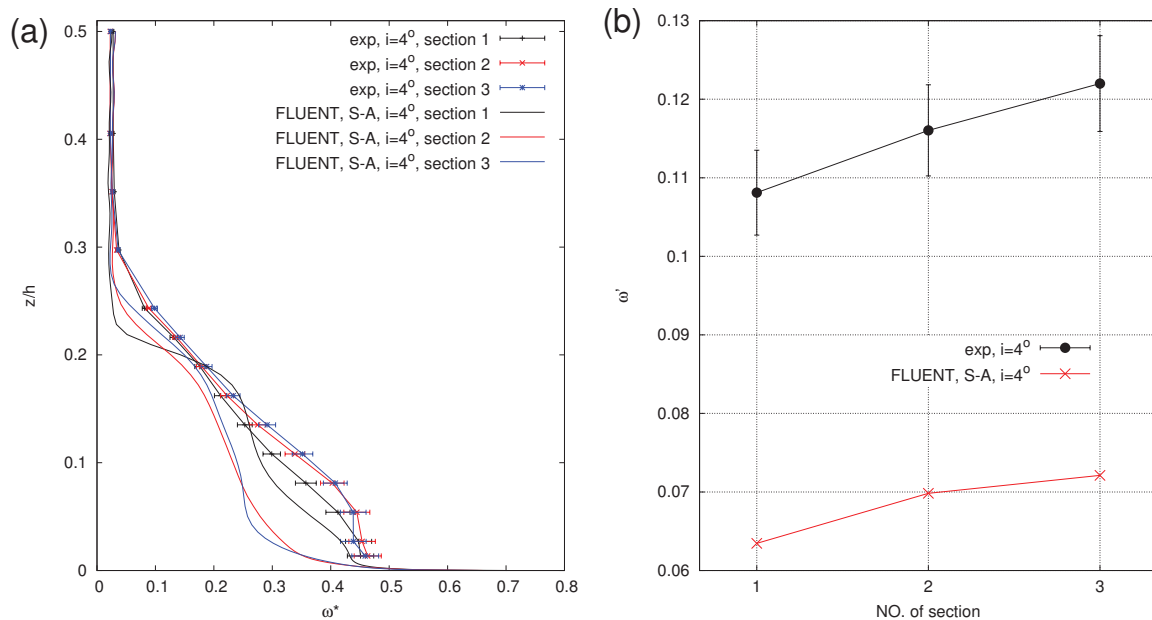


Figure 4.18: Comparisons of experimental and numerical results. Lines for visual aid only. (a) Pitchwise-mass-averaged total pressure loss coefficient ω^* , $i=4^\circ$; (b) mass-averaged total pressure loss coefficient ω' versus incidence, $i=4^\circ$.

4.4.2 Velocity vector and secondary flow vector

In order to show the development of the outlet flow, the total pressure losses coefficient and mean velocity vectors are shown in Figs. 4.19a-c, in which the distance is one blade pitch in the pitchwise direction. Therefore the comparison of the left and right edges can show the degree of the periodicity of the cascade in the measurement section. From the results in Figs. 4.19a-c, we know that the periodicity of our cascade is very good.

From the definition of total pressure losses $\omega = (P_{t\infty} - P_t) / (P_{t\infty} - P_{s\infty})$ and the relation (for the noncompressible flow)

$$P_t = P_s + 0.5\rho U^2$$

at each measurement point, total pressure losses cause by two sources. The first one is the decrease of the static pressure. The second one is the decrease of the magnitude of velocity. Because in our experiment the static pressure at the outlet section don't change very much, total pressure losses are mainly caused by the decrease of the magnitude of velocity. This is also supported by the phenomenon that the magnitude of the velocity is smaller in the high losses zone ($\omega > 0.4$), in Figs. 4.19a-c.

From the development of total pressure losses ω in Figs. 4.19a-c, a zone with high energy (small losses, $\omega < 0.05$) exists in each measurement section, illustrated as "zone A" in Fig. 4.19c. This zone is between the wake of the trailing edge and the corner stall, and moves away from the endwall, from the first to the third measurement section. At the same time its extent increases. This phenomenon is due the development of the flow in the middle of passage that has high momentum. The main flow lifts due to the blockage of corner stall, and batters the edge of the zone with high losses.

The secondary vector is defined as the three-dimensional velocity vector project to the plane perpendicular to the corresponding mid-span flow direction. In our experiment, the measurement sections are in y - z plan. The secondary flow vector \vec{V}_s is defined as

$$\vec{V}_s = \vec{V} - (\vec{V})_{mid-span} \quad (4.11)$$

where $(\vec{V})_{mid-span}$ is the mean velocity vector at mid-span corresponding to measurement point, i.e. they have the same y/s . The experimental secondary vectors are shown in Fig. 4.19d-f. At each measurement section, the positions of large magnitude of secondary flow vectors are consistent with that of large total pressure losses. This is because the total pressure losses mainly cause by the decrease of the magnitude of velocity; and the small magnitude of velocities induce to large magnitude of secondary flow. Generally speaking, the magnitude of secondary flow vectors increase from the first to the third measurement section, at the same distance from the endwall. The directions of the secondary vectors inside and outside the corner stall are inverse in each measurement section, as shown in Fig. 4.19f.

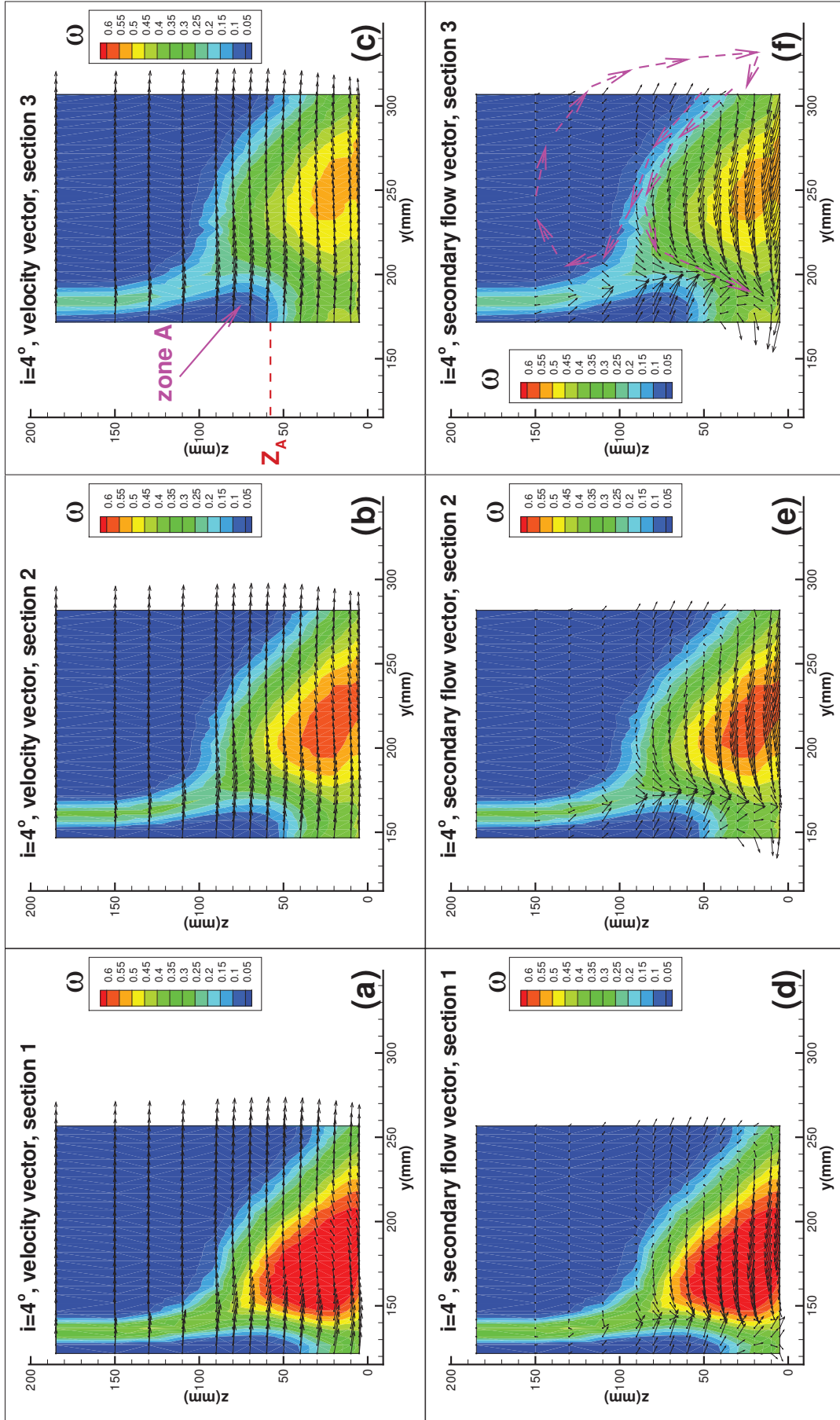


Figure 4.19: Experimental results of vector in the y - z plane, $i=4^\circ$. Markers indicate the positions of measurement points. Pink dashed lines indicate the directions of the secondary flow.

4.4.3 Two typical sections in the spanwise direction

In order to show in detail the development of the outlet flow, it is better to show the two-dimensional experimental results of the mean velocity vectors and the mean secondary flow vectors. Two typical sections are chosen: one is at mid-span ($z/h=50.0\%$); the other one is the section near the endwall and in the zone of corner stall ($z/h=5.4\%$).

Firstly, the results in x - y plane in Figs. 4.20a-c are discussed. According to the definition of secondary flow vectors (Eq. 4.11), the secondary flow vectors in x - y plane come from the vectors in the Fig. 4.20b subtracted from the corresponding vectors in Fig. 4.20a, as shown in Fig. 4.20c. In the plane near the endwall, the difference between the vectors decreases from the first to the third measurement section, because the development of the outlet flow is a typical process of mixing (Greitzer *et al.*, 2004, pp.274-277). At mid-span, the velocity keeps constant value in the main flow but not in the small region of wake where the behaviour is similar to that in the plane near the endwall. According to the definition of secondary flow vectors (Eq. 4.11), the secondary flow vectors in x - y plane come from the vectors in the Fig. 4.20b subtracted from the corresponding vectors in Fig. 4.20a, as shown in Fig. 4.20c.

Secondly, the results in y - z plane in Figs. 4.20d-f are discussed. According to the definition of secondary flow vectors (Eq. 4.11), the secondary flow vectors in y - z plane come from the vectors in the Fig. 4.20e subtracted from the corresponding vectors in Fig. 4.20d, as shown in Fig. 4.20f. Similar to the results in x - y plane, the difference between the vectors decreases from the first to the third measurement section, due to the turbulent mixing. The magnitudes of the vectors increase as well as the deviation angles, especially in the region of the corner separation. At mid-span, the velocity components in the spanwise direction are very small compared with the velocity components in the pitchwise direction. This means that the symmetry of the cascade is very good.

From Fig. 4.20, it is very difficult to see the difference of the flow velocity magnitude at different measurement section. For solving this problem, the flow velocity magnitudes are shown in Fig. 4.21, as well as the numerical results. With the development of the outlet flow, the velocity magnitude increases in the wake regions due to the mixing. At mid-span of each measurement section, the numerical results represent accurately the maximum magnitude of the vectors in the x - y plane, and the extent of the wake. However near the endwall, the numerical results obtain the correct development trend of outlet flow, but not the correct detailed parameters.

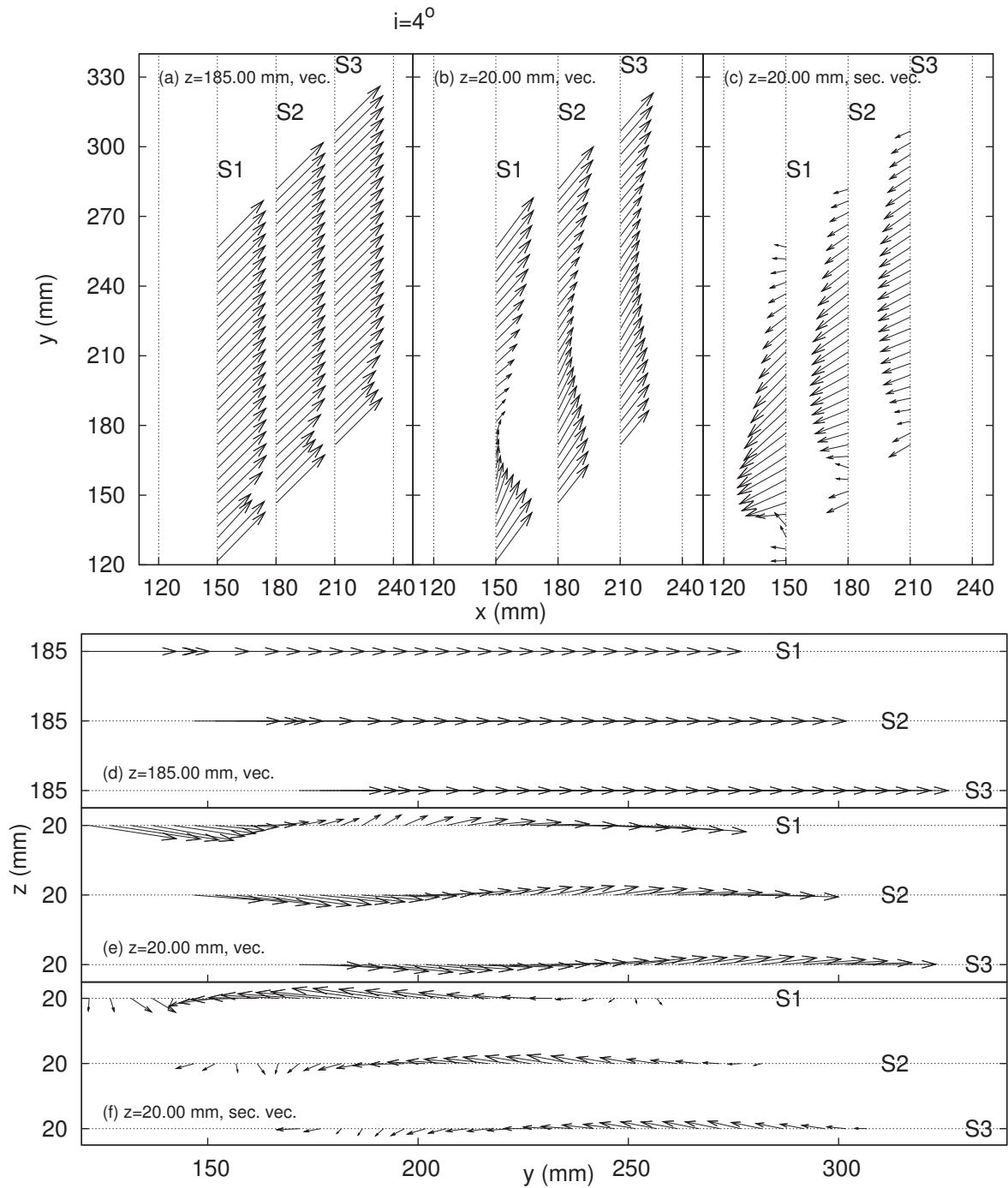
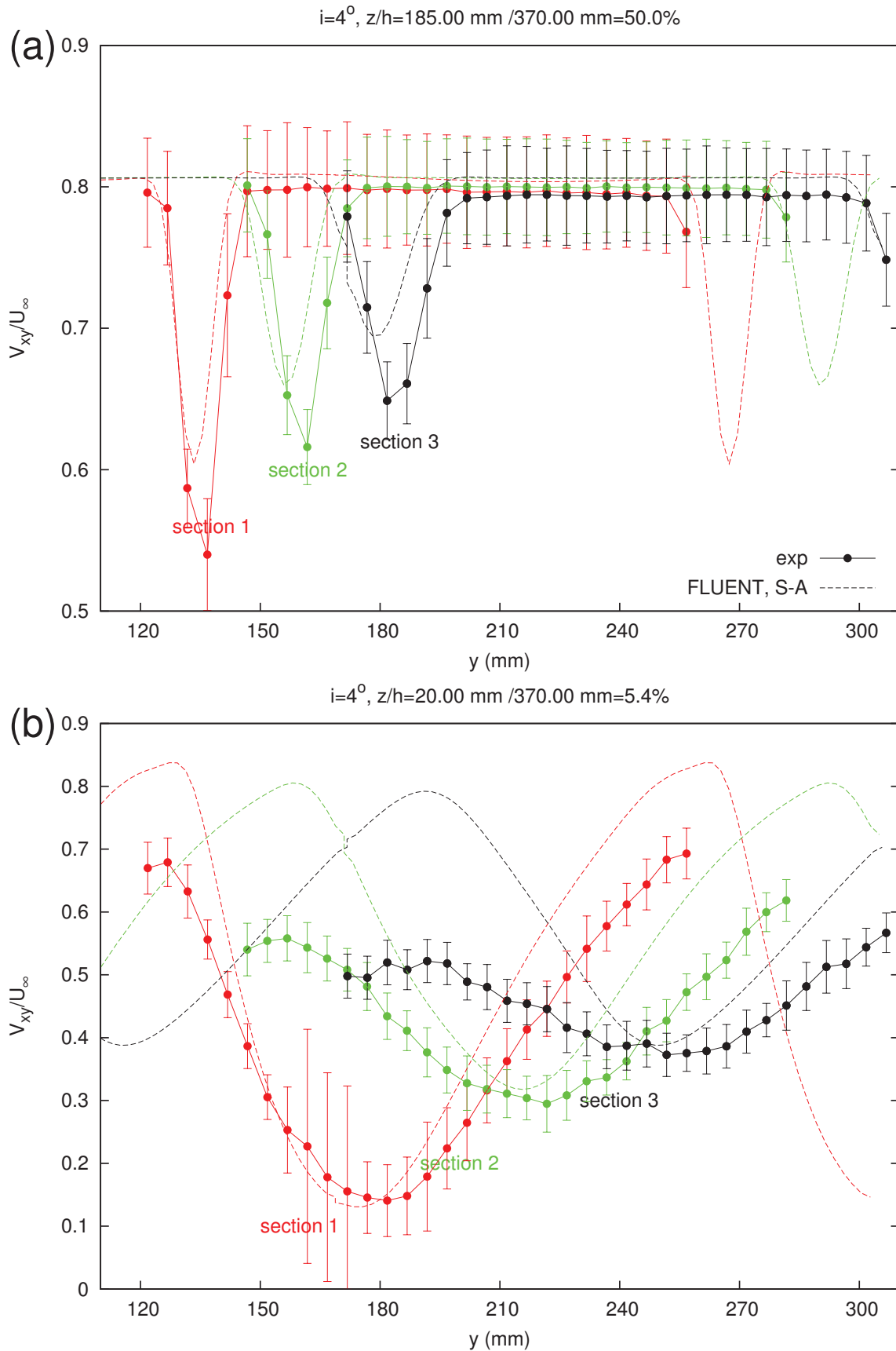


Figure 4.20: Experimental results of vector at three measurement sections, $i=4^\circ$. (a) Velocity vector \vec{V}/U_∞ in $y-z$ plane, $z/h=185.00$ mm/ 370.00 mm = 50.0% ; (b) velocity vector \vec{V}/U_∞ in $y-z$ plane, $z/h=20.00$ mm/ 370.00 mm = 5.4% ; (c) secondary flow vector \vec{V}_s/U_∞ in $y-z$ plane, $z/h=20.00$ mm/ 370.00 mm = 5.4% ; (d) velocity vector \vec{V}/U_∞ in $x-y$ plane, $z/h=185.00$ mm/ 370.00 mm = 50.0% ; (e) velocity vector \vec{V}/U_∞ in $x-y$ plane, $z/h=20.00$ mm/ 370.00 mm = 5.4% ; (f) secondary flow vector \vec{V}_s/U_∞ in $x-y$ plane, $z/h=20.00$ mm/ 370.00 mm = 5.4% .



4.5 Conclusions

The mean velocity profile and the streamwise normal stresses of inlet boundary layer are measured by hot-wire probes. The inlet flow boundary layer is fully turbulent. The turbulence intensity is about 0.8% in the main flow. These variables can be used to give boundary conditions for numerical simulations.

In order to investigate the effects of the incidence, measurements have been carried out at five incidences in a range of $i = -2^\circ \sim 6^\circ$. The static pressure on the blade shows that with the incidence increasing the location of the region where $C_p > 0.3$ on the pressure side moves upstream and its extent enlarges, the location of the region where $C_p < -0.3$ on the suction side moves also upstream but its extent reduces; and the global pressure forces in the x and y directions (noted as F_x^* and F_y^*) increase. The static pressure on the endwall shows that with the incidence increasing the location of the separation point gradually moves upstream and that the extent of the corner separation expands. At the same time, the ratio of the outlet pressure to the inlet pressure in the passage increases. The total pressure losses at the outlet show that with the incidence increasing the extent of high losses at a fixed outlet section increases.

The development of the outlet flow shows that the outlet flow is a typical mixing flow. In the outlet flow of the cascade, total pressure losses mainly stem from the decrease of the magnitude of velocity. A zone with high energy exists in each measurement section, named as "zone A" in the context. This phenomenon is due to the development of the flow in the middle of passage that has high momentum. The main flow lifts due to the blockage of corner stall, and batters the edge of the zone with high losses. The high energy in this zone could be used to control the corner stall. The directions of the secondary vectors inside and outside the corner stall are reverse in each measurement section.

Besides the experimental results, the numerical results of FLUENT with the S-A turbulence model are also used to understand the physics. At mid-span, the numerical simulation obtains acceptably results. However in the corner region, the numerical simulation only obtains the correct development trend, but not the correct detailed parameters, for example the pressure distributions and the total pressure losses distributions. The agreement at mid-span partly means that the experimental set-up is reliable. On the other hand, the disagreement in the corner region reflects the necessity of such experiment, which could provide a calibration database for the advanced CFD.

Chapter 5

Turbulent boundary layer at mid-span

Contents

5.1	Introduction	107
5.2	Influences of three factors in traditional TBL studies	108
5.3	Magnitudes of three factors in our case	109
5.3.1	Streamwise and wall-normal pressure gradients	109
5.3.2	Curvature	112
5.4	Mean velocity profiles	114
5.5	Backflow coefficient and histogram of velocity	119
5.6	Boundary layer thicknesses and shape factors	121
5.7	Determinations of skin friction and friction velocity	128
5.8	Mean velocity profiles in inner coordinate and velocity defect profiles	130
5.9	Pressure gradient parameters	131
5.10	Reynolds stresses	132
5.11	Second-order turbulent correlation coefficients	143
5.11.1	Ratio of Reynolds normal stresses $\overline{u_n'^2}/\overline{u_s'^2}$	143
5.11.2	Correlation coefficient $R_{u_s'u_n'}$	145
5.11.3	Structure parameter a_1	146
5.12	Triple correlations	147
5.13	Skewness and flatness	148
5.14	Examining scalings	150
5.15	Conclusions	152

5.1 Introduction

The subject of wall-bounded turbulent boundary layer (TBL) is one of the fundamental researches in fluid mechanics and has a distinguished history. It is not surprising that it has been being the topic of a number of researches. A recent review paper specializing the wall-bounded TBL is [Smits *et al.* \(2011\)](#).

The TBL with streamwise adverse/favourable pressure gradient (APG/FPG) and curvature occurs in many important technological devices such as diffusers and airfoils, and relates to the stability and efficiency of these devices. Therefore, lots basic investigations on the TBL have been dedicated to investigate the individual effects of the streamwise pressure gradient and of the curvature, as well as their combined effects. Through these basic investigations, considerable research findings exist, but they are mostly restricted to relatively simple geometries.

The purpose of this chapter is to study the TBL that develops at mid-span on the suction side of a compressor cascade blade, which constitutes a more complex geometry than those in the basic investigations but keeps quite simple compared to those encountered in a real engine. In our configuration (Fig. 5.1), the TBL is under the combined influences of three main factors: (i) streamwise pressure gradient, (ii) wall-normal pressure gradient and (iii) curvature of blade suction side. In the traditional TBL studies, the influences of streamwise pressure gradient and curvature have been considerably investigated, however this is not the case for the influence of wall-normal pressure gradient. Besides, the investigations at mid-span may improve the physical understandings of this TBL and could give some basic explanations of the characteristic of more complex TBLs such as that in the region of the corner stall.

In this chapter, influences of three factors in traditional TBL studies are introduced. The magnitude of the three influencing factors in our case are then introduced. Secondly, the mean feature of the TBL is presented through the profiles of mean velocities. An overview of the state of the TBL is then achieved using backflow coefficients of the streamwise velocity. The features of the boundary layer are completed with a calculation of the TBL thicknesses as well as the shape factors. Thirdly, the friction velocities as well as the skin frictions, which are not directly measured in the experiment, are then determined by indirect methods. This permits to present the mean velocity profiles in inner coordinates. Fourthly, some pressure gradient parameters proposed in the literature are applied to our configuration. Then the developments of Reynolds stresses, second-order turbulent correlation coefficients, skewness and flatness are investigated. At last, some scalings previously proposed to collapse the mean velocity and the Reynolds stresses profiles are examined using our experimental data.

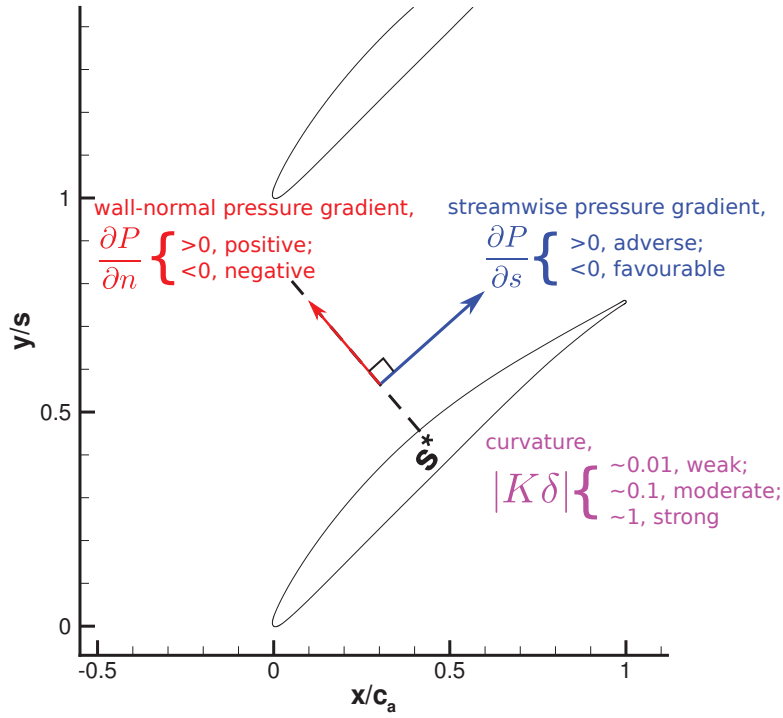


Figure 5.1: Three factors at mid-span.

5.2 Influences of three factors in traditional TBL studies

In the traditional TBL studies, the influences of streamwise pressure gradient and curvature have been considerably investigated. They have been reviewed in Section 2.3. However this is not the case for the influence of wall-normal pressure gradient. Because in most of the existing researches on TBLs, the mean pressure gradient in the wall-normal direction is neglected, which is true in many applications such as the boundary layers on flat plate and channel. One important derivation of this simplification leads back to the work of Bradshaw (1973). In this section, we re-examine the derivation of Bradshaw (1973) and underlines the influences of the wall-normal pressure gradient.

In order to investigate the influence of curvature, a long time ago Bradshaw (1973) derived the mean momentum equations in a 2D (s, n) system, where s is along the wall surface and n is in the wall-normal direction. They are Eqs. 2.15 and 2.16, which have been reviewed in Section 2.3.2. From the boundary layer assumption (i) the boundary layer thickness δ is much smaller than the distance along the surface s (*i.e.* $\delta \ll s$) and (ii) the curvature radius is relatively large (*i.e.* $s \lesssim R$), Bradshaw (1973) simplified Eq. 2.15 and Eq. 2.16 as

$$U_s \frac{\partial U_s}{\partial s} + U_n \frac{\partial U_s}{\partial n} = -\frac{1}{\rho} \frac{\partial P}{\partial s} - \frac{\partial \overline{u'_s u'_n}}{\partial n} + \nu \frac{\partial^2 U_s}{\partial n^2}, \quad (5.1)$$

$$-KU_s^2 = \frac{1}{\rho} \frac{\partial P}{\partial n} + \frac{\partial \overline{u_n'^2}}{\partial n}. \quad (5.2)$$

From Eq. 5.2, the influence of curvature is balanced by the sum of wall-normal pressure gradient ($\partial P/\partial n$) and normal gradient of Reynolds normal stress ($\partial \overline{u_n'^2}/\partial n$). Therefore, the curvature not only induces $\partial P/\partial n$, but also increases $\partial \overline{u_n'^2}/\partial n$. On the other hand, Eq. 5.2 also implies that $\partial P/\partial n$ suppresses $\partial \overline{u_n'^2}/\partial n$, i.e. the growth of $\overline{u_n'^2}$ in the wall-normal direction.

5.3 Magnitudes of three factors in our case

5.3.1 Streamwise and wall-normal pressure gradients

We initially present the global distribution of static pressure in the passage at mid-span, and then compare the magnitudes of pressure gradients in these two directions.

In our experiment, only the static pressures on the blade suction side were measured directly, but the static pressures in the whole passage were not. From the comparison between the experimental and numerical results of C_p (shown in Fig. D.2), the numerical results simulate properly the pressure distributions on both blade sides at mid-span. Therefore we can use the numerical results of FLUENT with the S-A turbulence model as a reference of the static pressure distribution in the passage at mid-span (see Fig. 5.2). The streamwise static pressure in the TBL decreases generally in the region near the leading edge where the flow accelerates, and then increases in the latter part. At the same time, the wall-normal static pressure increases generally from the suction side to the adjacent pressure side.

Besides the global view of the static pressure in the passage, we also want to compare the magnitudes of pressure gradients in the two directions. In the following part of this subsection, these two pressure gradients will be introduced and compared with each other at the same positions in the boundary layer on the suction side.

The streamwise pressure gradient $\partial C_p/\partial s$ can be represented by the pressure gradient on the blade suction side, which are deduced from the experiment results of the static pressure measured by the pressure taps on the blade and plotted in Fig. 5.3. The $\partial C_p/\partial s$ decreases at $0.10 < s^* < 0.24$ or $0.62 < s^* < 0.99$, and increases at $0.24 < s^* < 0.62$. The order of this streamwise pressure gradient is one.

For the wall-normal pressure gradients $\partial C_p/\partial n$, the numerical results are used. In order to be consistent with the measurements, the static pressure given by the CFD has been taken at

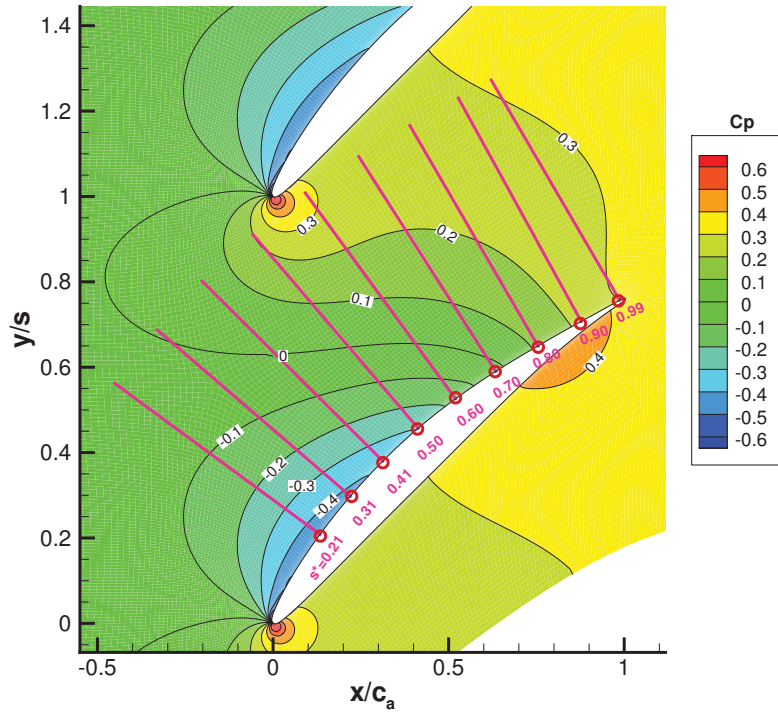


Figure 5.2: Numerical result of the contour of the static pressure at mid-span, $i=4^\circ$. CFD tool, FLUENT with the S-A turbulence model. Pink lines, LDA measurement stations. Red points, starting points on the suction side along LDA measurement stations.

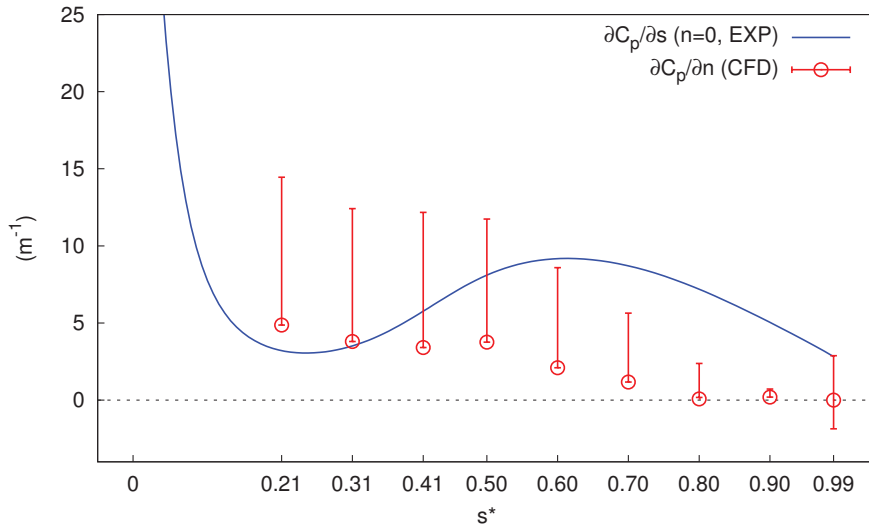
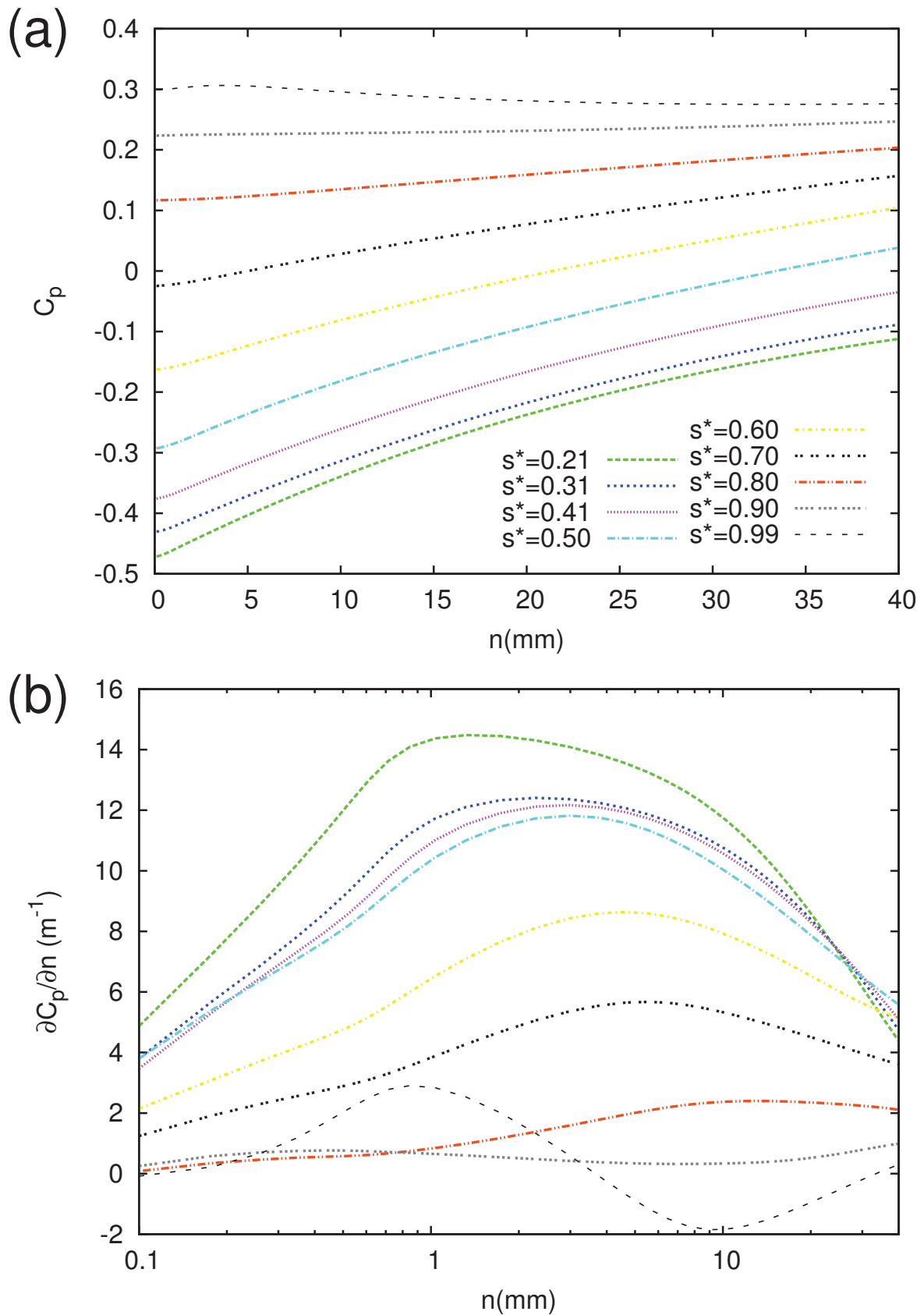


Figure 5.3: Streamwise and wall-normal pressure gradients on the blade suction side at mid-span, $i=4^\circ$. Blue curve line, experimental streamwise pressure gradient. Red lines, range of variation of these numerical wall-normal pressure gradients in the measurement stations. Red points, numerical wall-normal pressure gradients on the suction side at LDA measurement stations.



the LDA measurement stations. This corresponds to the red line in Fig. 5.2. The wall-normal pressure gradient presented in Fig. 5.4 are calculated at those locations. In this figure, the horizontal axis of the second sub-figure is in logarithmic form, in order to show more clearly the development of $\partial C_p/\partial n$ near the suction side. The $\partial C_p/\partial n$ are also shown in Fig. 5.3, in which the red line indicates the range of $\partial C_p/\partial n$ and the red point indicates the value at the point on the suction side at each measurement station. The development of $\partial C_p/\partial n$ in two different directions is discussed hereafter. One is along the suction side. In this direction, from the first to the last measurement station, the $\partial C_p/\partial n$ decreases from $s^*=0.21$ to $s^*=0.31$ and then keep approximately constant until $s^*=0.50$, following by a decrease until $s^*=0.80$ and then keeping approximately equalled to zero until $s^*=0.99$. The other one is normal to the suction side at each measurement station. At $s^*=0.21\sim 0.80$, the static pressures monotonically increase, leading to wall-normal positive pressure gradients (PPGs). At $s^*=0.90$, the static pressure keeps nearly constant, leading to approximately null wall-normal pressure gradient. At $s^*=0.99$, the static pressure firstly increases and then decreases gradually, as a result the wall-normal pressure gradient is positive in the inner part ($0.00\text{ mm} < n < 5.00\text{ mm}$) and negative in the outer part ($n > 5.00\text{ mm}$).

In summary, the TBL on the suction side at mid-span suffers from the streamwise APG and wall-normal PPG. The results can be divided into two parts. In the former part ($s^*=0.21\sim 0.50$), they have the same order of magnitude. In the latter part ($s^*=0.60\sim 0.99$), the wall-normal PPG is larger than the streamwise APG.

5.3.2 Curvature

The curvature of the blade suction side have be presented in Fig. 3.6 in Section 3.1. The blade suction side is convex where $0 < s^* < 0.94$, and is concave where $0.94 < s^* < 1$. Additionally the magnitude of K are large relatively in the former part where $0 < s^* < 0.70$ and is small relatively in the latter part where $0.70 < s^* < 1.00$.

The parameter $K\delta$ (δ , the thickness of boundary layer) could represent the order of the effects of curvature on the boundary layer properties (Patel & Sotiropoulos, 1997). Our experimental value at each measurement station are shown in Fig. 5.5, in which the value of δ will be introduced in Section 5.6. The curvatures are convex except at the last measurement station ($s^*=0.99$). The magnitude of $|K\delta|$ increases and then decreases, with the maximum value of 0.01889 at $s^*=0.60$. The magnitudes of $|K\delta|$ have the order of 0.01, which are generally regarded as weak curvature according to Patel & Sotiropoulos (1997).

According to Eq. 5.2, the effects of wall-normal pressure gradient and curvature can be represented by the term $\frac{U_s^2}{R}$ and $\frac{1}{\rho} \frac{\partial P}{\partial n}$, respectively. In order to compare the magnitudes of these two effects in Fig. 5.6, the wall-normal pressure gradient is compared with the parameter

$$K' = \frac{-K\rho_\infty U_{pw}^2}{P_{t\infty} - P_{s\infty}} \quad (5.3)$$

where U_{pw} is the potential flow velocity and will be introduced in Section 5.6. The effect of curvature is generally larger than that of wall-normal pressure gradient, especially in the former part where $0 < s^* < 0.70$. Therefore in our experiment the curvature does influence the boundary layer at mid-span.

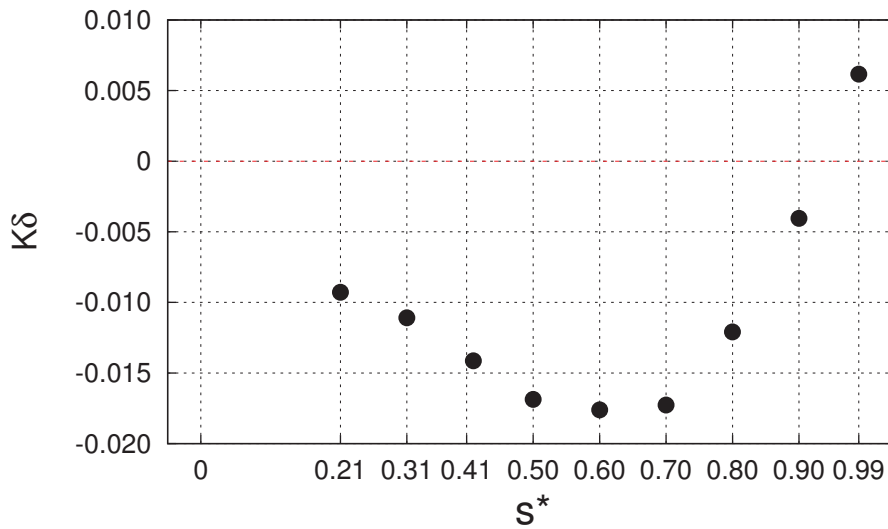


Figure 5.5: Values of $K\delta$ at LDA measurement stations.

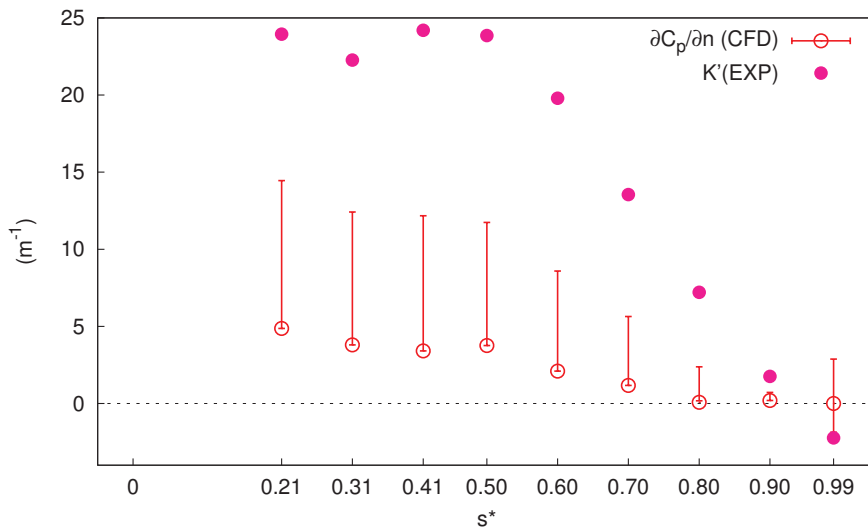


Figure 5.6: Effects of wall-normal pressure gradient and curvature at mid-span, $i=4^\circ$.

5.4 Mean velocity profiles

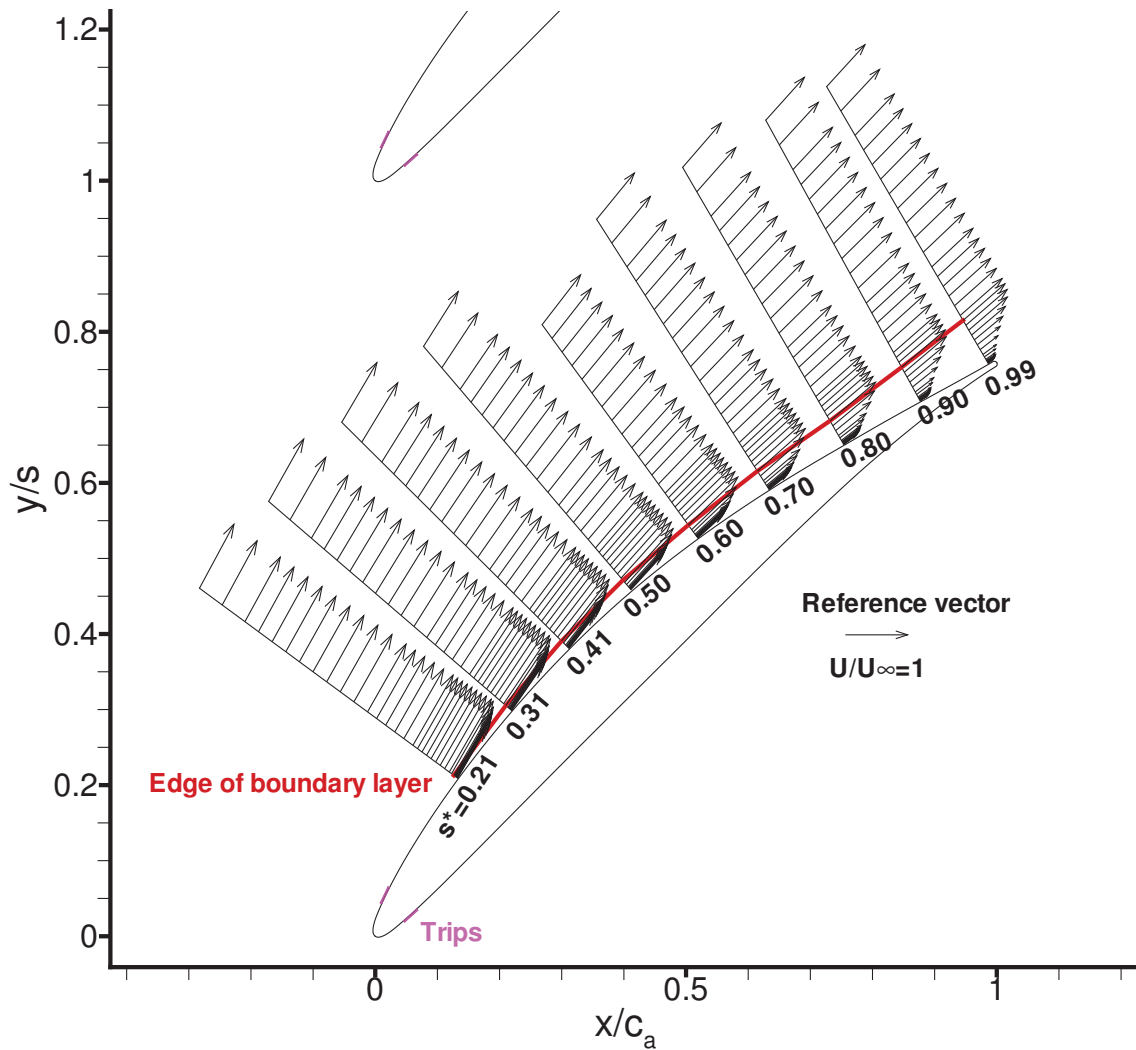


Figure 5.7: Experimental results of mean velocity vector \vec{U}/U_∞ at mid-span, $i=4^\circ$. Red solid line, the edge of the boundary layer by connecting every point where the mean velocity is largest at its measurement station.

In order to show the global view of the flow field in the passage at mid-span, the mean velocity vectors are shown in Fig. 5.7. In the vicinity of the suction side, the flow generally decelerates along the blade surface from the first to the last measurement stations. Even at the last measurement station, the streamwise velocity is much larger than zero, i.e. the boundary layer is far from separation, which is in accordance with the experimental results of the backflow coefficients (they will be presented in the next section).

The mean velocity components used in this chapter are the wall-tangential and wall-normal components U_s and U_n , respectively. U_s and U_n are also called streamwise and wall-normal velocities, respectively. For quantitative analysis, experimental U_s and U_n are shown together

in Fig. 5.8. To show more clearly the near wall region, the x-axes of Figs. 5.8b and 5.8c are in logarithmic form when $n < 10.00$ mm. This TBL decelerates along the blade surface and its momentum flux decreases very rapidly, mainly due to the effects of the streamwise pressure gradient. This phenomenon is similar to the traditional TBL on a flat-plate or an airfoil that only suffers a streamwise APG in the literature.

The numerical U_s are shown in Fig. 5.8b. The numerical tool is FLUENT with the S-A turbulence model. At each measurement station, the numerical U_s has the same trend as the experimental results. However, the positions of the points where the velocities have their local maximum value are not the same, neither the local maximum values. This local maximum value is noted as U_{max} and the distance from the corresponding point to the suction side is noted as n_{max} . At each measurement station, the numerical result of U_{max} is generally smaller than the experimental result; and the numerical result of n_{max} is generally larger than the experimental result. At each measurement station, the numerical U_s are much larger than the experimental ones in the boundary layer; they are nearly equivalent outside of the boundary layer. Another numerical velocity component U_n are also shown in Fig. 5.8c. Not similar to U_s , the differences between numerical and experimental U_n are obviously not only in the boundary layer but also outside of the boundary layer at each measurement station. Particularly, in the boundary layer generally where $n < 10.00$ mm, the numerical U_n are negative whereas the experimental U_n are positive.

The comparisons between experimental and numerical values of U_s and U_n indicate that the used CFD underestimates the influence of streamwise pressure gradient $\partial C_p / \partial s$ and overestimates the influence of wall-normal pressure gradient $\partial C_p / \partial n$, especially in the boundary layer. They need to be improved in the future work.

In order to show the developments of different parameters at the same measurement station, these parameters including mean velocities are also shown in Fig. 5.9. This figure will be discussed below.

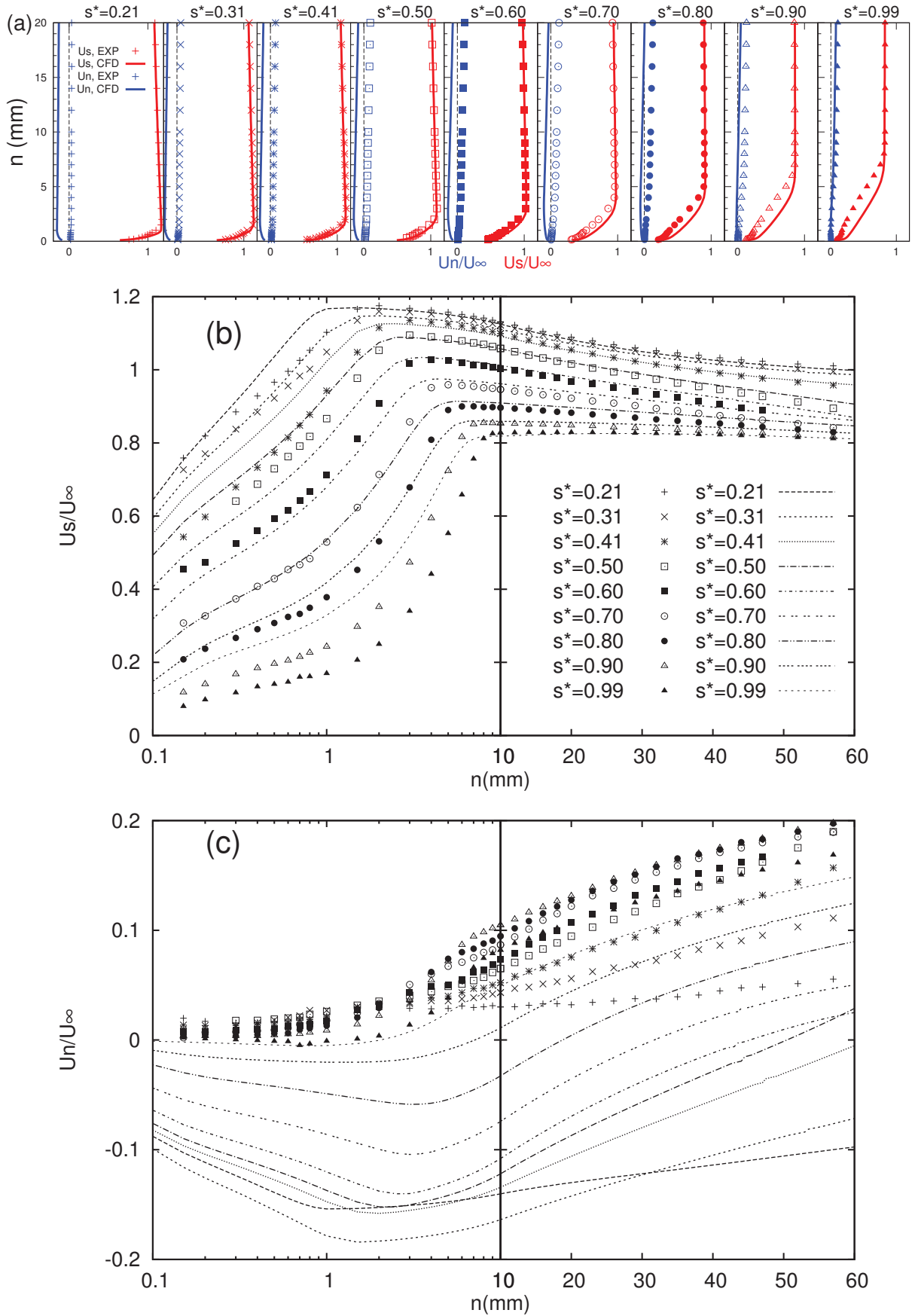


Figure 5.8: Experimental and numerical results of mean velocity at mid-span, $i=4^\circ$. Numerical tool, FLUENT with the S-A turbulence model. (a) U_s with red colour, U_n with blue colour; (b) U_s ; (c) U_n .

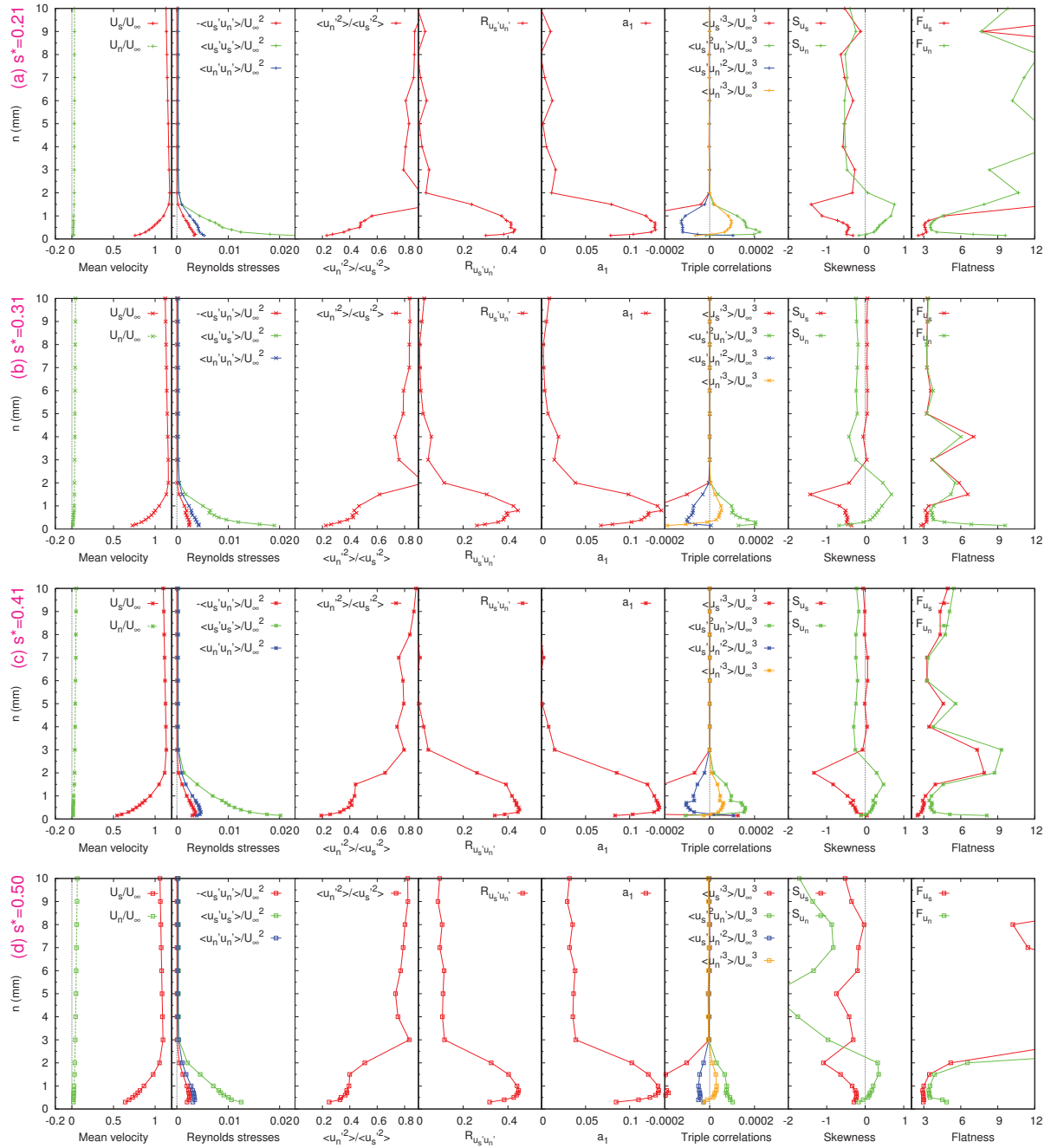


Figure 5.9: Experimental results shown together at each measurement station, $s^* = 0.21 \sim 0.50$.

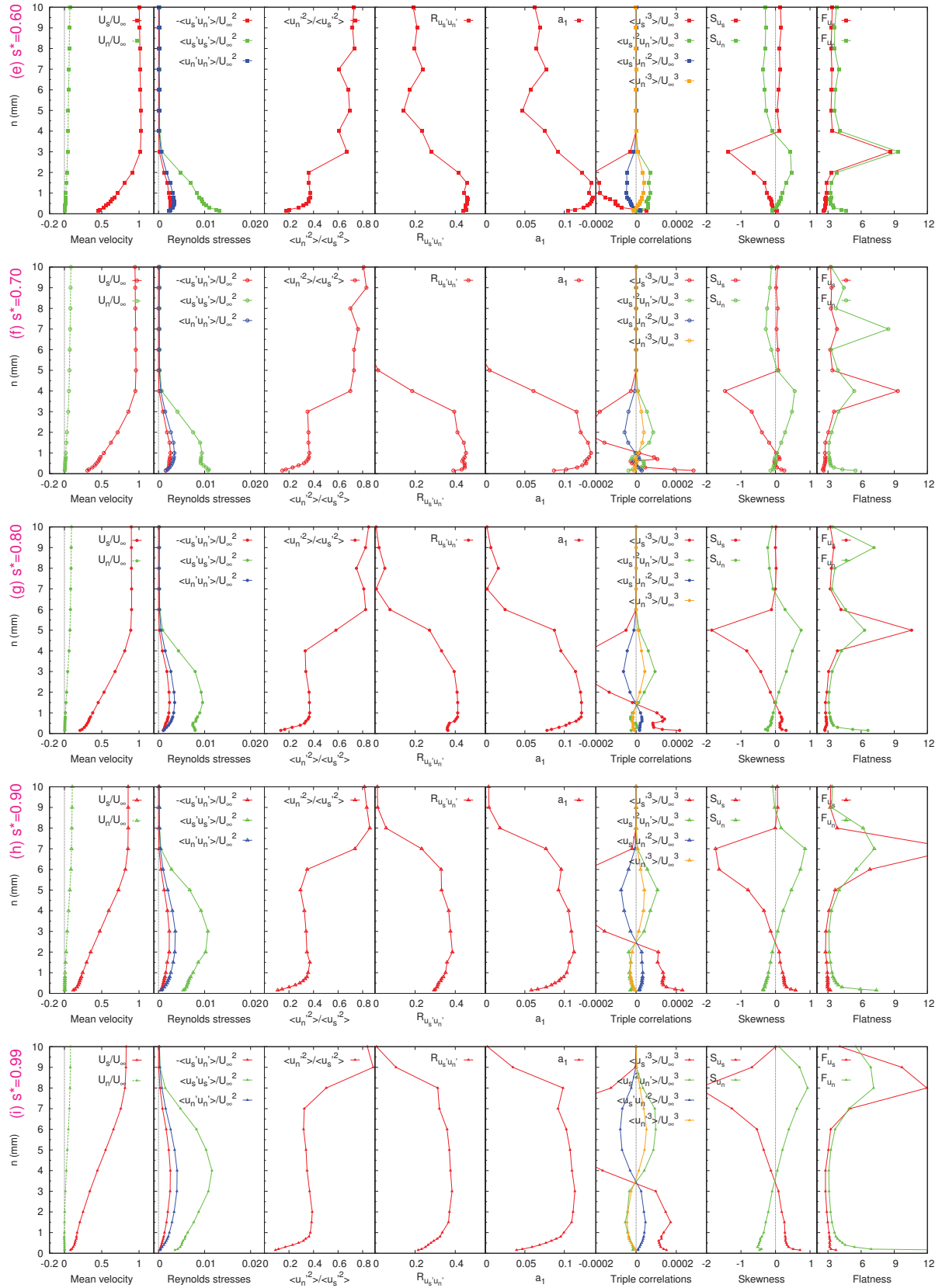


Figure 5.9: Experimental results shown together at each measurement station, $s^*=0.60\sim 0.99$.

5.5 Backflow coefficient and histogram of velocity

Backflow percent coefficient is a quantitative parameter to show the state of the boundary layer on the suction side at mid-span. In this thesis, backflow coefficients are defined by two different ways. In order to distinguish them, they are called the first and the second backflow coefficient η_1 and η_2 , and are defined by the Eq. 3.78 and Eq. 3.79 respectively. η_1 indicates the frequency percent of the backflow, whereas η_2 indicates the magnitude percent of the backflow.

In the literature, η_1 has been used by Simpson et al. (1981a; 1981b) to describe the turbulent separation process of 2D TBLs, as shown in Fig. 5.10. They claimed that incipient detachment occurs when the instantaneous backflow reaches 1%; intermittent transitory detachment occurs when the instantaneous backflow reaches 20%; transitory detachment occurs when the instantaneous backflow reaches 50%, and detachment occurs when the time-averaged wall shearing stress $\tau_w=0$.

In our experiment, the first and second backflow coefficients of the streamwise velocity have been calculated at mid-span and are shown in Fig. 5.11. In Fig. 5.11a, there is no point in $s^*=0.21\sim 0.70$. This means that $\eta_1 < 0.0001$ at these measurement stations. In Fig. 5.11b, there is also no point in $s^*=0.21\sim 0.80$. This means that $\eta_2 < 0.0001$ at these measurement stations. Therefore both the η_1 and η_2 increase with the distance from the surface at each measurement station, and increase also from the leading edge to the trailing edge at the same distance from the suction side. Both of these two backflow coefficients reach respectively their maximum value at the point ($s^*=0.99$ & $n=0.15$ mm). Their maximum values $\eta_1=0.055$ and $\eta_2=0.012$, which are much smaller than 1.0. According to the separation process of TBLs proposed by Simpson et al. (1981a,b), this TBL at mid-span is still in the state of incipient detachment even at the trailing edge. The turbulence boundary layer under investigation here is thus far from the state of separation.

Besides the backflow coefficients, histogram of velocity can also be used to show the state of the boundary layer. In the literature, bimodal histograms that have two peaks usually occur within the intermittent reverse flow region and associate with two different physical modes (e.g. Hobson et al., 1998; Simpson, 1996). A typical velocity histogram at point $s^*=0.99$ & $n=0.15$ mm is shown in Fig. 5.12. At this point both of the first and the second backflow coefficients reach their maximum value, which have been discussed in the preceding paragraph. Only one peak occurs in this histogram. Moreover, after checking the velocity histograms at all points at mid-span, bimodal histogram does not exist in the present TBL. Thus two physical modes do not exist in this TBL on the suction side at mid-span.

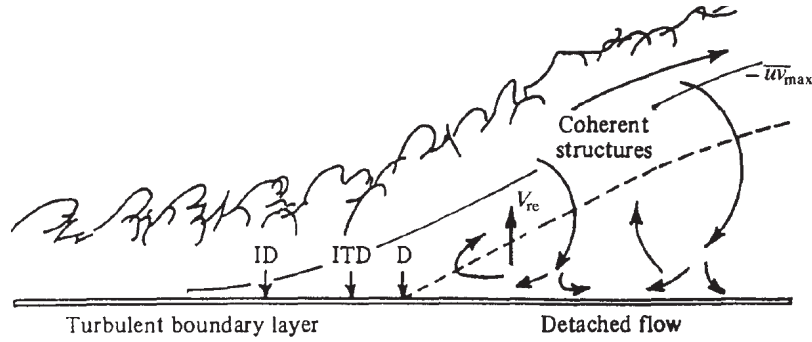


Figure 5.10: Separation process of TBLs proposed by Simpson et al. (1981a; 1981b): incipient detachment (ID), $\eta_1=0.01$; intermittent transitory detachment (ITD), $\eta_1=0.20$; transitory detachment (TD), $\eta_1=0.50$; detachment (D), $\tau_w=0$. The dashed line denotes $U=0$ locations, the solid line denotes maximum turbulent shear locations, V_{re} denotes the mean re-entrainment velocity along $U=0$.

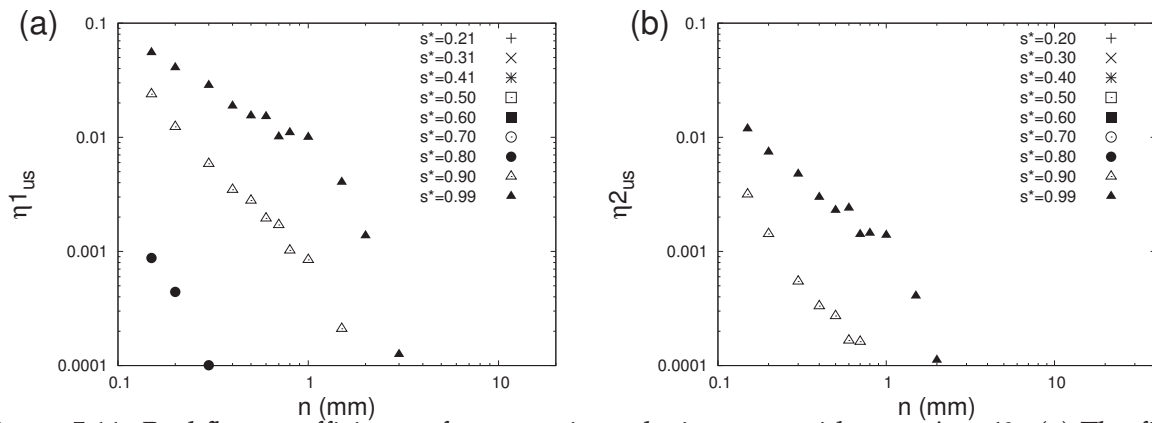


Figure 5.11: Backflow coefficients of streamwise velocity u_s at mid-span, $i = 4^\circ$. (a) The first backflow coefficient; (b) the second backflow coefficient.

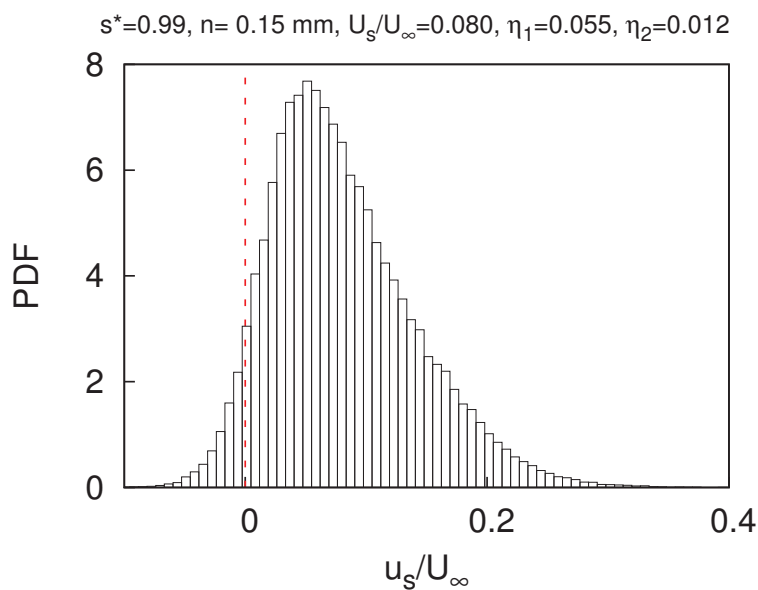


Figure 5.12: Example of histogram of streamwise velocity u_s at the point $s^*=0.99$ & $n=0.15$ mm.

5.6 Boundary layer thicknesses and shape factors

Table 5.1: Characteristic parameters of boundary layer.

s^*	0.21	0.31	0.41	0.50	0.60	0.70	0.80	0.90	0.99
x/c_a	0.13	0.22	0.31	0.41	0.51	0.63	0.75	0.89	0.99
$K(\text{m}^{-1})$	-5.044	-4.738	-5.237	-5.354	-4.722	-3.467	-1.972	-0.513	0.671
U_e/U_∞	1.176	1.160	1.135	1.095	1.027	0.959	0.900	0.855	0.828
U_{pw}/U_∞	1.187	1.175	1.155	1.114	1.048	0.977	0.914	0.858	0.831
$\delta(\text{mm})$	1.84	2.34	2.70	3.15	3.73	4.98	6.13	7.90	9.18
$K\delta$	-0.00928	-0.01109	-0.01114	-0.01687	-0.01761	-0.01727	-0.01209	-0.00405	0.00616
$\delta^*(\text{mm})$	0.20	0.24	0.41	0.42	0.70	1.13	1.70	2.62	3.63
$\theta(\text{mm})$	0.15	0.18	0.28	0.29	0.45	0.66	0.88	1.15	1.45
$\delta_3(\text{mm})$	0.26	0.32	0.48	0.50	0.76	1.07	1.39	1.77	2.21
H_{12}	1.343	1.351	1.478	1.455	1.549	1.732	1.942	2.269	2.499
H_{23}	0.568	0.569	0.585	0.586	0.596	0.615	0.632	0.652	0.657
H_{32}	1.760	1.757	1.710	1.706	1.677	1.626	1.581	1.534	1.521
H	0.928	0.922	0.863	0.858	0.830	0.791	0.765	0.745	0.740
$u_\tau\text{-LT (m/s)}$	2.552	2.438	2.043	2.005	1.662	1.292	0.999	0.714	0.563
$u_\tau\text{-fit(m/s)}$	2.400	2.200	1.880	1.800	1.540	1.200	0.910	0.650	0.500
$\text{Re}_\theta = \theta U_{pw}/\nu$	445	541	824	825	1202	1630	2041	2524	3076
P^+	0.002	0.003	0.010	0.020	0.034	0.069	0.124	0.231	0.447
β	0.068	0.117	0.495	0.956	2.353	6.009	12.232	25.038	51.640
Λ	0.070	0.104	0.221	0.445	0.404	0.352	0.235	0.148	0.116

Constants: $c_a=0.110$ m, $U_\infty=40.0$ m/s, $\nu=1.57 \times 10^{-5}$ m²/s.

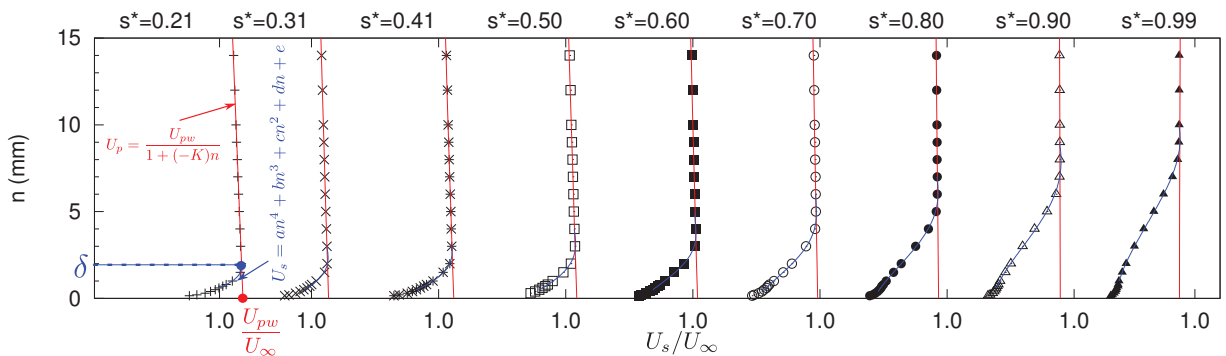


Figure 5.13: Illustration of the methods to determine the thickness of boundary layer and the potential flow velocity.

In the traditional TBL, the streamwise velocity increases until its maximum value that usually equal to the outer velocity. Consequently, the thickness of the boundary layer (δ) is traditionally defined as the distance from the wall to the position where the velocity reaches a certain percentage (for example 99%) of the outer velocity. However, in our experiment U_s decreases slowly after reaching a local maximum value at each measurement station, due to the existence of the wall-normal pressure gradient. Therefore, δ cannot be determined by the traditional method. In order to determine δ at each measurement station in our experiment, firstly the velocity profile near the boundary layer is fitted by a polynomial of fourth degree. Then we define δ as the distance from the wall to the position where the velocity is a local maximum. This method is illustrated in Fig. 5.13.

By connecting every point where the mean velocity is maximum at its measurement station, the red solid line in Fig. 5.7 shows the edge of the boundary layer, which is very thin. The displacement thickness δ^* , the momentum thickness θ and the energy thickness δ_3 are then calculated using the method mentioned by Patel & Sotiropoulos (1997), illustrated in Fig. 5.13. The solid lines correspond to a potential flow velocity distribution according to

$$U_p = \frac{U_{pw}}{1 + (-K)n} \quad (5.4)$$

where U_{pw} is the potential flow velocity at the wall (also see Fig. 5.13), and K is the curvature of the suction side (see Fig. 3.6). The integral thicknesses of the boundary layer should be defined by comparison of the viscous flow with the inviscid flow. Thus the proper definitions of the displacement (δ^*), the momentum (θ) and the energy thicknesses (δ_3) are

$$\int_0^{\delta^*} U_p dn = \int_0^{\delta} (U_p - U_s) dn \quad (5.5)$$

$$\int_0^{\theta} U_p^2 dn = \int_0^{\delta} U(U_p - U_s) dn \quad (5.6)$$

$$\int_0^{\delta_3} U_p^3 dn = \int_0^{\delta} U_s(U_p^2 - U_s^2) dn \quad (5.7)$$

According to Eq. 5.4, Eqs. 5.5~5.7 give

$$\frac{\ln[1 + (-K)\delta^*]}{(-K)} = \int_0^{\delta} \left(\frac{U_p - U_s}{U_{pw}} \right) dn \quad (5.8)$$

$$\frac{\theta}{1 + (-K)\theta} = \int_0^{\delta} \frac{U_s}{U_{pw}} \left(\frac{U_p - U_s}{U_{pw}} \right) dn \quad (5.9)$$

$$\frac{\delta_3[(-K)\delta_3 + 2]}{2[(-K)\delta_3 + 1]^2} = \int_0^{\delta} \frac{U_s}{U_{pw}} \left(\frac{U_p^2 - U_s^2}{U_{pw}^2} \right) dn \quad (5.10)$$

Because of $(-K)\delta^* \ll 1$ and $(-K)\theta \ll 1$, we have

$$\delta^* \approx \int_0^{\delta} \left(\frac{U_p - U_s}{U_{pw}} \right) dn \quad (5.11)$$

$$\theta \approx \int_0^{\delta} \frac{U_s}{U_{pw}} \left(\frac{U_p - U_s}{U_{pw}} \right) dn \quad (5.12)$$

$$\delta_3 \approx \int_0^{\delta} \frac{U_s}{U_{pw}} \left(\frac{U_p^2 - U_s^2}{U_{pw}^2} \right) dn \quad (5.13)$$

Some of the foregoing parameters have been calculated using our experimental data, and listed in Table 5.1. Expectably, the experimental U_e/U_∞ decreases throughout the boundary layer. In addition, experimental δ , δ^* , θ and δ_3 (see also in Fig. 5.14) increase slowly at $0.21 < s^* < 0.60$ and then increase rapidly in a mostly linear way at $0.70 < s^* < 0.99$.

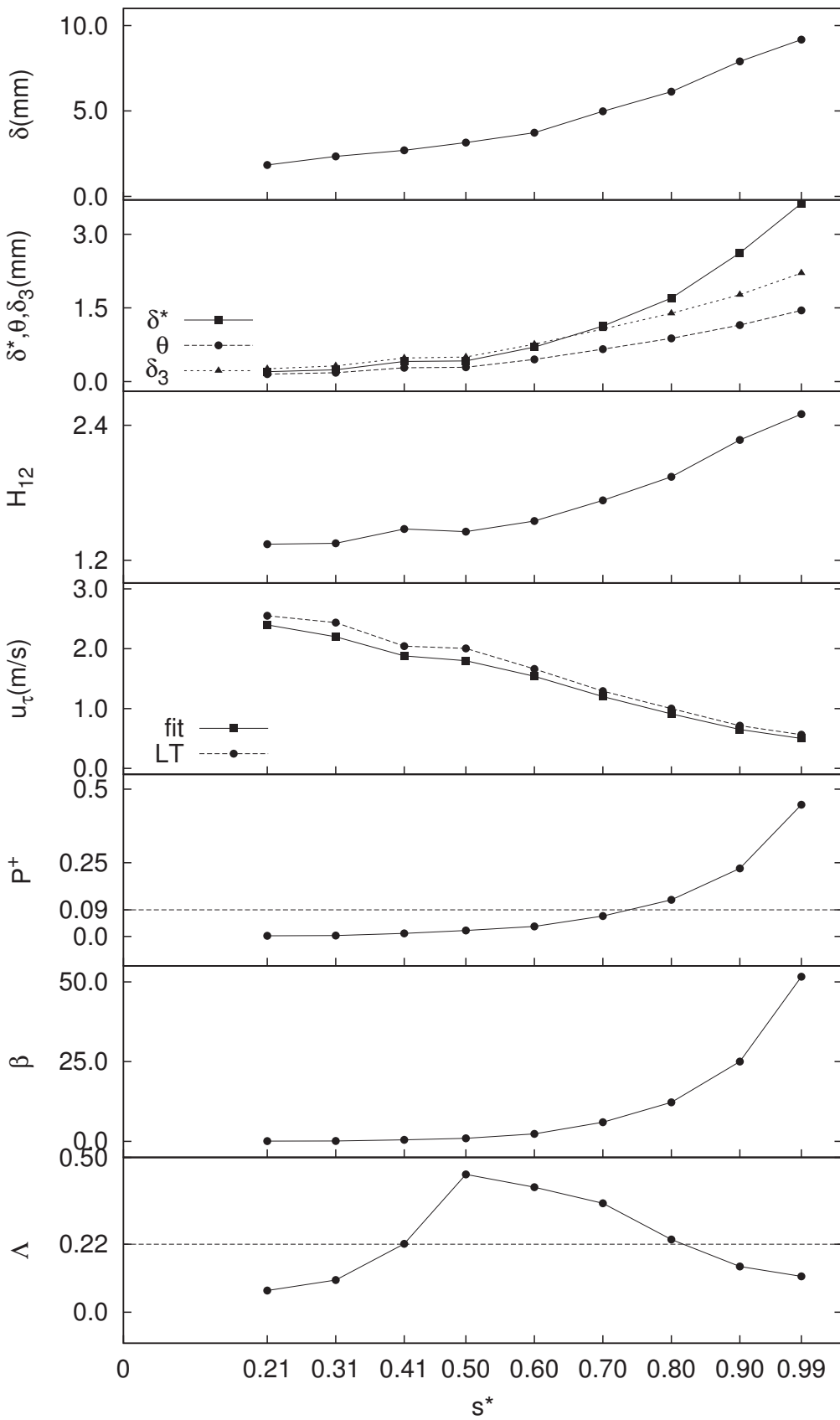


Figure 5.14: Boundary layer parameters. Lines for visual aid only.

Besides the thicknesses of boundary layer, three shape factor H_{12} , H_{23} and H_{32} are usually used to show the properties of boundary layers, and are defined as

$$H_{12} = \delta^* / \theta \quad (5.14)$$

$$H_{23} = \theta / \delta_3 \quad (5.15)$$

$$H_{32} = \delta_3 / \theta = 1 / H_{23} \quad (5.16)$$

The values of shape factors H_{12} , H_{23} and H_{32} , which have been investigated by many researches in the literature, vary considerably when separation occurs. This is because the shape factors are influenced by many factors, for instance the Reynolds number, the free-stream turbulence intensity and the boundary layer type.

In order to find a more reliable separation criterion, it is necessary to define another shape factor that fluctuates much less than H_{12} , H_{23} and H_{32} . For example, [Truckenbrodt \(1973\)](#) introduced a modified shape factor (reviewed by [Schlichting \(1979, pp.674-675\)](#))

$$H = \exp \left(- \int_{(H_{23})_{\infty}}^{H_{23}} \frac{dH_{23}}{(H_{12} - 1)H_{23}} \right) \quad (5.17)$$

The reference value $(H_{23})_{\infty}$ has been chosen as the lower limit of integration, because it represents an average value for flows without a pressure gradient. In addition, $H=1$ when $H_{23}=(H_{23})_{\infty}$. [Schlichting \(1979, p.674\)](#) reviewed that H varies with the sign of the pressure gradient: $H=1$ for ZPG, $H<1$ for APG, and $H>1$ for FPG. This implies that APG inclines to decrease the shape factor H , whereas FPG inclines to increase the shape factor H . [Schlichting](#) also reviewed the values of H when separations occur in the literature, and then suggested that the range $0.723 \leq H \leq 0.761$ describes velocity profiles that are prone to separate. These conclusions about H are shown in Fig. 5.15. By reviewing the experimental boundary layers with pressure gradients at that time, [Schlichting \(1979, pp.674-675\)](#) claimed that there is a relation between H_{12} and H_{32} (as shown in Fig. 22.5 in his book) if the slight effect of Reynolds number is neglected, He then mentioned an empirical relation between these two shape factors,

$$H_{32} = \frac{4H_{12}}{3H_{12} - 1} \quad (5.18)$$

This empirical relation is based on the assumption of power-law velocity profiles such as

$$\frac{U}{U_e} = \left(\frac{y}{\delta} \right)^{1/c} \quad (5.19)$$

with c constant, y the distance to the wall surface. The power-law velocity profile when $c=7$, usually called "one-seventh power law", seems to be applicable widely to pipe flows. Substituting Eqs. 5.16 and 5.18 into Eq. 5.17, and the reference value $(H_{23})_{\infty}$ being chosen as 0.556

(the typical value when $c=7$ in Eq. 5.19), Truckenbrodt's shape factor can then be expressed as

$$H = 0.5694 \cdot H_{23} \left(\frac{H_{23}}{H_{23} - 0.5000} \right)^{0.5} \quad (5.20)$$

After adjusting the constants in Eq. 5.20 to represent the experiments available at the time of **Schlichting**,

$$H = 0.5442 \cdot H_{23} \left(\frac{H_{23}}{H_{23} - 0.5049} \right)^{0.5} \quad (5.21)$$

Eq. 5.21 has been used by **Bernard et al. (2003)**, who investigated a boundary layer on a bump with the streamwise pressure gradient and the curvature.

Our experimental H_{12} are listed in Table 5.1, shown in Fig. 5.14. They are larger than 1.3, the typical value for a TBL on a flat plane. In addition, the shape factor H_{12} keeps nearly constant at the former measurement stations ($s^*=0.21\sim 0.60$), and then increases until the last measurement station in the latter part ($s^*=0.70\sim 0.99$).

Our experimental H_{23} and H_{32} are also listed in Table 5.1. In addition, they are also shown in Fig. 5.16. Their relation is not in agreement with the empirical relation of Eq. 5.18 (also shown in Fig. 5.16). This means that the assumption of power-law velocity profiles (Eq. 5.19) no longer holds in our experiment, due to the pressure gradients and the curvature. Eq. 5.19 is based on the assumption that there is a relation between H_{12} and H_{32} . If this assumption is also valid in our experiment, it can be expressed as

$$H_{32} = \frac{3.72H_{12}}{2.86H_{12} - 1} \quad (5.22)$$

using a least-square fitting of the experimental results, also shown in Fig. 5.16. Our experimental expression of Truckenbrodt's shape factor H can then be derived by the similar procedure that to derive Eq. 5.20 from Eqs. 5.16 and 5.18. Substituting Eqs. 5.16 and 5.22 into Eq. 5.17, and the reference value $(H_{23})_{\infty}$ being chosen as 0.556 (this value will be discussed below), Truckenbrodt's shape factor in our experiment can then be expressed as

$$H = 0.5218 \cdot H_{23} \left(\frac{H_{23}}{H_{23} - 0.5000} \right)^{0.538} \quad (5.23)$$

According to this new expression, our experimental H can be calculated at each measurement station, also listed in Table 5.1 and shown in Fig. 5.15. As mentioned above, the value of "0.556" used in the derivation is only an assumption. $(H_{23})_{\infty}$ is originally defined as the value of H_{23} in the reference TBL with streamwise ZPG. In our experiment besides the streamwise pressure gradient, the boundary layer also suffers the curvature and the wall-normal pressure gradient. It is thus very difficult to identify the reference value $(H_{23})_{\infty}$. However, $(H_{23})_{\infty}$ does not influence the slope of the curve of H . It only influence the constant of "0.5218" in Eq. 5.23 and thus just the position of the curve of Eq. 5.23 in Fig. 5.15.

Surprisingly, the magnitudes of the mean slope of Eq. 5.23 and Eq. 5.21 are nearly the same (see Fig. 5.15). This means that the boundary layer in our experiment is similar to that with only the streamwise APG, about the degree of separation. In addition, our experimental values of H at $s^*=0.90$ is equal to 0.740, and is in the range of $0.723 \leq H \leq 0.761$ when separations are prone to occur suggested by Schlichting (1979). However, the velocity profile at this measurement station is not yet separated.

We could associate the development of the boundary layer in our experiment with three factors: the convex curvature (except the region near the trailing edge, where it is weakly concave), the streamwise APG and the wall-normal PPG. Patel & Sotiropoulos (1997) claimed that both the streamwise APG and the convex curvature incline to induce separation. Although the combined influence of these two factors is not a simple summation of their individual effects claimed by Smits & Wood (1985), this combined influence should be stronger than the separate influence of the streamwise APG. Therefore, the boundary layer should be more inclined to separate under the combined influence of these two factors. Furthermore, we could infer that the third factor, the wall-normal PPG (see Figs. 5.3 and 5.4b), restrains the separation. The criterion H for separation boundary layers should take into account the influence of wall-normal PPG, and thus reduces to a smaller value for the boundary layer studied in this chapter.

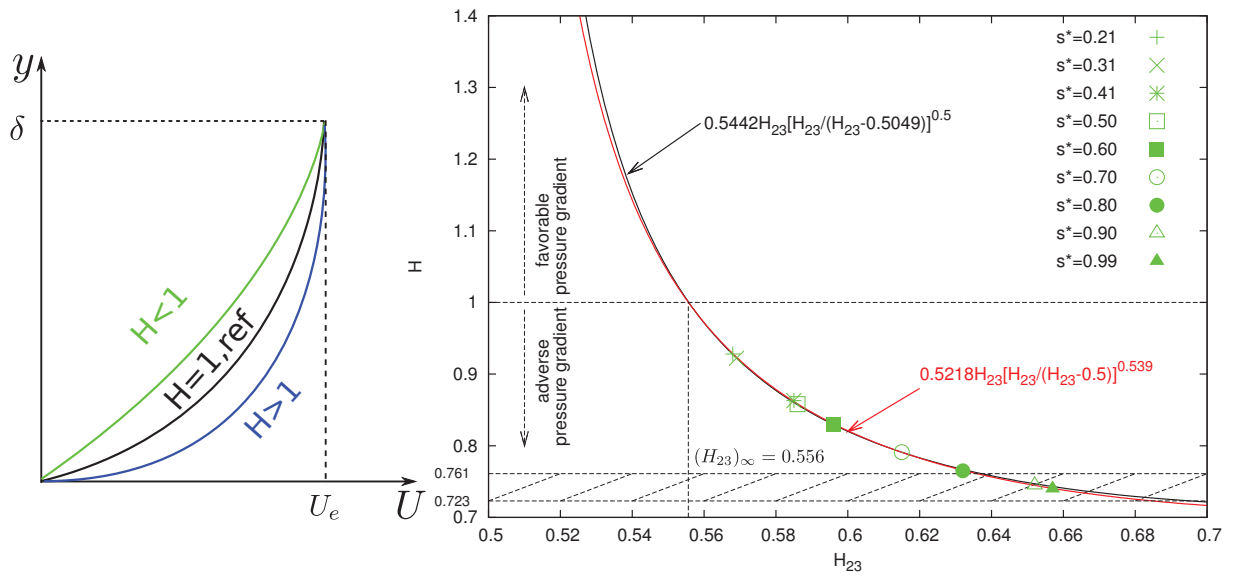


Figure 5.15: Relation between H_{23} and H .

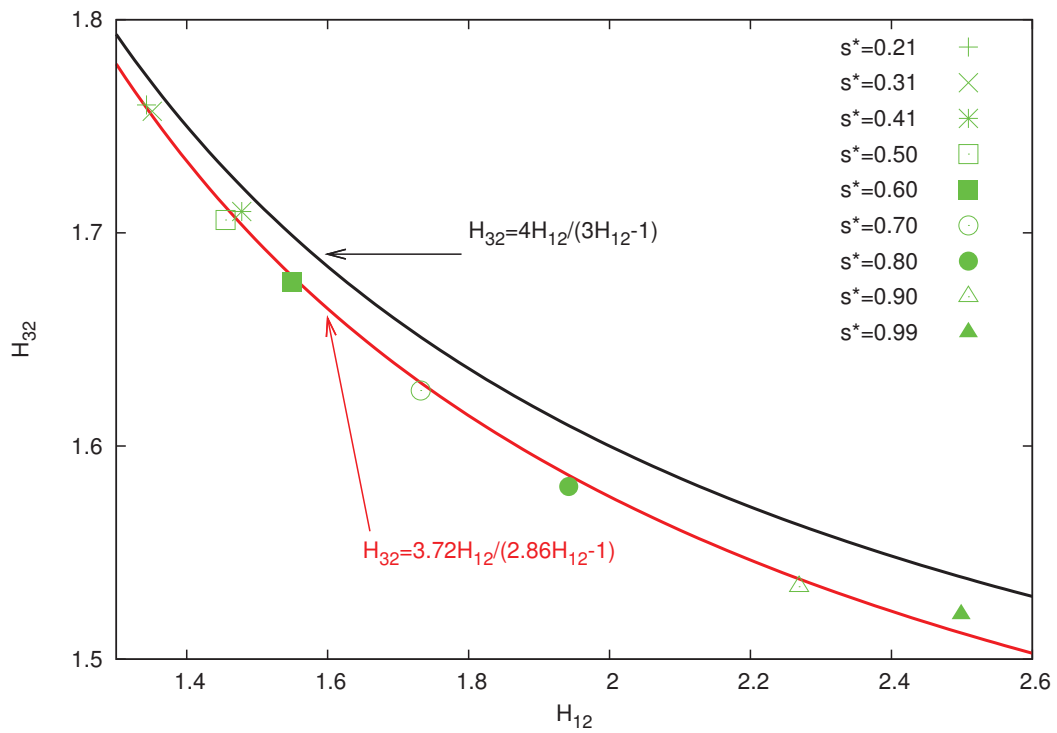


Figure 5.16: Relation between H_{12} and H_{32} .

5.7 Determinations of skin friction and friction velocity

Skin friction (C_f) and friction velocity (u_τ) are critical parameters in both experimental and numerical work. According to the relations

$$C_f = \tau_w / (1/2\rho U_e^2) \quad (5.24)$$

$$u_\tau = \sqrt{\tau_w / \rho} \quad (5.25)$$

friction velocity

$$u_\tau = U_e \sqrt{C_f / 2} \quad (5.26)$$

For a laminar boundary layer, the skin friction can be quite easily calculated theoretically, since we know the relation between velocity profile and shearing stress (Eq. 6.55 in P.159 of [Schlichting & Gersten \(1999\)](#)). For a TBL, however, the skin friction cannot be calculated theoretically, as such a relation is not established.

For pipes and channels, the wall friction can be determined with high accuracy from the pressure drop (typically <1% in u_τ). For boundary layer, the skin friction can be measured directly by two methods. The first method is the surface hot-film anemometry ([Bellhouse & Schultz, 1966](#); [Hodson *et al.*, 1994](#)). This method uses the films assembled on the surface, and then measures the wall shear stress at the sensor according to the heat transfer from the sensor. The second method is the oil-fringe imaging method ([Monson *et al.*, 1993](#); [Peterson & Plesniak, 2004](#)). This method relates the wall shear to the thinning rate of a line of oil placed on the surface. [Marusic *et al.* \(2010\)](#) claimed that the first method may be the best direct measurement method but its accuracy is still limited to no better than 1% to 2%, and it is also limited to gas flows and non rough surface conditions. The accuracy still needs to be improved, according to [Nagib *et al.* \(2007\)](#), because one ideally needs an accuracy of about 0.5% or better to draw definitive conclusions.

The skin friction can however be estimated indirectly, using a Log-law fit method. This indirect method estimates the skin friction by fitting the experimental velocity profile to the classical law of the wall, or “log law”,

$$U^+ = \frac{1}{\kappa} \ln(y^+) + B \quad (5.27)$$

where κ is the von Kármán constant, and B is the additive constant. The classical law of the wall has been reviewed in Section 2.3.1. This method is thus based on the assumption that a log-law region exists in the inner region of the TBL. Log-law fit is widely used in the literature

to determine the skin friction, even in experiments on curved surfaces or with flows suffering from pressure gradients. However this method has some disadvantages. First, the status of the law of the wall with the effects of the curvature or the pressure gradient remains unclear (Patel & Sotiropoulos, 1997). Second, the accuracy of this indirect method may be affected by the fact that the von Kármán constant κ is not a universal constant (Marusic *et al.*, 2010). From the classical view, κ was thought to be a universal constant (0.41). This has been challenged by considerable evidence. From the experiments summarized by Marusic *et al.* (2010), κ could change in a considerable range [0.37,0.421]. Marusic *et al.* also considered that κ depends on the flow conditions, such as flow types or boundary conditions; and how these parameters influence the von Kármán constant κ also needs to be investigated.

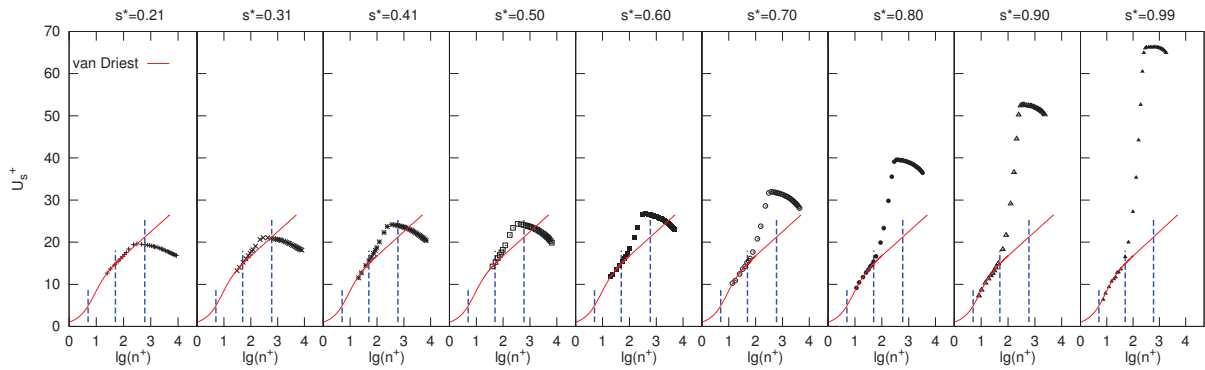
A second indirect method to estimate the skin friction is the use of empirical correlations, which are calculated from boundary layer parameters, such as the boundary layer thickness, the boundary layer shape factors or the Reynolds number. One of them is the so-called Ludwig-Tillmann empirical correlation (Ludwig & Tillman, 1950). This correlation fixes the skin friction coefficient from the Reynolds number based on the momentum thickness Re_θ and the shape factor H_{12} ,

$$C_f = 0.246Re_\theta^{-0.268}10^{-0.678H_{12}} \quad (5.28)$$

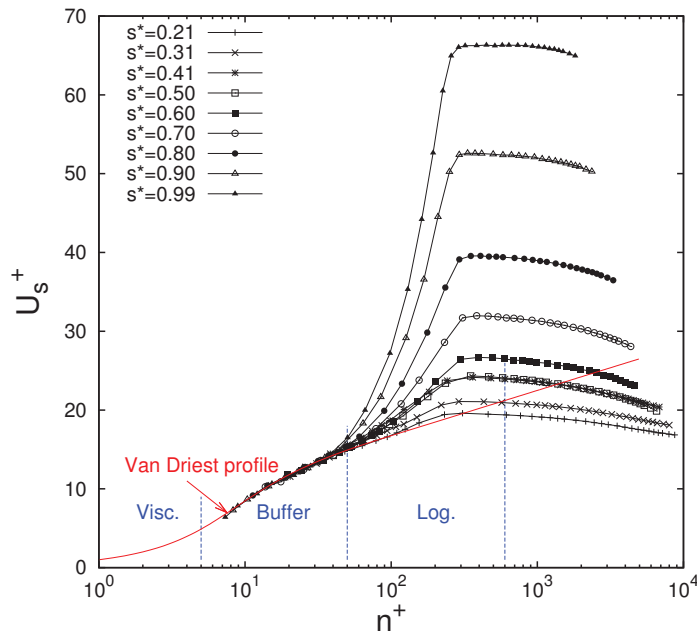
Piquet (2001, p.326) claimed that this empirical correlation may be safely used for $H_{12} < 2$ and for $Re_\theta > 10^3$ and produces acceptable results that agree with the measurement uncertainties until $H_{12} < 2.5$.

In our experiment the friction velocity was not directly measured. However, it has been estimated by using the two methods discussed above. We first derived the skin friction from a best fit to van Driest formula (Eq. 2.6) between $10 < n^+ < 50$. The second indirect method (Eq. 5.28) was also used, although the fact that some of the experimental H_{12} and Re_θ do not meet the requirements of this method. Indeed, the shape factor H_{12} in our experiment at the last measurement station is 2.58 (larger than 2.5) and Re_θ (listed in Table 5.1, shown in Fig. 5.14) is smaller than 10^3 at the former three measurement stations. The friction velocities of these two methods are listed in Table 5.1 and compared in Fig. 5.14. The first and the second methods are denoted as “fit” and “LT”, respectively. These two methods show the same trends in friction velocity. However, in comparison with the second method, the friction velocities of the first method are generally larger: 4.1% to 13.7% in the front part ($0.21 < s^* < 0.50$), and 2.5% to 6.4% smaller in the rear part ($0.60 < s^* < 0.99$). The skin friction and friction velocity used below were determined by the first indirect method, because of the limitation of using the second indirect method. Additionally, the friction velocity is just used for qualitative analysis due to its significant uncertainty.

5.8 Mean velocity profiles in inner coordinate and velocity defect profiles



(a) At each measurement station



(b) Plotted together

Figure 5.17: Mean velocity profiles in inner coordinate.

The skin friction and the friction velocity are already determined by indirect method discussed in the preceding section. Mean velocity profiles in inner coordinate and velocity defect profiles can then be obtained, as shown in Figs. 5.17.

The accuracy of the displacement device in the wall-normal direction to the blade surface made possible to acquire some data in the buffer layers at all measurement stations. The combined effects of the pressure gradients and the curvature appear mainly in the outer region, and reduce gradually the extend of the log region from the first to the last measurement stations. The wake region can be observed and is split into two parts, separated by an abrupt

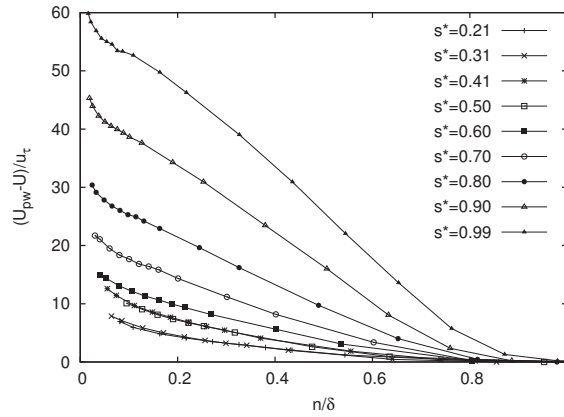


Figure 5.18: Velocity defect profiles. Lines for visual aid only.

change in the slope of the velocity profile. These data cannot provide definitive answers to the questions regarding the validity of the law of the wall, because we derived the skin friction as well as the friction velocity from the indirect method of the so-called log-law fit that is based on the existence of a log-law region. The experimental mean velocity defect profiles are shown in Fig. 5.18. These profiles do not collapse. This means that the traditional defect law is not applicable for this complex TBL.

5.9 Pressure gradient parameters

To represent the effect of pressure gradient and the state of a TBL with APG, there are a lot of pressure gradient parameters proposed in the literature. Some of these parameters will be introduced and calculated by using our experimental results.

The downstream development of a boundary layer depends both on the upstream history of the flow and on the local conditions. Based on this fact, Clauser (1954) defined an equilibrium boundary layer as one subjected to a constant force history and thus with a well-defined past. To evaluate the upstream history, he defined a pressure gradient parameter β .

$$\beta = \frac{\delta^*}{\tau_w} \frac{dp}{ds} \quad (5.29)$$

In this parameter, the pressure gradient is scaled by the wall shear stress τ_w and the displacement thickness δ^* . Clauser considered that the boundary layer is in equilibrium when β is maintained at a constant value. This means that the equilibrium boundary layer requires a changing pressure gradient since the displacement thickness and wall shear change as the flow develops in the pressure gradient. Our experimental β (listed in Table 5.1 and shown in Fig. 5.14) increases monotonically with s^* . This means that the TBL investigated here is far from equilibrium.

Patel (1965) investigated the effects of streamwise pressure gradient and suggested a pressure gradient parameter,

$$P^+ = \frac{1}{\rho} \frac{\nu}{u_\tau^3} \frac{dp}{ds} \quad (5.30)$$

He suggested that the threshold values for the onset of the processes of separation and relaminarization are $P^+=0.09$ and $P^+=-0.018$, respectively. Our experimental P^+ are listed in Table 5.1 and shown in Fig. 5.14. In our experiment, P^+ is always larger than 0.09 at the last three measurement stations ($s^*=0.80, 0.90, 0.99$). However, the average velocities do not separate in this region. This is not surprising, because P^+ only takes into account the effects of streamwise pressure gradient, but not the effects of the wall-normal pressure gradient and the curvature which cannot be neglected in our experiment.

Castillo & George (2001) investigated the TBLs with pressure gradient by using the equilibrium-type similarity analysis, and defined a pressure parameter

$$\Lambda = \frac{\delta}{\rho U_\infty^2} \frac{dp}{d\delta/ds} \quad (5.31)$$

They considered that Λ has a different fixed value for each case of zero ($\Lambda=0$), adverse ($\Lambda=0.22$) or favourable ($\Lambda=-1.92$) pressure gradients. Our experimental Λ (listed in Table 5.1 and shown in Fig. 5.14) are not always equal to 0.22, which is the value given for a TBL with APG. This may be due to the effects of the wall-normal pressure gradient and the curvature.

5.10 Reynolds stresses

In this section, the purpose is to present and interpret the developments of Reynolds stresses in our experiment. It is well known that the development of Reynolds stresses in a TBL shows both extensive effects of upstream flow and local effects (for example, the pressure gradient and the curvature). Thus we firstly investigate the individual effect of upstream flow in a TBL with ZPG. Secondly, the effect of APG is investigated by reviewing the investigations of TBLs with APG in the literature. Thirdly, we propose a new prediction of the development of Reynolds stresses under the combined effects of upstream flow and APG, based on the previous two steps. At last, our experimental results are presented and interpreted.

First of all, the effect of upstream flow in a TBL with ZPG is investigated using the DNS results of Schlatter & Örlü (2010), which contain extensive data in a large range of Reynolds number ($Re_\theta=670\sim 4060$)¹. The developments of Reynolds stresses are shown in Fig. 5.19. The two figures on the left are non-dimensionalized by the local friction velocity (u_τ) and the local

¹downloaded from <http://www.mech.kth.se/~pschlatt/DATA/>

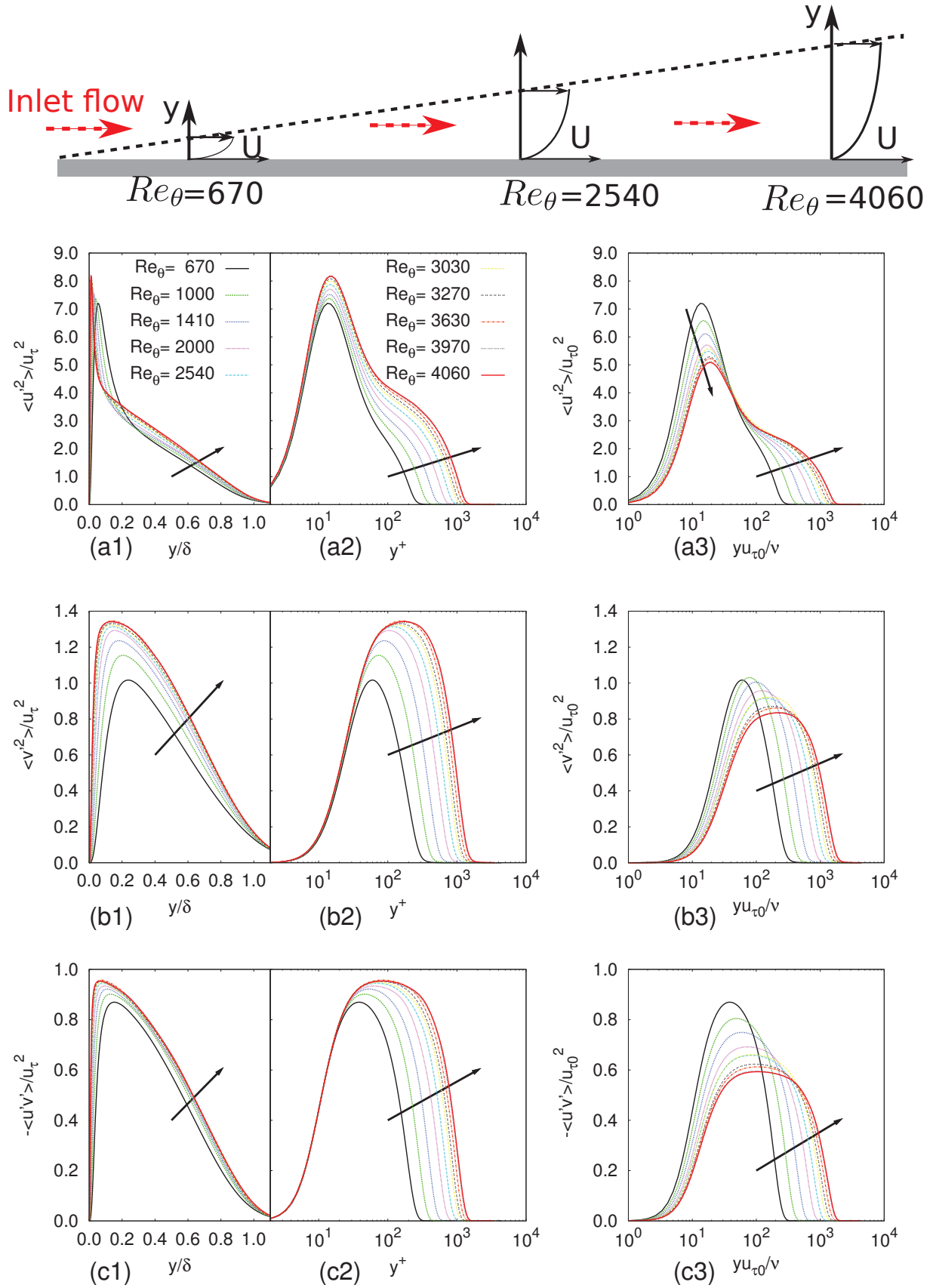


Figure 5.19: Developments of Reynolds stresses in a TBL with ZPG. DNS, from Schlatter & Örlü (2010). The arrows indicate the streamwise direction. Reference friction velocity $u_{\tau 0}$ is the friction velocity at the first line where $Re_\theta=670$.

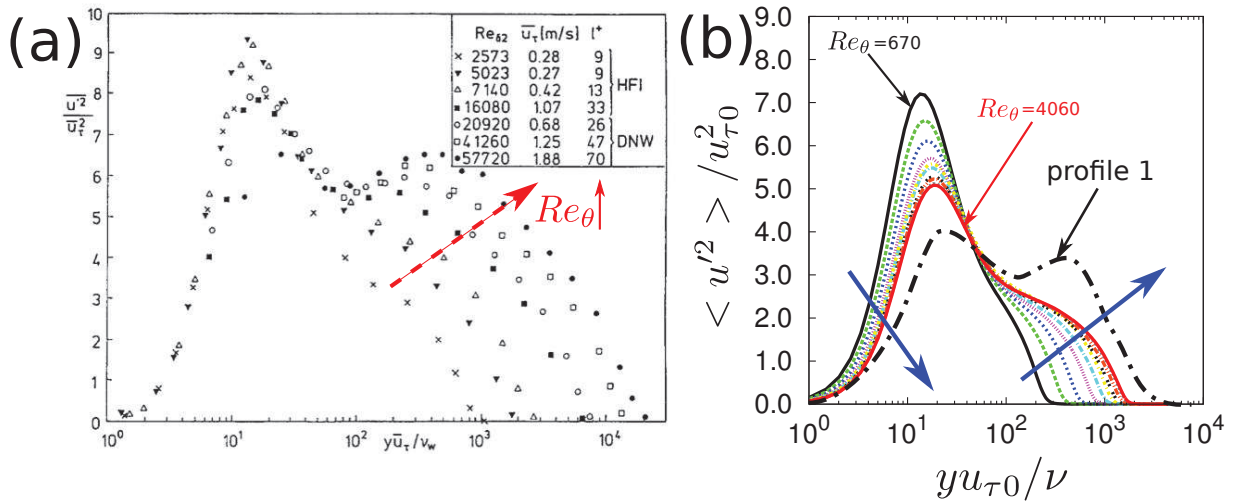


Figure 5.20: (a) Developments of Reynolds stresses $\overline{u'^2}/u_\tau^2$ with Re_θ in TBLs with ZPG, summarized by Fernholz & Finley (1996), also mentioned by the recent review of Marusic *et al.* (2010). (b) Effects of upstream flow on $\overline{u'^2}$, by adding profile 1 and profile 2 in Fig. 5.19a3. Blue arrows indicate the streamwise direction.

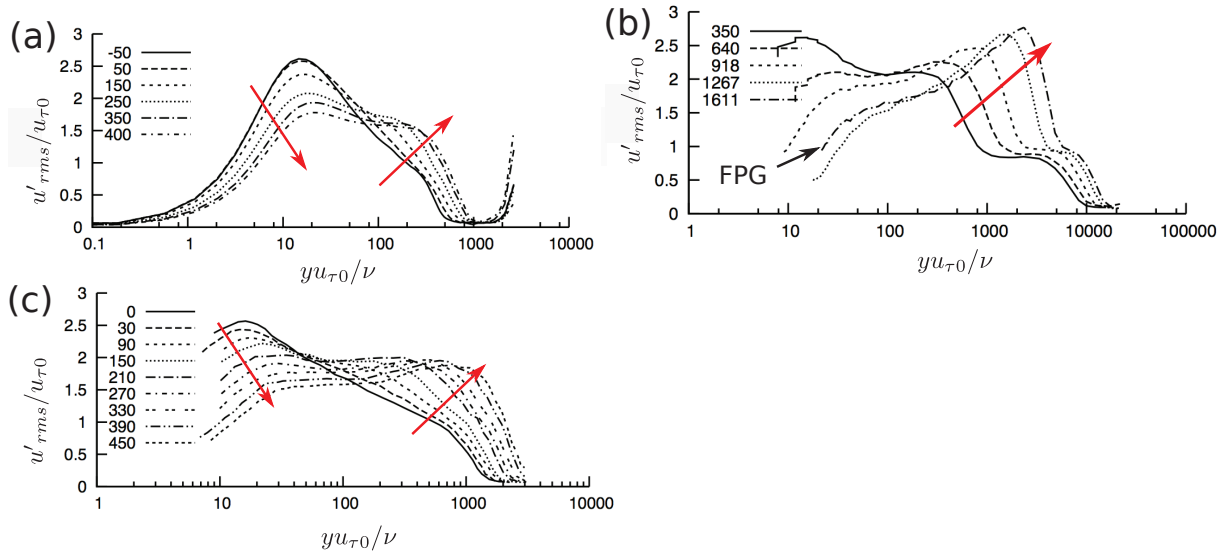


Figure 5.21: Development of $\overline{u'^2}$ in TBLs with APG. Experimental results, summarized by Shah *et al.* (2009). Red arrows indicate the streamwise direction. (a) DNS, $Re_\theta < 600$, Spalart & Watmuff (1993), (b) HWA, $Re_\theta = 7500 \sim 32000$ Bernard *et al.* (2003), (c) HWA, $Re_\theta = 1767 \sim 5705$, Materny *et al.* (2008). Reference friction velocity $u_{\tau 0}$ is the friction velocity at the reference measurement station at each measurement.

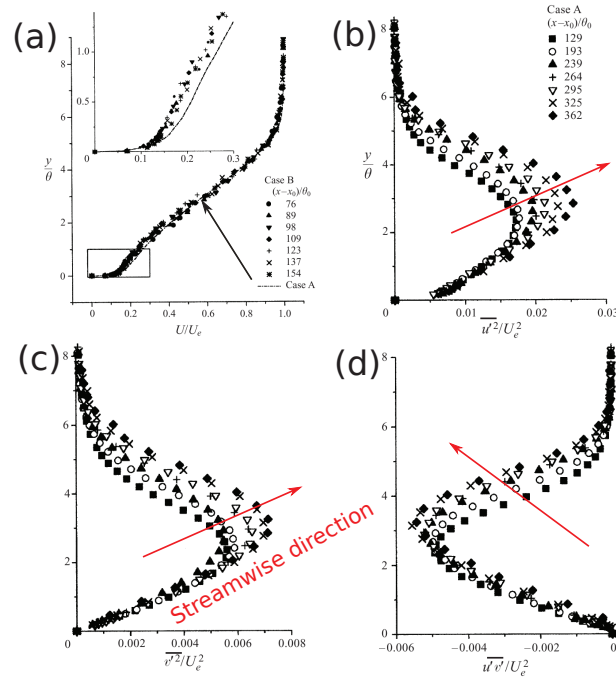


Figure 5.22: Developments of mean velocities and Reynolds stresses in a TBL with APG, from [Elsberry *et al.* \(2000\)](#). Red arrows indicate the streamwise direction. (a) mean velocity, (b) $\overline{u'^2}$, (c) $\overline{v'^2}$, (d) $\overline{u'v'}$.

thickness of the boundary layer (δ). The characteristics of these profiles have been introduced in section “Literature survey”. Here we only focus on the absolute evolutions. In Figs. 5.19(a3, b3 and c3), the reference friction velocity $u_{\tau 0}$ is the friction velocity at the reference station where $Re_{\theta}=670$. Therefore these figures show the absolute evolutions, through which we could see the effect of upstream flow.

For the streamwise development of $\overline{u'^2}$ (Fig. 5.19a3), the developments can be divided in to two parts, the inner and outer parts of the boundary layer. The inner part is the region where an inner peak exists. With the streamwise development, the absolute magnitude of $\overline{u'^2}$ at the inner peak decreases, and the location of the inner peak increases slightly. Outside the inner part is the outer part of the boundary layer. In the outer part the obvious phenomenon is that, with the streamwise development, the extent of the profile expands gradually and the amplitude of the profile decreases less rapidly. When Reynolds number increases, the appearance of an outer peak in the outer layer distribution of streamwise Reynolds stress have been reported by [Fernholz & Finley \(1996\)](#), as shown in Fig. 5.20a. This phenomenon has also be mentioned by the recent review of [Marusic *et al.* \(2010\)](#). The value at the outer peak is still smaller that at the inner peak. Additionally, the difference between the values at these two peaks decreases with Reynolds number. This trend can be represented by the “profile 1” in Fig. 5.20b with the DNS results discussed above.

The streamwise development of $\overline{v'^2}$ (Fig. 5.19b3) is different with that of $\overline{u'^2}$ (Fig. 5.19a3). In Fig. 5.19b3 with the streamwise development, the absolute magnitude of the inner peak

decreases, and the location of the inner peak increases slightly. At the same time, the extent of the high value region increases considerably; this is obviously different with that of $\overline{u'^2}$.

The streamwise development of $-\overline{u'v'}$ (Fig. 5.19c3) is similar to that of $\overline{v'^2}$ (Fig. 5.19b3). In summary, the effect of upstream flow on Reynolds stresses in a TBL with ZPG exists considerably, and therefore should be considered in the interpretation.

Besides the effect of upstream flow, we investigate the effect of APG on the Reynolds stresses by reviewing the investigations of TBLs with APG in the literature.

Shah et al. (2009) summarized the streamwise development of $\overline{u'^2}$ in TBLs with APG including experimental and numerical results in the literature. Some of their summarized cases are shown in Fig. 5.21. This figure shows the absolute evolution, because the velocity scale $u_{\tau 0}$ in this figure is defined as the value at the reference measurement station in each measurement. Fig. 5.21, especially the sub-figure 5.21a and 5.21c, shows clearly the history effect of the upstream flow (shown in Fig. 5.19a3). In a TBL with APG, a remarkable phenomenon, which has been extensively discovered and discussed in the literature, is that an outer peak occurs gradually and its location move away from the wall with the streamwise development, as those in Figs. 5.21b-c. *Shah et al. (2009)* considered that the outer peak is triggered by the APG. Soon after based on the observations of *Shah et al. (2009)*, *George et al. (2010)* did not agree with the interpretation of *Shah et al. (2009)*. Without detailed explanations, *George et al. (2010)* just claimed that the nature of the evolution and the position where the peak occurs depend on the upstream conditions and the imposed manner of the APG. Therefore the effect of APG needs to be studied further.

Because the outer peak already appears in TBLs with ZPG (see Fig. 5.20b) and the outer peak does not appear in TBLs with APG (e.g. Fig. 5.21a), therefore the APG is not the trigger for the appearance of the outer peak. In the TBL with APG of *Materny et al. (2008)*, the magnitude of streamwise Reynolds stress at the outer peak is already larger than that at the inner peak at the $Re_\theta < 5705$. Therefore we infer that the APG accelerates the appearance of the outer peak.

Besides in the profiles of $\overline{u'^2}$, the outer peaks are also found in the profiles of $\overline{v'^2}$ and $-\overline{u'v'}$ in TBLs with APG, for example *Elsberry et al. (2000)* (see Fig. 5.22) and *Skåre & Krogstad (1994)*.

Skåre & Krogstad (1994) examined an equilibrium TBL with APG, in which the Reynolds stresses profiles appear to be approximately self-similar in the downstream development. By inspecting the energy budget for the turbulent kinetic energy and Reynolds shear stresses, *Skåre & Krogstad* claimed that the most striking difference between the TBL with APG and the TBL with ZPG is that strong turbulent production occurs not only in the near wall region but also in the outer part of the boundary layer. Additionally, the peaks in the Reynolds stresses profiles are coincident with the maximum turbulent production in their transport equations.

The production of the turbulent kinetic energy is

$$-\overline{u'v'} \frac{\partial U}{\partial y} + (\overline{v'^2} - \overline{u'^2}) \frac{\partial U}{\partial x}$$

Usually the second-order production term $(\overline{v'^2} - \overline{u'^2}) \frac{\partial U}{\partial x}$ is not taken into account, but this term becomes more important in TBLs with strong APG, since the streamwise derivatives increase. In the experiment of [Skåre & Krogstad \(1994\)](#), this second-order production term contributes even up to 10% of the total production in the outer part of the boundary layer. In addition, the peak in $(\overline{v'^2} - \overline{u'^2}) \frac{\partial U}{\partial x}$ is not coincident with the maximum shear stress, and locates a little further out.

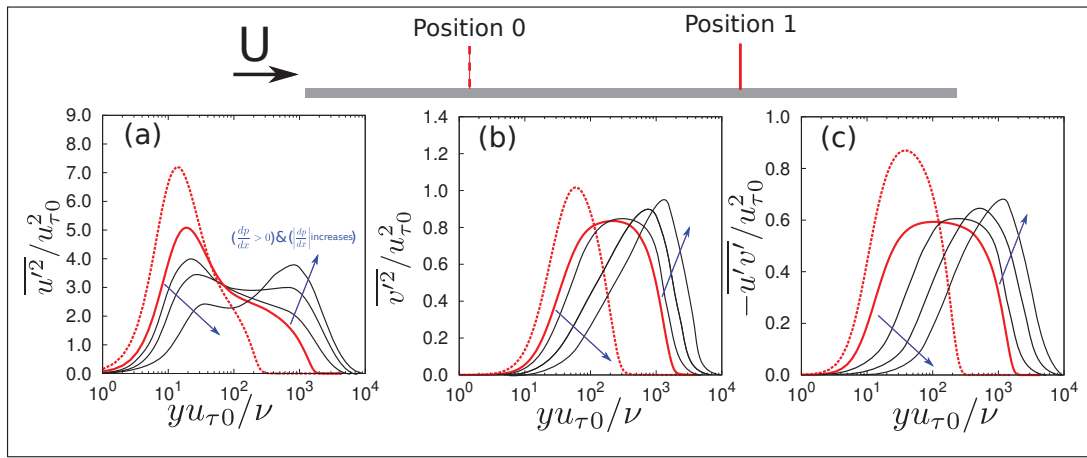


Figure 5.23: Proposed the absolute developments of Reynolds stresses under the effects of upstream flow and APG. $u_{\tau 0}$, reference friction velocity at reference position 0. Red dotted lines, profiles at reference position 0. Red solid lines, profiles at position 1 with ZPG. Black solid lines, profiles at position 1 with different APGs. Blue solid arrows, direction of APG increasing.

In the previous two paragraphs, the effects of upstream flow and APG were investigated. Based on these investigations, we propose a new prediction of the development of Reynolds stresses under the combined effects of upstream flow and APG, shown in Fig. 5.23, in which the reference friction velocity $u_{\tau 0}$ is the friction velocity at the reference position 0. With ZPG, the Reynolds stresses develop from the position 0 to the position 1 according to the pattern shown in Fig. 5.19. In Fig. 5.23, the black lines indicate the profiles with APG, and the magnitudes of APG increase in the direction of the blue arrows.

For $\overline{u'^2}$, the APG accelerates the development in a TBL with ZPG (see Fig. 5.23a). In the inner part, APG accelerates the decrease of $\overline{u'^2}$. In the outer part, APG accelerates the increase of $\overline{u'^2}$. Additionally, a peak occurs in the outer part of $\overline{u'^2}$, if the APG is strong enough. In the case that the magnitude of the APG is larger, the magnitude of $\overline{u'^2}$ at the peak is larger and the location of the peak is further from the wall.

Fig. 5.23b shows that the APG accelerates the decrease of $\overline{v'^2}$ in the inner part of boundary layer. In the outer part, the APG decreases the extent of large value region, and increases the

maximum value. If the APG is strong enough, a peak occurs in the outer part of $\overline{v'^2}$. The magnitude of the APG is larger, the magnitude of $\overline{v'^2}$ at the peak is larger and the location of the peak is further from the wall.

Fig. 5.23c shows the influence of APG on $-\overline{u'v'}$, which is similar to that on $\overline{v'^2}$ (in Fig. 5.23b).

Our experimental Reynolds stresses are plotted against different variables for different purposes. In order to show the absolute evolution, the Reynolds stresses ($\overline{u_s'^2}$, $\overline{u_n'^2}$ and $-\overline{u_s'u_n'}$) are non-dimensionalized by the reference velocity U_∞ and plotted against the distance to the wall n , shown in Fig. 5.24. In this figure, the symbol " $\langle \rangle$ " denotes the operator of time average, and is the same as the overline in parameters (e.g. $-\overline{u_s'u_n'}$). This symbol is also used in other figures in this chapter. For a more comprehensive analysis, Reynolds stresses are also non-dimensionalized by and plotted against other common parameters in Figs. 5.25~5.27. In Fig. 5.25, Reynolds stresses are non-dimensionalized by the reference velocity U_∞ and plotted against n/δ . In Fig. 5.26, Reynolds stresses are non-dimensionalized by the local friction velocity u_τ and plotted against n^+ ($n^+=nu_\tau/v$). In Fig. 5.27, Reynolds stresses are non-dimensionalized by the local friction velocity u_τ and plotted against n/δ .

According to the analysis shown in Fig. 5.23, our experimental results in Fig. 5.24 could be interpreted as a TBL with strong APG, except the experimental results at $s^*=0.31$ and 0.50. From the measurement error, the uncertainties at these two measurement stations are relatively large. The outer peak exists in all profiles of Reynolds stresses at the last four measurement stations $s^*=0.70\sim 0.99$. The peaks in the profiles of Reynolds stresses also occur in experiment of [Elsberry *et al.* \(2000\)](#), in which a TBL with APG was investigated. [Elsberry *et al.*](#) also found an inflection point profile that occurs in the mean velocity profile, and its location is very near the position of the observed peak in the streamwise turbulence intensity, as shown in Fig. 5.22. This phenomenon also exists in our experiment at the last four measurement stations $s^*=0.70\sim 0.99$ (Fig. 5.9).

The Reynolds shear stress $-\overline{u'v'}/u_\tau^2$ (in Figs. 5.26c and 5.27c) reaches a value which is considerably higher than 1. This can be interpreted by the effect of the strong APG in the experiment. This is because under the effect of the APG, at each measurement station the maximum value of $-\overline{u'v'}$ increases gradually; on the other hand, the local friction velocity u_τ decreases rapidly.

From the above interpretation of our experimental results, the streamwise APG can be responsible for the development of Reynolds stresses, and thus the effects of the curvature and the wall-normal PPG cannot be obviously observed directly from the development of Reynolds stresses.

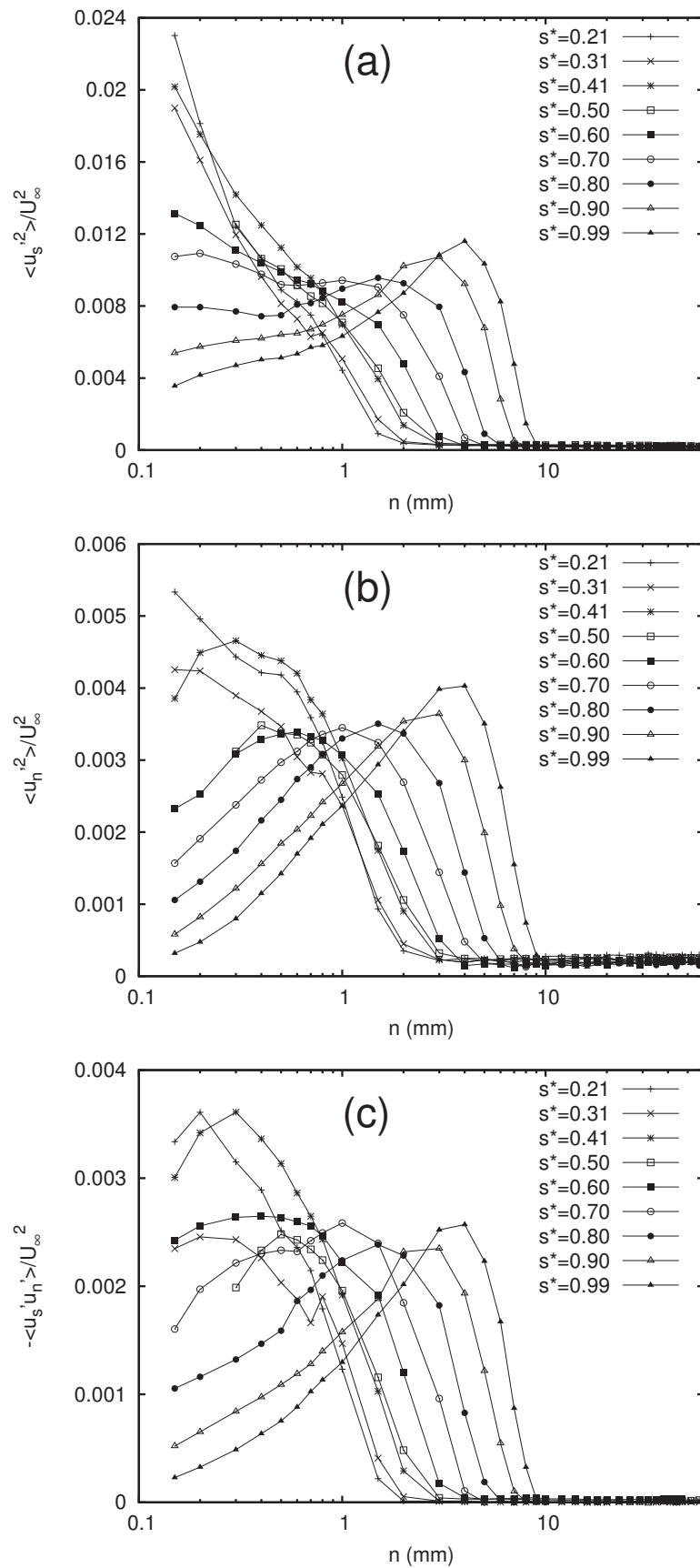


Figure 5.24: Reynolds stresses normalized by U_∞ plotted against n . Lines for visual aid only.

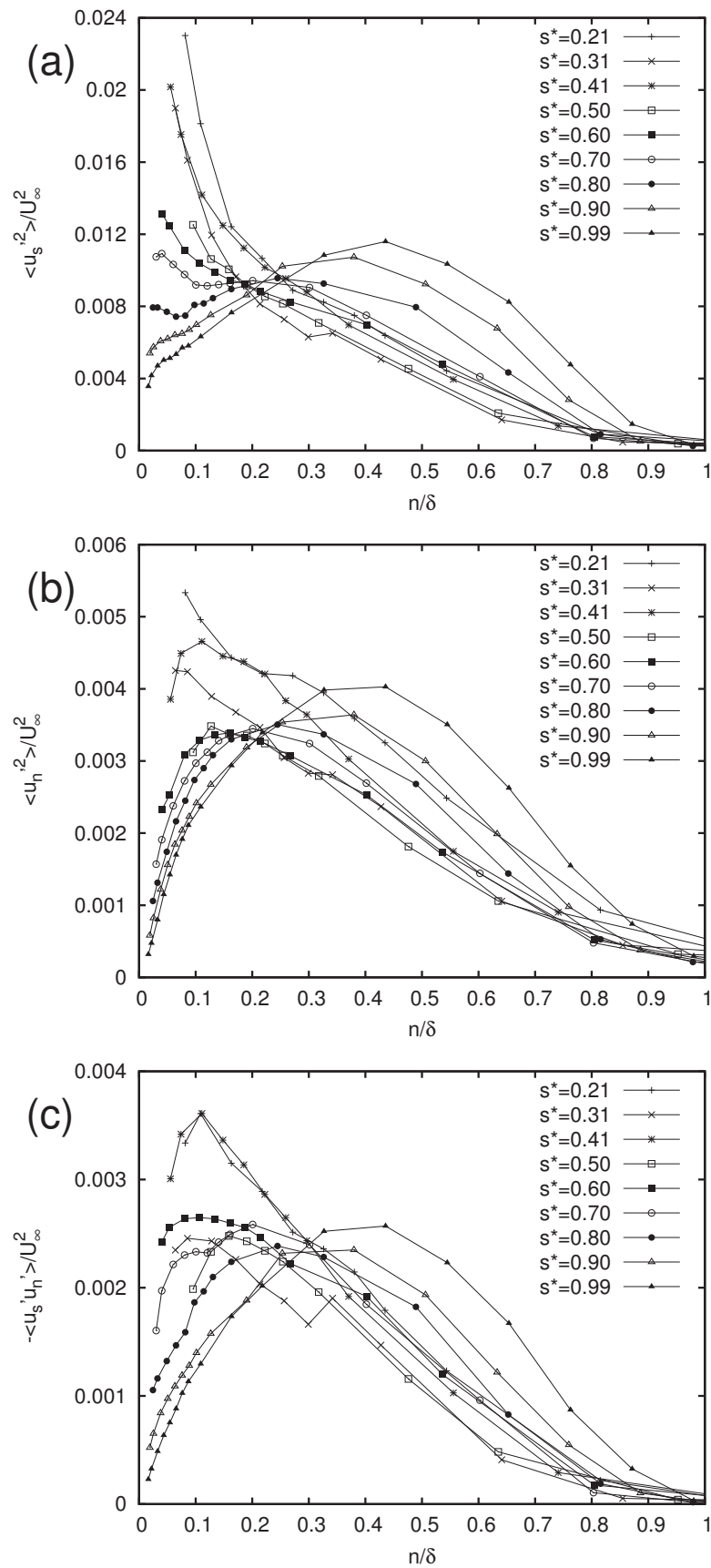


Figure 5.25: Reynolds stresses normalized by U_∞ plotted against n/δ . Lines for visual aid only.

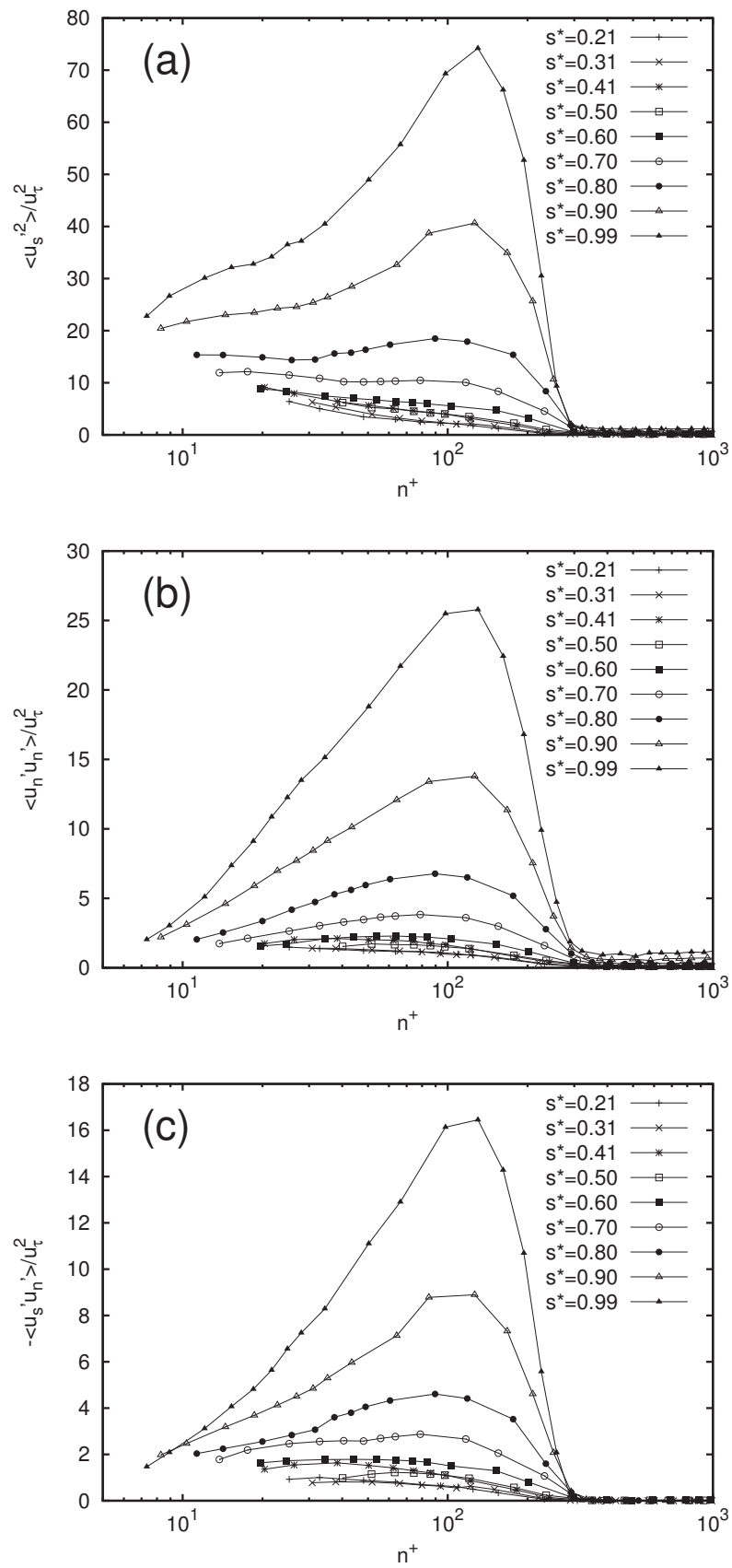


Figure 5.26: Reynolds stresses normalized by u_τ in inner variables. Lines for visual aid only.

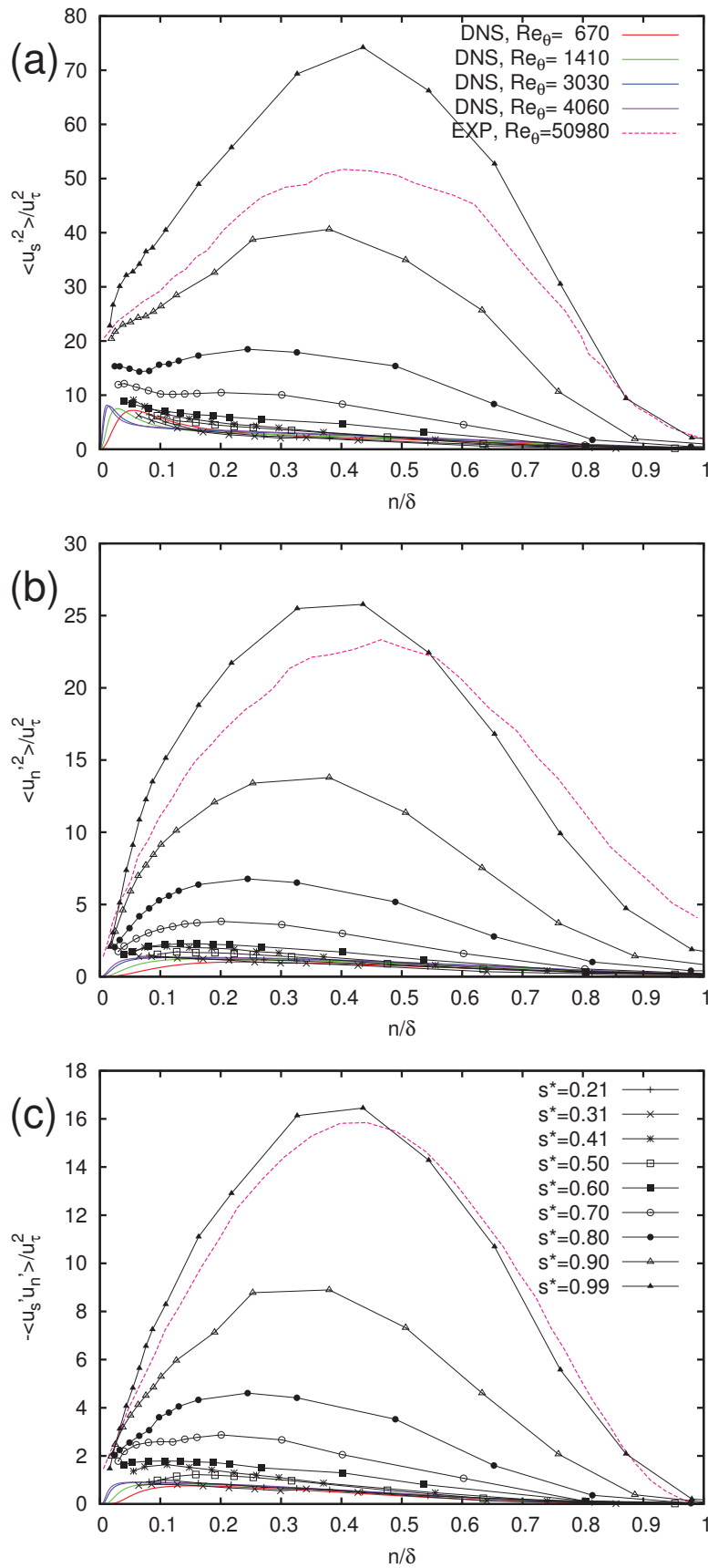


Figure 5.27: Reynolds stresses normalized by u_τ in outer variables. Lines for visual aid only.

5.11 Second-order turbulent correlation coefficients

The second-order turbulent correlation coefficients can show the structure of the turbulence. In this section, three of these coefficients will be discussed. To help analyze, some numerical and experimental results in the literature are plotted together with our experimental results. The added numerical results are those in a TBL with ZPG by DNS in a large range of Reynolds number ($Re_\theta=670\sim 4060$) from [Schlatter & Örlü \(2010\)](#). The added experimental results are from [Skåre & Krogstad \(1994\)](#), in which an equilibrium TBL with APG was investigated.

5.11.1 Ratio of Reynolds normal stresses $\overline{u_n'^2}/\overline{u_s'^2}$

The developments of $\overline{u_n'^2}/\overline{u_s'^2}$ in a TBL with ZPG can be seen from the DNS results shown in Fig. 5.28a. Very near the wall ($n/\delta\approx 0$), $\overline{u_n'^2}/\overline{u_s'^2}\approx 0$, mainly because $\overline{u_n'^2}$ should be zero owing to the influence of the wall. Then $\overline{u_n'^2}/\overline{u_s'^2}$ increases gradually in the near wall region. For the main part of the boundary layer, $\overline{u_n'^2}/\overline{u_s'^2}$ is roughly constant. When Re_θ increases, the extent of this plateau expands, and the value of this plateau keeps nearly constant. Until $Re_\theta=4060$, the plateau exists at $0.2 < n/\delta < 0.8$, the value of this plateau reaches 0.45. Near the boundary layer edge, $\overline{u_n'^2}/\overline{u_s'^2}$ grows, mainly because $\overline{u_n'^2}$ decays at a slower rate than $\overline{u_s'^2}$. In the outer layer of boundary layer, $\overline{u_n'^2}/\overline{u_s'^2}\approx 1$, because the turbulence is nearly isotropic there.

In the literature, there are a lot of investigations of the effects of streamwise APG and curvature on the development of $\overline{u_n'^2}/\overline{u_s'^2}$. [Aubertine & Eaton \(2005\)](#) experimentally investigated a non-equilibrium TBL with mild APG. They claimed that $\overline{u_n'^2}/\overline{u_s'^2}$ increases slightly as the APG is imposed. This is also confirmed by the experimental result of [Skåre & Krogstad \(1994\)](#) (also shown in Fig. 5.28a), who investigated a TBL with streamwise APG. [Patel & Sotiropoulos \(1997\)](#) reviewed the effects of curvature on the turbulence and claimed that the curvature increases $\overline{u_n'^2}/\overline{u_s'^2}$ in the outer boundary layer especially in the region of $0.5 < n/\delta < 1.0$.

Our experimental distributions of $\overline{u_n'^2}/\overline{u_s'^2}$ (see Fig. 5.28a) vary just a little in the inner boundary layer $n/\delta < 0.2$. However, the differences in the outer boundary layer $0.2 < n/\delta < 1.0$ are very significant. The value of the plateau decreases from ≈ 0.5 at $s^*=0.21$ to ≈ 0.30 at $s^*=0.99$. Moreover, the extent of the plateau increases obviously. This change is in the opposite trend compared with that with the influence of APG, which increases the value of the plateau in the profile of $\overline{u_n'^2}/\overline{u_s'^2}$ as mentioned above. Thus the two factors left, curvature and wall-normal PPG, should influence $\overline{u_n'^2}/\overline{u_s'^2}$. This is consistent with Eq. 5.2, from which we could infer that the wall-normal PPG suppresses considerably the growth of $\overline{u_n'^2}$ in the wall-normal direction especially in the outer boundary layer.

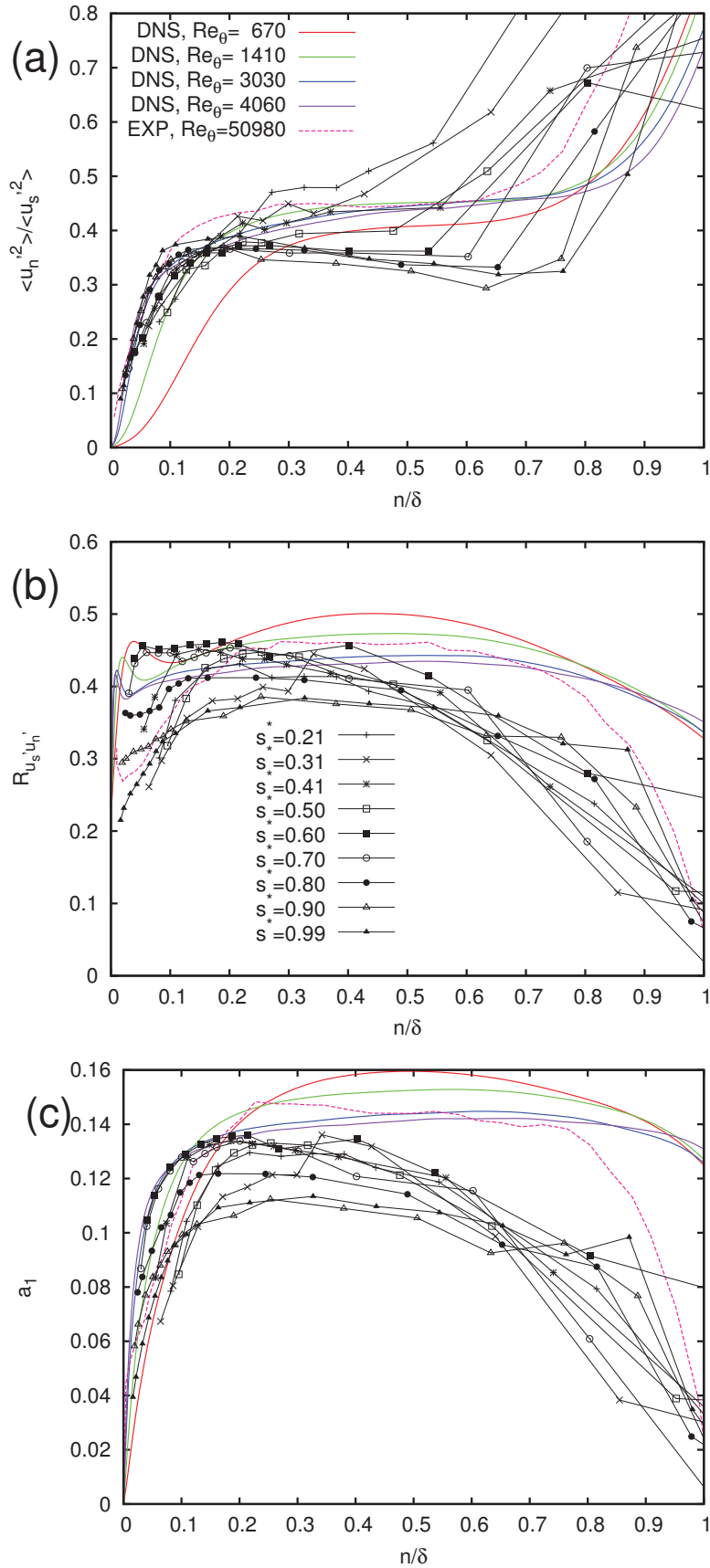


Figure 5.28: Second order correlation ratios (a) $\overline{u_n'^2} / \overline{u_s'^2}$ (b) $R_{u_s'u_n'}$ (c) a_1 . Lines for visual aid only. Color solid lines indicate the DNS results of Schlatter & Örlü (2010). Pink dotted lines indicate the experimental results of Skåre & Krogstad (1994).

5.11.2 Correlation coefficient $R_{u'_s u'_n}$

The correlation coefficient $R_{u'_s u'_n}$ is defined as

$$R_{u'_s u'_n} = \frac{-\overline{u'_s u'_n}}{\sqrt{\overline{u_s'^2}} \sqrt{\overline{u_n'^2}}} \quad (5.32)$$

The development of $R_{u'_s u'_n}$ in a TBL with ZPG can be seen from the DNS results in Fig. 5.28b. When $n/\delta=0$, $R_{u'_s u'_n} \approx 0$, because $\overline{u'_s u'_n}$ should be zero owing to the existence of the wall. With Re_θ increasing, the profile without pressure gradient shows a mostly constant correlation with a value of approximately 0.40.

In the literature, there are few investigations of the effects of streamwise pressure gradient and curvature on the development of $R_{u'_s u'_n}$. A rare investigation is the one of Skåre & Krogstad (1994), in which an equilibrium TBL with strong streamwise APG was investigated. They observed that $R_{u'_s u'_n}$ reaches a constant value for $0.2 < n/\delta < 0.7$ at each measurement station. Additionally, the level of $R_{u'_s u'_n}$ in their experiment varied between about 0.39 and 0.46, and no systematic streamwise-dependence in the data could be found. One of their results is shown in Fig. 5.28b. Eventually they considered that the scatter in the data represented measurement uncertainties rather than any physical effects.

In our experiment at each measurement station, $R_{u'_s u'_n}$ (see Fig. 5.28b) reaches roughly a constant value at $0.1 < n/\delta < 0.5$. Although the figure indicates that this level varies between about 0.38 and 0.46, no systematic streamwise-dependence in the data could be found, similar to the result of Skåre & Krogstad (1994). However, a remarkable phenomenon exists at the outer boundary layer $0.6 < n/\delta < 1.0$. This phenomenon is that our experimental $R_{u'_s u'_n}$ decreases more rapidly than other results, including that with ZPG (DNS results) and that with just a APG (experimental results of Skåre & Krogstad (1994)). As reviewed by Patel & Sotiropoulos (1997), the curvature reduces rapidly the Reynolds shear stress especially in the outer boundary layer. Therefore the development of $R_{u'_s u'_n}$ in our experiment can be interpreted as the combined influence of streamwise APG and the curvature. Here, the individual effects of the wall-normal pressure gradient on $R_{u'_s u'_n}$ cannot be distinguished.

5.11.3 Structure parameter a_1

The structure parameter a_1 is defined as the ratio of the shear stress $-\overline{u'_s u'_n}$ to the total turbulent kinetic energy k ,

$$a_1 = \frac{-\overline{u'_s u'_n}}{2k} \quad (5.33)$$

where $k = \frac{1}{2}(\overline{u'^2} + \overline{u'_n{}^2} + \overline{u'_z{}^2})$. Since the spanwise normal stress is not measured in our experiment, the turbulent kinetic energy is estimated by $k = \frac{3}{4}(\overline{u'^2} + \overline{u'_n{}^2})$. This is because $\overline{u'_z{}^2} \approx \frac{1}{2}(\overline{u'^2} + \overline{u'_n{}^2})$ according to Bradshaw & Galea (1967) and Cutler & Johnston (1989). Bradshaw (1967) claimed that the a_1 for a flat-plate boundary layer is generally taken to be constant and has a value of 0.15. The number of 0.15 is also usually used in the literature as the standard value of a_1 for a TBL with ZPG. However, from the DNS results in a TBL with ZPG shown in Fig. 5.28c, a_1 decreases with the Reynolds number, and is about 0.14 when $Re_\theta = 4060$.

In the literature, there are a lot of investigations of the effects of streamwise APG and curvature on the development of a_1 . It is widely accepted that the streamwise APG reduces a_1 (e.g. Aubertine & Eaton, 2005; Spalart & Watmuff, 1993). Skåre & Krogstad (1994) also considered that APG reduces a_1 , although their a_1 was about 0.14 nearly the same with the value for ZPG TBLs at a high Reynolds number (see Fig. 5.28c). Patel & Sotiropoulos (1997) reviewed the influences of curvature on turbulence, and claimed that the structure parameter a_1 decreases under the influence of convex curvature, specially in $0.7 < n/\delta < 1.0$.

The developments of our experimental a_1 (see Fig. 5.28c) are similar at different measurement stations. At each measurement station, it increases initially in the internal layer and then decreases in the outer part of the boundary layer, with a minimum value at the edge of the boundary layer. The maximum values of a_1 vary between 0.135 and 0.115, and no systematic streamwise-dependence in the data could be found. The decrease in a_1 is more significant especially in $0.5 < n/\delta < 1.0$. Comparing Fig. 5.28c with Fig. 5.28b, a_1 has a similar behavior with $R_{u'_s u'_n}$. Therefore the development on a_1 can be interpreted as the same reason for $R_{u'_s u'_n}$ discussed above: we have a probable combined influence of the streamwise pressure gradient and the curvature. The individual effects of the wall-normal pressure gradient on a_1 cannot be distinguished.

5.12 Triple correlations

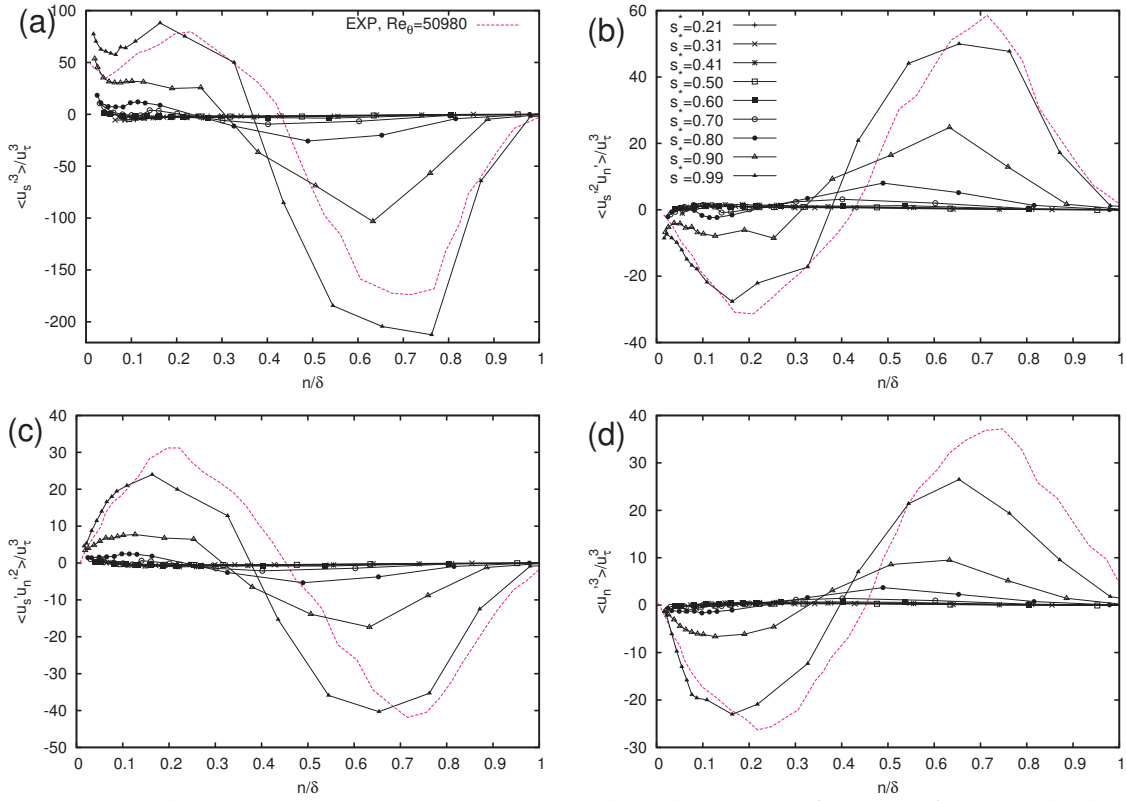


Figure 5.29: Triple correlations normalized by u_τ plotted against n/δ . Lines for visual aid only. The pink dotted lines are experimental results of Skåre & Krogstad (1994).

The triple correlations are associated with the transfer and redistribution of the turbulent energy in the boundary layer. One of the diffusion terms in the transport equation of $\overline{u'_i u'_j}$ in a two-dimensional incompressible flow is

$$\text{Dif}(\overline{u'_i u'_j}) = -\frac{\partial \overline{u'_i u'_j u'_k}}{\partial x_k} \quad (5.34)$$

For $\overline{u'^2}$, $\overline{v'^2}$ and $-\overline{u'v'}$, they are individually

$$\text{Dif}(\overline{u'^2}) = \frac{\partial(-\overline{u'^3})}{\partial x} + \frac{\partial(-\overline{u'^2 v'})}{\partial y} \quad (5.35)$$

$$\text{Dif}(\overline{v'^2}) = \frac{\partial(-\overline{u'v'^2})}{\partial x} + \frac{\partial(-\overline{v'^3})}{\partial y} \quad (5.36)$$

$$\text{Dif}(-\overline{u'v'}) = \frac{\partial \overline{u'^2 v'}}{\partial x} + \frac{\partial \overline{u'v'^2}}{\partial y} \quad (5.37)$$

From Eqs. 5.35~5.37, $\frac{\partial(-\overline{u'^3})}{\partial x}$ partly represents the local diffusion of $\overline{u'^2}$; $\frac{\partial(-\overline{u'^2 v'})}{\partial y}$, $\frac{\partial(-\overline{v'^3})}{\partial y}$ and $\frac{\partial \overline{u'v'^2}}{\partial y}$ partly represent the local diffusion of $\overline{u'^2}$, $\overline{v'^2}$ and $-\overline{u'v'}$, respectively. Normally $\overline{u'^2 v'}$

and $\overline{v'^3}$ have opposite sign to $\overline{u'^3}$ and $\overline{u'v'^2}$. According to Liu & Pletche (2008), $\overline{u'^3}$ represents the direction of energy diffusion in streamwise, while $\overline{v'^3}$ represents the direction of energy diffusion in the wall-normal direction.

Our experimental triple correlations normalized by the local friction velocity u_τ and plotted against n/δ are shown in Fig. 5.29. For comparison, the experimental results of Skåre & Krogstad (1994) are also shown in this figure. The maximum and minimum values of the triple correlations mainly depend on the local value of u_τ . Therefore the development of the triple correlations can also be interpreted as the influence of APG. The influences of the curvature and the wall-normal PPG on the development of triple correlations are not explicit here.

In order to show the absolute developments of different parameters at the same measurement station, the triple correlations are normalized by U_∞ , and plotted in Fig. 5.9. At each measurement station, all the triple correlations are approximately zero outside the boundary layer. Another obvious phenomenon is that they are also approximately equal to zero at the inflection point in the velocity profile, if this inflection point exists. According to the conclusions of Liu & Pletche (2008) introduced above, the directions of energy diffusion are different in the inner part and outer part. In the inner part the direction of the energy diffusion is right-bottom, while in the outer part the direction of the energy diffusion is left-top. If the inflection point does not exist in the profile of the mean streamwise velocity, the inner part is limited to a very thin region near the wall. If the inflection point exists, the inner part is from the wall to this inflection point.

5.13 Skewness and flatness

The skewness S_α describes the asymmetry of the probability distribution of α , and is defined as

$$S_\alpha = \overline{\alpha^3} / (\sqrt{\overline{\alpha^2}})^3 \quad (5.38)$$

where α is one of the velocity fluctuations u'_s or u'_n . A positive value of S_α implies that large positive values of α are more frequent than large negative values. For a Gaussian distribution, $S_\alpha=0$.

The flatness F_α is a measurement of the frequency of the occurrence of events far from the mean value, and is defined as

$$F_\alpha = \overline{\alpha^4} / (\sqrt{\overline{\alpha^2}})^4 \quad (5.39)$$

For the flow investigated in our experiment, the skewness and flatness are plotted in Fig. 5.30. In order to show their developments with different parameters, skewness and flatness are

also shown Fig. 5.9. The most obvious observation is that our experimental results are very similar to the results of Skåre & Krogstad (1994), especially at the last three measurement stations $s^*=0.80\sim 0.99$. In each measurement station (see Fig. 5.9), $S_{u'_s}$ decreases from a positive value near the wall, and then changes its sign near the location of the maximum stresses, and following reaches its minimum value at the edge of the boundary layer, and then decreases rapidly to zero. $S_{u'_n}$ is almost the opposite to $S_{u'_s}$. $F_{u'_s}$ decreases considerably from the very near wall region, and then keeps near the Gaussian value of 3, and then increases rapidly before the edge of the boundary layer, and reaches its maximum value near the edge of the boundary layer, and then decreases rapidly to the Gaussian value of 3. $F_{u'_n}$ has the similar behaviour as $F_{u'_s}$. Moreover, $F_{u'_n}$ is larger than $F_{u'_s}$ except in the region near the edge of the boundary layer. The present data therefore suggest that the strong pressure gradient has reversed the dominant direction of transport close to the surface, from being away from the wall in the ZPG case, to a situation dominated by motions towards the surface, according to Skåre & Krogstad (1994).

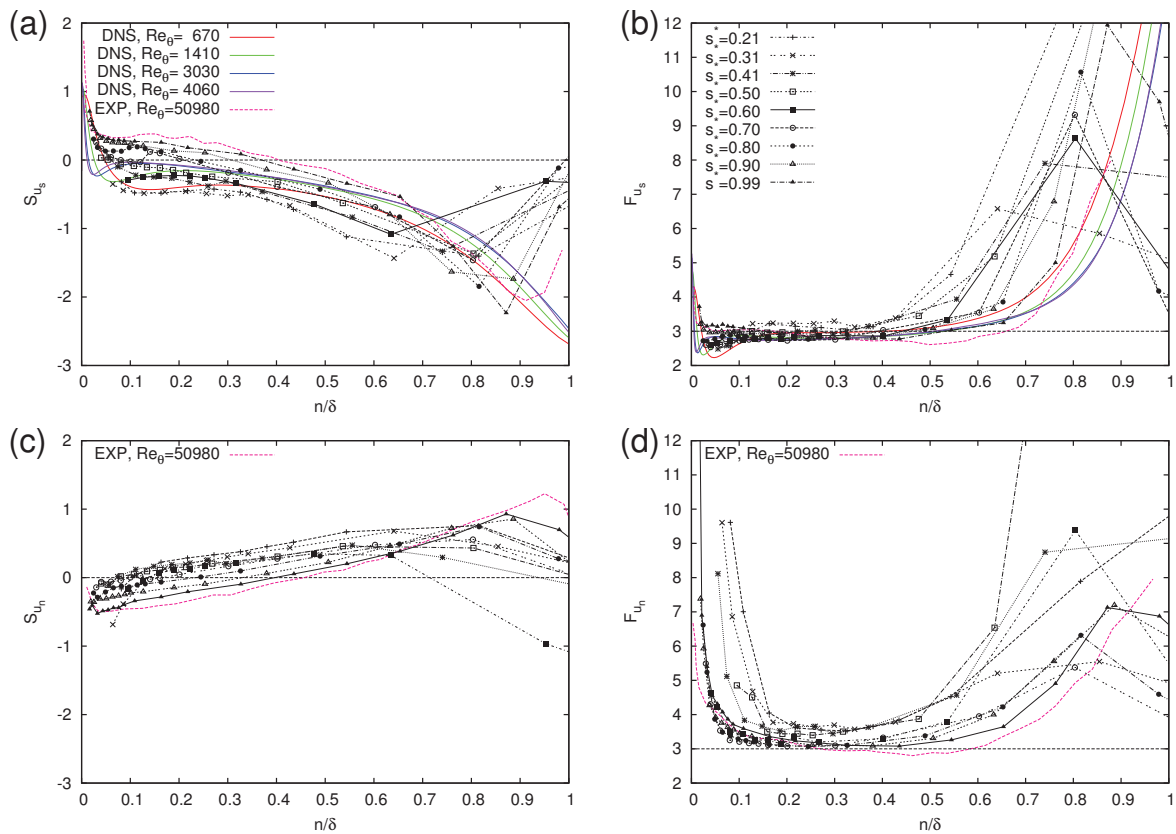


Figure 5.30: Skewness and flatness. Lines for visual aid only. Colour solid lines indicate the DNS results of Schlatter & Örlü (2010). The pink dotted lines are experimental results of Skåre & Krogstad (1994).

5.14 Examining scalings

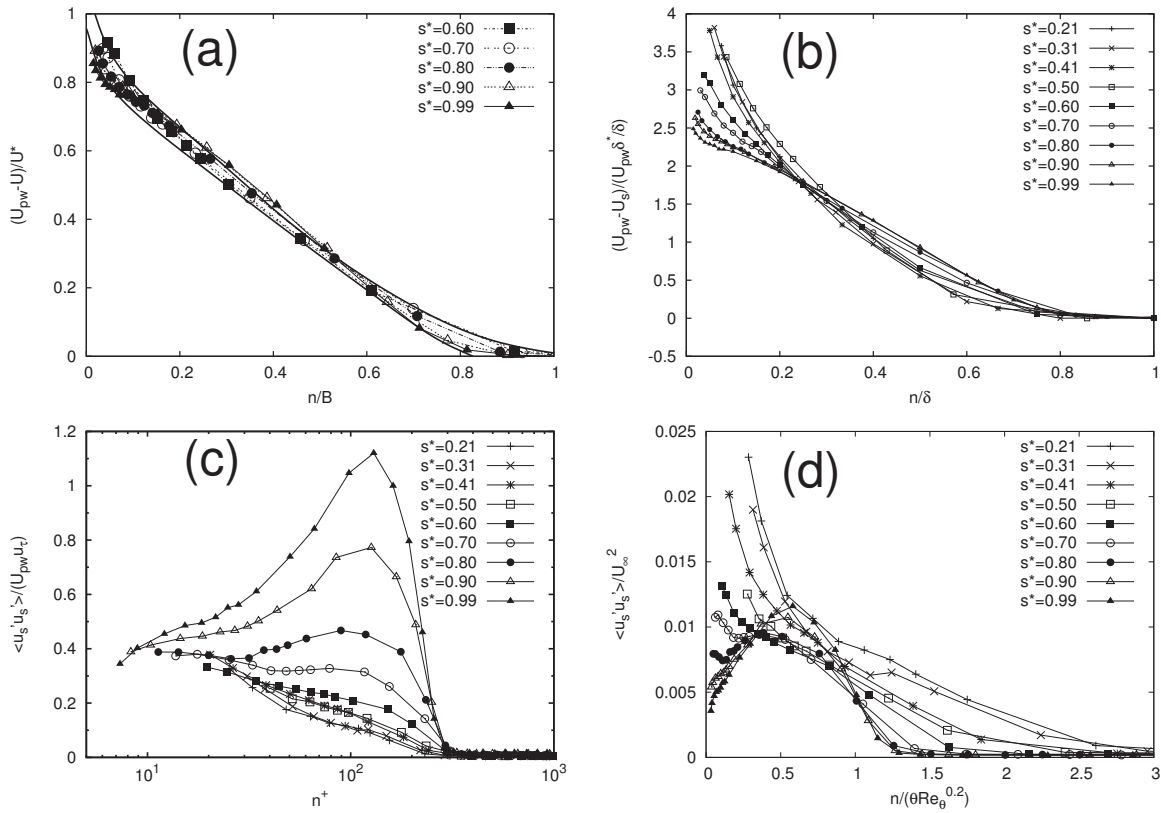


Figure 5.31: Examining scalings, the potential velocity U_{pw} is used in place of U_e . (a) Mean velocity profiles in Perry-Schofield coordinates, the two curves indicate the limits of scatter in Perry & Schofield (1973). (b) Velocity profiles normalized using the scaling variables proposed by Zagarola & Smits (1998a). (c) Streamwise normal component of turbulent stresses profiles normalized using the mixed scaling proposed by DeGraaff & Eaton (2000). (d) Reynolds stresses profiles using the scaling proposed by Elsberry *et al.* (2000).

Some previously proposed scalings applied to the mean velocity and the turbulence profiles in the inner and outer region of the boundary layer are examined using our experimental results.

Perry & Schofield (1973) proposed a universal empirical correlation for the inner and outer regions of TBLs with APG near separation. Their correlations are applied to a large number of all types of TBLs with APG on low curvature surface irrespective of whether they are in equilibrium or not, but with the restriction that $|\overline{u'v'}|_{max}/u_\tau^2 > 1.5$. Since the wall shear stress approaches zero at detachment, it is a poor parameter to use in order to describe the mean velocity profile behaviour away from the near-wall region. They used new velocity and length scales which are related to the maximum shear stress and its location from the wall. They

proposed the defect law for the outer flow mean velocity profile as

$$\frac{U_e - U}{U^*} = 1 - 0.4 \left(\frac{n}{B} \right)^{1/2} - 0.6 \sin \left(\frac{\pi n}{2 B} \right) \quad (5.40)$$

with $B = 2.86 \delta^* U_e / U^*$, where U_e is the local free-stream velocity, δ^* is the displacement thickness of boundary layer. The new velocity scale U^* can be determined from a measured velocity profile by analogy with the Clauser plot using the half-power instead of the log law. In our experiment, the restriction for this scaling that $|\overline{u'v'}|_{max} / u_\tau^2 > 1.5$ is respected only at the five latter measurement stations. The mean velocity profiles of these five measurement stations in Perry-Schofield coordinates are plotted in Fig. 5.31a. This figure shows that the velocity profiles agree very well with the Perry-Schofield profile.

Zagarola & Smits (1998b) proposed a new outer velocity scale, $U_e \delta^* / \delta$, for a TBL with ZPG on smooth wall. This new outer velocity scale was extended from that originally developed for the mean velocity profile of turbulent pipe flow proposed by Zagarola & Smits (1998a). Soon after theoretical justifications of this scaling were provided by Wosnik *et al.* (2000) and Castillo & George (2001) for boundary layers without and with pressure gradients, respectively. Brzek *et al.* (2007) considered that this scaling was able to remove the effects of roughness from the velocity profiles in outer variable. Fig. 5.31b shows the mean deficit profile proposed by Zagarola & Smits (1998a) for all the locations along the blade suction side surface. In our experiment, the profiles do not follow this scaling; this may be because the pressure parameter of Castillo and George, Λ is not constant.

DeGraaff & Eaton (2000) measured the Reynolds stresses for a flat-plate TBL with ZPG from Reynolds numbers $Re_\theta = 1430$ to 31000 , and proposed the mixed scaling $U_e u_\tau$ for $\overline{u'^2}$. Soon after Metzger *et al.* (2001) considered that the validity of this scaling over an extended Reynolds number range $Re_\theta = 1000 \sim 10^6$, using the experimental results in the literature. Marusic & Kunkel (2003) explained the reason for this scaling by analytical works. Fig. 5.31c shows our experiments using this scaling. Expectably this scaling does not work, because the TBL in our experiment may be affected by the more complex combined influence of the curvature and the streamwise APG and wall-normal PPG.

Elsberry *et al.* (2000) experimentally studied a TBL with APG and proposed to scale the Reynolds stresses by a new length scale $\theta Re_\theta^{0.2}$ and a constant velocity U_∞ . Fig. 5.31d shows our experimental results ($\overline{u'_s u'_s}$ as a representative) using this scaling. This scaling does not work expectably, because it relies heavily on experience and the APS in our experiment is much stronger.

5.15 Conclusions

There are two purposes to investigate the TBL on the suction side at mid-span. The first purpose is to apply the research findings in the literature to this TBL. The second purpose is to improve the physical understandings of corner separations, because this kind of TBL partly reflects the characteristic of the more complex TBL in the region of corner stall.

From the basic equation, the influence of curvature is balanced by the sum of wall-normal pressure gradient ($\partial P/\partial n$) and normal gradient of Reynolds normal stress ($\partial \overline{u_n'^2}/\partial n$). Therefore the influence of the wall-normal pressure gradient is partly implicit in the influence of the curvature. On the other hand, wall-normal pressure gradient contains Reynolds normal stress $\overline{u_n'^2}$ in the wall-normal direction.

The TBL at mid-span is under the combined influences of three main factors, the curvature, the streamwise pressure gradient and the wall-normal pressure gradient. The streamwise pressure gradient and the wall-normal pressure gradient have the same magnitude in the former part; the streamwise pressure gradient is larger than the wall-normal pressure gradient in the latter part. The magnitudes of $|K\delta|$ have the order of 0.01, which are generally regarded as weak curvature. The effect of curvature is generally larger than that of wall-normal pressure gradient, especially in the former part where $0 < s^* < 0.70$.

The TBL at mid-span is still in the state of incipient detachment even at the trailing edge, and far from the state of separation. In addition, this TBL is in strong non-equilibrium.

From the analysis of the shape factors, contrary to the streamwise APG and the convex curvature, the wall-normal PPG restrains the separation. This trend is not the same with the effect of the wall-normal PPG in the corner region, where the wall-normal PPG induces the flow to deviate towards the suction side and thus may cause the corner separations. The criterion of Truckenbrodt's shape factor (H) for the separation of the boundary layers should take into account the influence of the wall-normal PPG, in order to decrease the threshold under which boundary layer at mid-span should separate.

The development of Reynolds stresses in a TBL shows both extensive effects of upstream flow and local effects (for example, the pressure gradient and the curvature). Therefore these two effects have been investigated, before presenting our experimental results of Reynolds stresses. At first, the individual effect of the upstream flow in a TBL with ZPG has been investigated by using DNS results in the literature. Then the effect of APG has been investigated by reviewing the investigations of TBLs with APGs in the literature. For $\overline{u'^2}$, the APG accelerates

the development in a TBL with ZPG. In the inner part, APG accelerates the decrease of $\overline{u'^2}$. In the outer part, APG accelerates the increase of $\overline{u'^2}$. Additionally, a peak occurs in the outer part of $\overline{u'^2}$, if the APG is strong enough. In this case, the magnitude of the APG is larger, the magnitude of $\overline{u'^2}$ at the peak is larger and the location of the peak is further from the wall. For $\overline{v'^2}$, the APG accelerates the decrease of $\overline{v'^2}$ in the inner part of boundary layer. In the outer part, the APG decreases the extent of the large value region, and increases the maximum value. If the APG is strong enough, a peak occurs in the outer part of $\overline{v'^2}$. In this case, the magnitude of the APG is larger, the magnitude of $\overline{v'^2}$ at the peak is larger and the location of the peak is further from the wall. The influence of APG on $-\overline{u'v'}$, is similar to that on $\overline{v'^2}$.

From our experimental results, the streamwise APG can be responsible for the development of Reynolds stresses. The effects of curvature and wall-normal PPG cannot be observed directly from the development of Reynolds stresses. The outer peaks exist in all the profiles of Reynolds stresses at the last four measurement stations. Additionally, they occur near the positions of the inflection points in the mean velocity profiles.

Some second-order turbulent correlation coefficients have been investigated. From the development of $\overline{u'_n{}^2}/\overline{u'_s{}^2}$, the wall-normal PPG suppresses considerably the growth of $\overline{u'_n{}^2}$ in the wall-normal direction especially in the outer region of boundary layer. The development of $R_{u'_s u'_n}$ has a similar behavior to that of a_1 . The developments of these two parameters in our experiment can be interpreted as the combined influence of streamwise APG and curvature. The effects of the wall-normal pressure gradient were not obviously distinguished.

Some of the scalings for mean velocity or turbulence in TBLs with and without pressure gradients have been checked with the present data. Most of them do not work in this complex non-equilibrium TBL, and thus need to be improved.

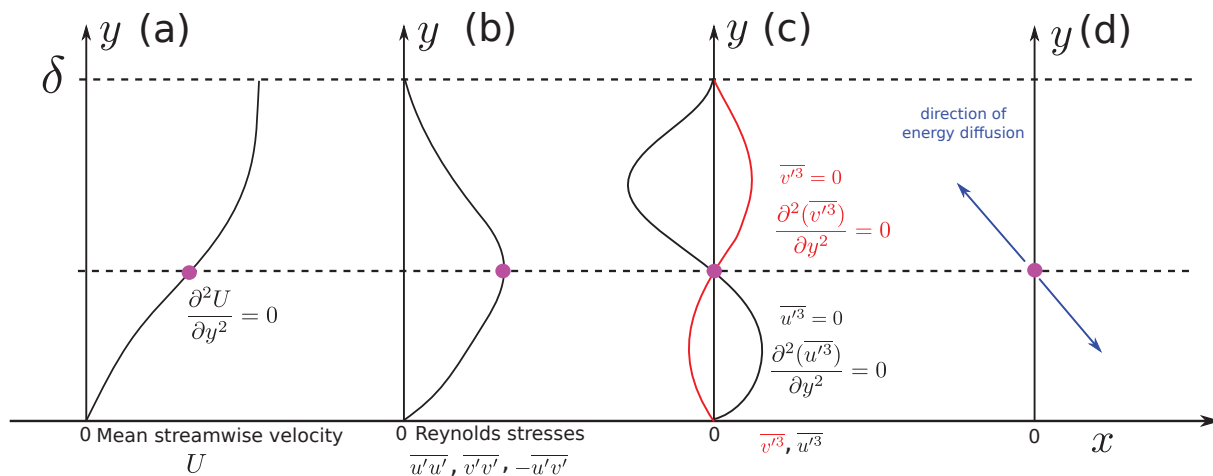


Figure 5.32: Characteristics of a special point in the TBL.

The remarkable phenomenon in this TBL at latter measurement station can be summarized as follows (see also Fig. 5.32):

- (a) An inflection point occurs in the profile of the mean streamwise velocity, i.e. $\partial U^2 / \partial y^2 = 0$.
- (b) The magnitude of the Reynolds stresses ($\overline{u'^2}$, $\overline{v'^2}$ and $-\overline{u'v'}$) reach their maximum values at this point. In addition, here the production terms in their transport equations are maximum.
- (c) $\overline{u'^3} = 0$ and $\overline{v'^3} = 0$. At the same time, inflection points occur in the profile of $\overline{u'^3}$ and $\overline{v'^3}$ i.e. $\partial^2(\overline{u'^3}) / \partial y^2 = 0$ and $\partial^2(\overline{v'^3}) / \partial y^2 = 0$.
- (d) The direction of energy diffusion thus changes near this point. Below this point, the direction is right-bottom. Above this point, the direction is left-top.

Chapter 6

Velocity flow field in corner stall

Contents

6.1	Introduction	156
6.2	Choice of incidence	156
6.3	Choice of experimental layout	158
6.4	Mean velocity	159
6.5	Comparisons of PIV and LDA	166
6.6	Backflow coefficients	169
6.7	Bimodal histograms of velocity	170
6.7.1	Review of bimodal histogram in the literature	170
6.7.1.1	In junction flow	170
6.7.1.2	In a linear compressor cascade	173
6.7.2	Illustration of bimodal histograms	174
6.7.3	Positions of bimodal points	176
6.7.4	Histogram decomposition	176
6.7.5	Development of histograms along the measurement station	178
6.7.6	Spectra of velocity components	185
6.7.7	Physics of bimodal behaviour	185
6.8	Conclusions	187

6.1 Introduction

In this chapter, the velocity flow field in the corner region will be investigated. First of all, the choice and the reason of incidence and experimental layout of velocity measurement are presented. Then the time averaged flow field in the corner region is presented. Moreover, backflow coefficients are used to explain the unsteady feature of the flow field. At last a significant phenomenon, the existence of bimodal histograms of velocity, is found in our experiment. Their features and physics are studied.

6.2 Choice of incidence

Our purpose is to measure a suitable flow field, in which (1) the extent of corner stall is as large as possible and (2) no separation exists at mid-span. One method to achieve this is to choose a suitable incidence.

Before the experiment, the criteria of separation in the literature (see Section 2.4.4) are used to predict the separation in our cascade.

The equivalent diffusion factor DF_{eq} (Eq. 2.24) is used to predict the separation at mid-span. In our cascade, the experimental and numerical DF_{eq} are shown in Fig. 6.1. The experimental DF_{eq} are calculated from the results of the five-hole pressure probe. The numerical tool is the FLUENT with the S-A turbulence model. The experimental and numerical results are in good agreement. Both results predict that the flow at mid-span does not separate at $i=4^\circ$ and separate at $i=6^\circ$.

Another factor, the diffusion parameter D (Eq. 2.28), is proposed by Lei (2006) to predict the size and strength of the corner stall. Because this parameter is based on the preliminary design flow variables and geometry, the continuous line that express the relation between D and the incidence i can be obtained, as shown in Fig. 6.2. The size and strength of the corner stall increase with incidence. From this prediction, the situation, in which large separation regions exist both on the suction side and on the endwall, appears when $i>8.3^\circ$.

The predictions of the criteria discussed above just give a preview of the flow field in our cascade, and will be checked using experimental results.

In the experiment, oil visualization is used to qualitatively show the size of the separation regions at mid-span and in the corner region (on the suction side and the endwall). At $i=4^\circ$, the flow does not separate at mid-span. At the same time, there are two obvious vortices, one is on the suction side and the other on the endwall (see Fig. 6.3). This means that the extent

of the corner stall is already considerably large. At $i=6^\circ$, the flow separates at mid-span before reaching the trailing edge. As a result, the incidence of 4° has been chosen.

Therefore in our experiment, the equivalent diffusion parameter DF_{eq} works very well and the diffusion parameter D is not valid. This may be because the diffusion parameter D did not consider the influence of blade aspect ratio, which plays a major role in the appearance of corner stall. Another reason could be the influence of trips (see Appendix C).

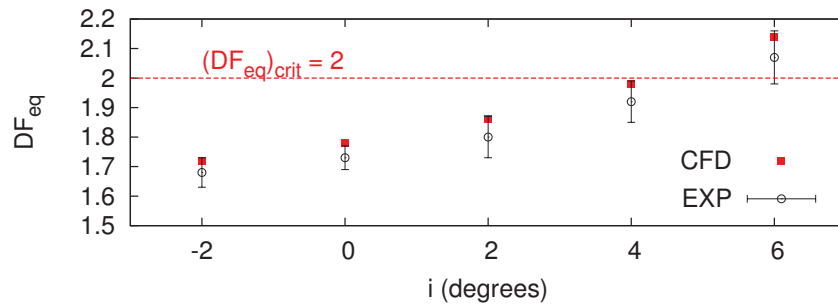


Figure 6.1: Experimental and numerical results of equivalent diffusion factor (DF_{eq}).

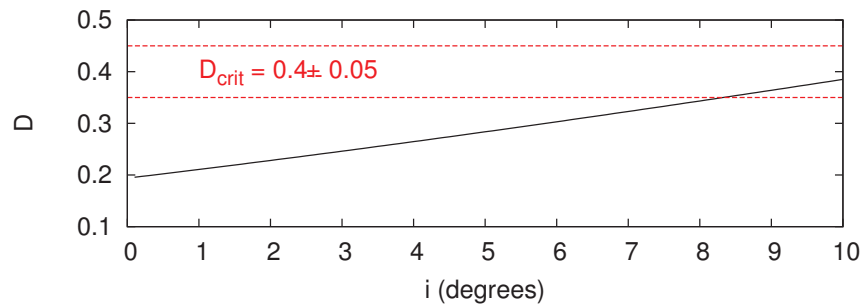


Figure 6.2: Relation between the diffusion parameter D and i .

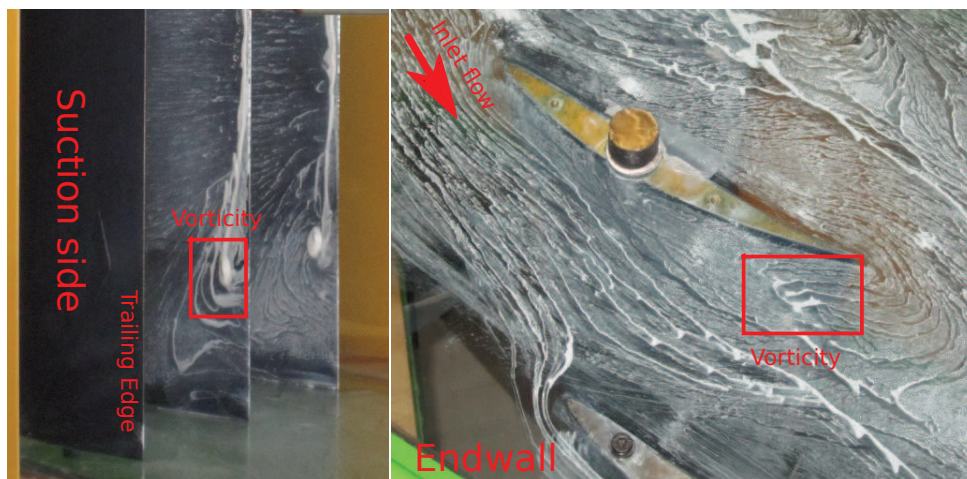


Figure 6.3: Results of oil visualization, $i=4^\circ$.

6.3 Choice of experimental layout

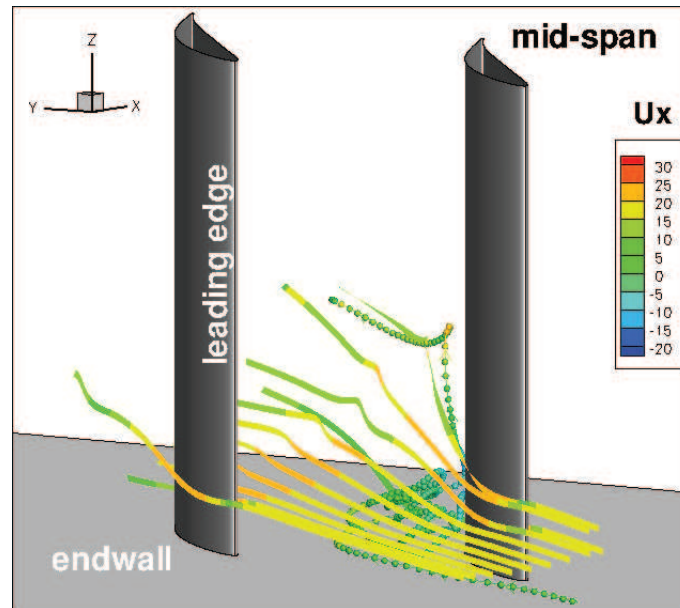


Figure 6.4: Topology of corner stall: streamlines colored by axial mean velocity. FLUENT with the S-A turbulence model.

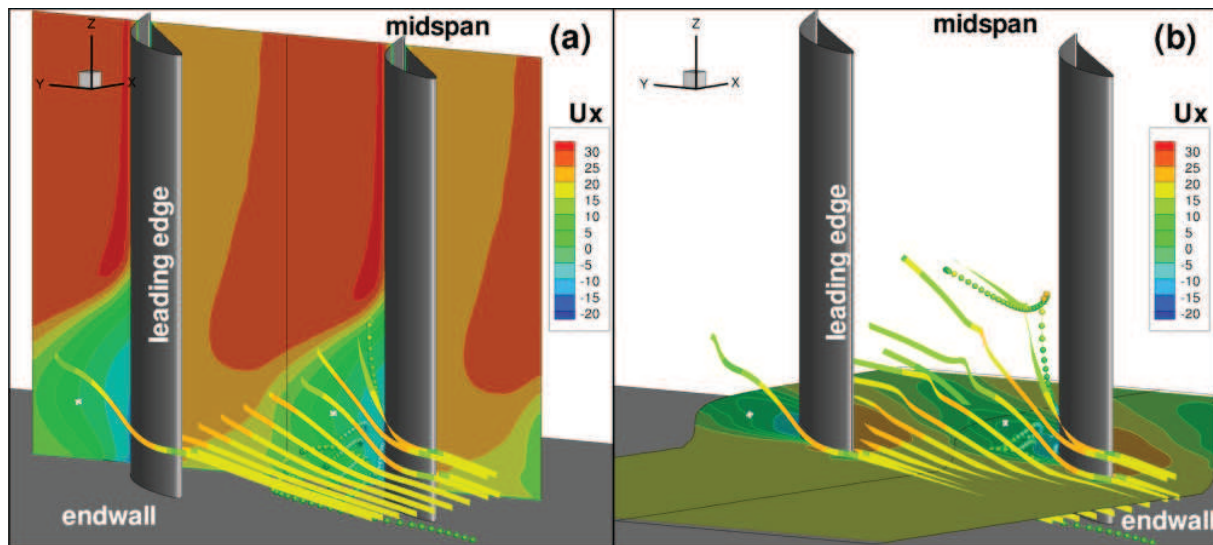


Figure 6.5: Two different experimental layouts: (a) perpendicular and (b) parallel to the axial direction.

The main features of corner stall are three-dimensional and unsteady. A topology of corner stall is illustrated in Fig. 6.4, through streamlines coloured by axial mean velocity. In this figure, the three-dimensional feature can be seen directly. The streamline in the boundary layer (the streamline with points) deviates toward the blade suction surface due to the strong pressure gradient in the blade passage. The blockage induced by the corner stall is obviously seen through the streamlines outside the corner region (the streamlines without points). Concerning the unsteady feature of the corner stall, which is mainly reflected in the movement of the streamlines over time, cannot be shown by these steady RANS simulation results.

The topologies of corner stall in the literature, which have been summarized in Section 2.4.2, are mainly based on the vortex and the streamlines in the corner region. In other words, these topologies mainly presented the 3D characteristic of corner stall, but not the unsteady characteristic. In this thesis, both the unsteady and the 3D characteristics are considered.

In general, there are two layouts of measurement section for PIV: perpendicular or parallel to the axial direction, as illustrated in Figs. 6.5a and 6.5b, respectively. The advantage of the first layout is that the results can clearly present the development of passage vortex. The disadvantage of this layout is that the measurement must be 3C, and the uncertainty in the axial velocity component is at least twice higher than that in other two velocity components. In comparison with the first layout, the second layout can provide the results to illustrate the development of the corner vortex in the spanwise direction. At the same time, this layout can be measured by 2C measurement technique. Additionally, the axial velocity component with relative smaller uncertainty should be obtained. In our experiment, the second layout was chosen. In the following, both LDA and PIV measurements are presented in sections parallel to the axial direction. The two velocity components (u_x, u_y) have been obtained in those sections.

6.4 Mean velocity

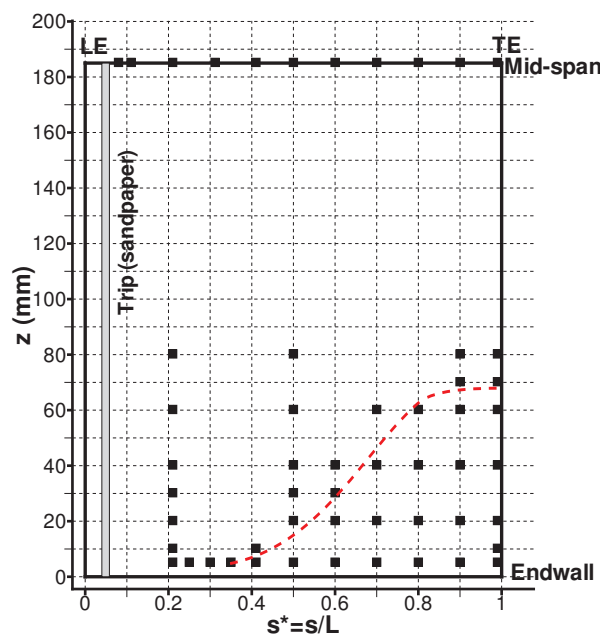


Figure 6.6: LDA measurement stations. Squares, the starting points of the measurement stations. Red dashed line, the connection line of separation points on the suction side according to 2D separation criterion.

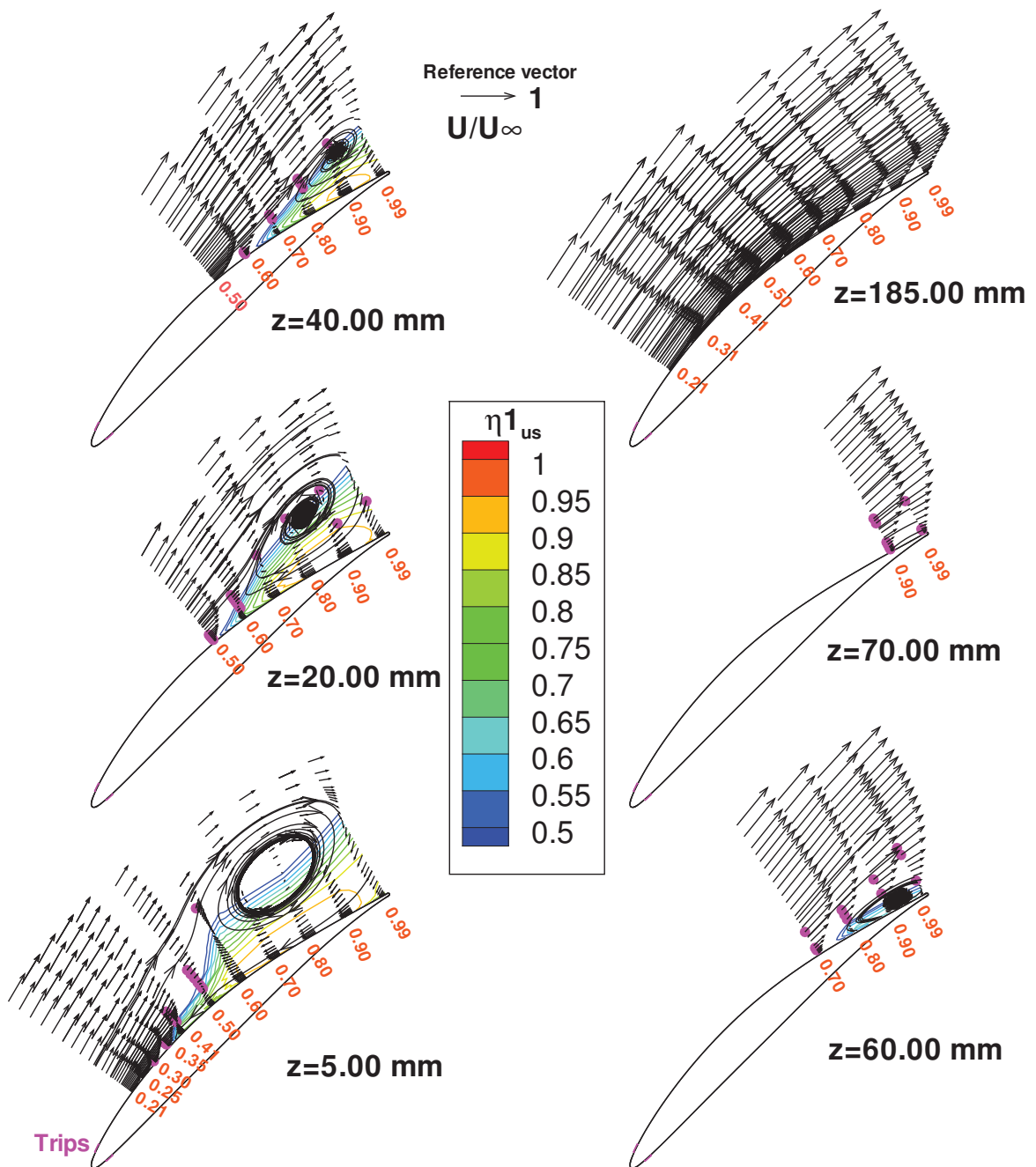


Figure 6.7: LDA experimental results of mean velocity vectors in the cross sections in the spanwise direction, colored by the first backflow coefficient $\eta_{1_{us}}$. Pink points, the points with bi-modal histograms.

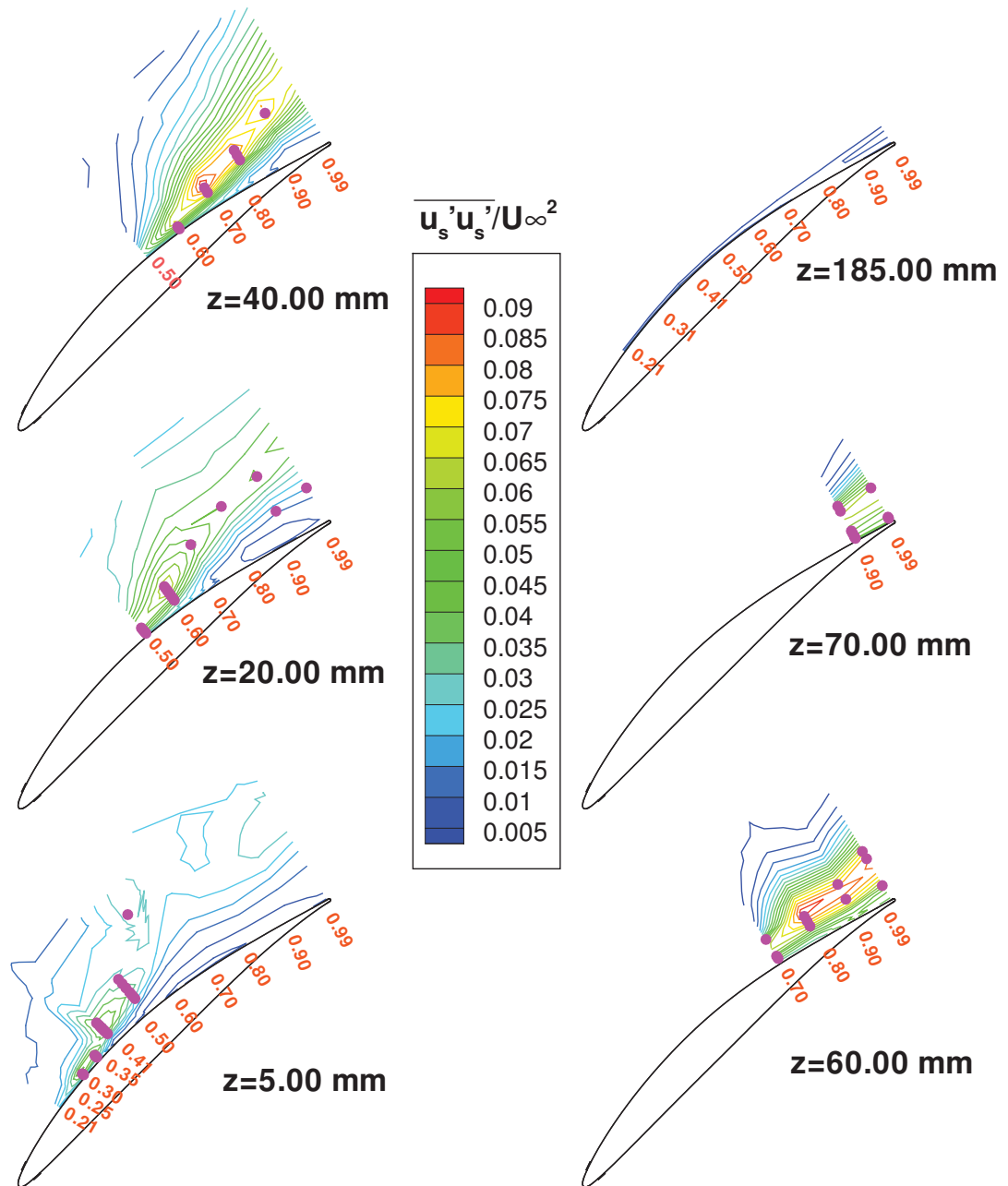


Figure 6.8: LDA experimental results of $\overline{u'_s u'_s} / U_\infty^2$ in the cross sections in the spanwise direction. Pink points, the points with bimodal histograms.

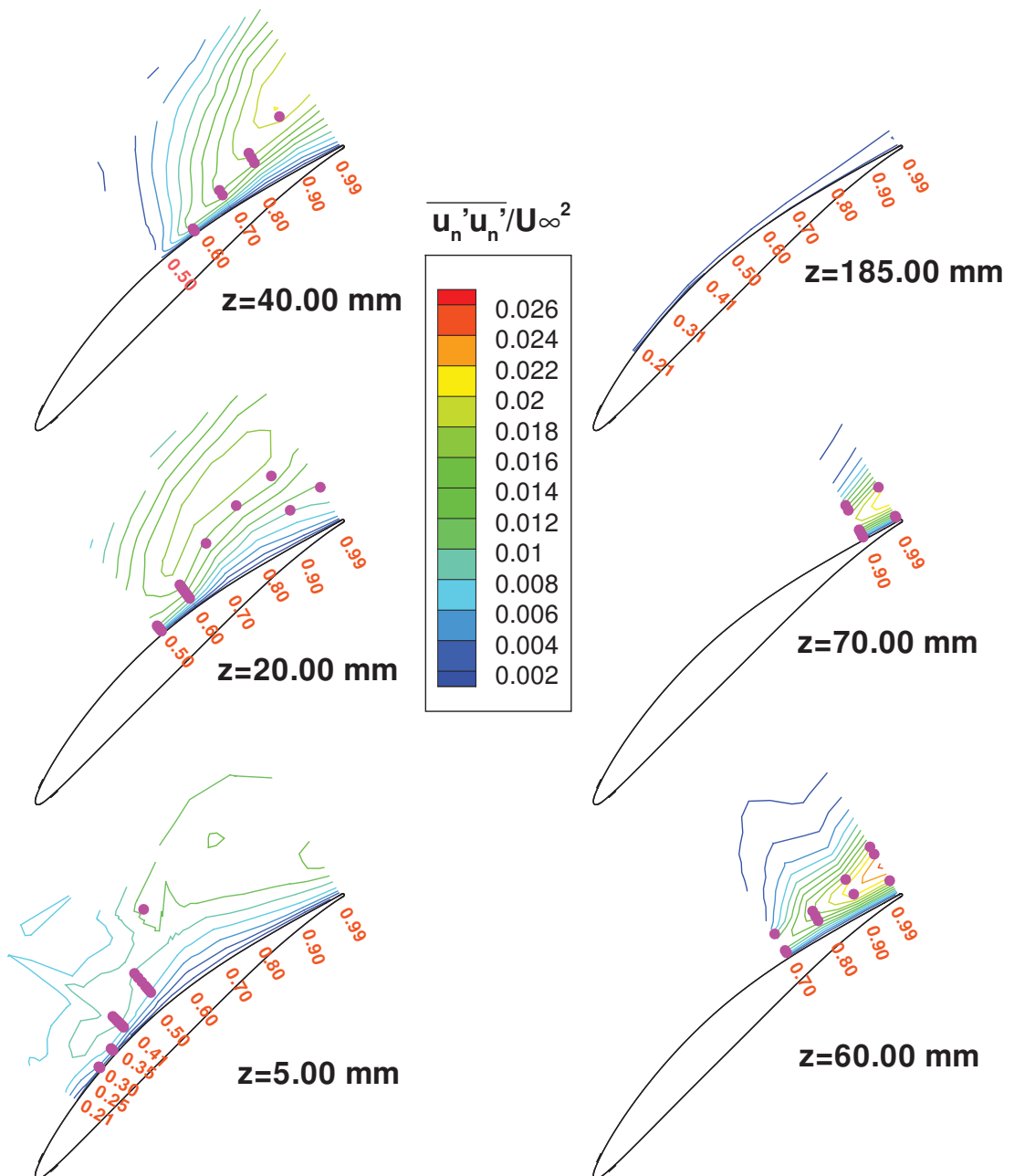


Figure 6.9: LDA experimental results of $\overline{u_n' u_n'} / U_\infty^2$ in the cross sections in the spanwise direction. Pink points, the points with bimodal histograms.

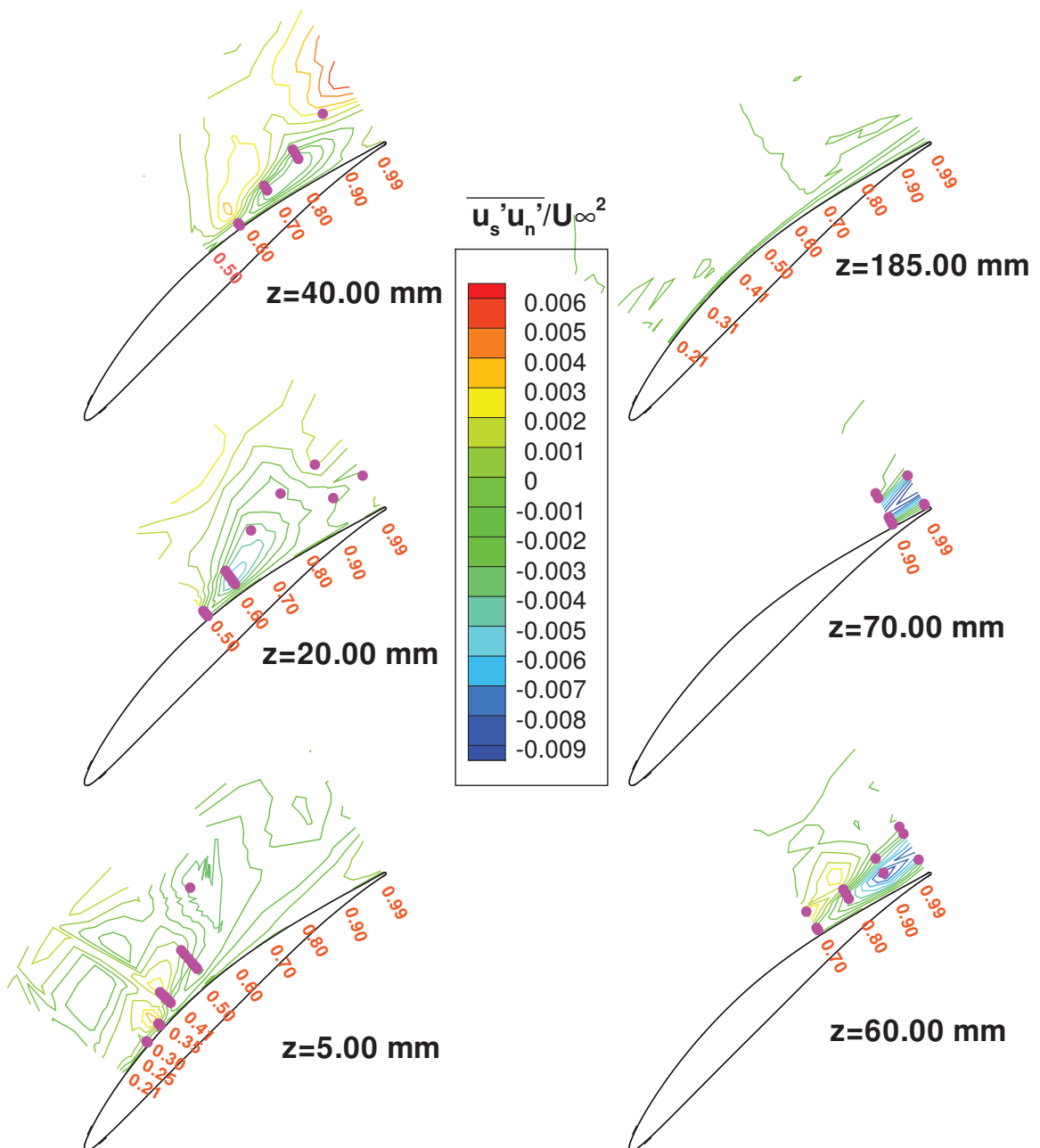


Figure 6.10: LDA experimental results of $\overline{u'_s u'_n} / U_\infty^2$ in the cross sections in the spanwise direction. Pink points, the points with bimodal histograms.

The LDA measurement stations are in the normal direction at the point located on blade suction side. In the process of LDA measurement, the required measurement stations are added gradually, in order to determine the separation point in the cross section and in the spanwise direction. The positions of the LDA measurement stations are shown in Fig. 6.6, in which the squares indicate the starting points of the measurement stations on the suction side.

In this figure, the red dashed line is the connection line of separation points on the suction side according to 2D separation criterion (*i.e.* the separation point is located at the point where $\partial U_s / \partial n = 0$). This red dashed line can be used to show the extent of separation region, despite the limitation of this 2D separation criterion to investigate the 3D separation.

The extent of the separation region is large relatively to the size of the blade. The flow separates at about $s^* = 0.35$ at the closest cross section to the endwall ($z = 5.00$ mm); and the extent of the separation region is about 70 mm in the spanwise direction.

In order to present the mean velocity in detail, the velocity vectors in six cross sections in the spanwise direction are shown in Fig. 6.7. In this figure, some streamlines are also shown to investigate the flow field. Generally speaking, the flow separates and a vortex thus exists in each cross section in the spanwise direction from $z = 5.00$ mm to $z = 60.00$ mm. Additionally, the extent of separation decreases when z increases.

At cross section $z = 5.00$ mm (closest to the endwall), the flow starts to separate and the extent of the separation region is larger compared with other cross section. The flow separates just downstream $s^* = 0.35$. The core of vortex is located at $n \approx 26$ mm & $s^* \approx 0.80$. Another significant phenomenon in this cross section is that the streamlines have a jump between $s^* = 0.50 \sim 0.60$.

At $z = 20.00$ mm, the flow separates just downstream $s^* = 0.50$; and the core of the vortex is located at $n \approx 20$ mm & $s^* \approx 0.85$. The jump of streamlines found at $z = 5.00$ mm disappears.

At $z = 40.00$ mm, the flow separates near $s^* = 0.65$; and the core of the vortex is located at $n \approx 15$ mm & $s^* = 0.90$. The extent of the separation region becomes a little oblate.

At $z = 60.00$ mm, the flow separates near $s^* = 0.75$; and the core of the vortex is located at $n \approx 4$ mm & $s^* = 0.95$. The extent of the separation region is very small and is just limited to the region near the trailing edge.

At $z = 70.00$ mm, the flow doesn't separate. However from the experimental results of back-flow coefficients that will be investigated below, the flow very near the suction side is close to separation.

At $z = 185.00$ mm (the mid-span), the flow is far from separation. It has been investigated in detail in Chapter 5.

In order to show a global view and assist in investigating the flow field, all the cross sections of LDA experimental results are shown in Fig. 6.11. In this figure, the red points and yellow points indicate the separation points and the cores of the vortex in the corresponding cross

section, respectively. This figure clearly shows that the flow separates in the corner region and the low-velocity flow accumulates in this region.

The experimental results of the Reynolds stresses are shown in Figs. 6.8~6.10, which will be used below. Besides the experimental results, the numerical results can be found in Appendix D.5. Generally speaking, all the numerical results can capture the overall pattern of corner stall, but not the flow details.

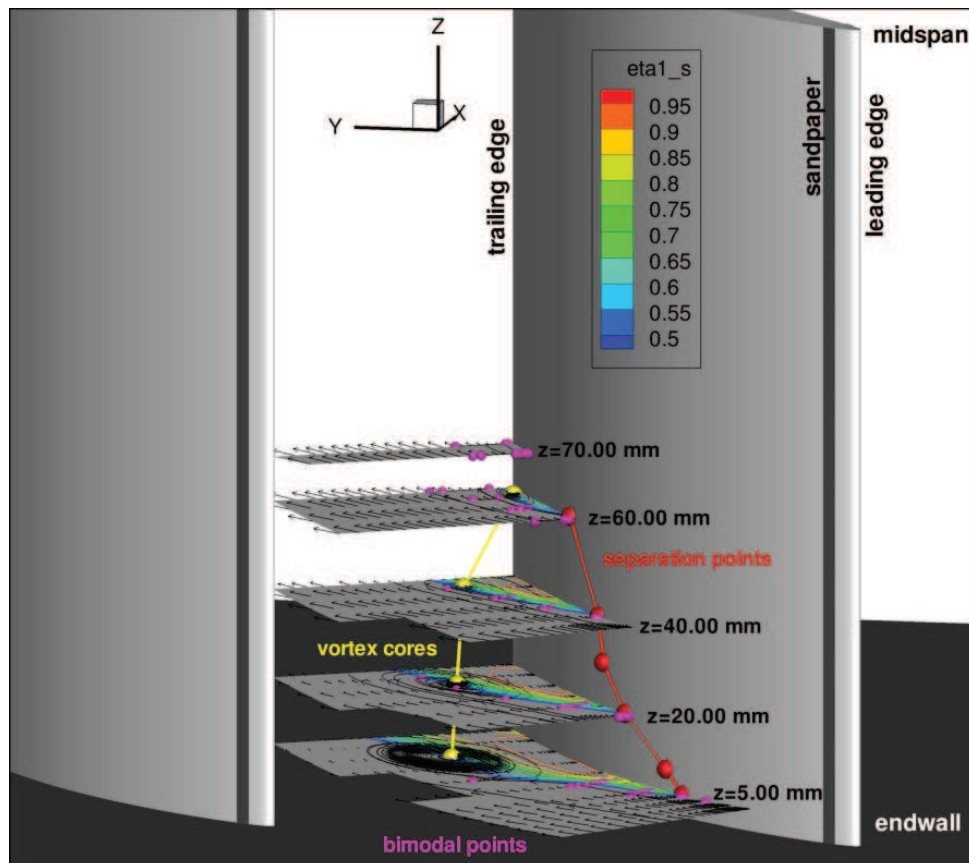


Figure 6.11: LDA experimental results. Red points, separation points. Yellow points, cores of vortices. Pink points, points with bimodal histograms.

6.5 Comparisons of PIV and LDA

The measurement methods of PIV and LDA have been introduced in Sections 3.2.5 and 3.2.6, respectively. The comparisons of the results of PIV and LDA will be presented in this section.

First of all, the global view of the velocity flow field are compared with Fig. 6.12a and Fig. 6.11. Both of these two experimental results show that the low velocity flow accumulates in the corner region. However, the extent of the corner stall of PIV is smaller than that of LDA. In the spanwise, the extents of corner stall of PIV and LDA are about 60.00 mm and 70.00 mm, respectively.

In order to show the differences in the pitchwise, the PIV and LDA experimental results at $z=20.00$ mm are compared. They are shown in Fig. 6.12b and Fig. 6.7, respectively. From the comparison, the extent of corner stall in the pitchwise of PIV is obviously smaller than that of LDA.

The mean velocities of PIV and LDA are then compared in some measurement stations. The measurement stations $s^*=0.80$ (near the trailing edge) at different distance from the end-wall ($z=185.00$ mm, 60.00 mm, 40.00 mm, 20.00 mm) are chosen.

The comparisons at $z=185.00$ mm (mid-span) are shown in Fig. 6.13b. Far from the blade surface ($z>3$ mm), the difference of each mean velocity component (the axial velocity U_x or the pitchwise velocity U_y) is less than 1%. Therefore the experimental results of PIV and LDA are in good agreement with each other. However this agreement does not exist near the blade surface ($z<3.00$ mm), where the difference of each mean velocity component is larger than 5% and increases significantly when approaching to the blade surface. This is obviously due to the problem of reflection of the PIV laser sheet close to the surface.

The comparisons at $z=20.00$ mm (very near the endwall) are shown in Fig. 6.13e. The differences between PIV and LDA are more than 200%, not only near the endwall but also far from the endwall. For example, the distances from the endwall to the points where $U_x=0.0$ of PIV and LDA are about 7.00 mm and 20.00 mm, respectively. Therefore at this measurement station the experimental results of PIV and LDA are totally different.

The comparisons at $z=60.00$ mm and 40.00 mm are shown in Figs. 6.13c-d. The comparisons at these two measurement stations are similar to that at $z=20.00$ mm. This shows that the difference increases from the mid-span to the endwall.

Because of the agreement of PIV and LDA at mid-span, this is not a problem of measurement instrumentation. The differences are generated by a change of the size of the separation in the corner region. It could be explained by a difference in the experimental set-ups when measuring the velocity with the two techniques. No obvious reason were found, but three

sources of difference have been identified:

- The first source is the difference of the position of the generator of seeding particles. In the experiment of PIV, the generator was laid in the inlet of the wind tunnel and upstream of the fan. In the experiment of LDA, the generator was laid in the cave of the wind tunnel.
- The second source is the difference of the intrusions in the set-ups. With the set-up of PIV (Figs. 3.26 and 3.27), the flow field is intruded by **the support equipment** of the laser head.
- A tent used to block the sun light has been placed upon the cascade in the experiment. This could modify the outlet conditions of the cascade.

The flow field at $i=4^\circ$ has also been measured by the oil visualization and the five-hole pressure probe. These results are shown in Fig. 6.3 and Fig. 4.14. The extents of corner stall can be determined indirectly from these experimental results. They are more consistent with the LDA measurements.

Therefore, the experimental results of PIV are only **qualitatively** used; and the experimental results of LDA are **quantitatively** used.

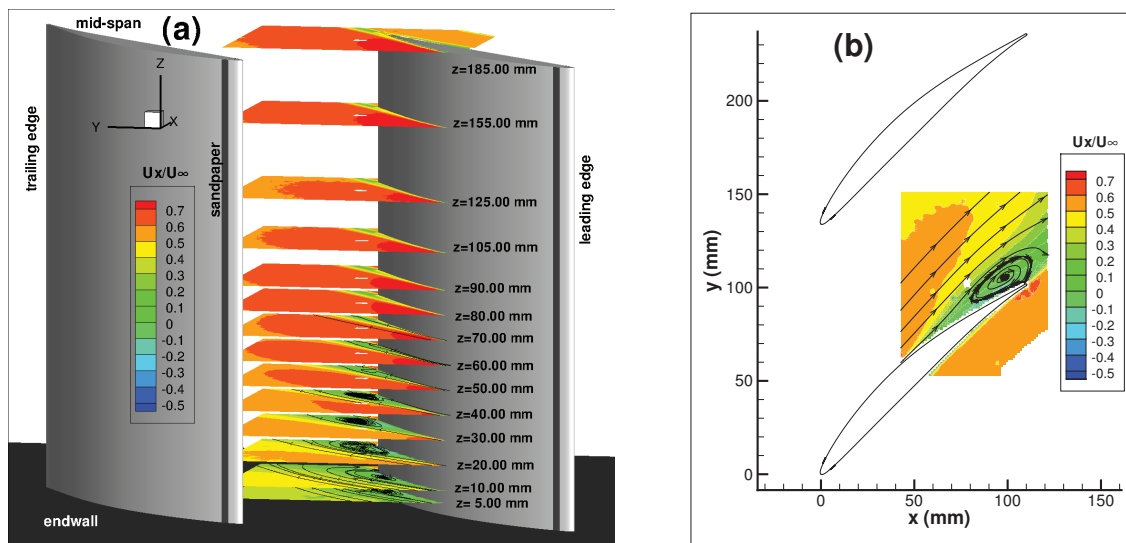


Figure 6.12: PIV results of mean axial velocity, $i=4^\circ$: (a) all measurement stations; (b) $z=20.00$ mm.

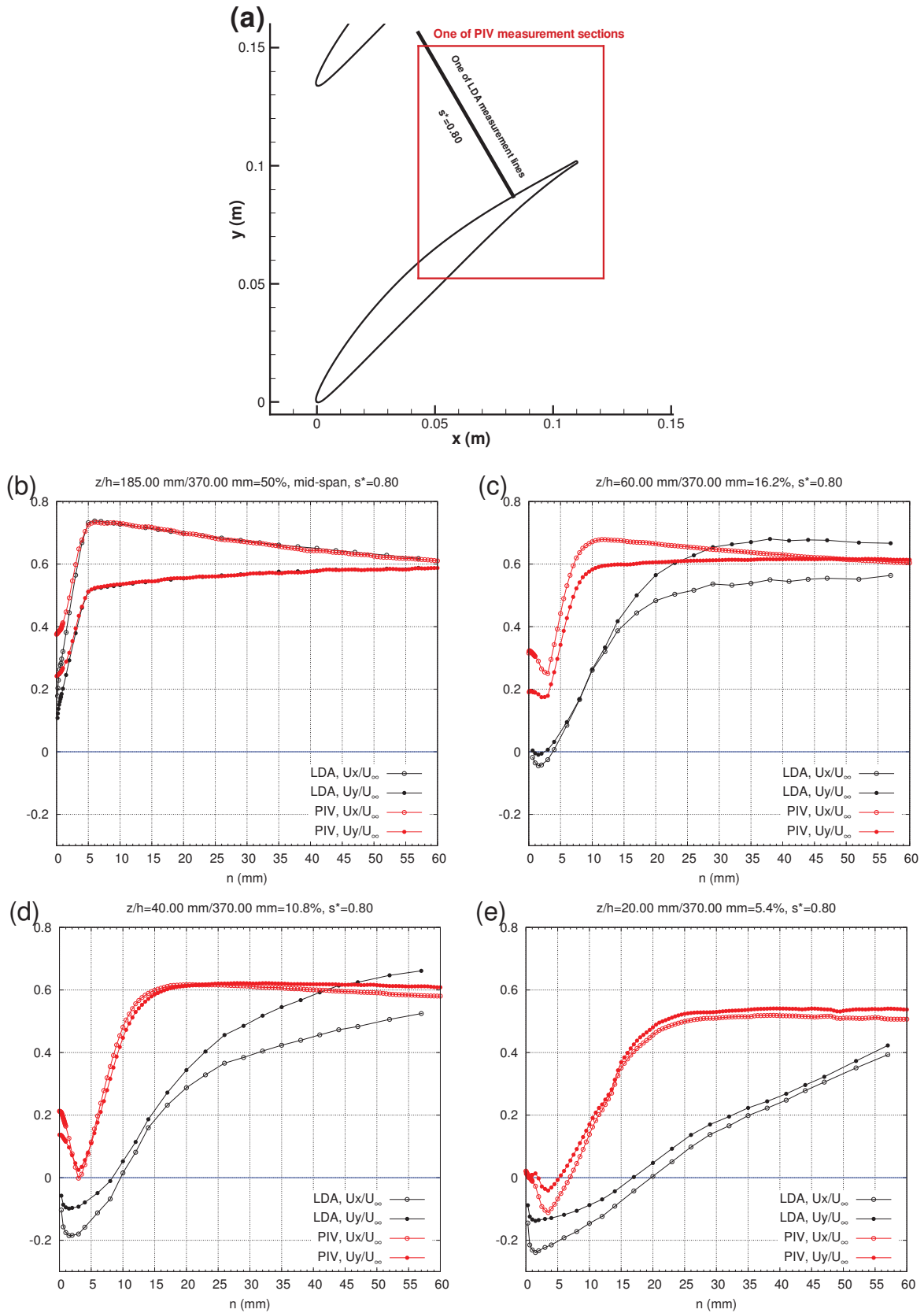


Figure 6.13: Comparison of mean velocities between LDA and PIV along the line $s^* = 0.80$ in $x - y$ plane, $i = 4^\circ$. (a) Location of the line $s^* = 0.80$; $z =$ (b) 185.00 mm, mid-span, (c) 60.00 mm, (d) 40.00 mm, (e) 20.00 mm.

6.6 Backflow coefficients

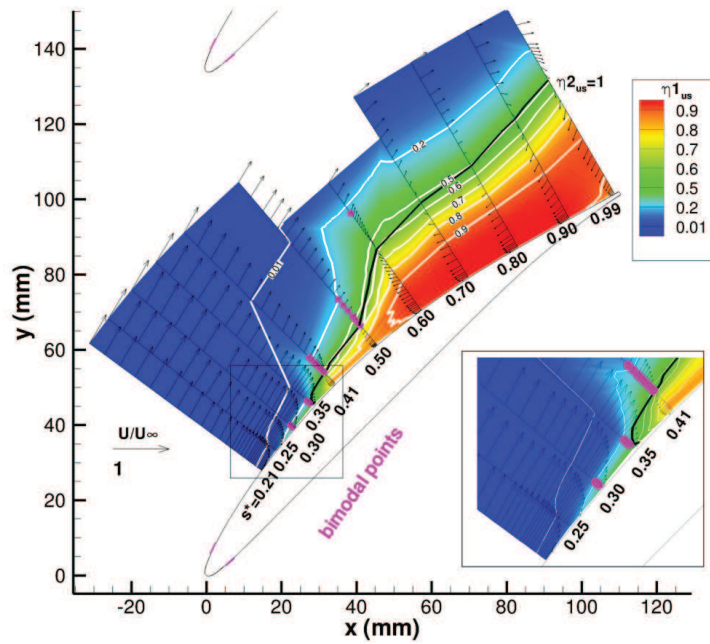


Figure 6.14: Experimental results of backflow percent coefficients in $z=5.00$ mm, including velocity vectors and the locations of bimodal points.

According to their definitions (η_1 , Eq. 3.78 and η_2 , Eq. 3.79), backflow percent coefficients can be used to explain the unsteady feature of the flow field. For example, η_1 has been used by [Simpson *et al.* \(1981a,b\)](#) to investigate the separation process of turbulent boundary layer (see Fig. 5.10).

In this section first of all, η_1 of the streamwise velocity component is used to analyze the development of the flow in the cross section $z=5.00$ mm (see Fig. 6.14). Generally speaking, $\eta_{1_{u_s}}$ increases reasonably in the separated region. In the first and second measurement stations $s^*=0.21$ and 0.30 , $\eta_{1_{u_s}} < 0.01$ in most of the parts while the flow is between the states of incipient detachment and intermittent transitory detachment (i.e. $0.01 < \eta_{1_{u_s}} < 0.2$) in region very near the blade surface. At the following measurement stations $s^*=0.30$ and 0.35 near the blade suction side, the flow already comes to the state between intermittent transitory detachment and transitory detachment (i.e. $0.2 < \eta_{1_{u_s}} < 0.5$). Then $\eta_{1_{u_s}}$ reaches 0.5 between $s^*=0.35$ and 0.41 . The extent of high $\eta_{1_{u_s}}$ jumps in the region $s^*=0.50$ and 0.60 . In the left measurement stations ($s^*=0.60 \sim 0.99$), backflow dominates most of the region.

Besides η_1 , η_2 of the streamwise velocity component is also shown in Fig. 6.14. The contour line $\eta_{2_{u_s}}=1$ (the black line) is inconsistent slightly with the contour line $\eta_{1_{u_s}}=0.5$. It means that the histograms of velocity in this region are not symmetrical which will be discussed in detail below.

6.7 Bimodal histograms of velocity

Bimodal histograms of velocity, which has two peaks, are found in our experiment. In this section at first, the bimodal histograms in the literature will be reviewed, in order to help to analyze this phenomenon in our experiment. Then the properties of velocity histograms in our experiment are presented, including the mathematical property, the positions and the development. Finally, an interpretation of the physics of bimodal behaviour is proposed.

6.7.1 Review of bimodal histogram in the literature

In order to help to analyze the phenomenon of bimodal histograms in our experiment, the bimodal histograms in the literature will be reviewed here. The bimodal histograms in the literature are mainly found and discussed in the junction flow. This phenomenon has also been found in a linear compressor cascade; however the physics was not completely interpreted in this situation.

6.7.1.1 In junction flow

Bimodal histograms that have two peaks widely exist in the junction flows. The junction flows occur when a boundary layer encounters an obstacle attached to the same surface. The most famous model of junction flow is Rood wing (named after its designer, Rood E. D.) mounted on a flat plate (see Fig. 6.15a). A comprehensive review of experimental studies of such flows and extensive discussion of their underlying physics can be found in [Simpson \(2001\)](#). There are also a lot of numerical simulations of such flows in the literature. A recent comprehensive review of both the experiments and simulations can be found in [Gand \(2011\)](#).

[Devenport & Simpson \(1990\)](#) were the first to report the bimodal velocity probability phenomenon using 3C LDA measurements around the Rood wing. The mean velocity vectors in the plane of symmetry in front of a Rood wing is shown in Fig. 6.15b. A typical bimodal histogram for streamwise velocity component is shown in the left top of this figure, and the bimodal flow zone for streamwise velocity component enclosed by solid line. [Devenport & Simpson \(1990\)](#) also showed that the flow in this zone switched aperiodically between two basic modes: the “backflow mode” and the “zero-flow mode”. In the backflow mode (see Fig. 6.15c), the return flow is able to penetrate far upstream and forms a strong wall reverse jet. In the zero-flow mode (see Fig. 6.15d), the return flow is unable to penetrate upstream and is ejected vertically upward away from the wall.

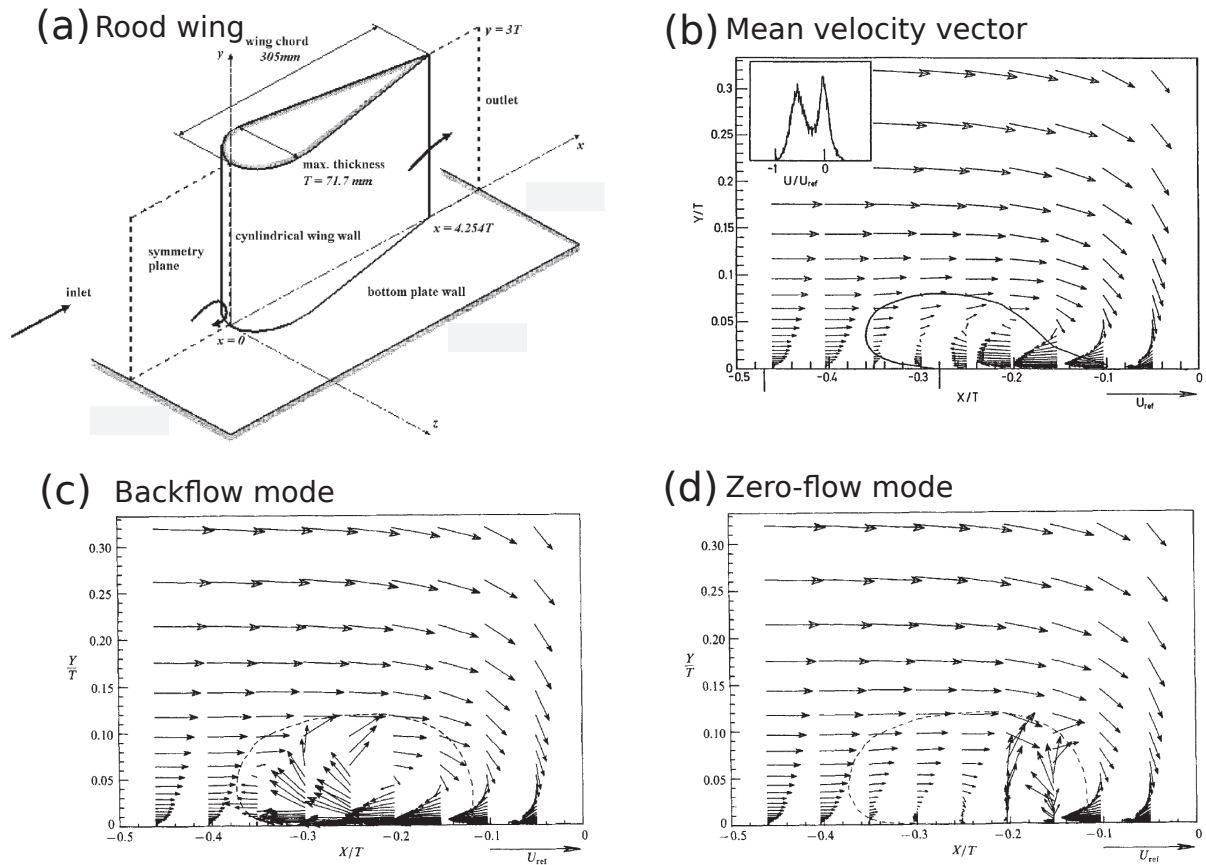


Figure 6.15: Junction flow, from [Deavenport & Simpson \(1990\)](#) and [Simpson \(2001\)](#).

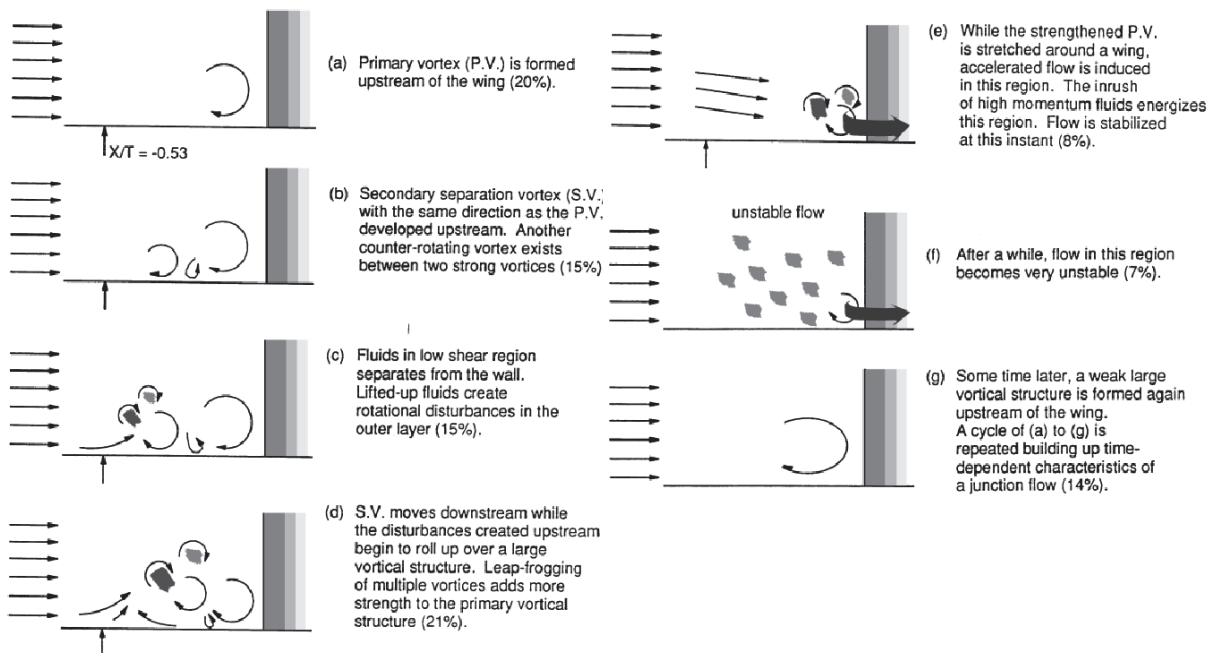


Figure 6.16: Descriptive model for the sequence of flow events in the nose region of a Rood wing-body junction, from [Kim et al. \(1991\)](#) and [Simpson \(2001\)](#). The percentage in parenthesis represents the approximate time proportion of the event.

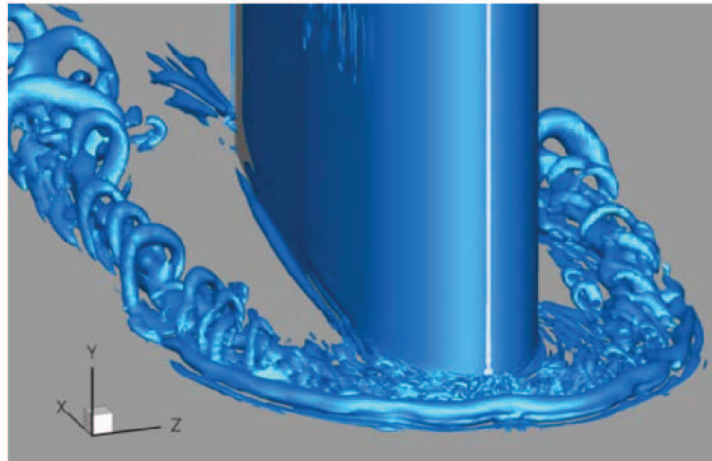


Figure 6.17: Instantaneous snapshot of 3D coherent structures around the wing visualized using the q criterion ($q=1.0$), DES from Paik *et al.* (2007).

Kim *et al.* (1991) proposed a schematic of the self-induced unsteady phenomena in front of the leading edge, as shown in Fig. 6.16. At the beginning of the sequence of flow events (Fig. 6.16a), a large horseshoe vortex exists in front of the leading edge, produced by high-velocity free-stream fluid impinging on and moving down the leading edge. Because the vortex lines of this flow are stretched around the wing, the cross-sectional area of the vortex decreases at increasing times (Figs. 6.16b-g). Meanwhile, a second separation vortex forms downstream of the separation (Fig. 6.16b), increasing with circulation strength at increasing times (Figs. 6.16c-d). Other third vortices can be formed (Figs. 6.16c-d). At some time, the second and third vortices merge together, merge with the front of the horseshoe vortex, or move up over the horseshoe vortex in leapfrog fashion before merging with the horseshoe vortex. The resulting merger creates a stronger large horseshoe vortex, which is stretched around the wing. During this phase of this aperiodic sequence, the forward flow moves much closer to the wing (Fig. 6.16e), and this acceleration briefly stabilizes the flow. The flow then becomes unstable (Fig. 6.16f), a new large-scale horse-shoe vortex forms, and the aperiodic process begins again (Fig. 6.16g).

This phenomenon is consistent with large-scale low-frequency unsteadiness of the instantaneous flow structure associated with the horseshoe vortex. To elucidate the physical mechanisms that lead to the onset of the bimodal dynamics, Paik *et al.* (2007) carried out numerical simulation for the experimental configuration of Devenport & Simpson (1990) using the detached eddy simulation (DES) approach. They visualized the instantaneous 3D structure of the horseshoe vortex using the q criterion¹, as shown in Fig. 6.17. They claimed that the bimodal dynamics is due to the continuous and aperiodic interplay of two basic states: an organized

¹ $q = \frac{1}{2} (\|\Omega\|^2 - \|\mathbf{S}\|^2)$, where $\|\Omega\| = \text{tr}[\Omega\Omega^t]^{1/2}$, $\|\mathbf{S}\| = \text{tr}[\mathbf{S}\mathbf{S}^t]^{1/2}$; $\mathbf{S} = 1/2[\nabla u + (\nabla u)^t]$, $\Omega = 1/2[\nabla u - (\nabla u)^t]$.

state with a coherent necklace-like horseshoe vortex, and a disorganized state with hairpin vortices wrapping around the horseshoe vortex. They argued also that the emergence of hairpin vortices is the result of a centrifugal instability.

6.7.1.2 In a linear compressor cascade

Bimodal histograms have also been found in the flow field at mid-span of a linear compressor cascade by [Hobson *et al.* \(1998\)](#). They measured the velocity flow field in the cascade using 1C LDA. Their measurement stations are shown in Fig. 6.18a. They presented three typical histograms of velocities at station 3. The first point is very near the suction side; the second point is a little farther but also in the boundary layer; the third point is further away and outside the boundary layer. The positions of these three points are also shown in Fig. 6.18a. The bimodal histogram only existed at the second point, as shown in Figs. 6.18b-c. However [Hobson *et al.* \(1998\)](#) only associated the bimodal histograms with the backflow coefficients, and did not interpret the physics of this phenomenon.

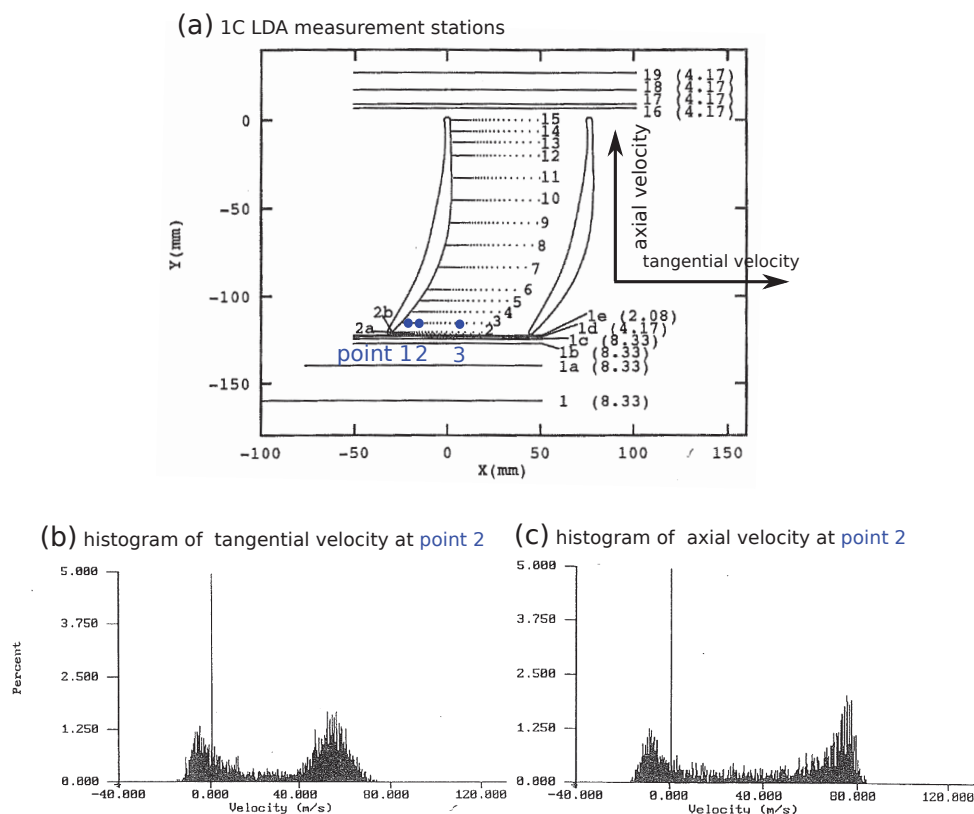


Figure 6.18: Bimodal histograms in a linear cascade, from [Hobson *et al.* \(1998\)](#). (a) LDA measurement stations; (b-c) the histograms of two velocity components at the point 2.

6.7.2 Illustration of bimodal histograms

In order to illustrate the phenomenon of bimodal histograms in our experiment, the point A ($z=5.00$ mm & $s^*=0.41$ & $n=6.50$ mm) is taken as an example. The position of the point A is illustrated in Fig. 6.19a. In the process of LDA experiment, the two velocity components measured at each measurement point are the axial velocity u_x , and pitchwise velocity u_y , which are in the Cartesian coordinate system of the cascade (e.g the (x, y) coordinates). This velocity has also been decomposed into local streamwise velocity u_s and normal velocity u_n , which are in the curvilinear coordinate system of the blade suction side (e.g the local (s, n) coordinates). The relation between these two decompositions is

$$\vec{u}_x + \vec{u}_y = \vec{u}_s + \vec{u}_n. \quad (6.1)$$

The directions of u_x , u_y , u_s and u_n at the point A are also shown in Fig. 6.19a.

The probability density function (PDF) of the 2D velocity at this point is shown in Fig. 6.19b. The corresponding contour of this 2D PDF is shown in Fig. 6.19c. Two peaks exist obviously in this PDF. This is the phenomenon of bimodal histogram. In Figs. 6.19b-c, the velocity components u_x and u_y are chosen to show the PDFs. According to Eq. 6.1, the PDFs using other two components u_s and u_n should also have two obvious peaks, i.e. the two peaks exist in the PDFs no matter which coordinate system is chosen.

The PDFs of velocity components in the (x,y) coordinates and the (s,n) coordinates are shown in Fig. 6.19d. In the PDFs of u_s , u_x or u_y , the relative position of the two distributions is so far that two peaks appear. On the contrary, in the PDF of u_n , the relative position of the two distributions is so close that only one peak appears. It is then worth checking if the velocity components u_s and u_n are statistically **independent** from each other.

According to the definition of **independent**¹, with the velocity expressed in the (s, n) coordinates, it leads to

$$\begin{cases} \text{if } P(u_s, u_n) = P_s(u_s) \cdot P_n(u_n) & , \text{ independent;} \\ \text{if } P(u_s, u_n) \neq P_s(u_s) \cdot P_n(u_n) & , \text{ non-independent.} \end{cases}$$

where P is the PDF of 2D velocities (u_s, u_n) ; P_s and P_n are PDFs of velocity components u_s and u_n , respectively. In the following sections, we will present the experimental results in local (s,n) coordinates and we will state the independency of u_s and u_n .

¹ In mathematics, continuous random variables X_1, \dots, X_n admitting a joint density are all **independent** from each other if and only if

$$P_{X_1, \dots, X_n}(x_1, \dots, x_n) = P_{X_1}(x_1) \cdots P_{X_n}(x_n)$$

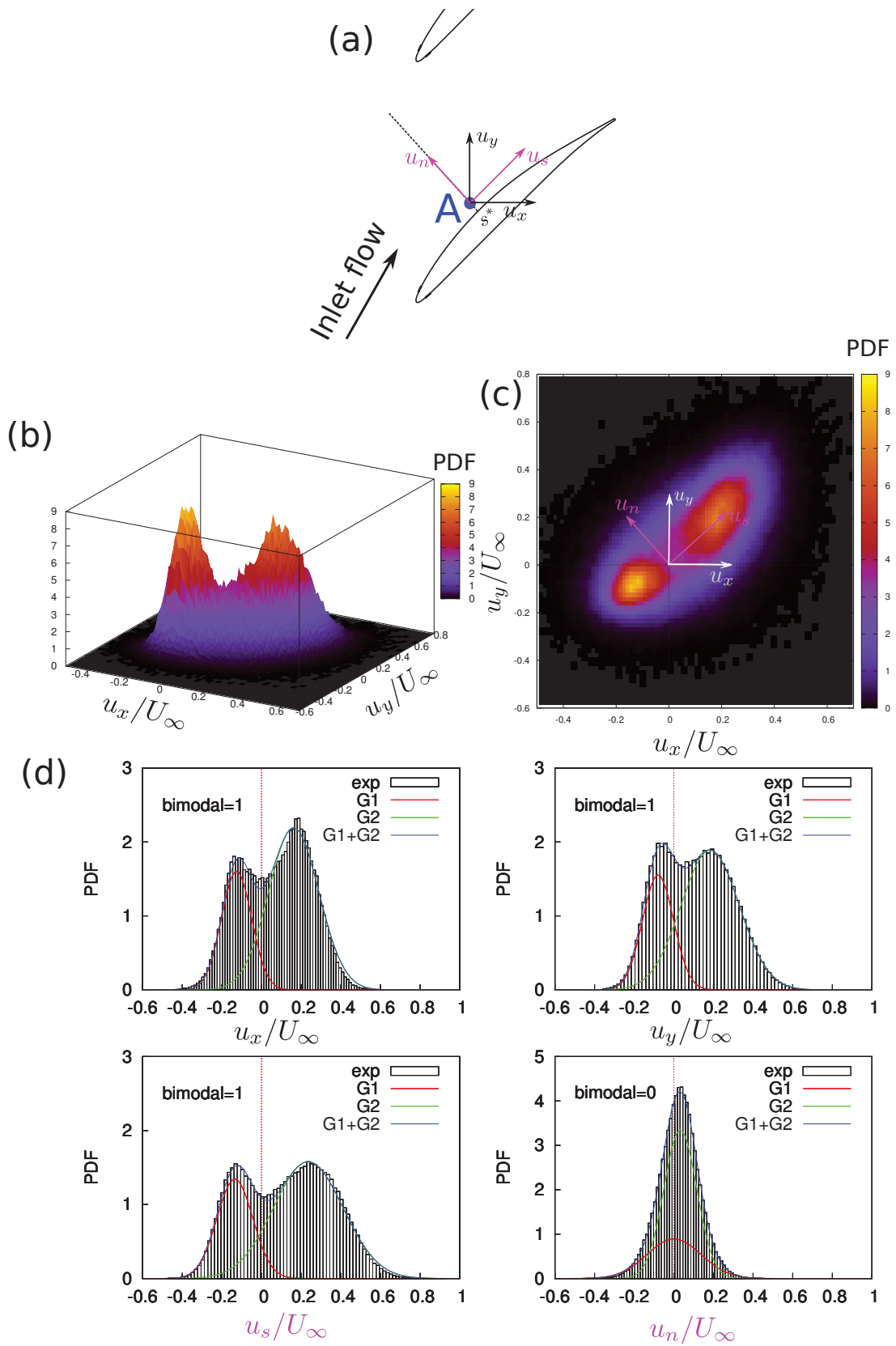


Figure 6.19: Illustration of bimodal behaviour at the measurement point $z=5.00$ mm & $s^*=0.41$ & $n=6.50$ mm.

6.7.3 Positions of bimodal points

From the literature of bimodal histogram reviewed in the previous section, the description of bimodal histogram is just that the histogram has two peaks. This description is qualitative. In order to determine the positions of the bimodal histograms without subjective effects, a quantitative description is needed. Here, the quantitative description (i.e. definition) can be expressed as below:

- Firstly, the PDF of a velocity component is fitted by a smooth line. If this fitting line has a local minimum value, the PDF is called **bimodal histogram**.
- If the PDF of u_s at a point is bimodal, then this point is called **bimodal point**.

In the thesis, the parameter “bimodal” denotes the bimodal property. The PDF is bimodal when “bimodal=1”, on contrary, “bimodal=0”.

The point A in Fig. 6.19 is taken as an example. According to the definition above, the PDFs of u_s , u_x and u_y are bimodal; while the PDF of u_n is not bimodal. Additionally, the point A is a bimodal point.

According to the definition of bimodal points in the previous section, the positions of bimodal points are shown in Figs. 6.7~6.11. Although the bimodal points do not exist in every measurement location, they exist in each cross section in the spanwise direction. The bimodal points mainly appear in the region around the mean interface of separated flow and non-separated flow, and in the region with large Reynolds stresses.

6.7.4 Histogram decomposition

In statistic, a bimodal distribution is a continuous probability distribution with two different modes. Additionally, the distribution of each mode is approximately Gaussian form. For example, the bimodal histograms in the work of [Devenport & Simpson \(1990\)](#) caused by two modes of the flow field, backflow mode and zero-flow mode (reviewed in Section 6.7.1.1). Inspired by this, we proposed that the bimodal histograms in our experiment are also caused by two modes in the flow field. In order to distinguish these two modes, first of all we try to fit the PDF using two Gaussian distributions.

The 1D PDF of velocity u_s , $P(u_s)$, will be fitted by two 1D Gaussian distributions $G_1(u_s; a_1, u_{s1}, \sigma_{u_{s1}})$ and $G_2(u_s; a_2, u_{s2}, \sigma_{u_{s2}})$ with mathematical consideration. The 1D PDF of velocity u_n , $P(u_n)$ will be fitted by two 1D Gaussian distributions $G_1(u_n; a_1, u_{n1}, \sigma_{u_{n1}})$ and $G_2(u_n; a_2, u_{n2}, \sigma_{u_{n2}})$ with mathematical consideration.

$$P(u_s) = G_1(u_s; a_1, u_{s1}, \sigma_{u_{s1}}) + G_2(u_s; a_2, u_{s2}, \sigma_{u_{s2}}) \quad (6.2a)$$

$$P(u_n) = G_1(u_n; a_1, u_{n1}, \sigma_{u_{n1}}) + G_2(u_n; a_2, u_{n2}, \sigma_{u_{n2}}) \quad (6.2b)$$

where

$$G_1(u_s; a_1, u_{s1}, \sigma_{u_{s1}}) = \frac{a_1}{\sqrt{2\pi} \cdot \sigma_{u_{s1}}} \exp\left(-\frac{(u_s - u_{s1})^2}{2\sigma_{u_{s1}}^2}\right) \quad (6.2c)$$

$$G_2(u_s; a_2, u_{s2}, \sigma_{u_{s2}}) = \frac{a_2}{\sqrt{2\pi} \cdot \sigma_{u_{s2}}} \exp\left(-\frac{(u_s - u_{s2})^2}{2\sigma_{u_{s2}}^2}\right) \quad (6.2d)$$

$$G_1(u_n; a_1, u_{n1}, \sigma_{u_{n1}}) = \frac{a_1}{\sqrt{2\pi} \cdot \sigma_{u_{n1}}} \exp\left(-\frac{(u_n - u_{n1})^2}{2\sigma_{u_{n1}}^2}\right) \quad (6.2e)$$

$$G_2(u_n; a_2, u_{n2}, \sigma_{u_{n2}}) = \frac{a_2}{\sqrt{2\pi} \cdot \sigma_{u_{n2}}} \exp\left(-\frac{(u_n - u_{n2})^2}{2\sigma_{u_{n2}}^2}\right) \quad (6.2f)$$

The Gaussian distribution with smaller streamwise velocity is defined as the first distribution.

The requirements are

$$\begin{cases} a_1, u_{s1}, u_{n1}, \sigma_{u_{s1}}, \sigma_{u_{n1}} \in \mathbb{R}, \\ a_2, u_{s2}, u_{n2}, \sigma_{u_{s2}}, \sigma_{u_{n2}} \in \mathbb{R}, \\ 0 < a_1 < 1.0, \\ 0 < a_2 < 1.0, \\ a_1 + a_2 = 1.0, \\ u_{smin} < u_{s1} < u_{s2} < u_{smax}, \\ \sigma_{u_{s1}} > 0, \\ \sigma_{u_{n1}} > 0, \\ \sigma_{u_{s2}} > 0, \\ \sigma_{u_{n2}} > 0. \end{cases} \quad (6.2g)$$

where u_{smin} and u_{smax} are the minimum and maximum values of u_s , respectively. After the fitting criterion (here is termination tolerance on the residual sum of squares) is specified, the solution of fitting is unique. In the thesis, the converged solutions have been obtained through MATLAB[®] code, which has been introduced in Appendix E.

After calculating, there are converged solutions for velocity components at each measurement point. Because the fitting depends on the assumption that the bimodal histograms in the experiment are caused by two modes of the flow field. The success of the fitting means that this assumption is reasonable. The fitting results of the velocity components at the measurement point A are also shown in Fig. 6.19d, in which the red and green lines indicate the first and the second mode respectively.

Some parameters that can be determined from the results of decomposition are introduced. These parameters will be used in the following sections.

In order to indicate the relative position of these two Gaussian distributions, we define a parameter α (taking u_s as an example),

$$\alpha = \frac{u_{s2} - u_{s1}}{\sigma_{u_{s1}} + \sigma_{u_{s2}}} \quad (6.3)$$

After the decomposition, the mean vectors of the first and second Gaussian distributions can be determined approximately (see Fig. 6.20). The mean vector of the first Gaussian distribution is from the origin point (0,0) to the point (u_{s1}, u_{n1}) . The mean vector of the second Gaussian distribution is from the origin point (0,0) to the point (u_{s2}, u_{n2}) . The angles of these two mean vectors are noted as θ_1 and θ_2 . In mathematics, Eq. 6.7.2 comes to

$$\begin{cases} \text{if } \theta_1 - \theta_2 = 0^\circ \text{ or } 180^\circ & , \text{ independent;} \\ \text{if } \theta_1 - \theta_2 \neq 0^\circ \text{ and } 180^\circ & , \text{ non-independent.} \end{cases}$$

Thus in the example of Fig. 6.20, the velocity components are non-independent.

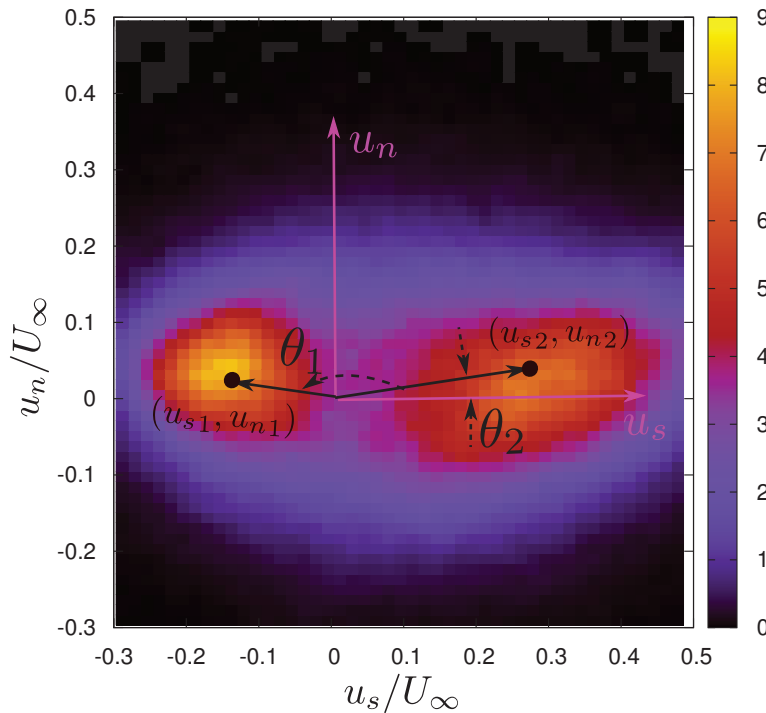


Figure 6.20: Sketch of angles θ_1 and θ_2 .

6.7.5 Development of histograms along the measurement station

In order to show the development of the histograms as a function of wall distance, measurement station $s^*=0.41$ & $z=5.00$ mm is taken as an example. It is located near the endwall and just downstream of the mean separation point in its cross section in the spanwise direction. The location of this measurement station can be seen in Fig. 6.7. The measurement points are within $0.30 \text{ mm} \leq n \leq 57.00 \text{ mm}$.

The series of 2D PDFs are shown in Figs. 6.21 and 6.22. We focus on the development of the peaks (e.g. when n increases). Near the endwall, only one peak exists. Then a second peak appears nearly at $n=4.50$ mm. Following, the first peak decreases gradually; at the same time

the second peak increases gradually. The first peak disappears nearly at $n=10.00$ mm; and only the second peak exists.

The corresponding PDFs of velocity components u_s and u_n are shown in Figs. 6.23 and 6.24, respectively. The bimodal PDFs don't exist in the PDFs of u_n . In fact after checking all the measurement points in the experiment, the bimodal PDFs never exist in the PDFs of u_n .

At this measurement station, the bimodal points are located mainly at $4.5 \text{ mm} \leq n \leq 10.00$ mm. Fig.6.25 summarizes the bimodal parameters at these bimodal points.

The parameter a_1 is the mixture coefficient, which defines the probability of the first Gaussian distribution. When n increases, a_1 decreases; this is caused by the decrease in the first mode possibility and then the increase of the second mode possibility ($a_2=1-a_1$).

The parameter σ is the standard deviation of a Gaussian distribution, which can express the concentration. The distribution is more concentrated, σ is smaller. In streamwise direction when n increases, $\sigma_{u_{s1}}$ increases and $\sigma_{u_{s2}}$ decreases. This means that the distribution of u_{s2} is more and more concentrated, and is opposite to that of u_{s1} . In normal direction, $\sigma_{u_{n1}}$ are always larger than $\sigma_{u_{n2}}$. When n increases, both of $\sigma_{u_{n1}}$ and $\sigma_{u_{n2}}$ increases slightly.

The parameters u_{s1} , u_{n1} , u_{s2} and u_{n2} express the positions of the mean vectors (see Fig. 6.20). In the streamwise direction, u_{s2} are always larger than u_{s1} , due to the Gaussian distribution with smaller streamwise velocity is defined as the first distribution. When n increases, both u_{s1} and while u_{s2} increases slightly. In the normal direction, the u_{n1} are always smaller a little than u_{n2} . When n increases, both u_{n1} and while u_{n2} increases slightly.

The parameter α (Eq. 6.3) is defined to indicate the relative position of these two Gaussian distributions. The origin objective of the definition of α is to find a parameter to indicate whether a histogram is bimodal or not (e.g. when α is larger than a critical value, the histogram is bimodal). All of the α are larger than 1.0. However the critical value of α is very difficult to fix, for example $\alpha=1.36$ and 1.24 in two non-bimodal points $n=12.00$ mm and 20.00 mm (in Fig. 6.23).

The parameter θ_1 and θ_2 are defined to show the angles of the first and second mean vectors (see Fig. 6.20). When n increases, θ_1 decreases and θ_2 keeps nearly constant, and the difference between these two angles ($\theta_1 - \theta_2$) decreases and is always smaller than 180° . According to Eq. 6.7.4, the two velocity components u_s and u_n are **non-independent** from each other.

The developments of these bimodal parameters at other measurement stations are similar to that at this measurement station.

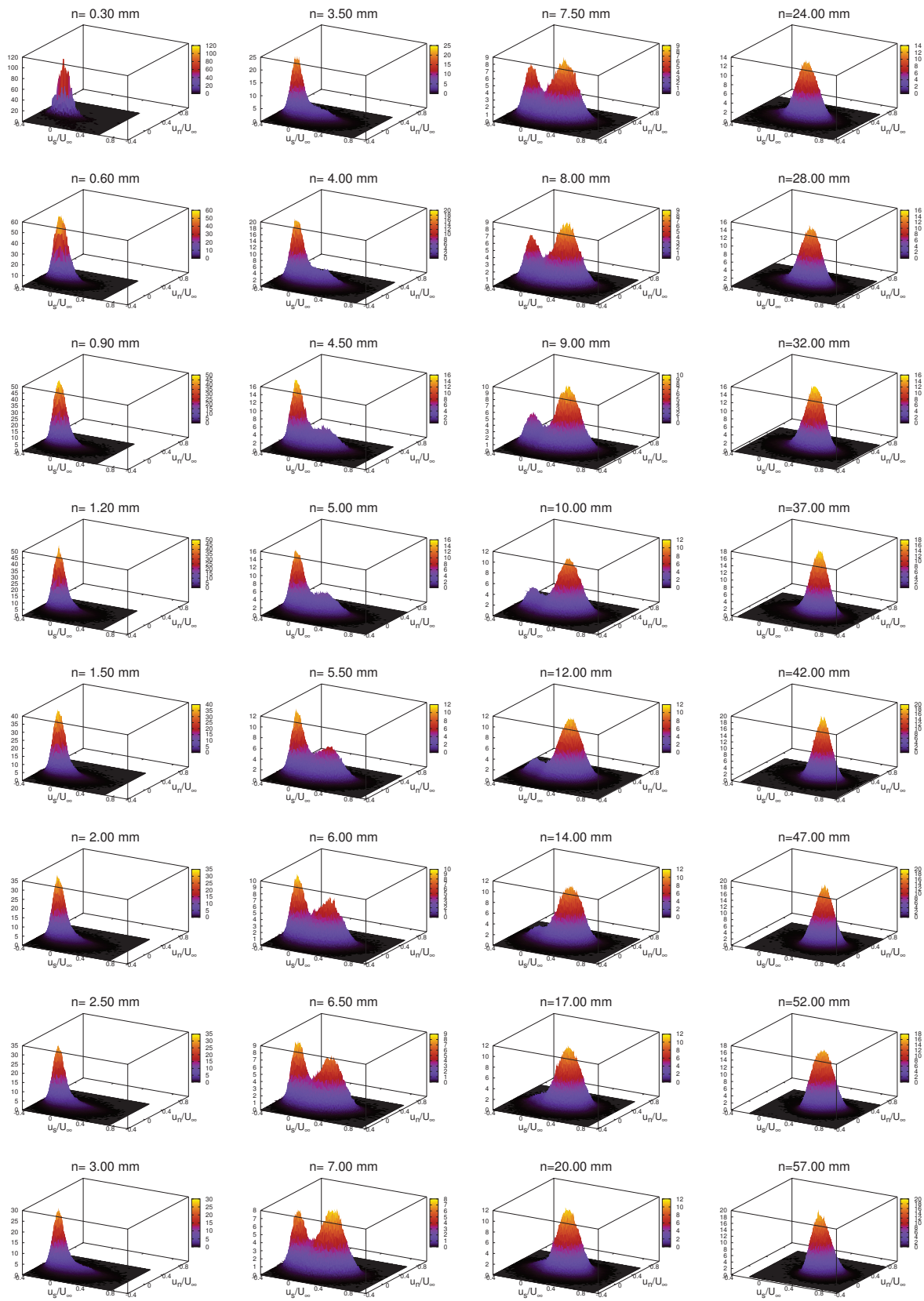


Figure 6.21: PDF of 2D velocity at the measurement station $z=5.00$ mm & $s^*=0.41$.

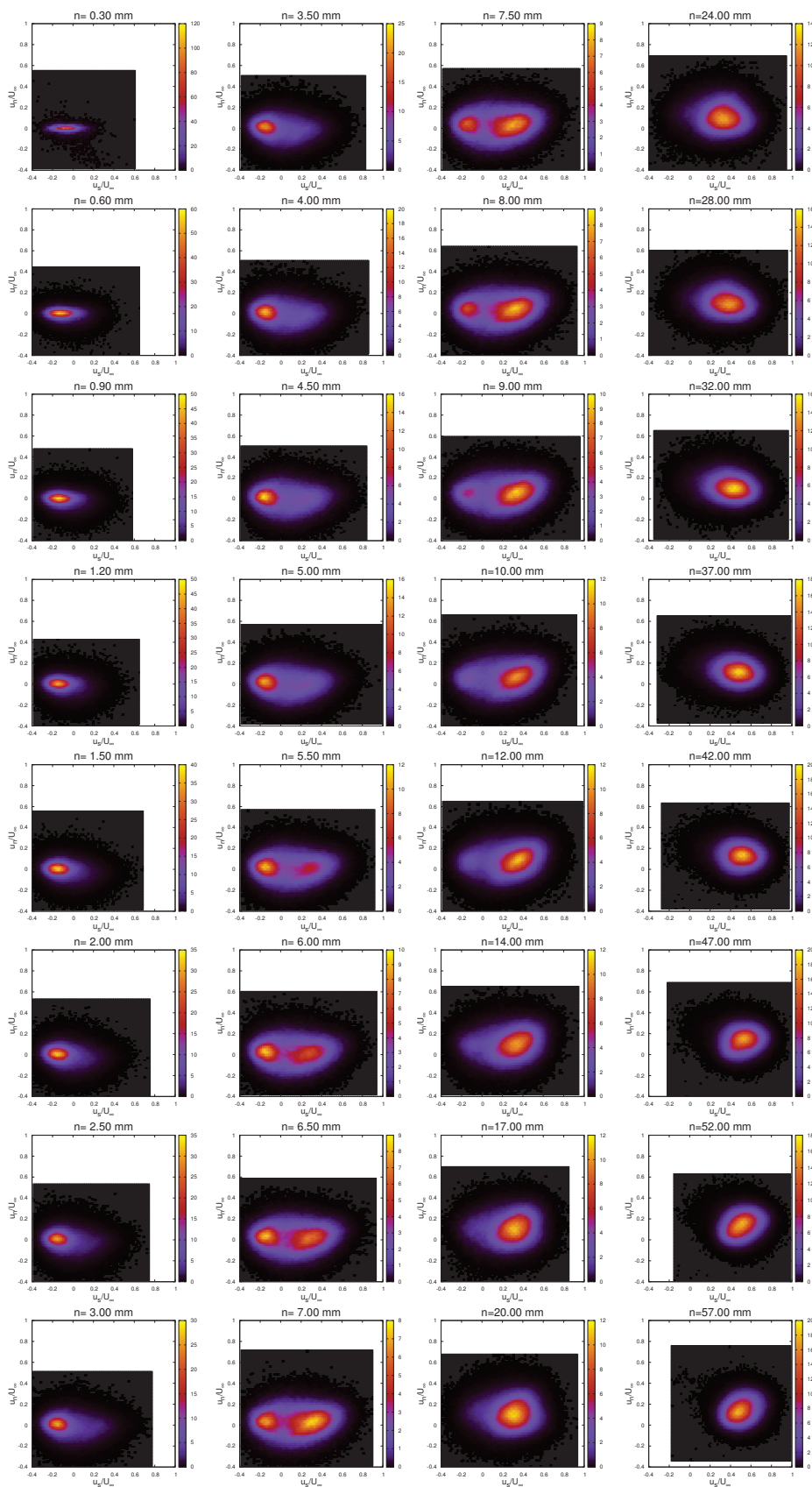


Figure 6.22: Contours of the PDF of 2D velocity at the measurement station $z=5.00$ mm & $s^*=0.41$.

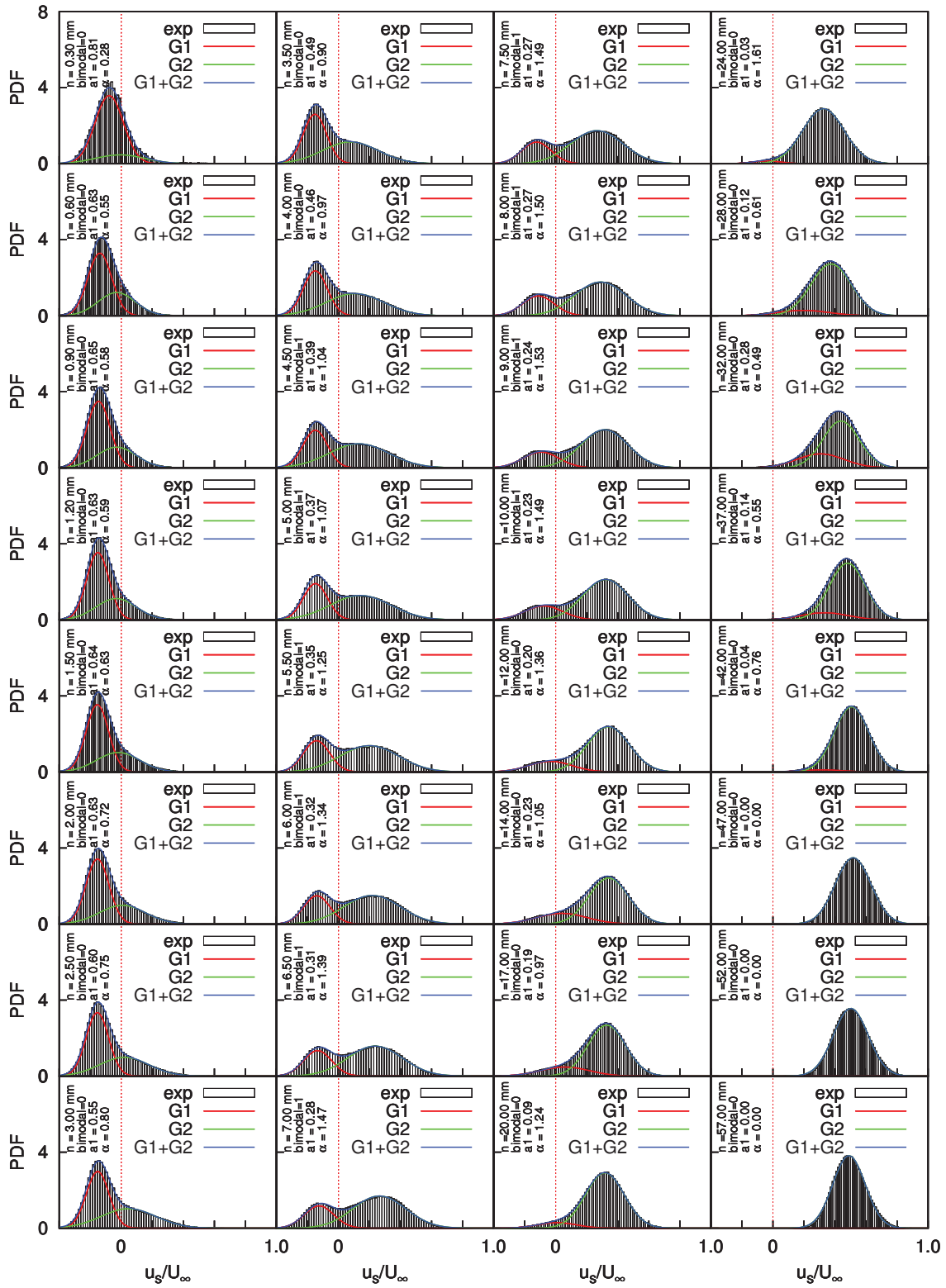


Figure 6.23: PDFs of u_s at the measurement station $z=5.00$ mm & $s^*=0.41$.

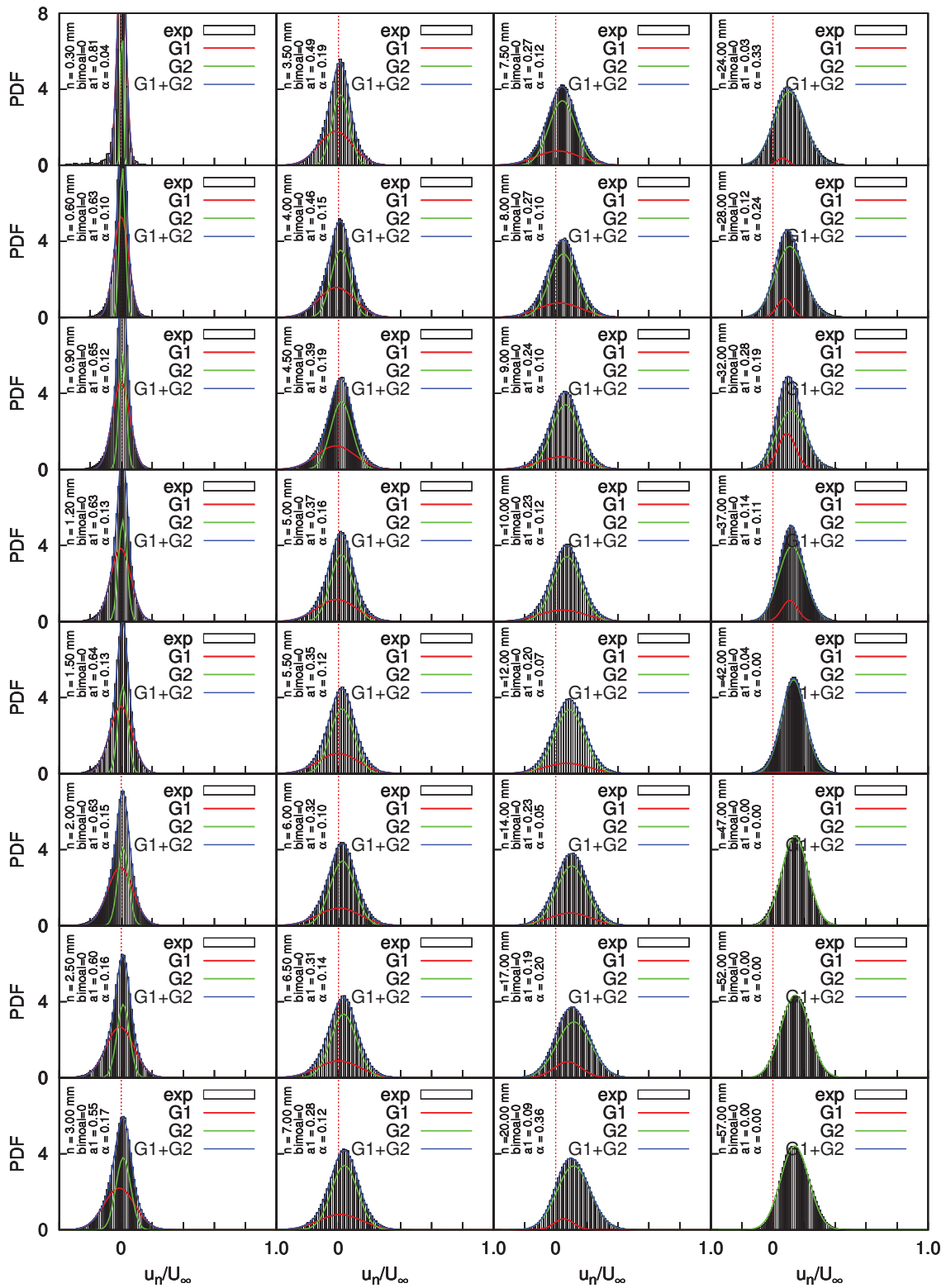


Figure 6.24: PDFs of u_n at the measurement station $z=5.00$ mm & $s^*=0.41$.

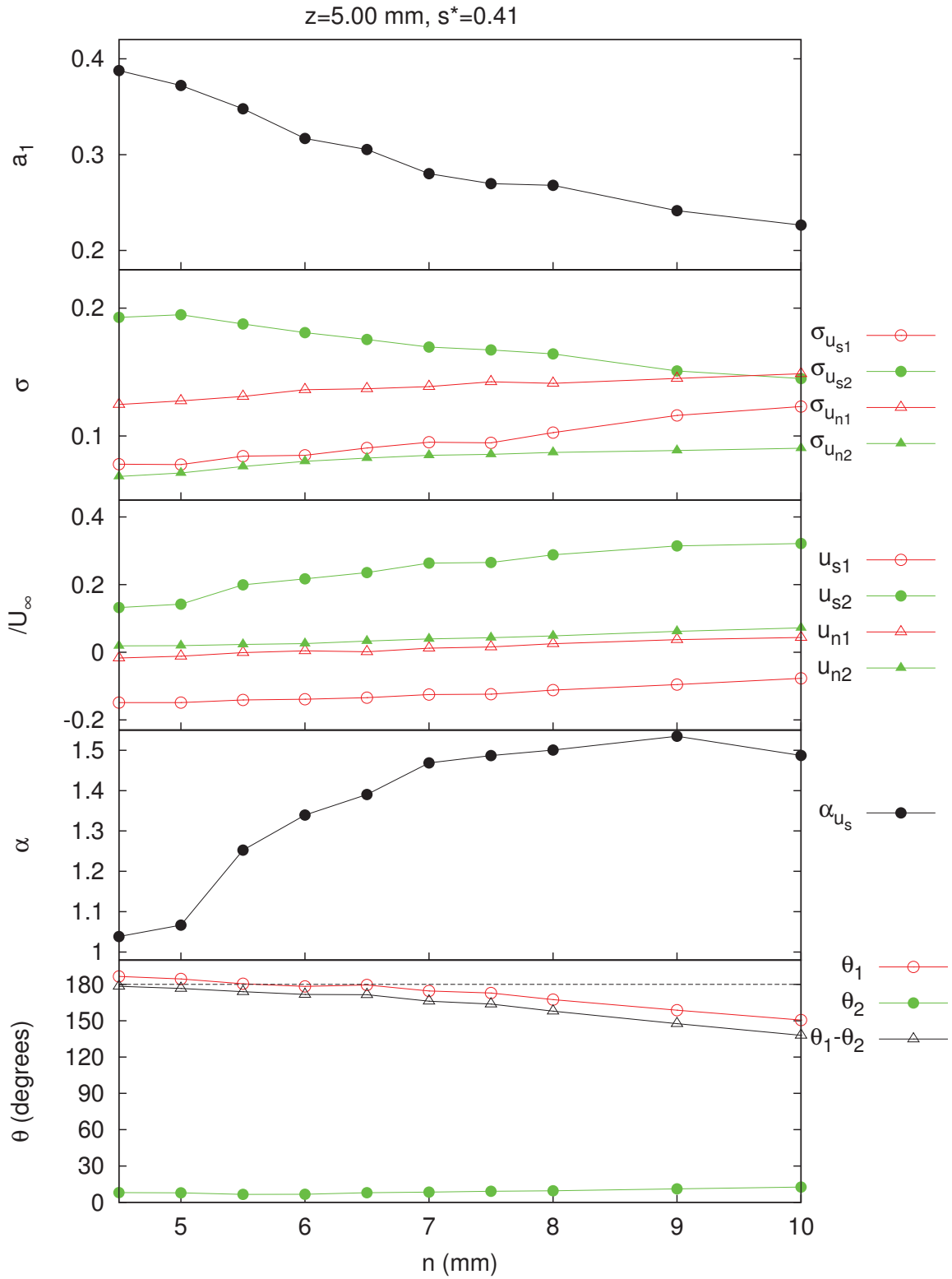


Figure 6.25: Bimodal parameters at the measurement station $z=5.00 \text{ mm}$ & $s^*=0.41$.

6.7.6 Spectra of velocity components

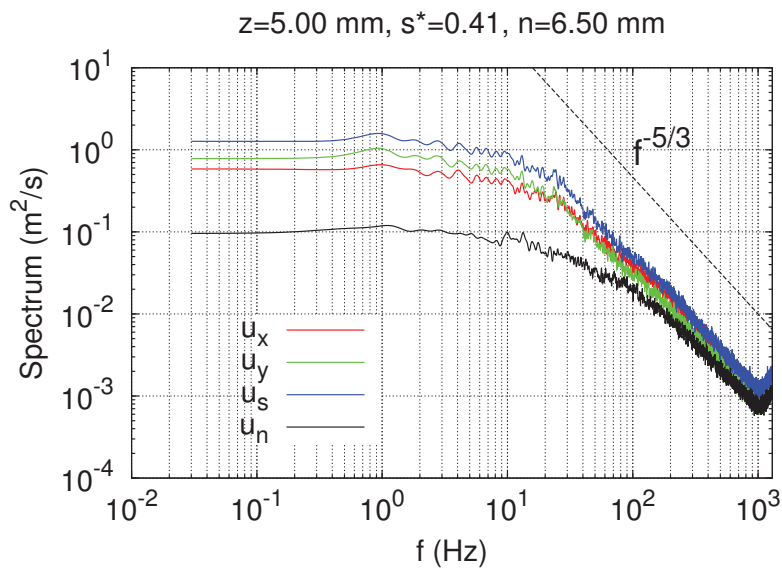


Figure 6.26: Spectra of instantaneous velocity components u_s , u_n , u_x , u_y at the measurement point $z=5.00$ mm & $s^*=0.41$ & $n=6.50$ mm measured by LDA.

In order to investigate the periodical properties of the two modes, the spectra of the velocity components measured by LDA have been calculated using the experimental results. However obvious peak does not exist in the spectra of the measurements, wherever the location of the measurement is. Fig. 6.26 shows typical results at the measurement point $z=5.00$ mm & $s^*=0.41$ & $n=6.50$ mm. Therefore the two modes are continuous and aperiodic. This is consistent with the studies with bimodal histograms reviewed in Section 6.7.1.1.

6.7.7 Physics of bimodal behaviour

So far we know that there are two modes in the corner region, which correspond to the two peaks in the histograms of velocity. From the positions of the bimodal points (in Figs. 6.7 and 6.11) and the development of histogram (e.g. in Fig. 6.22), the bimodal points mainly appear in the region near the mean interface of separated flow and non-separated flow.

In order to show the unsteady feature of the flow field, Fig 6.27 shows two instantaneous flow fields measured by PIV. There are a lot of vortices in the flow field and these vortices develop in the passage. The unsteady feature is mainly reflected in the fluctuation of the interface of the separation, especially the fluctuation of the separation point.

For example, at the time in Fig. 6.27a, the flow at the point P comes back compared with the direction of the main flow, that is to say the flow is already separates at the point P. However

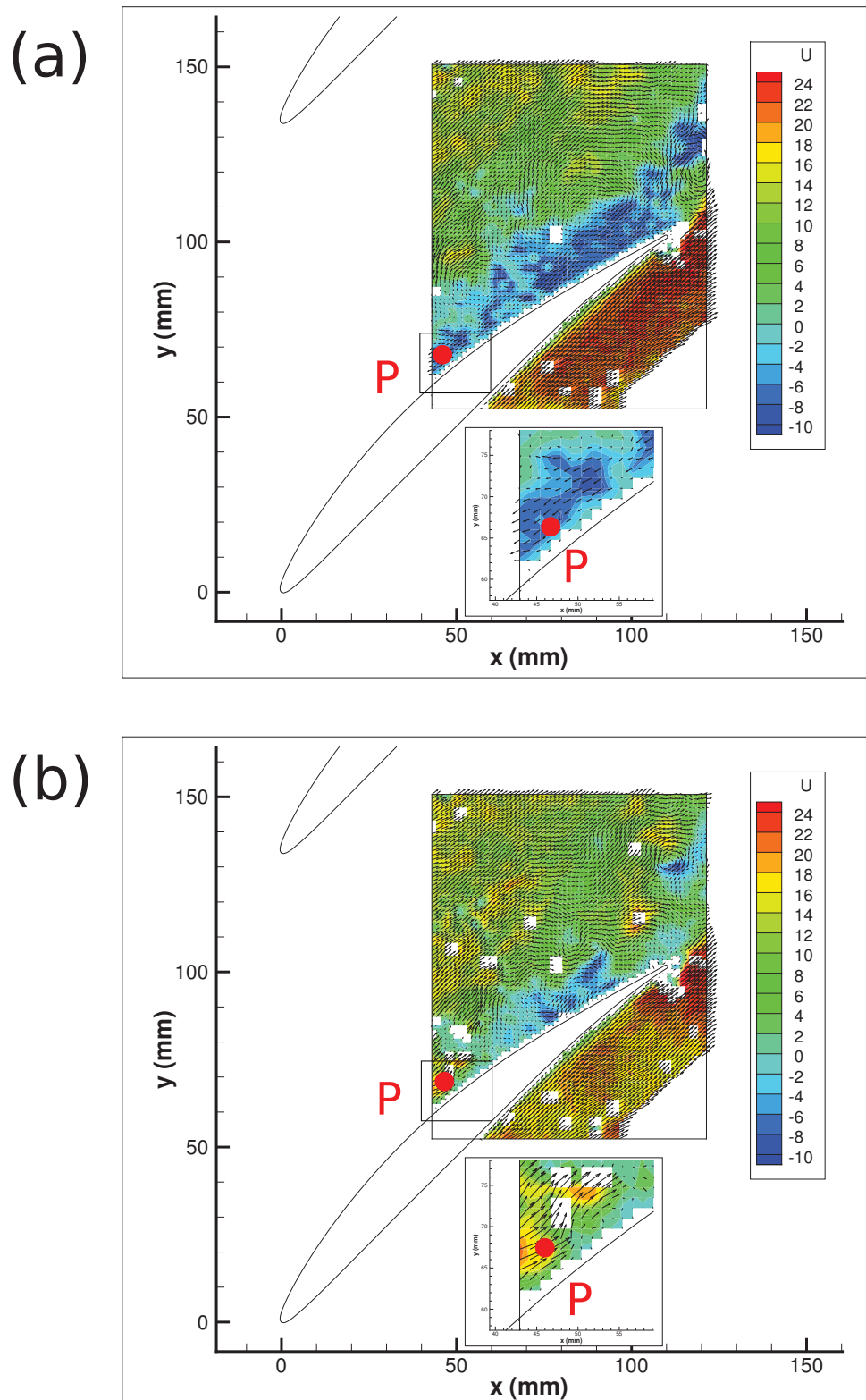


Figure 6.27: Instantaneous flow fields in the corner region, measured by PIV. Colored with axial velocity.

at another time in Fig. 6.27b, the flow at the point moves downstream, that is to say the flow is not separated at the point P.

For the bimodal histograms in the junction flow reviewed in Section 6.7.1.1, the physics is associated with the horseshoe vortex. Because the bimodal points also exist in the region near the suction side, we consider that the physical mechanism of bimodal histogram in our experiment is not associated with the horseshoe vortex.

In order to understand the bimodal phenomenon in the junction flow, Devenport & Simpson (1990) proposed two basic modes. Inspired by this, at a specified point we proposed two modes: large-scale mode and small-scale mode.

Large-scale mode is that the velocity at this point is influenced by an instantaneous large-scale vortex and $u_s < 0$, as shown in Fig. 6.27a. At this mode, the almost all the flow near the suction side comes back (likes a jet).

Small-scale mode is that the velocity at this point is influenced by an instantaneous small-scale vortex and $u_s > 0$, as shown in Fig. 6.27b.

In order to interpret more accurately the physics of bimodal behaviour in our experiment, extensive instantaneous results are needed. We propose that the numerical results of unsteady RANS or LES could be used to investigate further this physics.

6.8 Conclusions

The velocity flow field in the corner region, measured by 2C LDA and 2D PIV with the measurement at $i=4^\circ$, is presented and discussed in this chapter. After comparing and analyzing, the experimental results of PIV are only **qualitatively** used; and the experimental results of LDA are **quantitatively** used.

A significant phenomenon, bimodal histograms of velocity, is found in our experiment. The bimodal points mainly appear in the region around the mean interface of separated flow and non-separated flow. The two velocity components u_s and u_n are non-independent from each other. The bimodal dynamics is due to the aperiodic interplay of two basic modes. We propose two modes: large-scale mode and small-scale mode. **Large-scale mode** is that the velocity at this point is influenced by an instantaneous large-scale vortex and $u_s < 0$. **Small-scale mode** is that the velocity at this point is influenced by an instantaneous small-scale vortex and $u_s > 0$.

Chapter 7

Conclusions and Prospects

Contents

7.1 Conclusions	188
7.2 Prospects	191

7.1 Conclusions

A detailed and accurate experiment of 3D flow field through a linear compressor cascade has been set up. A series of RANS numerical simulations were carried out and one of them, using the S-A turbulence model, was taken as an example to be compared with the experimental results. An original and accurate database has been built, which can be used to evaluate and modify the CFD tools, both RANS and LES. Main conclusions are presented here.

1. The trips have been used close to the leading edge of the blades in order to induce the transition on the blade surface and eliminate the jump of the pressure distribution due to the transition with a separation bubble. The trips influence observably the flow fields near the sandpaper and change the thickness of the boundary layers.
2. The inlet flow conditions were measured by a five-hole pressure probe and hot-wire probes. The distance from the measurement points to the leading edge of the cascade was long enough to minimize the influence of the incidence. The differences in the inlet flow mean velocities measured by a five-hole pressure probe are less than 0.5% in the pitchwise direction at the inlet of this investigated zone in the cascade. The mean velocity

profiles, as well as the streamwise normal stresses, were measured by hot-wire probes. The closest distance to the wall is as small as $z^+ < 14$ and the number of measurement points is sufficient to describe correctly the inlet boundary layer. Therefore, these experimental results constitute information that is accurate enough to define the inlet boundary conditions for both RANS and LES simulations.

3. The experimental and numerical results have been used to investigate the influence of incidence (from -2° to 6°) on the pressure and losses. When the incidence increases, the loading of the blade moves toward the leading edge and, as expected, the global pressure forces in the streamwise and pitchwise directions increase. The extent of the region where the flow accelerates from the leading edge progressively narrows with incidence. The maximum losses as well as the extent of the losses increase with the incidence downstream of the corner region. The incidence of 4° has been chosen to measure the flow field, because the extent of corner stall is as large as possible and separation does not exist at mid-span.
4. An accurate study of the development at mid-span of the boundary layer, which is under the combined influences the curvature, the streamwise and the wall-normal pressure gradients, has been achieved.

From the basic equation, the influence of the curvature is balanced by the sum of the wall-normal pressure gradient ($\partial P / \partial n$) and the normal gradient of the Reynolds normal stress ($\partial \overline{u_n'^2} / \partial n$). Therefore the influence of the wall-normal pressure gradient is partly implicit in the influence of the curvature. On the other hand, the wall-normal pressure gradient contains Reynolds normal stress $\overline{u_n'^2}$ in the wall-normal direction.

From the investigation of the shape factors, the wall-normal PPG restrains the separation, contrary to the streamwise APG and the convex curvature. This trend is not the same with the effect of the wall-normal PPG in the corner region, where the wall-normal PPG induces the flow deviation towards the suction side and thus take part in the causes of the corner separations. The criterion of Truckenbrodt's shape factor (H) for the separation of the boundary layers should take into account the influence of the wall-normal PPG, in order to decrease the threshold under which boundary layer at mid-span should separate.

A new qualitative prediction of the development of Reynolds stresses on the combined effects of the upstream flow and the APG has been proposed. The streamwise APG can be

responsible for the development of the Reynolds stresses in the TBL in our experiment. The same conclusions cannot be transposed to the curvature and the wall-normal PPG whose effects cannot be directly observed in the development of the Reynolds stresses.

Most of the scalings dedicated to simple geometries do not work any more in our case with a complex non-equilibrium turbulence boundary layer.

5. The corner region produces a large 3D separation bubble for an incidence of 4° and permitted to obtain detailed measurements. In the outlet flow of the cascade, the highest part of the total pressure losses is caused by this separation. The mean velocity results show a mean 3D vortex with a center line which extends from the suction side of the blade (close to the trailing edge at about 60 mm from the endwall) to the endwall surface. This generates a large blockage and produces a deviation of fluid with high energy that passes through the inter blade channel. Downstream of the blades trailing edge, the wake close to the endwall are deviated towards the suction side by this fluid with a high energy that lifts towards the mid-span and the pressure side of the adjacent blade, and batters the edge of the zone with high losses.

The RANS simulations capture the overall pattern of corner separation. The mean vortex and the topology of the separation are similar, but they always tend to overestimate the size of the separation with, most of the time, a badly predicted location of the separation point and the positions of the vortex centers.

6. These miss-predictions of the CFD are mostly explained by the high unsteady and intermittent feature of the corner separation. The backflow coefficients and the bimodal histograms obtained in the corner region highlight this aspect. They show the existence of two modes which drive the flow and which have been identified in the streamwise velocity component. The first mode (large-scale mode) corresponds to a reverse jet ($u_s < 0$) due to the separation and the second mode (small-scale mode) corresponds to the freestream flow ($u_s > 0$), out of the separation. This bimodal aspect is not explicit in the normal components of the velocity, but it has been demonstrated that the two components are statistically non-independent, leading to the conclusion that the flow at the interface of the separation faces an aperiodic phenomenon that induced a high unsteadiness of the location of the interface. This unsteady and highly intermittent aspect is linked to the inspiration of vortices in the flow field, as presented with the PIV measurements.

7.2 Prospects

1. There are influences of the trips on the transition, the velocity flow field near the trips and the thickness of boundary layer. In order to consider the influence of the trips, the geometry of the trips should be inserted in the simulations.
2. The evolution of inlet turbulent boundary layers is very important for simulations to determine the decrease in turbulent kinetic energy in the streamwise direction. So it is necessary to improve the measurements of the evolution in the streamwise direction of the parameters of the inlet turbulent boundary layers that develops upstream of the cascade.
3. To better investigate the effects of incidence on the development of the separation region in the corner, oil visualization should be improved and performed for different incidences.
4. The physics of the 2 modes that induce bimodal histograms is not clearly understood. Some unsteady pressure measurements are planned in order to obtain the unsteady pressure field (and the driving force) on the blade and endwall surfaces. These measurements coupled with some LES simulations that are carried out at the moment in an other PhD thesis will be of great interest.

Appendix A

Uncertainty analysis

Contents

A.1 Total measurement error	192
A.2 Infinite number of samples	193
A.3 Finite number of samples	194
A.4 Uncertainty in the results derived from these primary measurements	195

All along, experimental accuracy is one of the most important information in the research (Celik *et al.*, 2008; Coleman & Steele, 1989, 1995). Recently, many journals have reaffirmed the importance of the numerical and experimental accuracy (e.g. Andrews, 2011; Friedmann, 2011). The main references are Coleman & Steele (1989) and Coleman & Steele (1995).

A.1 Total measurement error

The degree of inaccuracy or the total measurement error (δ) is the difference between the measured value and the true value. As shown in Fig. A.1, the total error is the sum of the bias error and the precision error.

$$\delta = \beta + \epsilon \tag{A.1}$$

The bias error (β) is the fixed, systematic, or constant component of the total error and it is sometimes referred to simply as the bias. The precision error (ϵ) is the random component of the total error and sometimes it is called the repeatability or repeatability error.

Usually it is not possible to specify what the exact bias and precision errors are in a given measurement of x . The statement about the value of x based on measurements is that with $C\%$

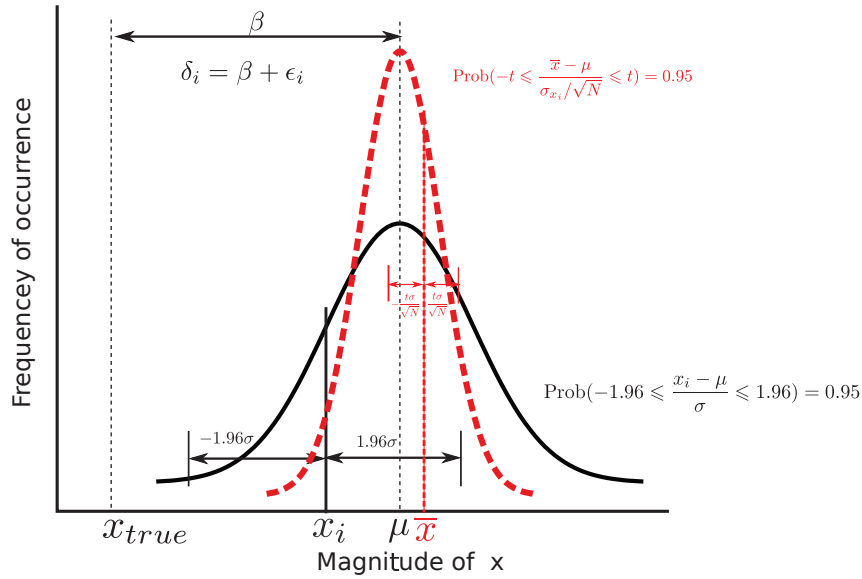


Figure A.1: Uncertainty analysis

confident that the true value of x lies within the interval

$$\bar{x} \pm \delta_x \quad (\text{A.2})$$

\bar{x} is Usually assumed to be the mean value of the N reading taken from the experiment, and δ_x is the uncertainty in x with $C\%$ confidence of the combination of bias and precision errors.

A.2 Infinite number of samples

For a population with a infinite number of samples, the mean of the population μ is defined by

$$\mu = \lim_{N \rightarrow \infty} \frac{1}{N} \sum_{i=1}^N x_i \quad (\text{A.3})$$

The standard deviation σ is defined by

$$\sigma = \lim_{N \rightarrow \infty} \left[\frac{1}{N-1} \sum_{i=1}^N (x_i - \bar{x})^2 \right]^{1/2} \quad (\text{A.4})$$

In a Gaussian distribution,

$$\text{Prob}(-1.96 \leq \frac{x_i - \mu}{\sigma} \leq 1.96) = 0.95 \quad (\text{A.5})$$

Thus, knowing that 95% of the population lies with $\pm 1.96\sigma$ of the mean μ , we can be 95% confident that a single reading will fall within this $\pm 1.96\sigma$ interval about the mean. Stated another way, $+1.96\sigma$ and -1.96σ are the upper and lower limits on the 95% confidence interval

for a single reading of x . We can also speak of $\pm 1.96\sigma$ as the 95% confidence limits. We can also be 95% confidence that the mean μ of the distribution will fall within $\pm 1.96\sigma$ of the single reading x_i .

A.3 Finite number of samples

In practice, for a population with an finite number of samples, the mean of the sample population \bar{x} is defined by

$$\bar{x} = \frac{1}{N} \sum_{i=1}^N x_i \quad (\text{A.6})$$

where N is the number of individual reading x_i . The sample standard deviation σ_{x_i} is defined by

$$\sigma_{x_i} = \left[\frac{1}{N-1} \sum_{i=1}^N (x_i - \bar{x})^2 \right]^{1/2} \quad (\text{A.7})$$

Note that the standard deviation is calculated dividing by $N-1$ rather than N . This is because only $N-1$ of the samples is independent of the mean.

The sample means are normally distributed with mean μ and standard deviation

$$\sigma_{x_i} = \frac{\sigma}{\sqrt{N}} \quad (\text{A.8})$$

The implications of this relationship are very important. One way to decrease the random component of the uncertainty in a measured value is take many readings and average them.

$$\text{Prob}(-1.96 \leq \frac{\bar{x} - \mu}{\sigma/\sqrt{N}} \leq 1.96) = 0.95 \quad (\text{A.9})$$

Thus it can say that with 95% confidence that the mean μ of the parent distribution is within $\pm 1.96\sigma/\sqrt{N}$ of the sample mean \bar{x} computed from N readings. The width of the 95% confidence interval in Eq. A.9 is narrower than the one in Eq. A.5 by a factor of $1/\sqrt{N}$.

Of course, because the true standard deviation σ of the distribution is unknown, in practice we have σ_{x_i} , the standard deviation of a finite sample of N readings. σ_{x_i} is only an estimate of the value of σ .

$\frac{x_i - \mu}{\sigma_{x_i}}$ and $\frac{\bar{x} - \mu}{\sigma_{x_i}/\sqrt{N}}$ is not normally distributed. Rather, it follows the t distribution with $N - 1$ degrees of freedom. And for the sample from a Gaussian population,

$$\text{Prob}(-t \leq \frac{x_i - \mu}{\sigma_{x_i}} \leq t) = 0.95 \quad (\text{A.10})$$

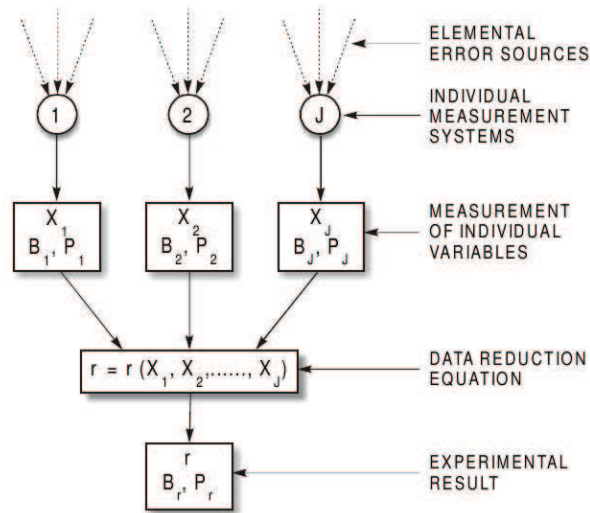


Figure A.2: Propagation of uncertainties into an experimental result (Coleman & Steele, 1995)

$$\text{Prob}\left(-t \leq \frac{\bar{x} - \mu}{\sigma_{x_i} / \sqrt{N}} \leq t\right) = 0.95 \quad (\text{A.11})$$

There is a 95% probability that the true value lies within

$$P_{x_i} = t \cdot \sigma_{x_i} \quad (\text{A.12})$$

$$P_{\bar{x}} = t \cdot \frac{\sigma_{x_i}}{\sqrt{N}} \quad (\text{A.13})$$

and where t is taken from table of t – distribution if $N < 31$ and $t = 2$ if $N \geq 31$.

The estimates of the precision limits $\delta_{\bar{x}}$ outlined above depend on the normal distribution of the measured variables. But it is relatively insensitive to deviation from normality in the error distributions of the measured variables.

A.4 Uncertainty in the results derived from these primary measurements

Measurements are made of individual variables, X_i , to obtain a result, r , which is calculated by combining the data for various individual variables through data reduction equations

$$r = r(X_1, X_2, \dots, X_J) \quad (\text{A.14})$$

Each of the measurement systems used to measure the value of an individual variable, X_i , is influenced by various elemental error sources. The effects of these elemental errors are manifested as bias errors (noted as B_i) and precision errors (noted as P_i) in the measured values of the variables, X_i . These errors in the measured values then propagate through the data reduction equation, thereby generating the bias error (noted as B_r), and precision error (noted as P_r) in the experimental result, r . Fig.A.2 provides a block diagram showing elemental error sources, individual measurement systems, measurement of individual variables, data reduction equations and experimental results.

The total uncertainty in the results, r , is the root-sum-square (RSS) of the bias and precision limits

$$U_r^2 = B_r^2 + P_r^2 \quad (\text{A.15})$$

The bias limit of the result is

$$B_r^2 = \sum_{i=1}^J \theta_i^2 B_i^2 + 2 \sum_{i=1}^{J-1} \sum_{k=i+1}^J \theta_i \theta_k B_{ik} \quad (\text{A.16})$$

and

$$\theta_i = \frac{\partial r}{\partial X_i}, \quad B_{ik} = \sum_{\alpha=1}^L (B_i)_\alpha (B_k)_\alpha \quad (\text{A.17})$$

where L is the number of elemental systematic error sources that are common for measurements of variables X_i and X_k .

In single tests for which there is $M = 1$ result at the same experimental set point, the precision limit of the result is given by

$$P_r^2 = \sum_{i=1}^J \theta_i^2 P_i^2, \quad P_i = t_i \sigma_i \quad (\text{A.18})$$

where t_i is the coverage factor and σ_i is the standard deviation of the sample of N readings of the X_i . $t = 2$ when $N \geq 10$ (Coleman & Steele, 1995) while when $N > 31$ (Coleman & Steele, 1989).

In multiple tests, for which there are $M > 1$ results at the same experimental set point, the uncertainty that should be associated with \bar{r} is

$$U_{\bar{r}}^2 = B_r^2 + (2S_r / \sqrt{M})^2 \quad (\text{A.19})$$

with B_r given by Eq. A.16 and

$$S_r = \left[\frac{1}{M-1} \sum_{k=1}^M (r_k - \bar{r})^2 \right]^{1/2}, \quad \bar{r} = \frac{1}{M} \sum_{k=1}^M r_k \quad (\text{A.20})$$

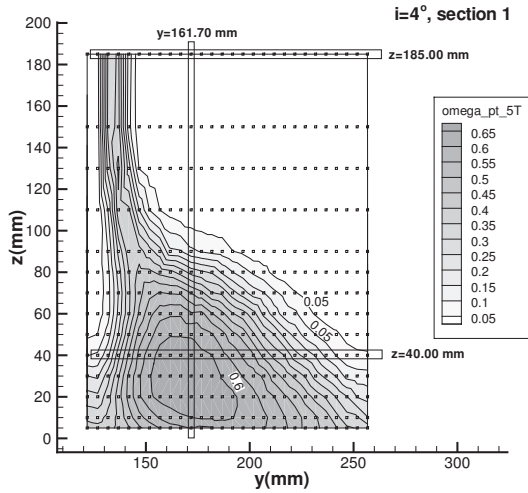
Appendix B

Correction of five-hole pressure probe according to total pressure gradient

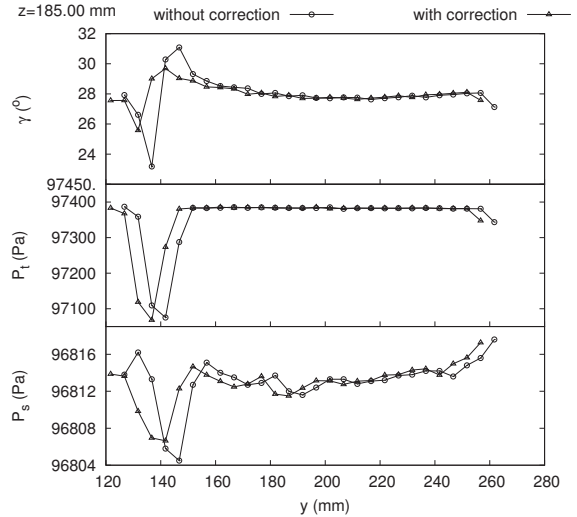
The total pressure gradient of the flow field induces error in the pressure probe measurements. A correction has been introduced in Section 3.2.3.2. The results of the pressure probe without and with corrections are compared here, and shown in Fig. B.1. To illustrate the difference between the results without and with correction, the experimental results measured in the first section at $i=4^\circ$ are selected and three typical lines are chosen. The first line ($z=185.00$ mm, in the y direction) locates at mid-span. The second line ($z=40.00$ mm, in the y direction) locates near the endwall and passes through the corner stall zone. The third line ($y=161.70$ mm, in the z direction) passes also in the corner stall zone and is normal to the first and second lines. For the first line and the second line, the total pressure P_t , the static pressure P_s and the velocity angle γ are compared. For the third line, the total pressure P_t , the static pressure P_s and the velocity angle β are compared.

Without and with corrections, the total pressure P_t and the static pressure P_s do not change too much even in the region with large total pressure gradients, however, the velocity angles β and γ vary significantly in these regions. This is due to the fact that the static pressure gradients of P_g and P_d are small in the measurement section, and so the $P'_{gd} = (P'_{g \rightarrow c} + P'_{d \rightarrow c})/2$ in the Eq. 3.2 is small, and C'_{p_t} and C'_{p_s} change correspondingly a little. In contrast, the changes in $P'_{c \rightarrow g}$, $P'_{c \rightarrow d}$, $P'_{c \rightarrow b}$ and $P'_{c \rightarrow h}$ in the Eq. 3.2 are larger due to the existence of the total pressure gradient, then leading to significant changes in C'_β and C'_γ .

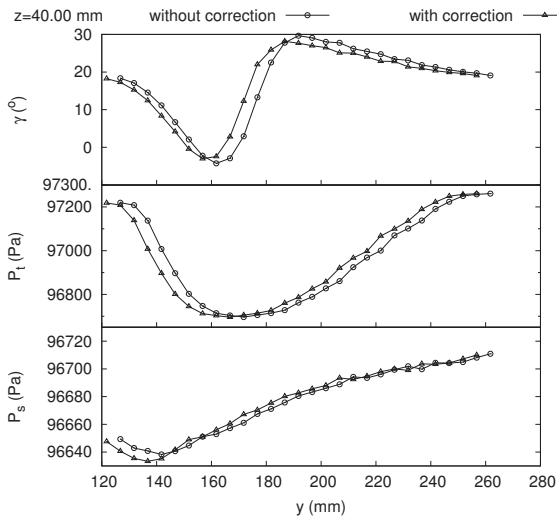
The difference between the results without and with correction in other measurement sections are similar to the first section at $i=4^\circ$ discussed above. All the experimental results used below are with correction according to the total pressure gradient.



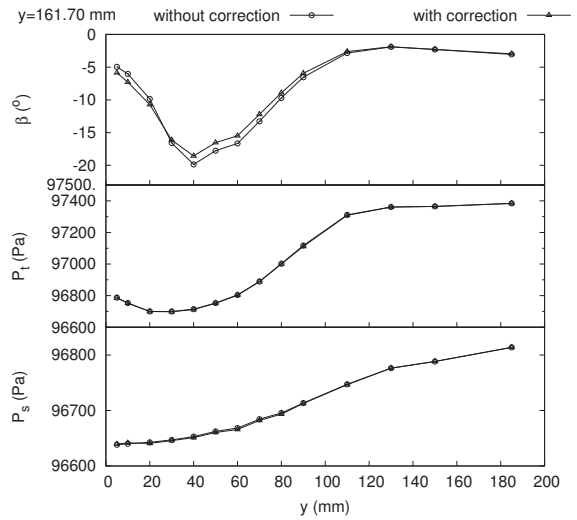
(a) Positions of three typical compared lines



(b) First line, $z/h=185.00\text{ mm}/370.00\text{ mm}=50.0\%$



(c) Second line, $z/h=40.00\text{ mm}/370.00\text{ mm}=10.8\%$



(d) Third line, $y=161.70\text{ mm}$

Figure B.1: Comparison of experimental results without and with correction according to the total pressure gradient. $i=4^\circ$, section 1. (a) The positions of three typical compared lines; (b) the first line ($z=185.00\text{ mm}$, in the y direction) locates at mid-span; (c) the second line ($z=40.00\text{ mm}$, in the y direction) locates near the endwall and passes through the corner stall zone; (d) the third line ($y=161.70\text{ mm}$, in the z direction) passes also in the corner stall zone and is normal to the first and second lines.

Appendix C

Influences of trips

Contents

C.1 Transition and extent of corner stall	200
C.2 Pressure distribution on the blade	200
C.3 Nearby flow field	201
C.4 Conclusions	202

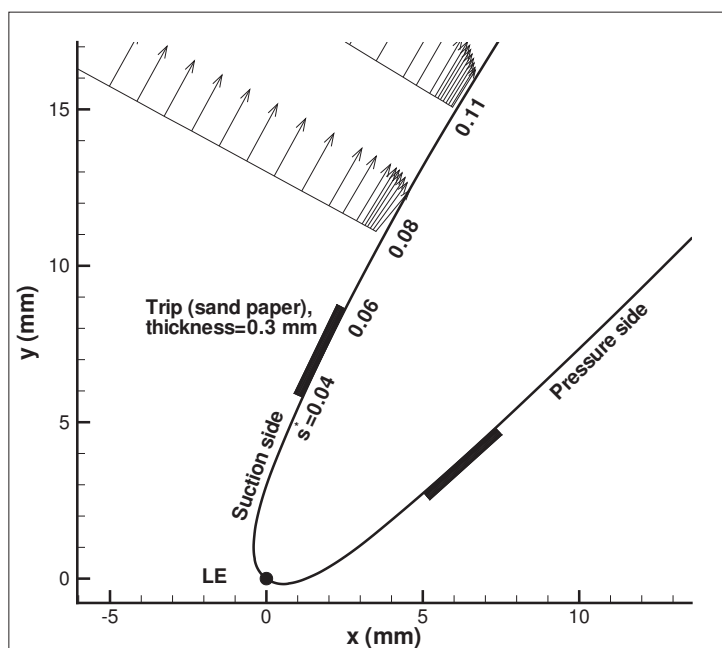


Figure C.1: Location of the trip and the velocity near the trip at mid-span.

The transition simulation is particularly complex to be performed with CFD, thus we wanted to remove this difficulty and focus the study only on the corner stall region. In order to ensure and fix the location of the boundary layer transition close to the leading edge, which has large consequences on the suppression of the separation bubbles that appear on both sides of the

blade and on the corner zone separation, sandpaper strips have been stuck at 6.0 mm from the leading edge of both the suction and the pressure sides of the blades. It means that the location of the trip is $s^* \approx 0.04-0.06$ (shown in Fig. C.1). The width in streamwise and thickness of the sandpaper are 3.0 mm and 0.3 mm, respectively. The grid size of the sandpapers is on of the ISO P600 (average particle diameter is about $25.8 \mu\text{m}$).

C.1 Transition and extent of corner stall



Figure C.2: Influence of the trips on the transition, $i=4^\circ$

The results of oil visualization both on pressure side and suction side without and with sandpapers are shown in Fig. C.2. On both the pressure and the suction sides, the separation bubbles appear without sandpapers and disappear with sandpapers. It means that the sandpapers force the transition near the leading edge.

Besides the transition, the extent of corner stall enlarged when the trips are used.

C.2 Pressure distribution on the blade

The pressure distributions on the blade with and without the trips are shown in Fig. C.3. The pressure distribution jumps at the region of transition ($0.5 < x/c_a < 0.7$). This is consistent with the conclusion of Cumpsty (2004, pp.327). When the boundary layer reattaches the suction side of the blade, the static pressures without and with the trips recover the same levels.

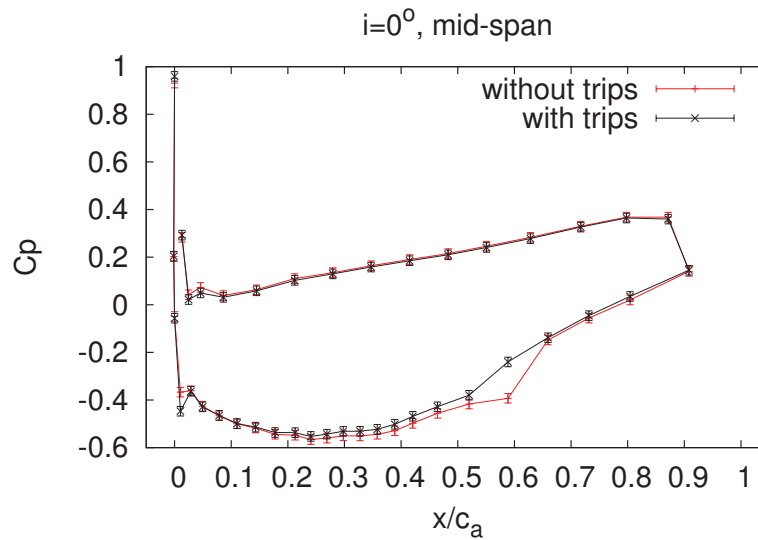


Figure C.3: Influence of the trips on pressure distribution on the blade. $i=0^\circ$, at mid-span. Lines for visual aid only.

C.3 Nearby flow field

In order to indicate the influence of the trip on the velocity, the experimental results near the trip are shown in Fig. C.4, including streamwise mean velocity, local turbulence intensity as well as Reynolds shear stress. The logarithmic scale in distance coordinate makes it easier to compare the values in the boundary layer near the blade surface.

In the experiment, the frequency of acquisition is very low (less than 100 Hz) when measuring the points $n < 0.30$ mm in the line $s^* = 0.08$. The density of particle is low at these points, because it is very difficult to seed the flow close to the wall in a boundary layer due to the influence of sandpaper. From the Comparison of the experimental results near the sandpaper ($s^* = 0.08, 0.11$) and far from the sandpaper ($s^* = 0.20, 0.30, 0.40$), it is obvious that the parameters of the flow downstream of the sandpaper change a lot under the influence of the sandpaper. The streamwise mean velocity decreases, local turbulence intensity increases and Reynolds shear stress decreases.

The experimental results of $s^* = 0.08, 0.11$ will not be presented anymore in the following of the research report, but the numerical simulations should take into account the trips, because of its influence in the boundary layer that develops downstream of it. This explains why the RANS calculations predict different losses at mid-span.

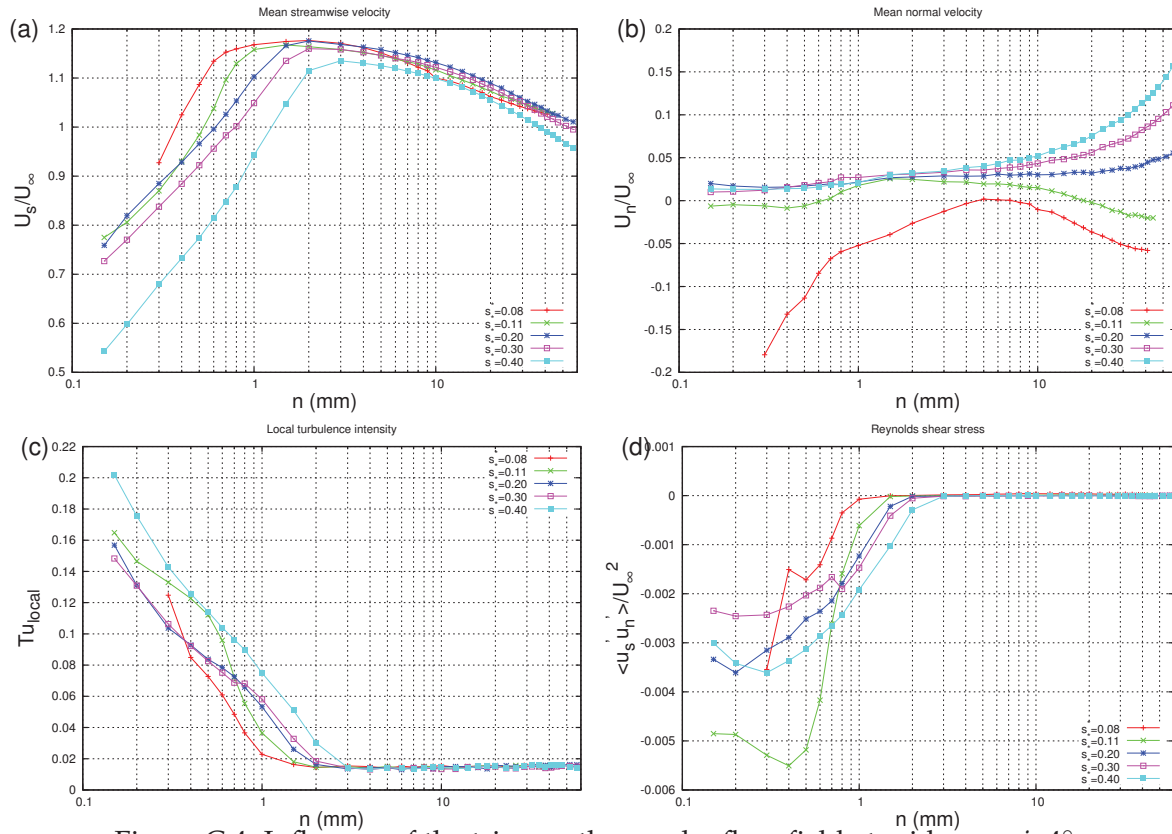


Figure C.4: Influence of the trips on the nearby flow field at mid-span, $i=4^\circ$.

C.4 Conclusions

The trips induce transition and pressure distribution jumps at the transition region. Additionally, the trips influence the nearby flow field.

In our experiment, the trips are used on both suction and pressure sides of all the blades. There are two main reasons.

The first reason is to gain a larger extent of corner stall, which is more easily measured in the experiment.

The second reason is to ensure and fix the location of the boundary layers transition. Our experimental data will be used to evaluate and improve the capability of CFD. The transition simulation is particularly complex to be carried out with CFD, thus the authors wanted to remove this difficulty and focus the study only on the development of the turbulent boundary layer and the corner stall region.

Appendix D

Numerical simulation

Contents

D.1 Turbulence models and boundary conditions	204
D.1.1 Standard $k-\epsilon$ and $k-\omega$ turbulence models	204
D.1.2 Inlet boundary conditions	204
D.2 Effects of incidence	205
D.3 Development of outlet flow	209
D.4 Outlet angles	210
D.5 Velocity field	211

In this thesis, the flow field is numerical simulated by three turbulence models in FLUENT: S-A, $k-\epsilon$ and $k-\omega$ turbulence models. The basic equations, the grid and the boundary conditions have been introduced in Section 3.5. Only some numerical results of the S-A turbulence model have been presented in the main body of this thesis, in order to help to understand the physics.

Some of the other numerical results are presented in this appendix. Before this, the standard $k-\epsilon$ and $k-\omega$ turbulence models and the inlet boundary conditions for these two turbulence models are introduced.

In this thesis, the numerical results are mainly used to help to understand the physics. From the comparison between the numerical results and the experimental results, it can come to the conclusion that all the numerical results can capture the overall pattern of flow field, but not the flow details.

Some issues are beyond the scope of this thesis. These issues are (1) which turbulence model performs better than others, (2) why this turbulence model performs better and (3) how to improve the turbulence model that not performs very well.

D.1 Turbulence models and boundary conditions

D.1.1 Standard k - ϵ and k - ω turbulence models

Besides the S-A turbulence model, the standard k - ϵ and k - ω turbulence models in FLUENT are also used to simulate the flow field of our cascade. The standard k - ϵ model is a semi-empirical model based on model transport equations for the turbulence kinetic energy (k) and its dissipation rate (ϵ). The model transport equation for k is derived from the exact equation, while the model transport equation for ϵ was obtained using physical reasoning and bears little resemblance to its mathematically exact counterpart. The standard k - ω model is an empirical model based on model transport equations for k and the specific dissipation rate (ω), which can also be thought of as the ratio of ϵ to k (i.e. $\omega = \epsilon/k$). The details of these two turbulence models can refer to [ANSYS \(2006\)](#).

D.1.2 Inlet boundary conditions

For k - ϵ and k - ω turbulence models, besides the inlet mean velocity it is necessary to specify values of various turbulence variables for inlet boundary condition, such as turbulent kinetic energy k , the turbulent dissipation rate ϵ and the specific turbulent dissipation rate ω . These turbulent variables can be estimated in terms of measured turbulence intensity. The turbulent kinetic energy k can be computed as,

$$k = \frac{3}{2} \overline{u'^2} \quad (\text{D.1})$$

The turbulent dissipation rate ϵ can be computed by

$$\epsilon = C_\mu \frac{\rho k^2}{\mu} \left(\frac{\mu_t}{\mu} \right)^{-1} \quad (\text{D.2})$$

The specific turbulent dissipation rate ω can be computed by

$$\omega = \frac{\rho k}{\mu} \left(\frac{\mu_t}{\mu} \right)^{-1} \quad (\text{D.3})$$

where C_μ is a turbulence model constant that usually has a value of 0.09, ρ is the density, μ is dynamic molecular viscosity and $\frac{\mu_t}{\mu}$ is the eddy viscosity ratio. In our experiment, $U_\infty = 40$ m/s, $T = 15^\circ$, so constants used are $\rho = 1.225$ kg/m³, $\mu = 1.78269 \times 10^{-5}$ kg/(m·s). The eddy viscosity ratio $\frac{\mu_t}{\mu}$ was not measured in the experiment, here we assume $\frac{\mu_t}{\mu} = 50$.

D.2 Effects of incidence

For the contours of static pressure and streamlines on the blade and the endwall at $i=4^\circ$, the numerical result of the S-A turbulence model has been shown in Fig. 4.8. The numerical results of the $k-\epsilon$ and $k-\omega$ turbulence models are shown in Fig. D.1. Compared with the experimental result of the static pressure on the blade that has been shown in Fig. 4.6, all the turbulence models obtain the mainly feature on the blade, but not the details (for example, the isoline $C_p=0.4$ on the pressure side).

The experimental and numerical results of static pressure distributions on the blade at $i=4^\circ$ are shown in Fig. D.2. To make the thesis more concise, only two representative sections are chosen here. The first one is at mid-span ($z/h=50.0\%$); and the other one is near the endwall and in the region of corner stall ($z/h=5.4\%$). All the turbulence models reproduce acceptably the pressure distributions on the blade at mid-span; however, fail to reproduce the pressure distributions near the endwall where the three-dimensional separations occur. The agreements at mid-span partly reflect that the experimental set-up is reliable. On the other hand, the disagreements in the corner region reflect the necessity of such experimental data, which could be used to calibrate the advanced CFD.

The experimental and numerical results of F_x and F_y (Eq. 4.7) at $i=4^\circ$ are shown in Fig. D.3, in which the experimental result and the numerical result of the S-A turbulence model have been shown in Fig. 4.10. The comparisons at other four incidence are similar to that at incidence of 4° . All the numerical results the same trend as the experimental result, and the values are smaller than the experimental result.

The experimental and numerical results of F_x^* and F_y^* (Eq. 4.8) are shown in Fig. D.4, in which the experimental result and the numerical result of the S-A turbulence model have been shown in Fig. 4.11. CFD tools can simulate very well the trend of these two pressure force parameters but under estimate the magnitude of these forces. The main reason might be the over prediction of the separation close to the endwall.

For the static pressure on the endwall at $i=4^\circ$, the experimental result has been shown in Fig. 4.12. The numerical result of the S-A turbulence model has been shown in Fig. 4.13. The numerical results of the $k-\epsilon$ and $k-\omega$ turbulence models are shown in Fig. D.5. All the numerical results have the pattern of the static pressure contours. However, the maximum value of the C_p are smaller than the experimental result.

For the total pressure loss at the outlet section 1, the experimental result has been shown

in Fig. 4.14. The numerical results of the S-A turbulence model has been shown in Fig. 4.15. The numerical results of the $k-\epsilon$ and $k-\omega$ turbulence models are shown in Fig. D.6. All the turbulence models obtain the same pattern of the contours of ω at the outlet section 1.

Experimental and numerical ω^* (Eq. 4.9) at the outlet section 1 at $i=4^\circ$ are shown in Fig. D.7a, in which the experimental result and the numerical result of the S-A turbulence model have been shown in Fig. 4.16a. All the numerical results have the same trend as the experimental result. Experimental and numerical ω' (Eq. 4.10) versus incidence are shown in Fig. D.7b, in which the experimental result and the numerical result of the S-A turbulence model have been shown in Fig. 4.16b. All numerical results have the same trend as the experimental result, and their values are smaller than the experimental result.

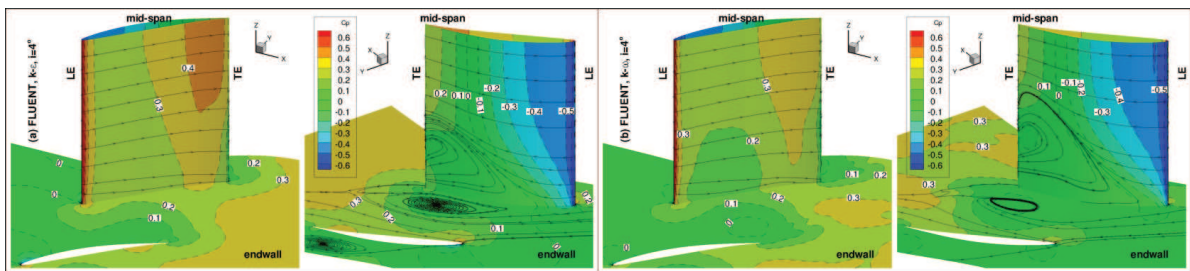


Figure D.1: Numerical results of static pressure and streamlines on the blade and then endwall at $i=4^\circ$. (a) The $k-\epsilon$ turbulence model; (b) the $k-\omega$ turbulence model.

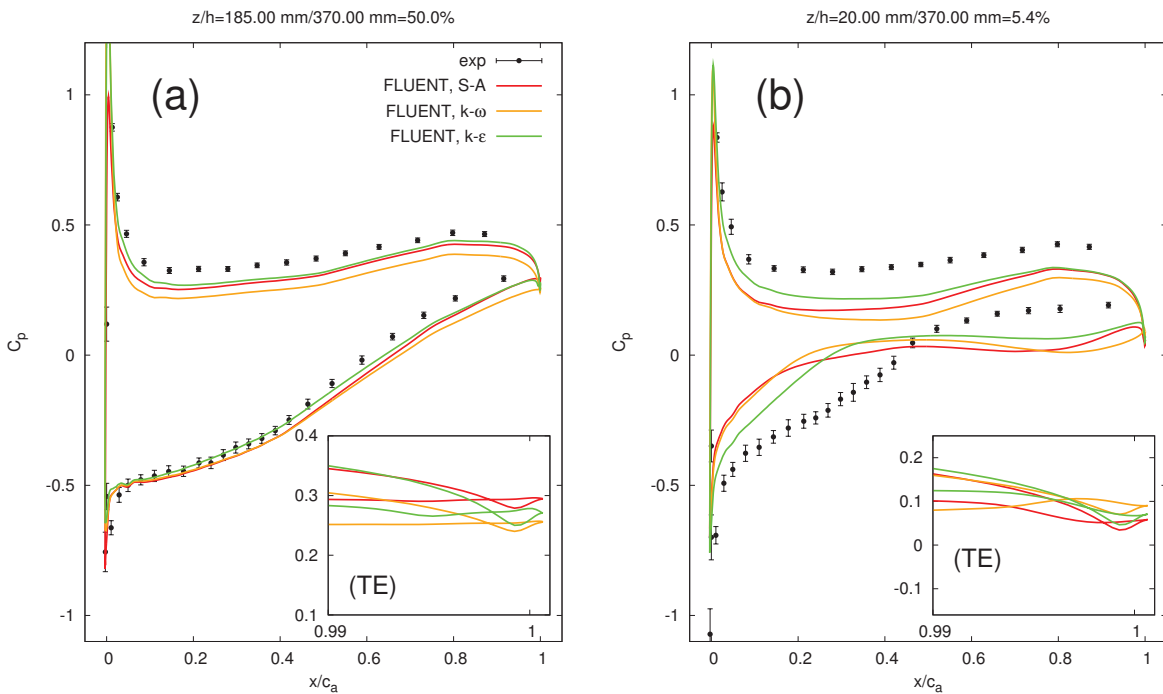


Figure D.2: Experimental and numerical results of C_p on the blade, $i=4^\circ$. (a) Mid-span; (b) near endwall.

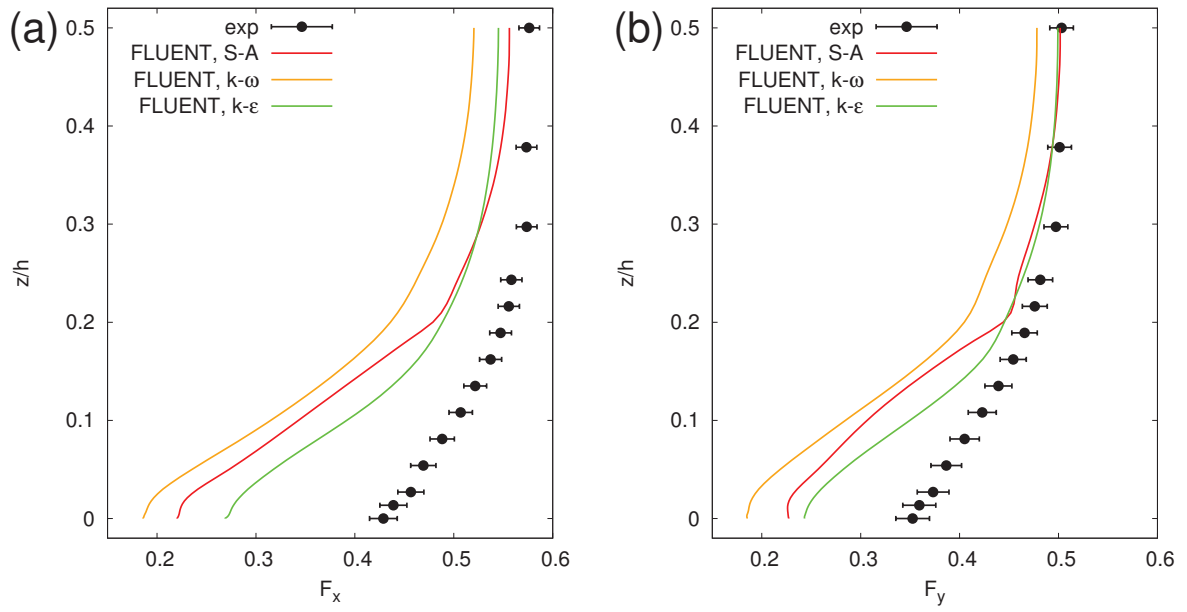


Figure D.3: Experimental and numerical F_x, F_y at $i=4^\circ$.

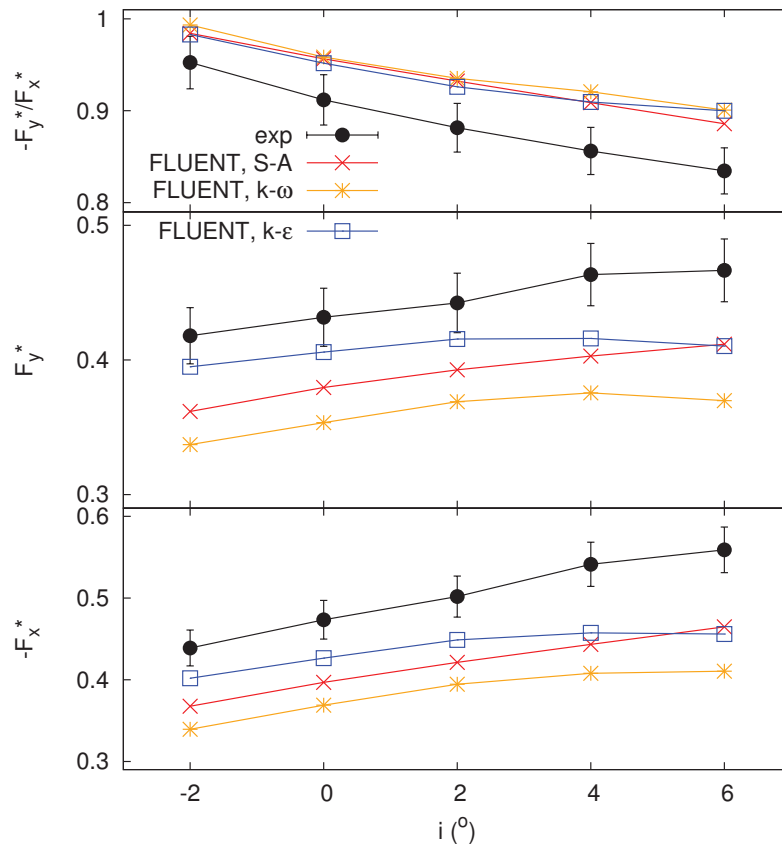


Figure D.4: Experimental and numerical F_x^*, F_y^* and F_y^*/F_x^* .

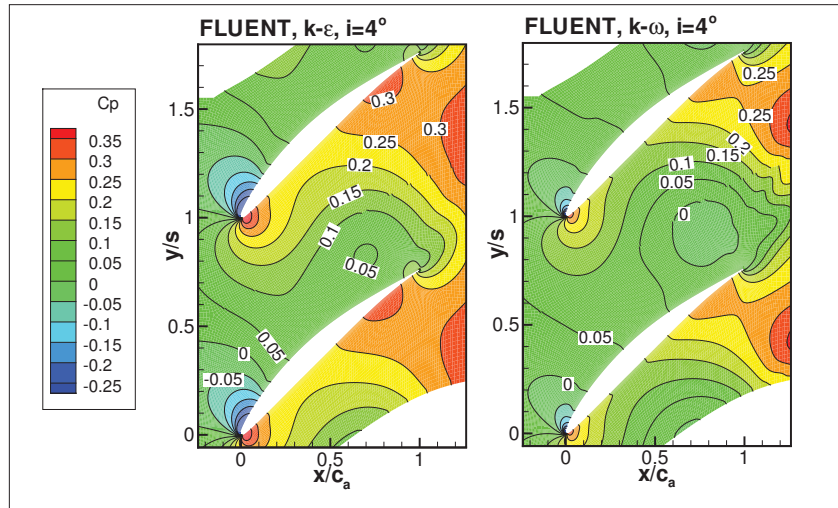


Figure D.5: Numerical results of static pressure coefficients on the endwall at $i=4^\circ$, including the $k-\epsilon$ and $k-\omega$ turbulence models.

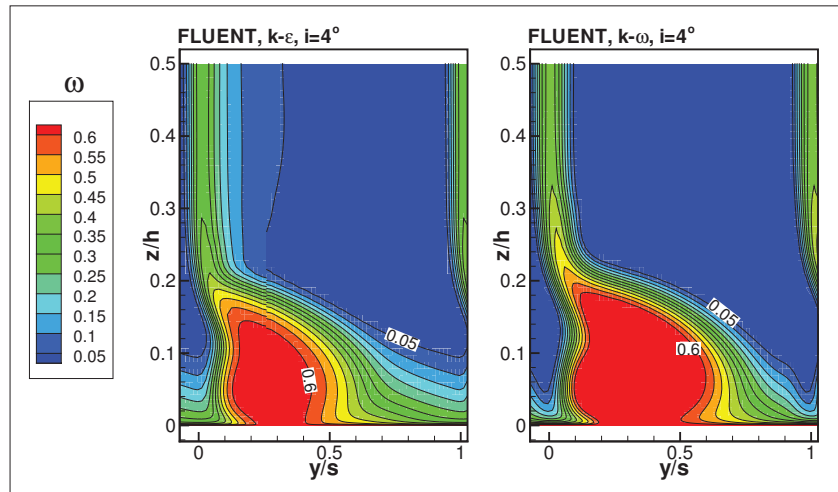


Figure D.6: Numerical results of exit total pressure loss coefficient at the outlet section 1 at $i=4^\circ$, including the $k-\epsilon$ and $k-\omega$ turbulence models.

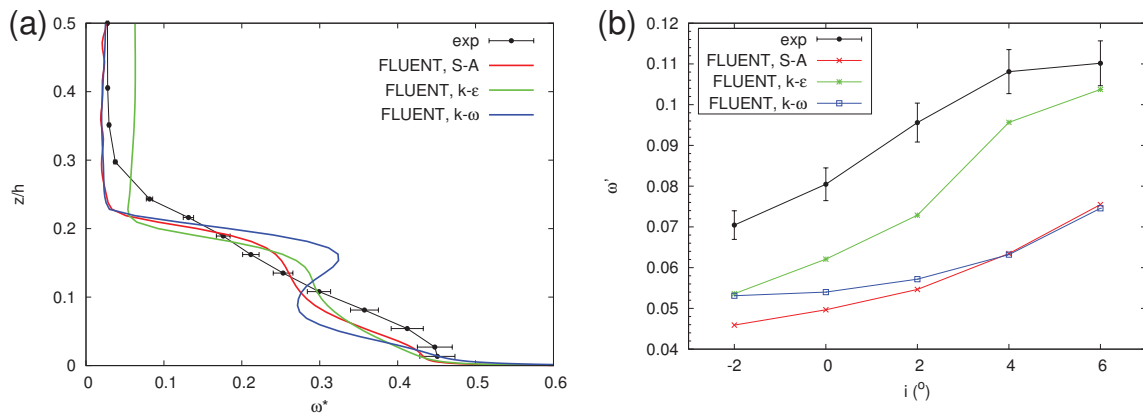


Figure D.7: (a) Experimental and numerical ω^* at the outlet section 1 at $i=4^\circ$, (b) experimental and numerical ω' versus incidence.

D.3 Development of outlet flow

Fig. D.8 shows the experimental and numerical developments of ω' in the outlet flow at $i=4^\circ$, in which the experiment result and the numerical result of the S-A turbulence model have been shown in Fig. 4.16b. The results of S-A and $k-\omega$ turbulence models have the same trend with the experimental result. The trend is that ω' increases from the first to the third measurement section. This means that there are additional losses in the process of development. The result of $k-\epsilon$ turbulence model are different with others, which keeps nearly constant.

Fig. D.9 shows the experimental and numerical magnitude of the vector in $x-y$ planes, in which the experimental result and the numerical result of the S-A turbulence model have been shown in Fig. 4.21. All the numerical results work very well at mid-span, but not work any more near the endwall.

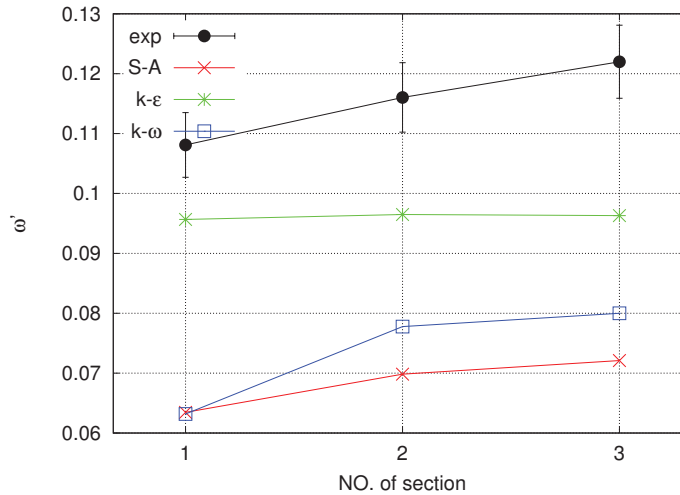


Figure D.8: Experimental and numerical developments of ω' in the outlet sections at $i=4^\circ$. Lines for visual aid only.

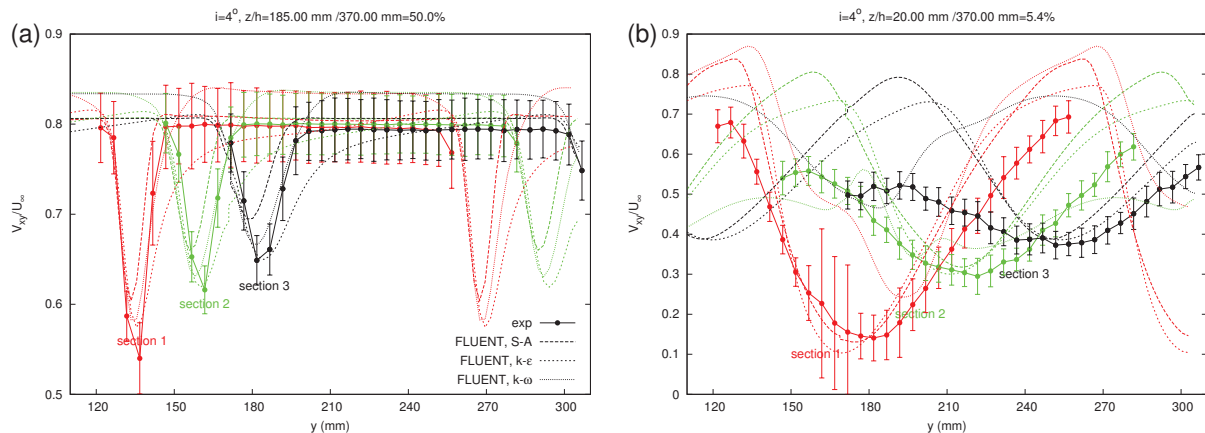


Figure D.9: Experimental and numerical results of magnitude of the vector in $x-y$ planes, $i=4^\circ$. (a) Mid-span; (b) near the endwall.

D.4 Outlet angles

Today the matching between the stages is a key for the simulation of multistage compressor, noted by [Cumpsty \(2010\)](#). The angles of outlet flow of course are key matching parameters, so it is necessary to compare these parameters between experimental and numerical results. Two angles θ_{xy} and θ_{xz} , as illustrated in Fig. D.10, reflect the deviation and lifting of the outlet flow in the cascade coordinate. The experimental and numerical results of outlet flow angles at $i=4^\circ$ at the first measurement sections are shown in Fig. D.11. The numerical results include that of three turbulence models in FLUENT. The experimental and all the numerical results are generally in good agreement at mid-span ($z/h=50.0\%$), compared with that at the position near the endwall ($z/h=5.4\%$).

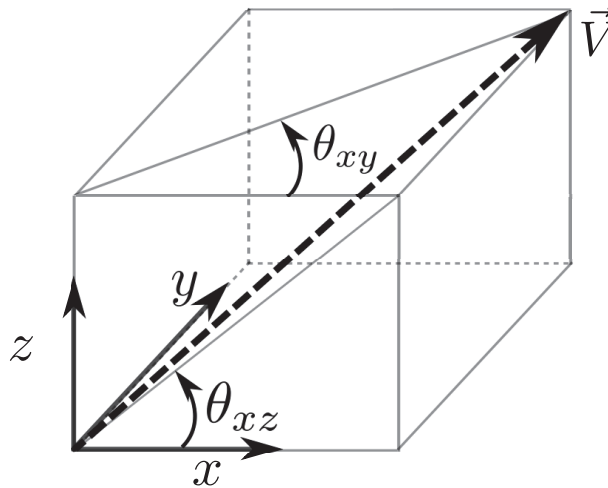


Figure D.10: Illustration of angles θ_{xy} and θ_{xz} in the coordinate of cascade.

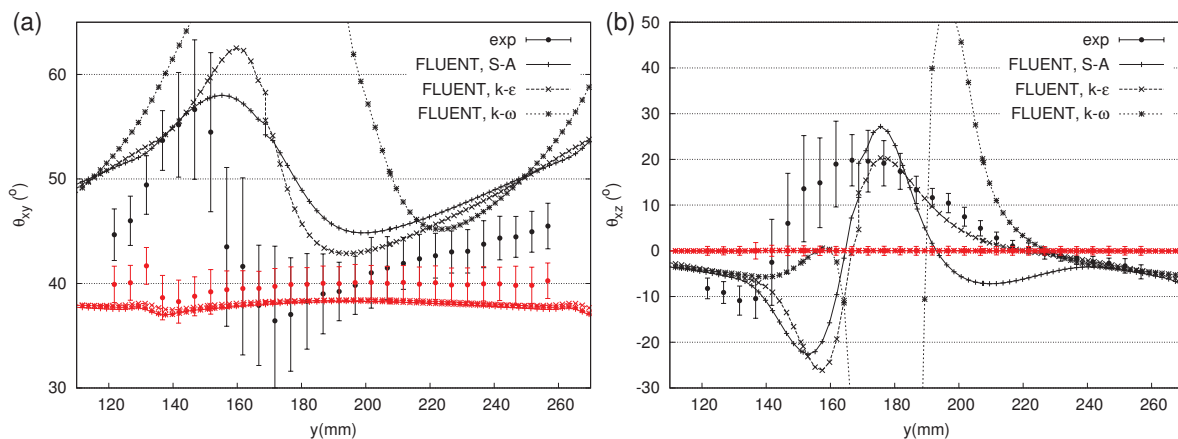


Figure D.11: Experimental and numerical results of angles at the first measurement sections, $i=4^\circ$. $z/h=20.00\text{ mm}/370.00\text{ mm}=5.4\%$, at mid-span, black lines; $z/h=185.00\text{ mm}/370.00\text{ mm}=50.0\%$, near the endwall, red lines.

D.5 Velocity field

In this subsection, the numerical results are compared with experimental results. Generally speaking, all the numerical results can capture the overall pattern of corner stall, but not the flow details.

The experimental and numerical of mean velocity fields in the plane $z=5.00$ mm are shown in Fig. D.12. The streamlines of LDA experiment have a jump between $s^*=0.50\sim 0.60$. All the numerical results do not obtain this feature. The separation points are summarized in Fig. D.12e. All of the numerical results do not correctly simulate the separation point. The numerical results earlier separate compared with the LDA experiment. The earliest separation occurs in the result of the $k-\omega$ turbulence model, which separates at $s^*=0.21$.

For each numerical result, there are two vortices in the passage. One is a main large vortex; the other one is relatively smaller one and occurs near the trailing edge. The first one is caused by the separation in the corner region. The second one is due to the relative motion between the backflow of corner separation and the rapid flow from the pressure side. The positions of these two vortex cores are also summarized in Fig. D.12e. All the numerical results do not correctly simulate the position of the first vortex, which is located between $s^*=0.80\sim 0.90$. In streamwise direction, the difference between the LDA experiment and the results of the $k-\omega$ turbulence model is the largest. For the distance from the first vortex core to the blade suction side, the result of the S-A turbulence model is the largest. In the LDA experiment, the position of the second vortex core is not obtained. In numerical results, the result of the S-A turbulence model is obviously different with other two numerical results. From the positions of the first and the second vortex, we know approximately that the extent of the corner separation. All the extent of numerical results are larger than that of LDA experimental results; and the extent of the $k-\omega$ turbulence model is the largest.

The numerical results of the streamlines in the second vortex are not the same. There are two styles. The first one is from the interface of the corner stall; the other one is from the adjacent passage near the pressure side. The numerical result of the S-A turbulence model is the first style. The other numerical results are the second style. This phenomenon depends on the relative strength of the corner separation backflow and the flow from the pressure side. When the local velocity of corner separation backflow is larger than the flow from the pressure side, the streamlines in the second vortex are from the interface of the corner separation. On the contrary, when the local velocity of corner separation backflow is smaller than the flow from the pressure side, the streamlines in the second vortex are from the adjacent passage near the pressure side.

The comparisons of mean velocity between the experimental and numerical results at four typical measurement stations are shown in Fig. D.13. At $s^*=0.35$, just forward the separation position of LDA experiment, the streamwise velocity components of numerical results are positive near the blade suction side. This is consistent with the streamlines in Fig. D.12, which indicate the separation of numerical results are forward that of LDA experiment. At $s^*=0.50$, the extent of backflow (where streamwise velocity component is negative) is small, and the extent of backflow will have a jump between $s^*=0.50\sim 0.60$. From the Fig. D.13c, the extent of the backflow of the numerical results are larger than that of LDA experimental results, except the $k-\omega$ turbulence model. At $s^*=0.80$, the flow field is in the region of corner separation and forward from the core of main vortex. From the comparison of streamwise velocity components shown in Fig. D.13e, we observe that the $k-\omega$ turbulence model gives more accurate results than other turbulence models. At $s^*=0.99$, the flow field is also in the region of corner separation but backward of the core of the main vortex. At $s^*=0.80$ and 0.99 , the $k-\omega$ turbulence model performs better than others.

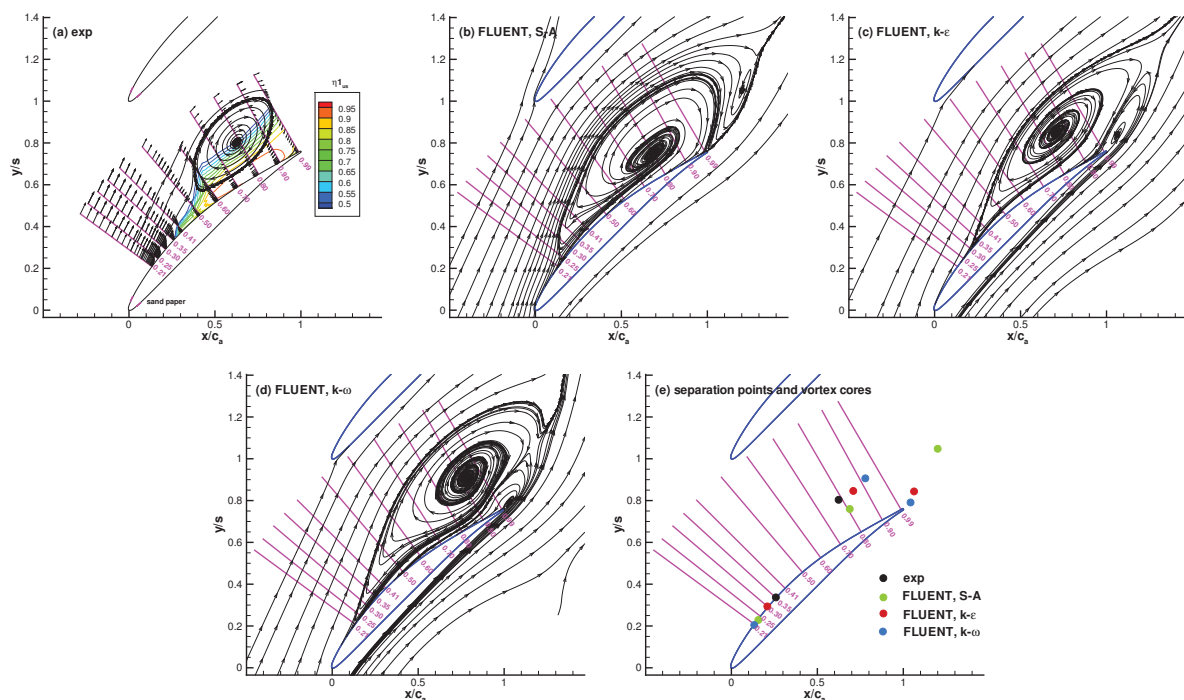


Figure D.12: Comparison of experimental and numerical results of mean velocity at $z=5.00$ mm, $i=4^\circ$. (a) LDA experiment; (b) S-A (c) $k-\epsilon$ (d) $k-\omega$ turbulent models; (e) statistics of separation points and vortex cores.

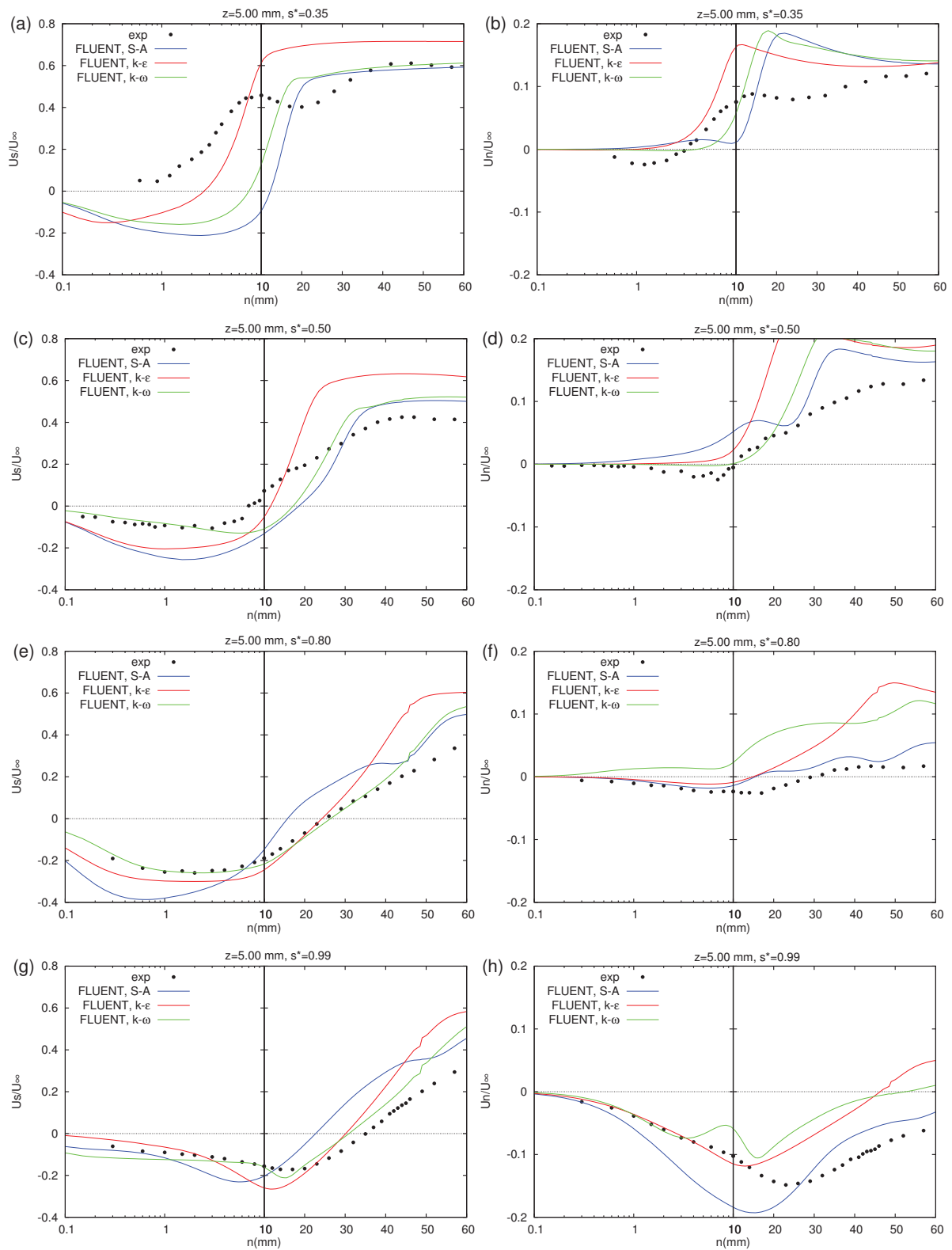


Figure D.13: Comparison of experimental and numerical results of mean velocities at $z=5.00$ mm, $i=4^\circ$.

Appendix E

Code for decomposition of PDF

The MATLAB[®] code used to decompose the PDF of a velocity component into two Gaussian distributions is introduced in this appendix.

```
%read the data of an example histogram
d=load('histogram-example.txt');
a=d(:,2);
b=d(:,1);
% read initial value
para=load('initial-values.txt');

% Create a function that represents two Gaussian distribution.
% The parameters are, in order:
% [mixture proportion, mean1, log of sigma1, mean2, log of sigma2]
% using log to make sure sigma1 and sigma2 are larger than zero
f=@(p,x)p(1)*normpdf(x,p(2),exp(p(3)))+(1-p(1))*normpdf(x,p(4),exp(p(5)));

%Fitting  $f$  to the histogram data using function "nlinfit":
c=nlinfit(a,b,f,[para]);

%plot
x=-0.8:0.005:1;
g1=c(1)*normpdf(x,c(2),exp(c(3)));
g2=(1.0-c(1))*normpdf(x,c(4),exp(c(5)));
g=g1+g2;
plot(a,b,x,g1,x,g2,x,g);

% write fitting parameters
fid=fopen("fitting-results.txt",'w');
fprintf( fid, strcat(repmat('%0.4e ',1,6),'\n'),c);
```

References

- ALBRECHT, H.E., BORYS, M., DAMASCHKE, N. & TROPEA, C. (2003). *Laser Doppler and phase Doppler measurement techniques*. Springer.
- ANDREWS, M.J. (2011). Guidelines for use of commercial software and diagnostics in articles for the journal of fluids engineering. *Journal of Fluids Engineering*, **133**, 010201.
- ANSYS (2006). Fluent 6.3 user's guide.
- AUBERTINE, C.D. & EATON, J.K. (2005). Turbulence development in a non-equilibrium turbulent boundary layer with mild adverse pressure gradient. *Journal of Fluid Mechanics*, **532**, 345–364.
- BAILIE, S.T., HILE, G.A. & PUTERBAUGH, S.L. (2008). Initial characterization of three-dimensional flow separation in a compressor stator. *AIAA 2008-5064*, 1–14.
- BAILLY, C. & COMTE-BELLOT, G. (2003). *Turbulence*. CNRS.
- BARANKIEWICZ, W.S. & HATHAWAY, M.D. (1998). Impact of variable-geometry stator hub leakage in a low speed axial compressor. *ASME 98-GT-194*.
- BARIO, F., LEBOEUF, F. & PAPAILIOU, K.D. (1982). Study of secondary flows in blade cascades of turbomachines. *Journal of Engineering for Power*, **104**, 497–509.
- BASKARAN, V., SMITS, A.J. & JOUBERT, P.N. (1987). A turbulent flow over a curved hill. Part 1. Growth of an internal boundary layer. *Journal of Fluid Mechanics*, **182**, 47–83.
- BASKARAN, V., SMITS, A.J. & JOUBERT, P.N. (1991). A turbulent flow over a curved hill. Part 2. Effects of streamline curvature and streamwise pressure gradient. *Journal of Fluid Mechanics*, **232**, 377–402.
- BELLHOUSE, B.J. & SCHULTZ, D.L. (1966). Determination of mean and dynamic skin friction, separation and transition in low-speed flow with a thin-film heated element. *Journal of Fluid Mechanics*, **24**, 379–400.
- BERNARD, A., FOUCAUT, J.M., DUPONT, P. & STANISLAS, M. (2003). Deceleration boundary layer: a new scaling and mixing length model. *AIAA Journal*, **41**, 248–255.
- BOILLOT, A. & PRASAD, A.K. (1996). Optimization procedure for pulse separation in cross-correlation PIV. *Experiments in Fluids*, **21**, 87–93.
- BRADSHAW, P. (1967). 'Inactive' motion and pressure fluctuations in turbulent boundary layers. *Journal of Fluid Mechanics*, **30**, 241–258.
- BRADSHAW, P. (1973). Effects of streamline curvature on turbulent flow. *AGARDograph No. 169*.

- BRADSHAW, P. & GALEA, P.V. (1967). Step-induced separation of a turbulent boundary layer in incompressible flow. *Journal of Fluid Mechanics*, **27**, 111–130.
- BRUUN, H.H. (1995). *Hot-Wire Anemometry, Principles and Signal Analysis*. Oxford Science Publications.
- BRZEK, B., CAL, R.B., JOHANSSON, G. & CASTILLO, L. (2007). Inner and outer scaling in rough surface zero pressure gradient turbulent boundary layers. *Physics of Fluids*, **19**, 065101.
- CASTILLO, L. & GEORGE, W.K. (2001). Similarity analysis for turbulent boundary layer with pressure gradient: outer flow. *AIAA Journal*, **39**, 41–47.
- CASTRO, I.P. & BRADSHAW, P. (1976). The turbulence structure of a highly curved mixing layer. *Journal of Fluid Mechanics*, **73**, 265–304.
- CELIK, I.B., GHIA, U., ROACHE, P.J., FREITAS, C.J., COLEMAN, H. & RAAD, P.E. (2008). Procedure for estimation and reporting of uncertainty due to discretization in CFD applications. *Journal of Fluids Engineering*, **130**, 078001.
- CHOI, M., BAEK, J.H., OH, S.H. & KI, D.J. (2008). Role of hub-corner-separation on rotating stall in an axial compressor. *Transactions of the Japan Society for Aeronautical and Space Sciences*, **51**, 93–100.
- CLAUSER, F.H. (1954). Turbulent boundary layer in adverse pressure gradients. *Journal of the Aeronautical Sciences*, **21**, 91–108.
- COLEMAN, H.W. & STEELE, W.G. (1989). *Experimentation and Uncertainty Analysis for Engineers*. John Wiley and Sons.
- COLEMAN, H.W. & STEELE, W.G. (1995). Engineering application of experimental uncertainty analysis. *AIAA Journal*, **33**, 1888–1896.
- COLES, D.E. (1956). The law of the wake in the turbulent boundary layer. *Journal of Fluid Mechanics*, **1**, 191–226.
- COMTE-BELLOT, G. (1998). Hot-wire anemometry. In R.W. Johnson, ed., *The Handbook of Fluid Dynamics*, chap. 34, CRC Press.
- CUMPSTY, N.A. (2004). *Compressor Aerodynamics*. Krieger Publishing Company.
- CUMPSTY, N.A. (2010). Preparing for the future: Reducing gas turbine environmental impact - IGTI scholar lecture. *Journal of Turbomachinery*, **132**, 041017.
- CUTLER, A.D. & JOHNSTON, J.P. (1989). The relaxation of a turbulent boundary layer in an adverse pressure gradient. *Journal of Fluid Mechanics*, **200**, 367–387.
- DEGRAAFF, D.B. & EATON, J.K. (2000). Reynolds-number scaling of the flat-plate turbulent boundary layer. *Journal of Fluid Mechanics*, **422**, 319–346.
- DENTON, J.D. (1997). Lessons from rotor 37. *Journal of Thermal Science*, **6**, 1–13.
- DEVENPORT, W.J. & SIMPSON, R.L. (1990). Time-dependent and time-averaged turbulence structure near the nose of a wing-body junction. *Journal of Fluid Mechanics*, **210**, 23–55.
- DOERING, C.R. (2009). The 3D Navier-Stokes problem. *Annual Review of Fluid Mechanics*, **41**, 109–128.

- DONG, Y., GALLIMORE, S.J. & HODSON, H.P. (1987). Three-dimensional flows and loss reduction in axial compressors. *Journal of Turbomachinery*, **109**, 354–361.
- DRING, R.P., JOSLYN, H.D. & HARDIN, L.W. (1982). An investigation of compressor rotor aerodynamics. *Journal of Engineering for Power*, **104**, 84–96.
- DRING, R.P., JOSLYN, H.D. & WAGNER, J.H. (1983). Compressor rotor aerodynamics. In *AGARD-CP-351*.
- DUNHAM, J. (1998). CFD validation for propulsion system components. *AGARD Advisor Report 355*.
- DURST, F., ZANOUN, E.S. & PASHTRAPANSKA, M. (2001). In situ calibration of hot wires close to highly heat-conducting walls. *Experiments in Fluids*, **31**, 103–110.
- ELSBERRY, K., LOEFFLER, J., ZHOU, D. & WYGNANSKI, I. (2000). An experimental study of a boundary layer that is maintained on the verge of separation. *Journal of Fluid Mechanics*, **423**, 227–261.
- EMERY, H.L.J., JAMES C, ERWIN, J.R. & FELIX, A.R. (1958). Systematic two-dimensional cascade tests of NACA 65-series compressor blades at low speeds. *NACA-report-1368*.
- EVANS, B.J. (1971). *Effects of free-stream turbulence on blade performance in a compressor cascade*. Ph.D. thesis, Cambridge University.
- FERNHOLZ, H.H. & FINLEY, P.J. (1996). The incompressible zero-pressure-gradient turbulent boundary layer: an assessment of the data. *Progress in Aerospace Sciences*, **32**, 245–311.
- FRIEDMANN, P.P. (2011). Editorial policy statement on numerical and experimental accuracy. *AIAA Journal*, **49**, 16.
- GAND, F. (2011). *Dynamique des écoulements de jonction en régime turbulent (In French)*. Ph.D. thesis, Université Pierre et Marie Curie.
- GBADEBO, S.A. (2003). *Three-Dimensional Separations in Compressors*. Ph.D. thesis, University of Cambridge.
- GBADEBO, S.A., HYNES, T.P. & CUMPSTY, N.A. (2004). Influence of surface roughness on three-dimensional separation in axial compressors. *Journal of Turbomachinery*, **126**, 455–463.
- GBADEBO, S.A., CUMPSTY, N.A. & HYNES, T.P. (2007). Interaction of tip clearance flow and three-dimensional separations in axial compressors. *Journal of Turbomachinery*, **129**, 679–685.
- GEORGE, W.K. (2006). Recent advancements toward the understanding of turbulent boundary layers. *AIAA Journal*, **44**, 2435–2449.
- GEORGE, W.K. (2007). Is there a universal log law for turbulent wall-bounded flows? *Philosophical Transactions of the Royal Society A*, **365**, 789–806.
- GEORGE, W.K. & CASTILLO, L. (1997). Zero pressure gradient turbulent boundary layer. *Applied Mechanics Reviews*, **50**, 689–729.
- GEORGE, W.K., STANISLAS, M. & LAVAL, J.P. (2010). New insights into adverse pressure gradient boundary layers. *DFD10 Meeting of the American Physical Society*.
- GODARD, A. (2010). *Etude numérique et expérimentale d'un compresseur aspiré (In French)*. Ph.D. thesis, Ecole Centrale de Lyon.

- GOODHAND, M.N. & MILLER, R.J. (2012). The impact of real geometries on three-dimensional separations in compressors. *Journal of Turbomachinery*, **134**, 021007.
- GREITZER, E.M., TAN, C.S. & GRAF, M.B. (2004). *Internal Flow: Concepts and Applications*. Cambridge University Press.
- HAH, C. & LOELLBACH, J. (1999). Development of hub corner stall and its influence on the performance of axial compressor blade rows. *Journal of Turbomachinery*, **121**, 67–77.
- HALSTEAD, D.E., WISLER, D.C., OKIISHI, T.H., WALKER, G.J., HODSON, H.P. & SHIN, H.W. (1997). Boundary layer development in axial compressors and turbines: Part 1-4. *Journal of Turbomachinery*, **119**, 114–127, 426–444, 225–237, 128–139.
- HOBSON, G.V., WILLIAMS, A.J.H. & GANAİM RICKEL, H.J. (1998). Laser-Doppler-velocimetry measurements in a cascade of compressor blades at stall. *Journal of Turbomachinery*, **120**, 170–178.
- HODSON, H.P., HUNTSMAN, I. & STEELE, A.B. (1994). An investigation of boundary layer development in a multistage LP turbine. *Journal of Turbomachinery*, **116**, 375–383.
- HUTCHINS, N., NICKELS, T.B., MARUSIC, I. & CHONG, M.S. (2009). Hot-wire spatial resolution issues in wall-bounded turbulence. *Journal of Fluid Mechanics*, **635**, 103–136.
- IBRAHIM, K., FIDRICH, M. & BACHALO, W. (1994). Evaluations of an advanced real-time signal processing system using the Fourier transform. *Proceedings of the 2nd International Conference on Fluid Dynamics Measurements and its Applications, Beijing, China*.
- ISO (1999). Evaluation of measurement data - guide to the expression of uncertainty in measurements (gum). *ISO, IEC, IFCC, BIPM, IUPAC, UIPAP, OIML, Norme NF ENV 13005*.
- JONES, M.B., NICKELS, T.B. & MARUSIC, I. (2008). On the asymptotic similarity of the zero-pressure-gradient turbulent boundary layer. *Journal of Fluid Mechanics*, **616**, 195–203.
- JORGENSEN, F.E. (2002). How to measure turbulence with hot-wire anemometers - a practical guide. *Dantec Dynamics, Publication NO.: 9040U6151*.
- JOSLYN, H.D. & DRING, R.P. (1985). Axial compressor stator aerodynamics. *Journal of Engineering for Gas Turbines and Power*, **107**, 485–493.
- KIM, S.A., WALKER, D.A. & SIMPSON, R.L. (1991). Observation and measurements of flow structures in the stagnation region of a wing-body junction. *Technical report of Virginia Polytechnic Institute and State University VPI-E-91-20*.
- KING, L.V. (1914). On the convection of heat from small cylinders in a stream of fluid: determination of the convection constants of small platinum wires with applications to hot-wire anemometry. *Philosophical Transactions of the Royal Society of London*, **214**, 373–432.
- LAKSHMINARAYANA, B. (1996). *Fluid Dynamics and Heat Transfer in Turbomachinery*. John Wiley and Sons, New York.
- LAVISION (2007). *Manual for DaVis 7.2, Item-Number(s):1105011-4*.
- LEI, V.M. (2006). *A Simple Criterion for Three-Dimensional Flow Separation in Axial Compressors*. Ph.D. thesis, Massachusetts Institute of Technology.

- LEI, V.M., SPAKOVSKY, Z.S. & GREITZER, E.M. (2008). A criterion for axial compressor hub-corner stall. *Journal of Turbomachinery*, **130**, 031006.
- LIEBLEIN, S. (1959). Loss and stall analysis of compressor cascades. *Journal of Basic Engineering*, 387–400.
- LIU, B., YU, X., LIU, H., JIANG, Y.H., HAOKANG & XU, Y. (2006). Application of SPIV in turbomachinery. *Experiments in Fluids*, **40**, 621–642.
- LIU, K. & PLETCHER, R.H. (2008). Anisotropy of a turbulent boundary layer. *Journal of Turbulence*, **9**, 1–18.
- LUDWIG, H. & TILLMAN, W. (1950). Investigations of the wall-shearing stress in turbulent boundary layers. *NACA-TM-1285*.
- MA, W., WANG, D. & LU, L. (2008). Investigation on improving the capability of prediction separation of Spalart-Allmaras turbulence model (In Chinese). *Journal of Aerospace Power*, **23**, 1474–1479.
- MARUSIC, I. & KUNKEL, J.G. (2003). Streamwise turbulence intensity formulation for flat-plate boundary layers. *Physics of Fluids*, **15**, 2461–2464.
- MARUSIC, I., MCKEON, B.J., MONKEWITZ, P.A., NAGIB, H.M., SMITS, A.J. & SREENIVASAN, K.R. (2010). Wall-bounded turbulent flows: recent advances and key issues. *Physics of Fluids*, **22**, 065103.
- MATERNY, M., DRÓZDŹ, A., DROBNIAK, S. & ELSNER, W. (2008). Experimental analysis of turbulent boundary layer under the influence of adverse pressure gradient. *Archives of Mechanics*, **60**, 449–466.
- MERZKIRCH, W. (1987). *Flow visualization*. Academic Press, 2nd edn.
- METZGER, M.M., KLEWICKI, J.C., BRADSHAW, K.L. & SADR, R. (2001). Scaling the near-wall axial turbulent stress in the zero pressure gradient boundary layer. *Physics of Fluids*, **13**, 1819–1821.
- MONSON, D., MATEER, G.G. & MENTER, F. (1993). Boundary-layer transition and global skin friction measurements with an oil-fringe imaging technique. *SAE technical paper series 932550, Aerotech '93, 27–30 September, Costa Mesa, CA*.
- MUTHANNA, C. & DEVENPORT, W.J. (2004). Wake of a compressor cascade with tip gap, part 1: Mean flow and turbulence structure. *AIAA Journal*, **42**, 2321–2331.
- NAGIB, H.M. & CHAUHAN, K.A. (2008). Variations of von Kármán coefficient in canonical flows. *Physics of Fluids*, **20**, 101518.
- NAGIB, H.M., CHAUHAN, K.A. & MONKEWITZ, P.A. (2007). Approach to an asymptotic state for zero pressure gradient turbulent boundary layers. *Philosophical Transactions of the Royal Society A*, **365**, 755–770.
- NOBACH, H. & BODENSCHATZ, E. (2009). Limitations of accuracy in PIV due to individual variations of particle image intensities. *Experiments in Fluids*, **47**, 27–38.
- OTTAVY, X. & HODSON, H. (2000). The effects of wake-passing unsteadiness in high loaded axial compressor blades design - case of a flat plate. Tech. rep., Whitte Laboratory, Cambridge University.
- PAIK, J., ESCAURIAZA, C. & SOTIROPOULOS, F. (2007). On the bimodal dynamics of the turbulent horse-shoe vortex system in a wing-body junction. *Physics of Fluids*, **19**, 045107.

- PATEL, V.C. (1965). Calibration of the Preston tube and limitations on its use in adverse pressure gradients. *Journal of Fluid Mechanics*, **23**, 185–208.
- PATEL, V.C. & SOTIROPOULOS, F. (1997). Longitudinal curvature effects in turbulent boundary layers. *Progress in Aerospace Sciences*, **33**, 1–70.
- PERRY, A.E. & CHONG, M.S. (2000). Interpretation of flow visualization. In A.J. Smits & T.T. Lim, eds., *Flow Visualization*, chap. 1, Imperial College Press.
- PERRY, A.E. & SCHOFIELD, W.H. (1973). Mean velocity and shear stress distributions in turbulent boundary layers. *Physics of Fluids*, **16**, 2068–2074.
- PETERSON, S.D. & PLESNIAK, M.W. (2004). Surface shear stress measurements around multiple jets in crossflow using the fringe imaging skin friction technique. *Experiments in Fluids*, **37**, 497–503.
- PINKERTON, R.M. (1936). Calculated and measured pressure distributions over the midspan section of the NACA 4412 airfoil. *NACA Report No. 563*.
- PIQUET, J. (2001). *Turbulent Flows Models and Physics*. Springer, 2nd edn.
- POPE, S.B. (2000). *Turbulent Flows*. Cambridge University Press.
- RAFFEL, M., WILLERT, C.E., WERELEY, S.T. & KOMPENHANS, J. (2007). *Particle Image Velocimetry - A Practical Guide*. Springer, 2nd edn.
- SACHDEVA, A. (2009). *Study and control of three dimensional flow separations in a high pressure compressor stator blade row with boundary layer aspiration*. Ph.D. thesis, Ecole Centrale de Lyon.
- SCHLATTER, P. & ÖRLÜ, R. (2010). Assessment of direct numerical simulation data of turbulent boundary layers. *Journal of Fluid Mechanics*, **659**, 116–126.
- SCHLICHTING, H. (1979). *Boundary Layer Theory*. McGraw-Hill.
- SCHLICHTING, H. & GERSTEN, K. (1999). *Boundary Layer Theory*. Springer, 8th edn.
- SCHREIBER, H.A., STEINERT, W. & KÜSTERS, B. (2002). Effects of Reynolds number and free-stream turbulence on boundary layer transition in a compressor cascade. *Journal of Turbomachinery*, **124**, 1–9.
- SCHULZ, H.D. & GALLUS, H.E. (1988). Experimental investigations of the three-dimensional flows in an annular compressor cascade. *Journal of Turbomachinery*, **110**, 467–478.
- SCHULZ, H.D., GALLUS, H.E. & LAKSHMINARAYANA, B. (1990a). Three-dimensional separated flow field in the endwall region of an annular compressor cascade in the presence of rotor-stator interaction: Part 1-quasi-steady flow field and comparison with steady-state data. *Journal of Turbomachinery*, **112**, 669–678.
- SCHULZ, H.D., GALLUS, H.E. & LAKSHMINARAYANA, B. (1990b). Three-dimensional separated flow field in the endwall region of an annular compressor cascade in the presence of rotor-stator interaction: Part 2-unsteady flow and pressure field. *Journal of Turbomachinery*, **112**, 679–688.
- SETTLES, G.S. & TENG, H.Y. (1983). Flow visualization methods for separated three-dimensional shock wave/turbulent boundary-layer interactions. *AIAA Journal*, **21**, 390–397.
- SHAH, S.I., LAVAL, J.P. & STANISLAS, M. (2009). A specific behaviour of adverse pressure gradient near wall flows. *Proceeding of the WALLTURB International Workshop, Lille, France, April 21-23*.

- SIMPSON, R.L. (1996). Aspects of turbulent boundary-layer separation. *Progress in Aerospace Sciences*, **32**, 457–521.
- SIMPSON, R.L. (2001). Junction flows. *Annual Review of Fluid Mechanics*, **33**, 415–443.
- SIMPSON, R.L., CHEW, Y.T. & SHIVAPRASAD, B.G. (1981a). The structure of a separating turbulent boundary layer. Part 1. Mean flow and Reynolds stresses. *Journal of Fluid Mechanics*, **113**, 23–51.
- SIMPSON, R.L., CHEW, Y.T. & SHIVAPRASAD, B.G. (1981b). The structure of a separating turbulent boundary layer. Part 2. Higher-order turbulence results. *Journal of Fluid Mechanics*, **113**, 53–73.
- SKÅRE, P.E. & KROGSTAD, P.A. (1994). A turbulent equilibrium boundary layer near separation. *Journal of Fluid Mechanics*, **272**, 319–348.
- SMATI, L. (1997). *Contribution au développement d'une méthode numérique d'analyse des écoulements instationnaires. Applications aux turbomachines*. Ph.D. thesis, Ecole Centrale de Lyon.
- SMITS, A.J. & WOOD, D.H. (1985). The response of turbulent boundary layers to sudden perturbations. *Annual Review of Fluid Mechanics*, **17**, 321–358.
- SMITS, A.J., MCKEON, B.J. & MARUSIC, I. (2011). High-Reynolds number wall turbulence. *Annual Review of Fluid Mechanics*, **43**, 353–375.
- SPALART, P. (2006). Turbulence: Are we getting smarter? *Fluid Dynamics Award Lecture, 36th Fluid Dynamics Conference and Exhibit, San Francisco, CA, 5-8 June*.
- SPALART, P. & WATMUFF, J. (1993). Experimental and numerical study of a turbulent boundary layer with pressure gradients. *Journal of Fluid Mechanics*, **249**, 337–371.
- SPALART, P.R. & ALLMARAS, S.R. (1992). A one-equation turbulence model for aerodynamic flows. *AIAA-92-0439*.
- SPALART, P.R. & ALLMARAS, S.R. (1994). A one-equation turbulence model for aerodynamic flows. *La Recherche Aérospatiale*, **1**, 5–21.
- SPALDING, D.B. (1961). A single formula for the law of the wall. *Journal of Applied Mechanics*, **28**, 455–458.
- SREENIVASAN, K.R. (1989). The turbulent boundary layer. *Frontiers in experimental fluid mechanics*, **46**, 159–209.
- STANISLAS, M., OKAMOTO, K., KÄHLER, C.J., WESTERWEEL, J. & SCARANO, F. (2008). Main results of the third international PIV challenge. *Experiments in Fluids*, **45**, 27–71.
- STRAZISAR, A.J. & DENTON, J.D. (1995). CFD code assessment in turbomachinery - a progress report. *IGIT Global Gas Turbine News, May/June*, 12–14.
- SUDER, K.L. (1996). Experimental investigation of the flow field in a transonic, axial flow compressor with respect to the development of blockage and loss. *NASA-TM-107310*.
- SUDER, K.L. & CELESTINA, M.L. (1996). Experimental and computational investigation of the tip clearance flow in a transonic axial flow compressor rotor. *Journal of Turbomachinery*, **118**, 218–229.

- SWAMY, K.M.M. & KUMARAN, R.S. (2009). Estimation of turbomachinery flow losses through cascade testing, seminar on Loss Mechanisms in Steam and Gas Turbines, held at M.S. Ramaiah School of Advanced Studies.
- TRUCKENBRODT, E. (1973). *Neuere Erkenntnisse über die Berechnung von Strömungsgrenzschichten mittels einfacher Quadraturformeln.*
- VAN DRIEST, E.R. (1956). On turbulent flow near a wall. *Journal of the Aeronautical Sciences*, **23**, 1007–1011, 1036.
- WANG, D., LU, L. & LI, Q. (2009). Improvement on SA model for predicting corner separation based on turbulence transport nature. *AIAA 2009-4931*.
- WANG, Y. & DEVENPORT, W.J. (2004). Wake of a compressor cascade with tip gap, part 2: Effects of endwall motion. *AIAA Journal*, **42**, 2322–2340.
- WENGER, C.W., DEVENPORT, K.S., WILLIAM JAAND WITTMER & MUTHANNA, C. (2004). Wake of a compressor cascade with tip gap, part 3: Two-point statistics. *AIAA Journal*, **42**, 2341–2346.
- WESTERWEEL, J. (1997). Fundamentals of digital particle image velocimetry. *Measurement Science and Technology*, **8**, 1379–1392.
- WESTERWEEL, J. (1998). Effect of sensor geometry on the performance of PIV interrogation. *Proceedings of the 9th International Symposium on Applications of Laser Techniques Applied to Fluid Mechanics, Lisbon, Portugal*, 37–55.
- WESTERWEEL, J. (2000). Theoretical analysis of the measurement precision in particle image velocimetry. *Experiments in Fluids*, **Supplement 1**, 3–12.
- WISLER, D.C. (1985). Loss reduction in axial flow compressors through low-speed model testing. *Journal of Engineering for Gas Turbines and Power*, **107**, 354–363.
- WOSNIK, M., CASTILLO, L. & GEORGE, W.K. (2000). A theory for turbulent pipe and channel flow. *Journal of Fluid Mechanics*, **421**, 115–145.
- YU, X. & LIU, B. (2010). A prediction model for corner separation/stall in axial compressors. *ASME GT2010-22453*.
- ZAGAROLA, M.V. & SMITS, A.J. (1998a). Mean-flow scaling of turbulent pipe flow. *Journal of Fluid Mechanics*, **373**, 33–79.
- ZAGAROLA, M.V. & SMITS, A.J. (1998b). A new mean velocity scaling for turbulent boundary layers. *Proceedings of FEDSM'98*.

List of Figures

1.1	High-loss regions in compressors (Wisler, 1985).	3
1.2	Schematic representation of the flow field in an axial flow compressor rotor passage.	3
2.1	The variation of the constants in the law of the wall (κ , B and Π) with Reynolds number.	9
2.2	Developments of Reynolds stresses in a TBL with ZPG	11
2.3	Variation of maximum of Reynolds shear stress ($-\overline{u'v'}$) with the Reynolds number.	11
2.4	Influences of curvature	16
2.5	Impact of corner separation (Barankiewicz & Hathaway, 1998).	18
2.6	Topology of the corner stall, proposed by Schulz <i>et al.</i> (1990a).	20
2.7	Topology of corner stall, proposed by Hah & Loellbach (1999).	20
2.8	S and D , when Re , AR , δ/c are constant (Lei <i>et al.</i> , 2008).	25
3.1	General view of the cascade in LMFA, Ecole Centrale de Lyon.	30
3.2	Side and top views of the cascade.	30
3.3	Parameters of blade.	31
3.4	Notation for cascade, in the coordinates of cascade.	32
3.5	Sketch of trips.	33
3.6	Curvature of the blade suction side.	33
3.7	Arrangement of the blade and the endwall.	35
3.8	Pressure taps on the blade.	35
3.9	Pressure taps on the endwall.	36
3.10	Photo and scheme of the five-hole pressure probe.	37
3.11	Calibration data of the five-hole pressure probe.	39
3.12	Sketch of the effects of total pressure gradient on the angle measured by a pressure probe.	40
3.13	Coordinate of the five-hole pressure probe.	40
3.14	Arrangement of the five-hole pressure probe.	41
3.15	Measurement positions of the five-hole pressure probe.	41
3.16	An example of absolute and relative uncertainties of static pressure on the blade.	42
3.17	An example of absolute and relative uncertainties of static pressure on the endwall.	43
3.18	An example of uncertainties of results measured by the five-hole pressure probe.	51
3.19	A basic CTA circuit.	53
3.20	Dantec probe (from the web of Dantec). The dimensions are in millimeters.	53
3.21	Hot-wire probe mounting and positioning: (a) a snap in the experiment; (b) circuit diagram for probe positioning; (c) position of hot-wire and influences of vibration.	54
3.22	Hotwire calibration.	55
3.23	Transfer function between bridge voltage and velocity.	56
3.24	Absolute and relative errors of mean velocity measured by HWA.	57

3.25	PIV principle, adopted from Dantec.	58
3.26	Set-up of PIV.	59
3.27	PIV measurement sections (perpendicular to the spanwise direction).	59
3.28	Displacement histogram of a typical flow field.	60
3.29	Convergence statistics at the reference points, $x/c_a=0.683$ and $y/s=0.827$	61
3.30	Absolute and relative uncertainty for the magnitude of the velocity $\sqrt{U_x^2 + U_y^2}$	63
3.31	LDA principle from Dantec.	64
3.32	Set-up of LDA.	66
3.33	Examples of measurement stations.	66
3.34	Velocity decomposition.	67
3.35	LDA measurement stations.	67
3.36	Absolute and relative errors of mean velocity measured by LDA.	72
3.37	Test procedure.	74
3.38	Skewness of inflow.	74
3.39	Periodicity of the test section at outlet.	75
3.40	Grid distribution.	80
4.1	Measurements used in this chapter.	83
4.2	Experimental results of inlet boundary layer, measured by HWA.	85
4.3	Spectra of streamwise velocity at the point where $z=0.17$ mm and $z^+=15.9$, measured by HWA.	87
4.4	Evolution of boundary layer in streamwise direction.	88
4.5	Sketch of evolution of boundary layer in streamwise direction.	88
4.6	Experimental distribution of C_p on the blade at five incidences.	92
4.7	Experimental distribution of C_p on the blade at $i=4^\circ$	92
4.8	Numerical results of static pressure and streamlines on the blade and endwall at five incidences.	93
4.9	Experimental and numerical results of static pressure on the blade at five incidences.	94
4.10	Experimental and numerical F_x and F_y at five incidences.	95
4.11	Experimental and numerical F_x^* , F_y^* and F_y^*/F_x^*	95
4.12	Experimental static pressure coefficients on the endwall at five incidences.	96
4.13	Numerical static pressure coefficients on the endwall at five incidences.	96
4.14	Experimental exit total pressure loss coefficient at the outlet section 1 at five incidences.	97
4.15	Numerical exit total pressure loss coefficient at the outlet section 1 at five incidences.	97
4.16	Experimental and numerical ω^* and ω'	98
4.17	Experimental results of the total pressure losses coefficient distributions.	99
4.18	Comparisons of experimental and numerical results of ω^* and ω'	99
4.19	Experimental results of vector in the y - z plane, $i=4^\circ$	101
4.20	Experimental results of vector at three measurement sections, $i=4^\circ$	103
4.21	Experimental and numerical results of magnitude of the vector in $x - y$ planes, $i=4^\circ$	104
5.1	Three factors at mid-span.	108
5.2	Numerical result of the contour of the static pressure at mid-span.	110
5.3	Streamwise and wall-normal pressure gradients at mid-span.	110
5.4	Numerical results.	111
5.5	Values of $K\delta$ at LDA measurement stations.	113
5.6	Effects of wall-normal pressure gradient and curvature at mid-span, $i=4^\circ$	113
5.7	Experimental results of mean velocity vector \vec{U}/U_∞ at mid-span, $i=4^\circ$	114

5.8	Experimental and numerical results of mean velocity at mid-span, $i=4^\circ$	116
5.9	Experimental results shown together at each measurement station, $s^*=0.21\sim 0.50$	117
5.9	Experimental results shown together at each measurement station, $s^*=0.60\sim 0.99$	118
5.10	Separation process of TBLs.	120
5.11	Backflow coefficients of streamwise velocity u_s at mid-span, $i = 4^\circ$	120
5.12	Example of histogram of streamwise velocity u_s at the point $s^*=0.99$ & $n=0.15$ mm.	120
5.13	Illustration of the methods to determine the thickness of boundary layer and the potential flow velocity.	121
5.14	Boundary layer parameters. Lines for visual aid only.	123
5.15	Relation between H_{23} and H	127
5.16	Relation between H_{12} and H_{32}	127
5.17	Mean velocity profiles in inner coordinate.	130
5.18	Velocity defect profiles. Lines for visual aid only.	131
5.19	Developments of Reynolds stresses in a TBL with ZPG.	133
5.20	(a)Developments of Reynolds stresses $\overline{u'^2}/u_\tau^2$ with Re_θ in TBLs with ZPG. (b) Effects of upstream flow on $\overline{u'^2}$	134
5.21	Development of $\overline{u'^2}$ in TBLs with APG.	134
5.22	Developments of mean velocities and Reynolds stresses in a TBL with APG.	135
5.23	We propose absolute developments of Reynolds stresses under the effects of upstream flow and APG.	137
5.24	Reynolds stresses normalized by U_∞ plotted against n	139
5.25	Reynolds stresses normalized by U_∞ plotted against n/δ	140
5.26	Reynolds stresses normalized by u_τ in inner variables.	141
5.27	Reynolds stresses normalized by u_τ in outer variables.	142
5.28	Second order correlation ratios	144
5.29	Triple correlations.	147
5.30	Skewness and flatness.	149
5.31	Examining scalings.	150
5.32	Characteristics of a special point in the TBL.	153
6.1	Experimental and numerical results of equivalent diffusion factor (DF_{eq}).	157
6.2	Relation between the diffusion parameter D and i	157
6.3	Results of oil visualization, $i=4^\circ$	157
6.4	Topology of corner stall.	158
6.5	Two different experimental layouts.	158
6.6	LDA measurement positions.	159
6.7	LDA experimental results of mean velocity vectors in the cross sections in the spanwise direction.	160
6.8	LDA experimental results of $\overline{u'_s u'_s}/U_\infty^2$ in the cross sections in the spanwise direction. Pink points, the points with bimodal histograms.	161
6.9	LDA experimental results of $\overline{u'_n u'_n}/U_\infty^2$ in the cross sections in the spanwise direction. Pink points, the points with bimodal histograms.	162
6.10	LDA experimental results of $\overline{u'_s u'_n}/U_\infty^2$ in the cross sections in the spanwise direction. Pink points, the points with bimodal histograms.	163
6.11	LDA experimental results of mean velocity vectors.	165
6.12	PIV results of mean axial velocity, $i=4^\circ$: (a) all measurement stations; (b) $z=20.00$ mm.	167

6.13	Comparison of mean velocities between LDA and PIV along the line of $s^*=0.80$ in $x-y$ plane, $i=4^\circ$	168
6.14	Experimental results of $z=5.00$ mm.	169
6.15	Junction flow, from Devenport & Simpson (1990) and Simpson (2001)	171
6.16	Descriptive model for the sequence of flow events in the nose region of a Rood wing-body junction.	171
6.17	Instantaneous snapshot of 3D coherent structures around the wing using the q criterion.	172
6.18	Bimodal histograms in a linear cascade, from Hobson et al. (1998) . (a) LDA measurement stations; (b-c) the histograms of two velocity components at the point 2.	173
6.19	Illustration of bimodal behaviour at the measurement point $z=5.00$ mm & $s^*=0.41$ & $n=6.50$ mm.	175
6.20	Sketch of angles θ_1 and θ_2	178
6.21	PDF of 2D velocity at the measurement station $z=5.00$ mm & $s^*=0.41$	180
6.22	Contours of the PDF of 2D velocity at the measurement station $z=5.00$ mm & $s^*=0.41$	181
6.23	PDFs of u_s at the measurement station $z=5.00$ mm & $s^*=0.41$	182
6.24	PDFs of u_n at the measurement station $z=5.00$ mm & $s^*=0.41$	183
6.25	Bimodal parameters at the measurement station $z=5.00$ mm & $s^*=0.41$	184
6.26	Spectra of instantaneous velocity components.	185
6.27	Instantaneous flow fields in the corner region, measured by PIV. Colored with axial velocity.	186
A.1	Uncertainty analysis	193
A.2	Propagation of uncertainties into an experimental result (Coleman & Steele, 1995)	195
B.1	Comparison of results without and with correction according to the total pressure gradient.	198
C.1	Location of the trip and the velocity near the trip at mid-span.	199
C.2	Influence of the trips on the transition, $i=4^\circ$	200
C.3	Influence of the trips on pressure distribution on the blade.	201
C.4	Influence of the trips on the nearby flow field at mid-span, $i=4^\circ$	202
D.1	Numerical results of static pressure and streamlines on the blade and then endwall at $i=4^\circ$	206
D.2	Experimental and numerical results of C_p on the blade, $i=4^\circ$	206
D.3	Experimental and numerical F_x, F_y at $i=4^\circ$	207
D.4	Experimental and numerical F_x^*, F_y^* and F_y^*/F_x^*	207
D.5	Numerical results of static pressure coefficients on the endwall at $i=4^\circ$	208
D.6	Numerical results of exit total pressure loss coefficient at the outlet section 1 at $i=4^\circ$	208
D.7	Experimental and numerical of ω^* and ω'	208
D.8	Experimental and numerical developments of ω' in the outlet sections at $i=4^\circ$	209
D.9	Experimental and numerical results of magnitude of the vector in $x-y$ planes, $i=4^\circ$	209
D.10	Illustration of angles θ_{xy} and θ_{xz} in the coordinate of cascade.	210
D.11	Experimental and numerical results of angles at the first measurement sections, $i=4^\circ$	210
D.12	Comparison of experimental and numerical results of mean velocity at $z=5.00$ mm, $i=4^\circ$	212
D.13	Comparison of experimental and numerical results of mean velocities at $z=5.00$ mm, $i=4^\circ$	213

List of Tables

3.1	Half thickness of NACA 65-009 airfoils, in the coordinates of blade.	31
3.2	Geometric parameters of the cascade.	32
3.3	The location of surface pressure ports on the blade, in the coordinates of blade.	35
3.4	The location of surface pressure ports on endwall, in the coordinates of cascade.	36
3.5	Uncertainties of 1D hot-wire outside the boundary layer.	57
3.6	Parameters of LDA sensor.	66
3.7	Relative errors of parameters measured by LDA in the region far from the wall.	72
4.1	Summary of measurements used in this chapter.	83
4.2	Parameters of 1D hotwire probes.	85
4.3	Parameters of inlet boundary layers measured by HWA.	85
5.1	Characteristic parameters of boundary layer.	121

AUTORISATION DE SOUTENANCE

Vu les dispositions de l'arrêté du 7 août 2006,

Vu la demande du Directeur de Thèse

Monsieur F. LEBOEUF

et les rapports de

Monsieur M. STANISLAS
Professeur - Ecole Centrale de Lille - Cité Scientifique - 59655 Villeneuve d'Ascq cedex

Et de

Monsieur X. SUN
Professeur - Beihang University - School of Jet Propulsion - Fluid Mechanics and Acoustics Laboratory -
37# Xueyuan Road - Haidian District - 100083 BEIJING - CHINE

Monsieur MA Wei

est autorisé à soutenir une thèse pour l'obtention du grade de **DOCTEUR**

Ecole doctorale MECANIQUE, ENERGETIQUE, GENIE CIVIL ET ACOUSTIQUE

Fait à Ecully, le 10 février 2012

P/Le directeur de l'E.C.L.
La directrice des Etudes

